STRUCTURAL RESPONSE EVALUATION USING NON-UNIFORM SENSOR ARRAYS

A Dissertation

by

MAOPENG FANG

Submitted to the Office of Graduate and Professional Studies of
Texas A&M University
in partial fulfillment of the requirements for the degree of

DOCTOR OF PHILOSOPHY

Chair of Committee,	John M. Niedzwecki
Committee Members,	Charles P. Aubeny
	H. Joseph Newton
	Norris Stubbs
Head of Department,	Robin Autenrieth

December 2013

Major Subject: Ocean Engineering

Copyright 2013 Maopeng Fang

ABSTRACT

Sensor arrays strategically deployed on various offshore structures may provide valuable information in addressing issues related to the complex dynamic response behavior due to varying environments, changing hydrodynamics and purposely attached engineering devices. The current work was devoted to developing techniques to (1) optimize the sensor array according to specific engineering goals, (2) use response data obtained from the sensors to evaluate structures‟ extreme responses, (3) extract modal parameters, and (4) analyze strength conditions. The computational tool developed in this study integrated genetic algorithms, modal recognition techniques, damage detection methods, time series and spectral analysis methods. Genetic algorithms, originally proposed for solving optimization problems based on natural selection, have demonstrated capabilities in obtaining the optimal sensor array configurations in extracting a single mode or two modes simultaneously. This finding laid the foundation for further modal recognition and damage analysis.

The first application discussed herein focused on response evaluation of long and flexible subsea transmission lines; specifically, evaluating the performance of flow-induced vibration suppression devices and buoyancy elements. With laboratory data, the study demonstrated that airfoil fairings, ribbon fairings and helical strakes can all effectively suppress the undesired vibrations in a uniform current; however, the first two devices were not quite effective, especially airfoil fairings, when the structures were subjected to combined loads of current and waves (though all devices significantly increased the damping). In addition, the study showed modal parameters extracted with optimized sensor arrays can help detect, locate and size damages in a structure via numerical simulation (though the performance of the methodology may decrease with localized non-uniform strength profiles and excessive marine growth).

The second application extended the methodologies from 1-D beam-like structures to 2-D plate-like structures. These studies focused on strength analyses of various ice sheet formations. The results illustrated, in spite of the exponentially

increased computational volume, fine-tuned genetic algorithms can still locate near optimal sensor arrays regardless of boundary conditions and placement restrictions due to complicated Arctic environments. Furthermore, the damage detection methodology utilized herein proved to be able not only to detect weak regions but also to detect strengthened areas in ice sheets, for example an ice ridge, thus complete strength analyses of selected ice sheet formations can be conducted.

To all the members of my family

Thank you, Uncle Ruihe and Aunt Enying, for your caring support in my life

ACKNOWLEDGEMENTS

I would like to express my gratitude to my advisor Dr. John M. Niedzwecki during my doctoral studies at Texas A&M University. I thank him for his guidance on developing concentration, discipline and clear focus in conducting research. I thank him for his advice on practicing critical thinking and efficient communication skills to be a good researcher individually and collectively. Considering my foreign background, I thank him for helping me pass through the cultural barriers. I would also like to extend my gratitude to my advisory committee members Dr. Norris Stubbs, Dr. H. Joseph Newton and Dr. Charles P. Aubeny for their input and guidance throughout this research as well as course works I learnt from them on System Identification, Time Series and Numerical Methods for Geotechnical Engineering.

I gratefully acknowledge the financial support for my research by the Wofford Cains‟13 Senior Endowed Chair in Offshore Technology. I would also like to acknowledge Dr. Jianmin Yang, Dr. Runpei Li, Dr. Shixiao Fu and Mr. Leijian Song from Shanghai Jiao Tong University for their help on the experimental data and insightful discussions.

I would like to thank my friends for their help and support. I enjoyed discussing various research topics with Dr. Xiaochuan Yu, Dr. Zhiyong Su, Dr. Amir H. Izadparast, Mr. Gilbert A. Malinga, Mr. Yanbin Bai, Miss Ying-Po Liao, Mr. Rajesh Kumar Doddi, Mr. Yucheng Zhao, Mr. Hooi Siang Kang and my other fellow friends. I am deeply thankful for all my family members for their emotional and financial support over the years. Finally I gratefully thank my wife Adelle Xue Yang, who has been supporting me, encouraging me and inspiring me.

TABLE OF CONTENTS

Page

LIST OF FIGURES

LIST OF TABLES

1. INTRODUCTION

As the offshore industry has ventured into ultra-deep waters in recent years, there has been an ever-increasing demand for better safety and environmental security. The deepest semi-submersible platforms can operate in water depth of over 7000 ft while the deepest Spar platform sets the record as 8000 ft. Operations in those water depths pose serious challenges to design and maintenance of critical system components such as risers, mooring lines and pipelines. Service lives of such critical components are controlled by the motion-induced fatigue due to cyclic environmental loads and vessel motion, and by various damages and defects incurred during manufacturing, installation and operations due to collision, internal and external corrosion, and excessive pressure and temperature. This study focuses on developing a computational tool that integrates data obtained from sensor arrays optimized in number and location to get access to changes of structures‟ dynamic and modal behavior. The computational tool can be implemented to assess the structure‟s responses, identify regions of concern along the structure regarding possible failures, and guide the exploitation of information for other engineering purposes.

Structures‟ dynamic and modal behavior obtained from sensors can be used to evaluate the performance of vibration suppression devices. One example is the suppression of undesired flow-induced vibrations (FIV) of slender offshore structures. The phenomenon may be moderate in scale but have long-term damage consequences. Many concepts and devices have been investigated in suppressing FIV, see for example Zdravkovich (1981), Every et al. (1982), Taggart and Tognarelli (2008) and Kumar et al. (2008). It is well known that flow-induced vibrations can be mitigated by modifying the structural parameters to shift the natural frequencies of the system away from the range of the external excitation or by disrupting the wake formation. The performance of FIV suppression devices varies according to the type of structure and the surrounding environment. In general, the performance is judged by the degree of FIV suppression and drag reduction. The two most frequently used devices, helical strakes and airfoil

fairings, when fully installed, can reduce 70 – 90% of the vibration for the former and 80% or more of the vibration for the latter (Blevins, 1990). However, the strakes may increase the drag coefficient on the order of 1.5 - 2.0 or more as reported by Allen et al. (2007). The airfoil fairings have excellent hydrodynamic performance if they are fully functioning but at times may experience flutter instability issues (Slocum et al., 2004). In addition, the airfoil fairings have stringent requirements in free-rotation. Other types of devices have been explored. Every and King (1979) reported that a bare cylinder wrapped with a circular wire can suppress up to 50% of the vibration at subcritical and supercritical Reynolds numbers. Owen and Bearman (2001) tested a cylinder with hemispherical bumps, and the vibration magnitude and the drag coefficient were reduced by 47% and 25%, respectively, for Reynolds numbers in the range of 10^3 to 10^4.

Structures‟ dynamic and modal behavior obtained from sensors can also be used to identify structural damages or defects in regions of concern at a sufficiently early stage to prevent a major failure. It is of practical value to use unequally spaced measurements, since damages on structures oftentimes occur at certain areas. Here we consider free-spanning subsea pipelines that are used in the offshore industry for the transport of recovered hydrocarbon from oil and gas reservoirs to onshore facilities. Some subsea pipelines might be suspended above the seabed due to scouring effects from waves and currents or a preexisting uneven seabed, as shown in Fig. 1.1 at the Ormen Lange field 120 km of the west coast of Norway (Holden et al., 2006). Corrosion can be a problem for free-spanning pipelines and the middle points typically suffer the most due to additional accumulation of water and marine growth as shown in Fig. 1.2. The growth rate of corrosion in the middle may be faster than in other regions and can result in a deeper corrosion defect depth over time (Bai and Bai, 2005).

It is recognized that experimental measurements of usually kinematic data with certain sensors are most useful in evaluating the responses due to the complicated physics of marine risers with choke and kill lines, buoyancy units, and flow suppression devices. Often times there are also physical restrictions in placing the sensors due to installed equipment or certain desired positions being physically unreachable. With the

advances in sensor technology, there is a need to develop methods that will provide guidance on the minimization of the number of sensors and optimization of their spatial placement. Moe et al. (2004) and Niedzwecki and Moe (2005) conducted an experimental study and data analysis of basic response behavior of steel catenary risers with uniformly distributed sensors. Li et al. (2011) reported an experimental investigation of risers‟ FIV responses with staggered buoyancy on a cylinder with an L/D ratio of 263, where the measurements of strain information were recorded using equally spaced Fiber Bragg Grating (FBG) sensors. In a recently reported research investigation of FIV behavior, Niedzwecki and Fang (2012) demonstrated that non-uniformly spaced sensors are capable of retrieving mode shapes and other modal parameters with the modified time domain decomposition (TDD) method (Kim, Stubbs and Park, 2005). In this study, a sensor based approach with optimized number and location is proposed for the analysis. Multiple sensors, on one hand can measure the structure response with or without suppression devices, and on the other hand, can lay a foundation for damage detection through extracted mode shapes and other modal parameters, and form the main body of the computational tool developed in this study.

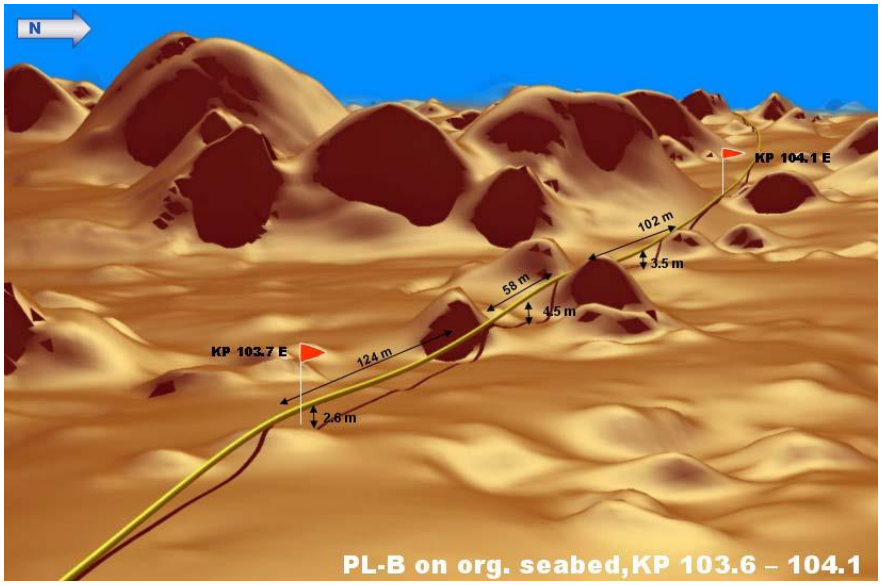

Fig. 1.1 Example of uneven seabed and the free-spanning pipeline (Holden et al., 2006).

Fig. 1.2 An example of a free spanning pipeline with moderate marine growth (courtesy of Richard Whitcombe).

1.1 Suppression of Flow-Induced Vibration

Slender structures horizontally deployed underwater, such as free-spanning pipelines and certain structural members of Jacket platforms can be subjected to damage of FIV due to combined loads of current and waves. The challenge to the proposed research effort is two-fold: (1) limited information exists on the study of current plus wave interaction with offshore structures (Sarpkaya, 2010), and (2) the scale of the structures in use can be large. Nielsen et al. (2002) reported a free-spanning pipeline with a length to diameter ratio (L/D) of 846 in a project at the Ormen Lange field. The ratio is much larger than the currently accepted value of 120 proposed by Det Norske Veritas (DNV, 1998).

A brief summary of some FIV experiments studying the response of horizontally mounted cylinders is presented in Table 1.1. The studies presented can be divided into 3 groups depending on L/D ratios and FIV suppression devices used in the tests. The first group focused on FIV suppression performance of devices on small L/D ratio (<30) cylinders, where the experimental setup facilitated testing devices with multiple

geometries in high Reynolds number flow. Allen et al. (2007) tested 5 different airfoil fairings with chord to thickness ratios (c/t) ranging from 1 to 2 at supercritical flow regime. Special efforts were made to find the most economical configuration of airfoil fairings. The results showed a short airfoil fairing with c/t of 1.18 was overall the best choice since it was cost effective and simultaneously reduced the root-mean-squared (RMS) cross-flow responses from 0.43D to 0.13D.

The second group of experiments studied FIV of flexible cylinders with intermediate to large L/D ratios, and focused on multi-modal motions, the effects of pretension, and the coupling effects between in-line and cross-flow vibrations. Typical examples of the experiments are Li et al. (2005), Prastianto et al. (2007) and Wilde and Huijsmans (2005), with L/D ratios being 213, 269 and 788 in subcritical flow regime. The note of Table 1.1 described flow regime in Re number. In-line vibrations were responses along the flow direction while cross-flow vibrations perpendicular to the flow direction. Li et al. (2005) tested the bare cylinder in 27 current velocities from 0.1 to 1.5 m/s and 2 pretensions of 200 and 600 N. No frequency lock-in or resonance, in another word, the vortex shedding frequency occurred in FIV approached to the natural frequency of the structure, was observed. Prastianto et al. (2007) reported an experiment at a relatively low uniform current velocity of 0.2 m/s, at which both the 3^{rd} and 9^{th} mode were excited with the lower mode being dominant. Similarly, Wilde and Huijsmans (2005) showed in a test with current velocity of 1.0 m/s and pretension of 900 N, the 5^{th} or 6^{th} mode was dominant and the 11^{th} or 12^{th} mode participated. As demonstrated by the aforementioned studies, multi-modal responses were frequently observed in FIV of long cylinders, and dominant modes excited were affected by current velocities and pretensions. Strong coupling effects between in-line and cross-flow responses were also observed in those studies.

The third group of research experiments studied the performance of various FIV suppression devices on long, flexible and horizontal cylinders. It is highlighted here that due to the limitation of experimental facilities, experiments of this kind are scarce. The studies publically available are Trim et al. (2005), Allen et al. (2008) and Jhingran et al.

(2012). Coverage density of the devices, defined as the ratio between the combined length of FIV suppression devices and the total length of the structure, is a very important issue because of the economical concern where a tradeoff must be made to get the least coverage and the best FIV suppression effect. Trim et al. (2005) compared helical strakes with 2 geometries, 17.5D pitch, 0.25D height versus 5D pitch, 0.14D height. The cylinder with an L/D ratio of 1400 was towed in subcritical flow regime. The experiments demonstrated the configuration of 17.5D pitch, 0.25D height was more effective in mitigating FIV than the configuration of 5D pitch, 0.14D height, by providing one-order-of-magnitude smaller fatigue damage. Coverage of 91%, 82%, 62% and 41% of strakes were studied and the results indicated strake performance declined rapidly when coverage was smaller than 82%. Allen et al. (2008) conducted experiments using a cylinder with an L/D ratio of 463 in subcritical to critical flow regime, and compared the performance of a helical strake (17.5D pitch, 0.25D height) and an airfoil fairing (c/t ratio 1.5). Both devices were in 40% partial coverage and deployed from one end. The results revealed strakes and fairings can both effectively suppress the responses in the covered end, while in the bare end, airfoil fairings outperformed strakes by providing more damping overall. Jhingran et al. (2012) conducted a joint collaboration with Shell, Marintek and MIT to study the effects of buoyancy spacing on FIV responses using a similar experimental setup as Trim et al. (2005) with a long cylinder of an L/D ratio of 1267. Buoyancy spacing was investigated by adjusting the length of buoyancy elements and the length of gaps in between. The test cylinder was 38 m in length and 30 mm in diameter. The diameter of the buoyancy element was 80 mm. The test matrix included 5 arrangements of staggered buoyancy elements with different lengths of the buoyancy elements and the gap segments. The results showed that an arrangement of equal portion of buoyancy and gap had the least amount of curvature response in the pipe and hence provided the best fatigue life performance.

Table 1.1 Summary of laboratory experiments with horizontal cylinder configurations.

Recent Studies	Year	L/D	Range of Re 10^3	Flow Regime[1]	Mass Ratio	FIV suppression Devices	Suppression Coverage %	Environmental loads
Allen	2007	14	700 – 1,500	Supercritical	1.39	Airfoil Fairings	100	Uniform Current
Brown	2008	26	47 – 130	Subcritical	1.15	Ventilated Trouser	100	Uniform Current
Li	2005	213	4 – 60	Subcritical		None		Uniform Current
Prastianto	2007	269	0.8 – 4	Subcritical		None		Shared Current
Wilde	2005	788	8 – 48	Subcritical		None		Uniform Current
Allen	2008	463	100 – 400	Subcritical to Critical	1.80[2]	Airfoil Fairings / Helical Strakes	40	Uniform Current
Trim	2005	1407	8 – 65	Subcritical	1.60	Helical Strakes	41 - 100	Uniform Current
Chitwood	1997	760	7 – 23	Subcritical	0.91	None		Uniform Current Regular Wave Irregular Wave Current + Irregular Wave
					0.91	Airfoil Fairings	40 - 100	Uniform Current Regular Wave Current + Regular Wave
					0.91	Ribbons	40 - 100	Uniform Current Regular Wave Current + Regular Wave

Notes:

1. Flow Regime: Sub-critical, $\mathrm{Re} < 2\times10^5$; Critical, $2\times10^5 < \mathrm{Re} < 6\times10^5$; Super-critical, $\mathrm{Re} > 6\times10^5$.
2. The mass ratio is defined as the mass of the bare cylinders without any fairings divided by the mass of the displaced water.

1.2 Sensor Optimization

Sensor optimization in number and placement has received much attention recently, mainly in three areas: system/modal identification, damage detection and control engineering. The first two topics are of particular interests in the present study. Doebling et al. (1996), Sohn et al. (2004) reviewed literatures spanning more than a decade on structural health monitoring. The reviews covered various subtopics pertaining to data acquisition, signal processing, data analysis and structural health condition evaluation output. Sensor placement was considered as a bridge connecting those subtopics. Data analyses procedures are usually altered to fit the format of the measurements including kinematic signals such as displacement, acceleration, and strain; and environmental signals such as temperature, current speed, or wave height.

In system/modal identification areas, when only a small number of sensors and their locations are available, sensor optimization is often adopted to obtain the best estimations of structural parameters and/or modal parameters. Many primitive approaches were developed via engineering judgment and practical considerations, e.g., by placing sensors near the antinodes of lower modes, and/or by placing sensors near areas where protection and maintenance of the sensors were relatively easy to access. These approaches were better than random placement but there was no guarantee the solutions they found were optimal. Many advanced models were proposed to systematically search for the optimal sensor array. Kammer (1991) used optimized sensor arrays of a small size to identify up to 15 bending modes of a large space structure. The best sensor placement was obtained via Effective Independence method, which maximizes the determinant of the Fisher Information Matrix and thus minimizes the estimated errors of the modes. Kirkegaard and Brincker (1994) analyzed the parametric identification of modal parameters up to the second mode of a simply supported beam with optimized sensors. It seemed optimal sensors were less sensitive to noise-to-signal ratio if the sensor number increased. Stubbs and Park (1996) extended Shannon‟s sampling theorem in time domain to spatial domain, and successfully reconstructed the mode shapes with only a few measuring points. A rule of optimal

sensor placement was formulated based on the results, and then was demonstrated by three examples, resulting in sensor number reductions of 36%-42% to obtain the same amount of modal information.

Scientists and engineers in the oil and gas industry took great efforts in the development of sensor optimization techniques due to the significant interests in monitoring and maintenance of subsea transmission lines, e.g., risers and pipelines. Optimized sensor arrays in riser analysis can help solve two issues: (1) to effectively locate the critical fatigue damage areas by finding the correct dominant modes, which may constantly change due to flow induced vibrations; and (2) to help reduce the unnecessary conservatism in FIV fatigue evaluation by using high quality field data in support of design and validation instead of approximated data extrapolated from small scale model tests. Several procedures were proposed in the modal recognition of long and flexible cylindrical structures. Kassen (2001) utilized minimum mean square estimation error to find the six optimal sensors in recovering and identifying the flow-induced vibration modes of a 683 m long riser with the help of a finite element model. The optimal sensor array showed improvement in the form of a smaller error over the actual sensor array implemented in the field, which came from engineering judgment. It is noted here that the author adopted a near-exhaustive search in the whole domain (excluding impractical solutions from all possible sensor combinations) to avoid being trapped in a local minimum and missing the global solution. Though the computation was still affordable due to the relatively small size of the possible locations, advanced techniques are needed to solve similar optimization problems. When designing sensor arrays for riser systems, Natarajan et al. (2006, 2007) adopted an approach of distributing sensor arrays in clusters near the region of great interests and a few distant sensors away from the main clusters to calibrate the model. The approach was proven beneficial in multiple problems for it built in available information in the design, for example, for steel catenary risers, a strain sensor cluster can be placed near the touchdown point if maximum bending is of interest or an acceleration sensor cluster can be placed shortly below the water level where current and vessel motion is strong if the

FIV induced fatigue is of importance. The authors used modal clarity index and its root mean square average, which was based on modal decomposition and can quantify the difference of neighboring modes, to measure the performance of different sensor arrays. A total of 73 candidate sensor configurations, with different number of sensors, cluster position, sensor spacing were compared with this technique for a typical Gulf of Mexico steel catenary riser. Results showed sensor spacing was not a significant factor and placing clusters near the middle of the riser provided more recognizable mode shapes.

Sensor placement was also an important topic in damage detection. Better sensor arrays can increase the successful rate of diagnosing damage while reducing false detection rate. Worden (1995, 2001) used neural networking method to select the optimal sensor arrays on a cantilever plate with predefined stiffness losses at various locations. In order to approximate the real case in the field, restrictions on the sensor numbers were placed on the design and the study focused on finding the damage with limited information. The results showed the method can effectively locate the damage if it was near the fixed end than the free end, which was reasonable for elements near the fixed end have more weights in the total stiffness of the structure.

Sensor optimization, which consists of optimizations of sensor number and location, has to solve two main questions: (1) how to evaluate one candidate sensor array; and (2) how to achieve the optimal placement correctly and efficiently. Yi et al. (2012) reviewed the available evaluation criteria, in another word the objective functions, including modal assurance function, mean square error, measured energy per mode, etc. The above-mentioned criteria were mainly about system/modal identification. Another type of criteria is damage detection related for example false positive detection rate for a preset damage scenario. In terms of methodologies to obtain the optimal sensor arrangement, there are three major categories: (1) deterministic, (2) sequential sensor placement methods, and (3) combinatorial optimization methods. Staszewski and Worden (2001) gave a focused review on combinatorial methods, among which genetic algorithm, simulated annealing, tabu search and neural network were

prevailing. Different optimization schemes are usually crossly compared, or compared with exhaustive search, which are costly but most reliable.

The genetic algorithm is a method for solving optimization problems based on natural selection of survival of the fittest. The fact that genetic algorithm can be applied on problems with objective functions being discontinuous, non-differentiable, random or nonlinear, makes it very suitable for sensor optimization. A typical genetic algorithm has phases of initialization, evaluation with a predefined fitness function, parent selection, and reproduction with crossover and/or mutation. A good introduction to genetic algorithms is provided in the classical textbook by Coley (1999).

The application of genetic algorithm in sensor optimization focuses on searching for the optimal sensor array with the best fitness values among many candidates. Yao, Sethares, and Kammer (1993), Liu et al. (2008) employed genetic algorithm to find the optimal sensor array which can yield the best estimation of mode shapes. The former study used determinant of the Fisher Information Matrix, which tended to provide more credible estimate when it got larger, to find the optimal solution. The latter study compared three different evaluation criteria in selecting the best sensor arrays: modal strain energy (MSE) method, and two modified modal assurance criteria (MAC1 and MAC2); results showed MAC1 and MAC2 were better than MSE by identifying 3 more modes with 5 sensors. Guo et al. (2004), Rao, Srinivas and Murthy (2004), Gao and Rose (2006), implement the genetic algorithm to detect damages of various mechanical and civil structures. Similarly to Yao, Sethares, and Kammer (1993), Guo et al. (2004) maximized the Fisher Information Matrix to achieve the best estimate of the damage coefficients. Rao, Srinivas and Murthy (2004) applied residual force indices to detect different degrees of damages on a truss structure, a cantilever beam, and a simple frame. In the study by Gao and Rose (2006), non-vibration based local damage detection sensors were adopted to monitor their neighboring areas. The objective function was to minimize the false detection rate while minimizing the number of sensors. Results showed sensor number and capacity of each individual sensor were two competing

factors when achieving the best damage detection performance while keeping cost low, thus tradeoff must be made.

To overcome the problem that best fitness values was hard to converge, Yao, Sethares, and Kammer (1993) proposed an improved genetic algorithm where certain portion of the best parent solutions were always retained to the next generation instead of being dismissed after each generation. Results showed the improved genetic algorithm converged much quicker and more precisely at the maximum at which the original genetic algorithm didn‟t achieve. In the reproduction phase, sometimes, children solutions were identical to their parents, resulting in lower efficiency. Liu et al. (2008) introduced a forced-mutation function if that happened. The improved approach accelerated the convergence by 20-30%. Constraint is also an important factor of genetic algorithm. Due to the tendency of spreading out the solutions to cover the whole domain in genetic algorithm, certain children solutions may jump out of the predefined constraints. Guo et al. (2004) developed a scheme to ensure the children solutions were always inside the boundaries. The new algorithm was demonstrated by a truss structure, and was 61.7% and 52.9% faster in convergence than the forced mutation method and the penalty function method.

Many times, multiple objectives are of concern and need to be optimized simultaneously therefore multi-objective genetic algorithms were developed. A set of sensor array often times is required to fulfill two or goals simultaneously, e.g. the same sensor array may try to capture two dominant modes simultaneously, or to capture two different modes sequentially due to the change of environments. The procedures to obtain efficient and correct optimal solutions for multiple objective problems using multi-objective genetic algorithms (MOGA) were illustrated and discussed in Horn, Nafpliotis and Goldberg (1994), Deb et al. (2002) and Konak, Coit and Smith (2006). Prior to the induction of MOGA, multiple objectives were achieved by converting multi-objective to single objective problems, specifically, assigning weights to different objectives and summing them up later, or defining objectives as constraints of the problem. Those approaches were at best approximations of the real problems thus not

satisfactory. To address this issue, Horn, Nafpliotis and Goldberg (1994) utilized the concepts of (1) the Parent front, where solutions were compared with each other in the multi-objective domain for dominance and dominant solutions were listed on the Pareto front; and (2) niching, where solutions were assigned discounting factors based on how crowded the solution neighborhood were, high discounting factors for crowded areas and low discounting factors for less crowded area, in order to spread out the population of solutions and converge as close to the Pareto optimal as possible. The proposed niched Pareto genetic algorithm was successful in Schaffer"s F2 problem, a real-values simple two-objective function, and an open problem in hydro-systems. However, the algorithm had the following issues: heavy computational volume, lack of elitism and need for specifying the sharing factor for niching. Deb et al. (2002) proposed Nondominated Sorting Genetic Algorithm II (NSGA-II), a fast and elitist muli-objective genetic algorithm to help alleviate those issues. Considering the complexity nature of multi-objective engineering optimization problems, Konak, Coit and Smith (2006) conducted an overall review of available methods and provided a step-by-step tutorial to apply multi-objective genetic algorithms in solving real-life problems. The general approaches were utilized in this study to address the multi-objective sensor optimization problem.

1.3 Damage Detection

In this study, damage is defined as changes in either material and/or geometric properties introduced into structural systems, which cause harmful or undesired effects on the utility of the structures (Farrar and Worden, 2007). Damage can accumulate in engineering structures due to cyclic environmental loads, extreme conditions or accidents during the construction, installation or operation stages. The results include changes of the material property, geometry and response behavior in forms of stiffness losses, cutting damages or corrosion cracks (Chance, 1994, Abdul Razak and Choi, 2001). It is desired to evaluate the structural damage in terms of number of occurrences, location and severity by examining the structural static and dynamic response behavior before and after the damage. Because of the potential in preventing disasters and

extending the service lives of engineering structures, damage detection techniques have received great attention in civil, mechanical, aerospace, offshore and other fields. In a broad view, damage detection techniques include global methods and localized methods. Global methods are generally based on structures‟ vibration responses, which can be further grouped into modal-based, time domain and other methods. Localized methods weigh more on the geometric and material properties of the damaged structures. Typical examples are ultrasonic inspection, magnetic field inspection and visual check (McCann and Forde, 2001). For extensive reviews, see Doebling et al. (1998), Fan and Qiao (2011) and Stubbs (2011).

The most significant rating criterion in comparison of existing damage detection approaches is the four-level criterion, proposed by Rytter (1993). Specifically, a damage detection method will be judged upon whether it can 1.) determine whether damage has occurred, 2.) locate the damage, 3.) determine the severity of the damage, and 4.) evaluate the remaining life of the structure. In the effort of identifying the most promising methodology, Stubbs (2011) introduced a four "maturity" criterion on a level 3 method which will be ranked upon whether it 1.) has a defendable theoretical basis, 2.) has been validated with a numerical model, 3.) has been validated with a controlled laboratory test, and 4.) has been validated by a field experiment.

The focus of the current work is modal-based methods, which utilize basic modal parameters such as modal frequencies, modal damping, mode shapes, mode shape curvatures or combination of those parameters to detect possible damage. The offshore industry pioneered this research from 1970s to the middle of 1980s by using changes in natural frequencies to detect damages of steel structures. Though some progress was made, the search was forced to a halt due to the findings that changes in natural frequencies and modal damping ratios before and after damage were not significant enough to detect damage in a robust way. Especially for offshore structures, changes in natural frequencies resulting from damage were very difficult to be differentiated from increased mass of the structure due to marine growth (Doebling, 1996). Some recent studies continued to show the controversy of using natural frequencies and mode shapes

as damage indicator. Carrasco (1997) demonstrated the natural frequencies computed up the 5th mode had negligible differences before and after the damage. Hu and Wu (2009) computed natural frequencies up to the 10th mode of a thin plate of 246 mm by 246 mm before and after a small surface crack. The differences in natural frequencies were less than 0.5%. Direct comparison of mode shape has controversy upon whether the mode shape can be a good damage indicator or not. Alampalli (2000) showed mode shape is difficult to detect damage. However, Fayyadh (2011) successfully demonstrated mode shapes of the damaged structure deviate in the neighborhood of the damaged area with clear direction. The numerical example used in this article was a finite element model of a concrete beam. The method is promising because it is capable of indicating possible damaged areas with simple information. The down side is that the accuracy of the localization was doubtful. Fox (1992) showed mode shape can be used to detect damage but it depended on the selection of modes.

Mode shape curvatures seemed a better indicator than mode shape alone and appeared to be more sensitive to damages. Pandey, Biswas and Samman (1991) showed changes in mode shape curvatures can be used to detect damage. The methods were validated with finite element models of a simply supported beam and a cantilever beam with various degrees of damage severity. The curvatures were computed from displacement mode shapes using a central difference approximation. However, mode shape curvatures derived from displacement mode shapes via differentiation can have numerical errors and may even affect the damage detection results. Chance (1994) showed that differentiated mode shape curvatures were not sensitive to damages, rather, strain mode shapes directly measured were better indicators. Though essentially derived from similar information, strain mode shapes seemed superior to curvatures in avoiding the numerical errors.

Pandey and Biswas (1994) showed that changes in flexibility can be used to detect the damage of a structure. The methodology was validated with numerical examples of a cantilever beam, a free-free beam and a simply supported beam, followed by an experimental example of a W12X16 I beam with 33 measurements. Catbas (2008)

used modal flexibility based deflections and curvatures from dynamic data as an indicator of damage, which behaved well in both laboratory experiments of a steel grid model and real-life tests of the Seymour Bridge.

Modal strain energy by far was found to be the most promising modal parameter in evaluating damage. The Damage Index Method (DIM), proposed by Stubbs, Kim and Topole (1992), was based on the assumption that fractional strain energy ratio remained unchanged when a structure was subjected to certain damage. The fractional strain energy ratio was the ratio between the strain energy stored in each individual element and all the elements. DIM was a level 3 method, which can detect, locate and size the damage. The method was validated by a field test of I-40 bridge (Stubbs, 1995), making it one of the most matured methods. Farrar and Jauregui (1997) made a direct comparison of damage index method, mode shape curvature method, change in flexibility method, change in uniform load surface curvature method and change in stiffness method by evaluating four degrees of damage occurred on a girder of I-40 bridge. Results showed damage index method was the most robust method which can use the least amount of information, i.e. only 2 modes, but make the most correct evaluation of the damages of all four degrees. Though DIM itself can differentiate damages of different severity, there was still room in the quantification stage. Seyedpoor (2012) proposed a two stage damage detection technique which used a modal-strain-energy-based index to accurately detect and locate the damage and in the meantime, used particle swarm optimization technique to quantify the detected damage. Shi et al. (1998, 2000, 2002) firstly assumed a stiffness loss occurred with coefficient alpha, and then proposed change ratio of modal strain energy stored in individual elements before and after the damage to detect and locate single or multiple damage. The computed model strain energy change ratio for each element was then manipulated to solve the individual stiffness loss coefficient alpha, which stabilized at the damaged extent when enough mode numbers were used in the computation. The quantification of the damage hence can be made.

Though the majority of the studies were carried out on beam-like structures (Pandey et al. 1991, 1994, Change 1994, Nicholson 2000, Stubbs et al. 1992, 1995, Wang and Qiao 2008, Fayyadh 2011), some recent works were conducted on higher level structures such as truss, frame, and especially plate-like structures. Carrasco et al. (1997), Doebling et al. (1997) and Shi et al. (1998) utilized truss structures to develop the damage detection techniques. In the development of modal strain energy change ratio method, Shi et al. (2000, 2002) studied a two-story steel frame structure. Barroso and Rodriguez (2004) used a four-story building, which was a benchmark structure initiated by ASCE to further develop damage index method without having the undamaged structure information.

Choi and Stubbs (1997), Cornwell, Doebling and Farrar (1999) extended the theoretical framework of damage index method for plate-like structures. Then, Choi and Stubbs validated the method with a finite element thin plate model simply supported on four edges. The identification of the damaged areas was processed via a probability approach. Cornwell, Doebling and Farrar (1999) validated the method with a controlled laboratory test of an aluminum plate. Two cuts of increased severity degrees were gradually applied onto the plate. Results showed that in the most severe case, the methodology was able to detect both damages. However, when the severity levels of two cut were not comparably high, the methodology had problems of identifying both, i.e. finding one but missing the other. Yam, Li and Wong (2002) conducted sensitivity studies of static and dynamic indices to detect damage of a plate. The deflection curvature was found to be the most sensitive parameter in the static tests while the curvature mode shape method (CMS), which used difference of curvature mode shapes before and after the damage, and strain frequency response function (SFRF), which used the difference of strain transfer functions before and after the damage, were superior to modal frequency in the dynamic tests. CMS method was verified by a laboratory test of an intact and a damaged thin plate. Hu and Wu (2009) developed a scanning damage index for a free-free aluminum plate in order to overcome the issues of detecting small surface cracks instead of major damages. The scanning damage index will scan the plate

subarea by subarea. Damage indices computed in all the subareas summed up and yield a more pronounced index which clearly identified the damage.

Modal-based approaches abovementioned in detecting, locating and sizing damages have been successful to some extent, but still face significant challenges and limitations. Some methodologies made inappropriate assumptions that sufficient information such as detailed structural parameters and baseline structure were available. In addition, it was sometimes assumed that sensors can be placed anywhere with any number. For example, Carrasco (1997) deployed 273 tri-axial accelerometers on a truss structure to collect sufficient, even redundant data. Taking into the frequency response functions in 3 directions, multiple coherence functions, force auto spectrum and other information, in each test, a total of 1,155 functions had to be stored and solved. Another limitation of many damage detection techniques was that they had no problem of detecting very severe damages but were unable to detect small damages. Chance (1994) was able to evaluate a damaged structure with 90% stiffness loss. However, a very important condition that those methodologies were hoping to tackle was that the structure can still be repaired. It was of much less value if the method can only detect a near "wasted" structure. False-positive analysis should also be given attention other than merely to detect the damage for they can cause significant down-time in the usage of those engineering structures. Fortunately some researchers such as Barroso (2004), Farrar et al. (1997) and Choi and Stubbs (1997) made an effort in understanding the false-positive behavior of their methods. Finally, methodologies developed for one application shall not be blindly implemented to another scenario without proper modifications. For example, when applying damage detection techniques developed for steel structures on structures made by other materials, say concrete or ice, the in-situ conditions of those materials should be considered. Take ice for example, because of its creeping behavior under static loads, the dynamic measurements should be short and in higher modes to lower the effect from the creeping strain. Depending on the application, elastic behavior dominance of the ice vibration may be assumed to facilitate the analysis.

1.4 Strength Analysis of Ice

As the search for oil and gas reserves expands toward previously inaccessible high Arctic waters, first year and multi-year ice features pose a significant hazard to offshore platforms used for exploration and production, therefore sea ice management in the protection of the facilities becomes an urgent and important issue. The focus of the current study in analyzing the strength of sea ice formations in support of ice management is to locate and evaluate the weakness of a given ice plate using its dynamic response behavior as an indicator. This section discusses the motivation of the study, and explores relevant aspects of the physical properties of sea ice. In addition, a list of assumptions and simplifications are presented. The postulates form the basis of the numerical simulations.

ISO 19906 (2010) defines ice management as "active processes used to alter the ice environment with the intent of reducing the frequency, severity or uncertainty of ice actions". Ice management has two main purposes, to ensure safety of personnel and assets facing the threats of various ice features during installation and operation, and to extend the uptime and reduce the downtime of the production with ice threats correctly identified if possible mitigated, hence increase the overall hydrocarbon recovery. The main business and technical drivers of conducting specific strength analysis of sea ice, as part of a broad ice management plan are listed below.

There is huge potential of oil and gas reserves in Arctic and sub-Arctic waters, especially in deep waters and ultra-deep waters which are subjected to ice loads. United States Geological Survey estimated undiscovered and technically recoverable resources (UTRR) including 90 billion barrels of oil, 1670 trillion cubic feet of natural gas in north Arctic Circle, on top of already discovered 40 billion barrels of oil and 1100 trillion cubic feet of natural gas (USGS, 2008). Considering the total area of the Arctic Circle covers 8% of the earth"s surface area, those resources account for 22% of undiscovered, technically recoverable resources in the world. 84% of the resources are expected in offshore regions. By contrast, UTRR of the whole Gulf of Mexico potentially can reach 45 billion barrels of oil and 232 trillion cubic feet of natural gas as noted by Humphries,

Pirog and Whitney (2010) in a report for Congress. Deepwater and ultra-deepwater regions in the Arctic or sub-Arctic contain significant amount of hydrocarbon resources abovementioned. Aggarwal and D'Souza (2011) reviewed some important lease areas for oil and gas in Arctic or sub-Arctic regions across the globe, namely in Barent Sea, Kara Sea, Offshore Newfoundland, Offshore Greenland. Those resources are generally in the water depths of 300-3000 m.

The increase of water depth for the resources forces the drilling and production activities to move from shallow water with fixed structures to relatively deep water with floating systems. However, the capabilities in handling ice loads that fixed structures usually have are no longer available for floating systems. Aggarwal and D'Souza (2011) reported that the Hibernia gravity based platform, a fixed structure, at a water depth of 80 m can endure ice loads in the range of 1200-1500 MN. By contrast, Howell, Duggal and Lever (2001) showed that the Terra Nova FPSO, floating in a water depth of 96 m with a strong 3X3 chain mooring system can only sustain 20 MN loads. Snel (2008) suggested the strongest design of chain mooring system that may possibly be achieved, with a minimum breaking load (MBL) of 31 MN of 24 mooring lines, can provide a max capacity of 77 MN with an offset of 33 m, which was nearly 4 times larger than Terra Nova FPSO but still not enough to provide adequate support. The difference in load capacities between fixed and floating structures requires specific measures to take care of the ice threats.

The ice loads exerted on the structures can be significantly reduced by decreasing the general sizes of the ice features. Croasdale, Bruce and Liferov (2009) studied the reduction of ice loads when thick ice features were broke down to pieces of size in the order of the offshore structure. Empirical analysis suggested the loads exerted by large pieces of ice were affected by the width, the thickness and pressure imposed by surrounded pack ice. Results showed an ice feature with 125 m width and 0.5 m thickness exerted a load of 7.75 MN on the structure, while a smaller ice piece with 50 m width and same thickness exerted a load of 5.08 MN. When the ice thickness increased to 2 m, 125 m wide ice piece gave a load of 43.84 MN while 50 m wide a load of 28.76

m. The study demonstrated that smaller and thinner ice features exerted lower loads on the structures; therefore it is of particular interest to break the large pack ice into smaller scales.

Successful ice management is regarded by many as the key to ensure safe recovery of the hydrocarbon resources in icy waters. Edmond, Liferov and Metge (2011) summarized four typical activities in an ice management plan: ice feature surveillance, ice threat identification, physical management of the threat and ensuring learned lessons effectively implemented. Ice management in general treats icebergs and pack ice differently, the former of which is not the focus of the current study but interested readers may check a comprehensive study conducted by Eik (2011). Pack ice refers to sea ice formed in arctic regions drifting in large areas. When dealing with pack ice, a typical ice management plan is to break up the coming ice into smaller pieces to create a safe channel using icebreaker fleet so that the offshore rig can be protected. Hamilton et al. (2011) discussed some key considerations of accomplishing the complex goal using limited amount of icebreakers, and investigated the performance of various ice management tactics against measured ice data with a simulation-based technology. A successful ice management for pack ice shall always keep the offshore platform in a managed channel, and deliver small enough ice floes to the offshore rigs downstream.

Locating and evaluating the weak regions of a given ice sheet belongs to the activity of ice feature surveillance, which would provide valuable information for the identification of the ice threats and the physical management. The reverse application of damage detection techniques is used here to break the formations instead of repairing them with the detected weakness information. Two steps will be taken in the process. The first is to extend the damage detection technique from beam-like structures to plate-like structures with necessary modifications. Cornwell, Doebling and Farrar (1999) conducted the extension and developed the governing equations for plate-like structures. The methodology was programed in Matlab and validated by a numerical example and an experiment of an aluminum plate.

The next step is to make reasonable assumptions and simplifications to account for those unique properties of sea ice in the formulation of detecting weak regions with vibration measurements. Those assumptions and simplifications must be made carefully. On one hand, ice is very complex in its type, condition and mechanical behavior. It can be ductile and creep at low stresses, but also be very brittle at high stresses. On the other hand, one big problem in analyzing ice is lack of data. A great portion of experimental studies on ice is laboratory based and conducted on pure ice and in small scales. It is generally difficult to extrapolate the results in such conditions to sea ice with specific features on a large scale, from 10 - 20 meters to several kilometers. Knowing the nature of the simplifications and assumptions will help the process, which will start from reviewing the micro-structure of ice as fundamentals, and then the mechanical properties of the sea ice, followed by the global properties. The assumptions made in the current study will be listed at the end of the brief review.

From the prospective of ice‟s micro-structure, two features are of great importance. One is the natural crystal structure of pure ice, which consists of oxygen and hydrogen molecules. The structure has a lattice-like formation and a weaker bond perpendicular to lattices, as illustrated in Fig. 1.3 (Sanderson, 1988**)**. The features of oxygen and hydrogen form a hexagonal shape in the lattices which is referred as a “basal plane” as shown in Fig. 1.3b. c-axis refers to the axis perpendicular to the “basal plane” as shown in Fig. 1.3c. A perfect crystal of ice would be strong for all the bonds are made use of. The micro-structure of ice has three properties: the first is the formation has strict rules in selecting molecules which stopped chemical substances, in another word: salt can hardly go into the lattice structure of ice. As a result, though developed in a strong saline solution which is the sea water, sea ice itself contains negligible amount of salt hence the mechanical properties of sea ice don‟t significantly differ with pure ice; the second property is that imperfections and defects exist in the ice structure, which allow some free travel of hydrogen atoms between bonds, resulting in the creeping behavior of ice. In material science, creep deformation is permanent deformation, refers

to the tendency of a solid material to move slowly under stresses. The third property is that the lattices would affect the homogeneous property of ice.

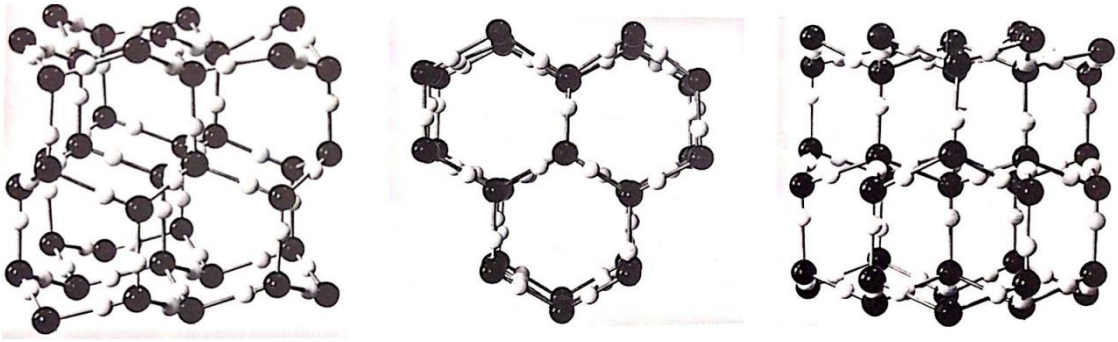

(a) Genral view (b) “basal plane” (c) c-axis

Fig. 1.3 The micro-structure of pure ice (Sanderson 1988).

The existence of brine pocket is the other important feature of the micro structure, which specifically refers to sea ice. During the freezing process, brine water is typically trapped in pockets. As discussed earlier, pure ice will expel salt. Since the brine pockets move toward cold sources (melt at warmer brine waters and freeze at cold icy areas), and temperature profile vary seasonally, some brine channels form resulting in a faster salt expelling rate. The less salt it contains, the stronger the ice is. Lake and Lewis (1970) discussed the process of salt rejection by sea ice through the brine channels, as illustrated in Fig. 1.4. The longer the ice is formed, the more efficient the salt expulsion is. The existence of brine pockets and brine channels would explain the strength behavior of sea ice, which is strongly related to age, in another word, the amount of salt been expelled.

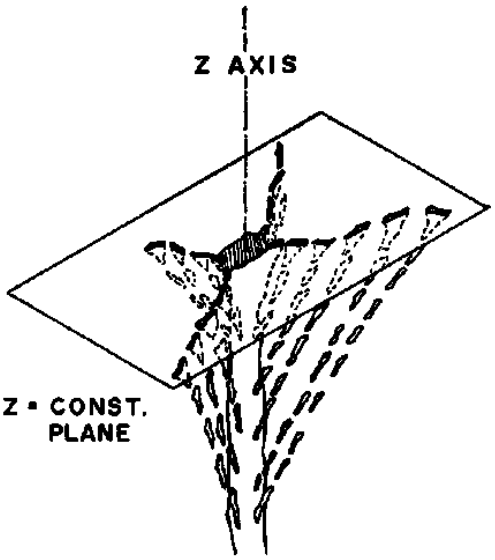

Fig. 1.4 A brine channel of sea ice (Lake and Lewis, 1970).

Sanderson (1988) conducted a general review of ice mechanics, aiming to preserve the knowledge gained in the active exploration and production of oil and gas resources in 1970s-1980s in Arctic and sub-Arctic waters, after a catastrophic down-turn in the late 1980s. The review studied strain/strain rate, homogeneity, Poisson ratio, temperature as parameters that can affect the elastic modulus of ice, which was the basis of dynamic analysis.

Unlike conventional metals engineers are familiar with, under a given stress, the deformation strain of ice will increase gradually with time. In another word, ice is not a full elastic material. Squire (1996) gave a comprehensive review of the issue of strain rate, including instantaneous elastic strain, delayed elastic strain or primary creep strain, secondary or permanent creep strain and tertiary creep. When a stress is applied on ice, it will immediately behave elastic but also starts to creep. The dominance of elastic strain and creep strain depends on the loads applied, specifically, the larger the load is, the shorter time it takes for creep strain to take dominance. For stresses in the range of 1-5 MPa, the deformation due to creep will surpass elastic response after 5-200 s (Sanderson, 1988). For static problem with huge ice loads like 1-5 MPa, creep is

important; for dynamic problems with medium amount of stresses and in short time frame, the total strain is often dominated by the elastic strain. Squire (1996) studied a series of problems involving moving loads on ice, i.e. a vehicle passes by an ice sheet quickly, in which the assumption of elastic strain dominance was made due to the short time frame. The same principle will be adopted in the current study of ice strength analysis because it fits in the same category of dynamic analysis.

Homogeneity is another factor that distinguishes ice from other conventional materials such as steel or concrete. Grain structures of ice include granular and columnar, which depend on the alignment of the c-axes of the ice (Weeks and Gow, 1980). If the c-axes display randomness, the ice is granular which makes the ice an isotropic material. Most lab studies are carried on granular ice. Granular ice can be found in icebergs, glaciers and surface layers of lake ice. The other type is columnar ice, in which the crystal structures are formed regularly where c-axes of ice micro-structure stay in the similar direction. The ice is orthotropic and can be found in lower layers of lake ice and river ice.

The elastic modulus of pure ice doesn‟t vary much with either temperature or Poisson ratio, but varies significantly with porosity resulting from either brine water or air. Weeks and Mellor (1984) reported at 10% porosity, the elasticity modulus of pure ice dropped to 7 GPa from 9.5 GPa at zero porosity. However, for sea ice, the porosity varies with temperature and salinity hence the Young‟s modulus of sea ice typically displays dependency on temperature and brine volume (Timco and Weeks, 2010). Frankenstein and Garner (1967) studied the relationship between brine volume, temperature and salinity. When temperature varied between -0.5 ^{o}C and -22.9 ^{o}C, the relationship is:

$$v_b = S_i\left(\frac{49.185}{|T_i|} + 0.532\right) \tag{1.1}$$

where v_b is brine volume with a unit of ppt (part per thousand by volume), S_i is salinity, T_i is temperature, with unit of ^{o}C.

Note salinity of sea ice is generally related to the thickness of the ice. Kovacs (1996a) analyzed a large data base and summarized two relationships between the salinity and the thickness. For first year ice,

$$S_i = 4.606 + \frac{91.603}{h} \tag{1.2}$$

For multi-year ice,

$$S_i = 1.85 + \frac{80217.9}{h^2} \tag{1.3}$$

where h is the thickness, unit is in cm.

ISO 19906 (2010) provided an alternate relationship between salinity and ice thickness

$$S_i = \begin{cases} 13.4 - 17.4\,h, & h \le 0.34\,m \\ 8.0 - 1.62\,h, & h > 0.34\,m \end{cases} \tag{1.4}$$

Note in Eq. 1.4, the unit of h is in m.

The measurements of Young‟s modulus of sea ice from different studies show scatter because of differences attributed to environment, season and measuring technique. It is important to note the condition of the sea ice when the measurement is made.

An empirical relationship between the elasticity modulus of sea ice and the brine volume was proposed by Cox and Weeks (1988)

$$E = 10 - 0.351\,v_b \tag{1.5}$$

ISO 19906 (2010) provided another empirical equation for Young‟s modulus of sea ice against brine volume, which is

$$E = E_{fi}\left(1 - \sqrt{\frac{v_T}{1000}}\right)^4 \tag{1.6}$$

where E_{fi} is Young‟s modulus for fresh water; v_T is the total void volume, including brine volume and air volume.

Poisson ratio is an important parameter for ice‟s elastic behavior. Weeks and Assur (1967) reported the Poisson ratios for pure ice was approximately 0.33 ± 0.03, and proposed an empirical equation dependent on temperature

$$\mu = 0.333 + 0.06105e^{(T_i/5.48)} \tag{1.7}$$

where T_i is temperature, with unit of ^{o}C.

Significant amount of knowledge on sea ice‟s physical properties on a large scale, in another word, ice morphology, is gained during field observations and experiments. This is different from ice‟s micro-structure and ice mechanical behavior findings made in laboratory studies. Sea ice morphology is very complex yet most crucial for the oil and gas industry, involving the type and age of ice, particular geometric feature developed in the stage of formation and evolution, and ice movement.

The type and age of ice are common labels to distinguish ice features. Generally according to its origins, floating ice features can either originate from frozen sea water away from land, which developed to be pack ice, or from land-based glacier ice, which breaks up from shore and develops to be icebergs. For pack ice, age is normally the most useful identification variable, which varies in existence time, seasonality, thickness and other parameters. Young ice develops in early winter, roughly 30 cm thick. First year ice (FYI) develops in mid-winter and spring, can grow to a thickness of 1-2.5 m. Its maximum thickness is typically measured between April to May in Arctic Waters. Second year ice (SYI) is ice that survives a summer. Multi-year ice (MYI) is ice that survives multiple summers. The current trend is not to differentiate SYI and MYI due to technical difficulty and real need. MYI typically matures in 5-10 years away from shore and can grow up to 4-6 m thick. Technically speaking, land-fast ice is a type of MYI which develops and extends itself from shore. Land-fast MYI can go up to 15-30 m thick, say Queen Elizabeth Islands of Canada in the far north of Canada and to the west of Greenland (Marcellus and Morrison, 1982). It is worth noting that the thickness of ice varies greatly according to its location. Though icebergs generally are big, they can still be classified again according to their sizes. Large icebergs in the size of 50-100 m above water, weigh 10, 000, 000 tons; Medium icebergs in the size of 15-50 m above water,

can weigh 2, 000, 000 tons. Small icebergs in the size of 5-15 m above water and 15-60 in overall size, can weigh 100, 000 tons. Duggal (2013) in a university lecture mentioned 100, 000 tons icebergs are generally the design cases for floating systems such as FPSO to disconnect from mooring lines and risers, which is categorized as a small iceberg as heavy as such.

Particular geometric features of pack ice develop during the stages of formation and evolution and are of special interests in the current study. Those features include ice ridges (ice keels and sails), rubbles and melting pools of brine water. Ice ridges are developed from relative motions between separate ice sheets and can have many forms depending on the motion. If two ice sheets move towards each other and collide, compression ridge or pressure ridge may be generated. If two ice sheets move laterally and collide, shear ridge may be generated. Sometime, rafting ridge may be developed when two ice sheets over-ride and under-ride each other. Ridges display as concentrated ice compared to other relatively flat areas. During the formation of ridges, pieces of ice plates may pile together underneath the pack ice during the collision. Those piles of ice pieces are given a name of rubble. Rubbles appear to be loosely connected with large portion of brine waters trapped in between hence rubbles can be relatively weak. The depth of a rubble can be quite deep. However, during the seasonal variation of weather, ice rubbles will melt, reform, consolidate and eventually settle down as stronger ridges. Fig. 1.5 illustrated the formation of ice ridges.

(a) two ice sheets collide (b) an ice rubble (c) an ice ridge

Fig. 1.5 The formulation of an ice ridge.

Multi-year ice ridges are much stronger than first year ice ridges. Fully developed old ice ridges typically contain smooth sails and keels, which are above and below the water. A lot of effort was made to study the specific properties of multi-year ice ridges because they appear to be the toughest part hence may potentially be the most destructive towards both the fixed and floating oil and gas facilities, and towards the pipelines buried in the seabed. The thickness of a multi-year ice ridge in Beaufort Sea can be 10-12 m with a 6 m average thickness of the pack ice. Statistically speaking in Beaufort Sea, the keel depth is 3.3 times of that for the sail height of the MYI ridges (Dickins and Wetzel, 1981). A melting pool of brine water, which generally occurs for multi-year ice, is another interesting feature of some pack ice. It initially may come from brine waters expelled to the surface through the brine channels discussed earlier, and surprisingly may grow deeper and larger. The mechanism behind this is perhaps the brine water pools do not reflect sunlight as the ice and snow do, which is a low albedo effect. The heat received from the light will help the brine pools to be relatively warmer and melt more ice. Melting pools of brine water are areas of ice with smaller thickness and hence can be weaker.

The last part of the discussion on sea ice morphology is ice movement, which can change the occurrence of ice for a specific field. Currents and global motions may transport ice away from its origin and pose surprise encroachment, e.g. the ice features

encountered at Shtokman gas field come from north-eastern Barent Sea and possibly Kara Sea (Edmond, Liferov and Metge, 2011). The gyro current at Beaufort Sea also brings ice around the area on a large scale. Time is an important factor as well. Sea ice from other areas arrives at Shtokman gas field approximately every 2.6 years. The ice concentration may increase rapidly from 2/10 to 8/10 within a few hours (Edmond, Liferov and Metge, 2011). That fast movement may pose challenges in designing the oil and gas facilities. For example, the Terra Nova FPSO was designed to be able to disconnect buoy within 4 hours (no major damage), or 15 min emergent disconnection (causing damage) and 2-3 days to reconnect.

At this point, several simplifications and assumptions can be made here to conduct dynamic analysis with numerical simulations on a sea ice sheet with the purpose of strength analysis, especially locating and evaluating weak regions:

- Small deformation of ice occurs during the vibration;
- Ice plates can be regarded as thin plates considering the large size and relatively small thickness;
- Elastic behavior of ice dominate the vibration provided the external forces are low in magnitude and recorded vibration data are short in time span;
- Young‟s modulus varies according the brine volume;
- Brine volume is dependent on salinity and temperature only;
- Linear temperature profile from the top to the bottom of the ice sheet;
- Poisson ratio of sea ice changes with temperature profile only;
- Water provides linear buoyancy stiffness during the vibration;
- The ice can be divided into multiple laminas with gradually varied Young‟s modulus; in each lamina, the ice is homogeneous and isotropic, mainly granular.

1.5 Research Objectives

The current study aims to develop a computational tool that:

- Integrates data from sensors to characterize modal information
- Optimizes the number and location of sensor arrays

- Identifies regions of concern regarding potential failure
- Guides exploitation of information for other engineering purposes

In the first part of the study, two experimental investigations of riser models with length to diameter ratios of 760 and 263 will be used as application examples for 1-D beam-like structures. Sensor measurements in different formats such as accelerations and strains will be fed into the computational tool as input. Performance of various FIV suppression devices and buoyancy elements with varied coverage density will be investigated with the help of computed modal responses. In addition, the 1-D sensor arrays will be explored in number and placement using genetic algorithm in pursuit of the optimal configuration for modal recognition and possible failures.

The methodologies developed for the 1-D problem will be extended to a 2-D ice sheet in a numerical simulation. Facing the challenges of increased complexity of a sea ice, the genetic algorithm will be modified to address sensor optimization with limited number and restricted placement. Effect of buoyancy stiffness for a floating ice sheet and ice shapes will be considered in the damage detection procedures.

2. METHODOLOGY

The research focuses on the development of a computational tool to investigate and implement changes in dynamic/modal behavior of structures. Fig. 2.1 presents the modular concept overview of the tool which consists of data flow and the processing flow. In the computational tool, the structure and the sensor array, which are tested experimentally or simulated numerically to generate laboratory or field data as input, go through a sequence of processing modules, and then yield response assessment as output.

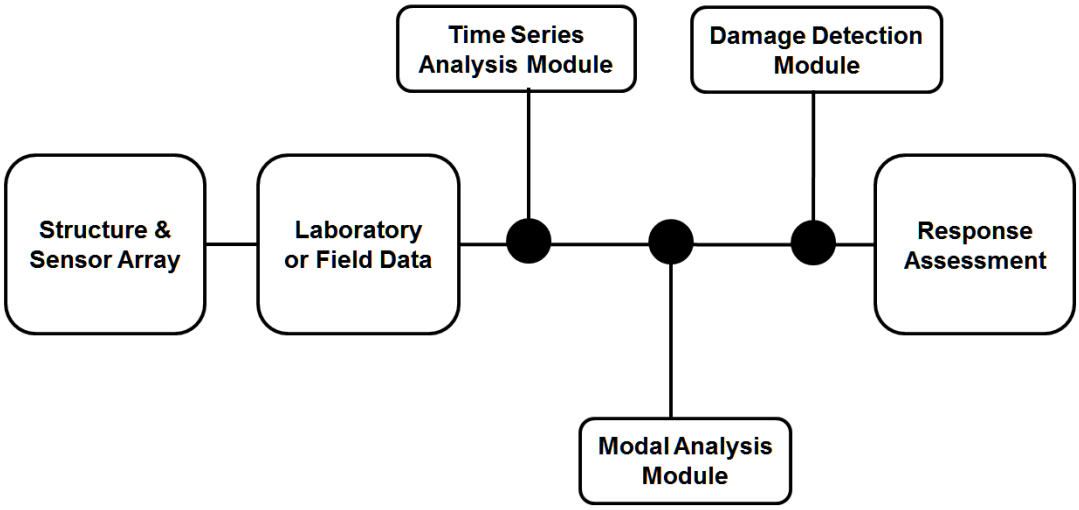

Fig. 2.1 Modular concept overview of the computational tool.

The processing flow includes 3 modules. A brief review of the input data and each module is given here using flow induced vibration analysis as an example. If the input laboratory/field data are collected experimentally, the measurements of the structure‟s responses are from a predesigned experiment, where multiple sensors including accelerometers, string-pots, load cells, wave probes and other sensors are

mounted on the structure. If the input laboratory/field data are collected numerically, the system response is simulated using finite element codes with a theoretical basis in the work of Niedzwecki and Liagre (2003). In the next step, the laboratory/field data go through the time series analysis, modal analysis and damage detection modules sequentially to compute the response assessment. The time series analysis module has two tasks: one is to estimate the displacements through double integration of the acceleration data collected with multiple accelerometers, and the other is to compute basic statistical results such as maximum, minimum and standard deviation. Response envelopes are part of the end results of this module. The modal analysis module employs the data processed by the previous module to identify the modal parameters of the system such as mode shapes, natural frequencies, and in the meantime, to provide a basis for active health monitoring of structural damages in the later part of the program. The time domain decomposition method (TDD), which is based on the development of an energy matrix and singular value decomposition technique, is modified and improved to suit the need for the modal analysis module (Kim, Stubbs and Park, 2005). One benefit of using TDD technique is that it is capable of extracting the modal parameters with the sensor information only. A detailed discussion of TDD technique, with input of acceleration, displacement or strain is presented in Section 2.1.

The damage index method, as the core of the damage detection module, uses ratios of strain energy (stored in the intact and damaged structures) between individual elements and the summation of all elements to develop a damage index (Stubbs, Kim and Topole, 1992). This method has been shown to be reliable in the first three performance metrics of damage detection, noted by Rytter (1993) and Stubbs (2011). More specifically, the method can 1.) determine whether damage has occurred, 2.) locate the damage, and 3.) determine the severity of the damage. The fourth level, which involves evaluating the remaining life of the structure, can be determined using empirical equations of fatigue life estimation. The current study focuses on damage detection up to level 3. In addition to the original damage index method, different weighting methods to account for multiple modes are employed. For example, one

weighting method is the damage index method in physical space. The energy is formed in physical space, where the displacements are estimated with modal information and flexibility matrix. The traditional damage index method computes the damage indices for each mode and uses the summation of damage indices of all modes in equal weights as the final result. The benefit of the damage index method in physical space is that it provides a reasonable way of combining information of all modes; hence it might be more accurate in locating and sizing the damage. The formulation of damage index method for both beam-like and plate-like structures is presented in Section 2.2.

One critical issue of implementing the computational tool is to use optimized sensors. The goal is not only to find the best locations of sensors, but also to estimate the least number of sensors required for the current job. As reviewed in the introduction, various strategies were adopted in the sensor optimization process to facilitate system/modal identification, damage detection, and structural health monitoring. In terms of methodologies, prevailing evolutionary algorithms such as genetic algorithms, simulated annealing and neural network algorithms are common options in solving the combinatory problem of selecting the best sensor array with specific goals. In this study, genetic algorithm will be used to help find the optimized sensor arrays, both for beam-like and plate-like structures. Details on the use of the genetic algorithm for sensor array optimization are discussed in section 2.3.

2.1 Time Domain Decomposition

2.1.1 TDD with Acceleration or Displacement Input

Modal analysis of structures is based on the assumption that the dynamic response of a linear system can be expressed as the summation of infinite modes. Applying TDD with acceleration input has four steps:

1.) obtain the modal equations for acceleration,

2.) apply filters to isolate single degree of freedom (SDOF) singles of the targeted i^{th} mode,

3.) form energy matrix to obtain the mode shape curvature for the i^{th} mode,

4.) obtain the modal contribution factor, and the damping ratio.

Beginning with a simple one-dimensional array of p unequally spaced sensors, the acceleration time history of vibrations in cross-flow direction can be assumed as the summation of infinite modes

$$\ddot{Y}(z,t) = \sum_{i=1}^{\infty} \ddot{c}_i(t)\ \varphi_i(z) \tag{2.1}$$

where, $\ddot{Y}(z,t)$ is the cross-flow acceleration with a size of $p \times 1$, $\ddot{c}_i(t)$ the scalar value, is the modal contribution factor, $\varphi_i(z)$ is the mode shape at the i[th] mode respectively with a size of $p \times 1$. Accordingly for p sensors one can only extract up to the p^{th} modal parameters without aliasing. Then the first equation can be expressed as

$$\ddot{Y}(z,t) = \sum_{i=1}^{p} \ddot{c}_i(t)\ \varphi_i(z) + \underbrace{\sum_{i=p+1}^{\infty} \ddot{c}_i(t)\ \varphi_i(z)}_{e_1(t)} \tag{2.2}$$

where $e_1(t)$ denotes a truncation error due to higher modes.

Spectral analysis and filter theory are applied to isolate the signal of the i[th] mode $\ddot{Y}_i(z,t)$ from the array signals. The power spectral densities for all sensors are generated and overlapped to find the energy concentration bandwidth for the targeted mode. Digital filters are designed and used to create a mode-isolated discrete-time response within the appropriate bandwidth. In this analysis a 20[th] order Butterworth band-pass filter was selected based on visual inspection, but in the implementation one can choose the optimal filter for the mode isolation process. Assume

$$\ddot{Y}_i(z,t) = \ddot{c}_i(t)\ \varphi_i(z) + \underbrace{\sum_{j=1}^{p-1} \ddot{d}_j(t)\ \psi_j(z)}_{e_2(t)} \tag{2.3}$$

where $\ddot{Y}_i(z,t)$ contains the i[th] mode and assumed orthogonal noise modes denoted as $e_2(t)$, which results filtering error in addition to the residual error from $e_1(t)$.

Eq. 2.3 can be rewritten as matrix format,

$$[\ddot{Y}_i(z,t)] = \{\varphi_i(z)\}\{\ddot{c}_i(t)\}^T + \sum_{j=1}^{p-1}\{\psi_j(z)\}\{d_j(t)\}^T \tag{2.4}$$

If N samples are recorded, $[\ddot{Y}_i(z,t)]$ is a p by N matrix.

Utilizing the orthogonality between components of the signal in modal space and the noise space, an energy matrix can be formulated as

$$[E(i)] = [\ddot{Y}_i(z,t)]\ [\ddot{Y}_i(z,t)]^T = U\,\Omega\,U^T \tag{2.5}$$

where,

$$U = [\varphi_i(z), \psi_1(z), \psi_2(z), \ldots \psi_{p-1}(z)] \tag{2.6}$$

$$\Omega = \begin{bmatrix} s(i) & & & & \\ & \sigma(1) & & & \\ & & \sigma(2) & & \\ & & & \ldots & \\ & & & & \sigma(p-1) \end{bmatrix} \tag{2.7}$$

The singular value decomposition technique (SVD) is then utilized to decompose the constructed energy matrix, and from Eq. 2.6, the mode shape can be deduced from the first column of U. The modal contribution factor with the mode shape obtained previously can be evaluated from the following equation

$$\{\ddot{c}_i(t)\}^T = \frac{1}{\varphi_i(z)^T\ \varphi_i(z)}\,\varphi_i(z)^T\,[\ddot{Y}_i(z,t)] \tag{2.8}$$

For the targeted mode, the modal value of the critical damping ratio can be estimated using the Half-Power Bandwidth method applied to Eq. 2.8.

A flow chart of TDD with acceleration input is presented in Fig. 2.2a. The formulation for TDD with displacement input is nearly the same except the input signal being displacement instead of acceleration, and modal contribution factor being $[c_i(t)]$ instead of $[\ddot{c}_i(t)]$. A flow chart of TDD with displacement is also presented in Fig. 2.2b.

Several features of time domain decomposition technique approach make it especially suitable for offshore structure application as in the case of flow-induced vibration analysis. First, the technique utilizes the measured ambient excitation for the

modal analysis. This is an important point as the laboratory experiments were conducted at relatively low Reynolds numbers and field data will typically be in the super critical flow regime. Thus, the methodology presented is valid for the analysis of field data. Secondly, the computation of single value decomposition process only depends on the number of sensors, but as noted the subsequent frequency resolution is important. Finally, the technique allows direct estimates of the mode shape from the measured data without making assumptions or idealizations. The current study noted the practical implementation issues regarding optimal filter selection and subsequent solutions and the need for use of the zoom technique in some cases in order to more accurately estimate of the modal critical damping ratios.

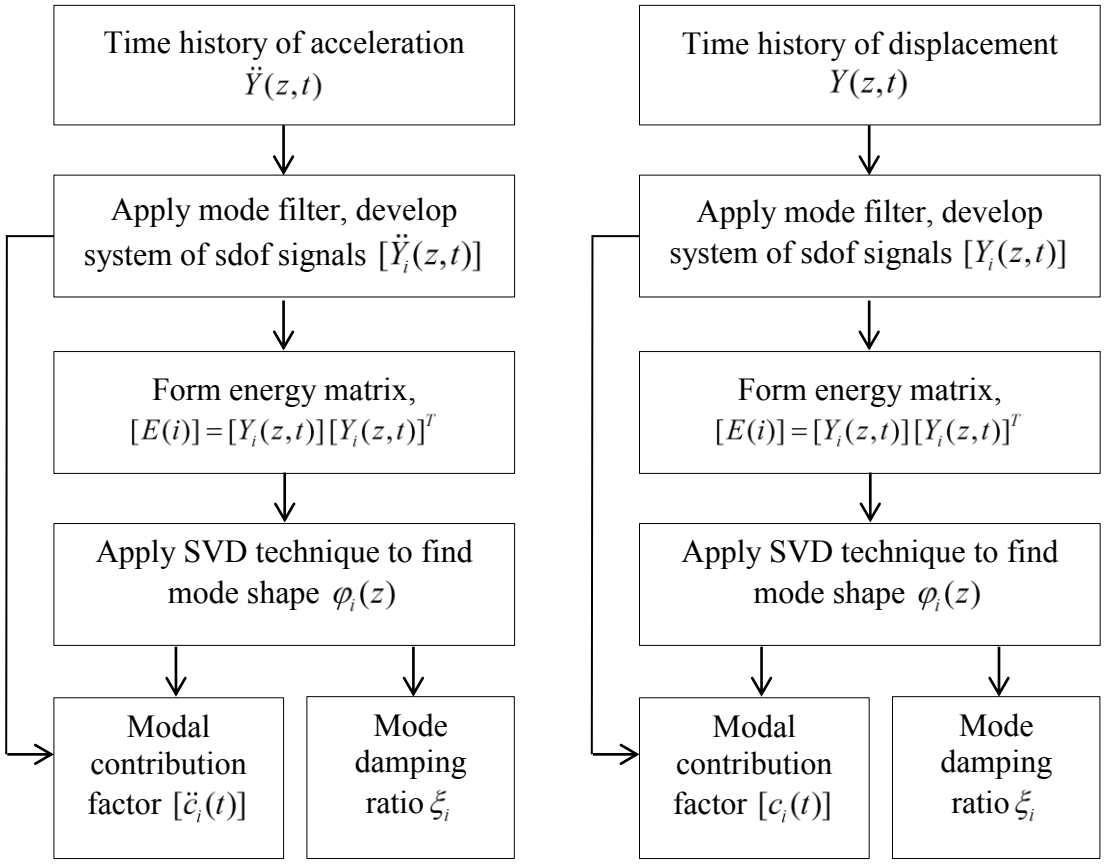

(a) with acceleration input (b) with displacement input

Fig. 2.2 Flow chart of TDD with acceleration or displacement input.

2.1.2 TDD with Strain Input

The formulation of TDD with strain input is very similar to that of acceleration or displacement input though some differences do exist. An additional step is needed to convert the obtained curvature modal contribution factors and mode shape curvatures to modal contribution factors and mode shapes. Similarly, applying TDD with strain input has five steps:

1.) derive the modal equations for strain,
2.) apply filters to isolate SDOF singles of the targeted ith mode,
3.) form energy matrix to obtain the mode shape curvature for the ith mode,
4.) obtain the curvature modal contribution factor, the modal contribution factor, and the damping ratio, and
5.) perform a double integration of the mode shape curvature to obtain the mode shape.

Given the displacement function $Y(z,t)$ of a beam, the modal representation can be expressed as

$$Y(z,t) = \sum_{i=1}^{\infty} c_i(t)\ \varphi_i(z) \tag{2.9}$$

where, $c_i(t)$ is the modal contribution factor for the ith mode, $\varphi_i(z)$ is the modal shape for the ith mode.

The curvature $\kappa(z,t)$ of the beam is the double derivative of the deflection,

$$\kappa(z,t) = \frac{\partial^2 Y(z,t)}{\partial z^2} = \sum_{i=1}^{\infty} c_i(t)\,\frac{\partial^2 \varphi_i(z)}{\partial z^2} \tag{2.10}$$

The beam curvature κ is a function of strain ε and radius R which can be expressed as

$$\kappa = \frac{\varepsilon_y}{y} = \frac{\varepsilon_R}{R} = \frac{\varepsilon}{R} \tag{2.11}$$

If the strain measurement is attached to the outside of the tube, the strain is at R, therefore is short for ε_R.

A short derivation for this relationship based on Euler-Bernoulli Beam theory can be found in Gere and Timoshenko (1997). Therefore,

$$\varepsilon(z,t) = R\,\kappa(z,t) \tag{2.12}$$

From here, the measured strain time history can be expressed as the summation of products of modal curvature contribution factors and mode shape curvatures

$$\varepsilon(z,t) = \sum_{i=1}^{\infty} C_i(t)\ \frac{\partial^2 \varphi_i(z)}{\partial z^2} \tag{2.13}$$

where, $C_i(t) = R\,c_i(t)$, denote the curvature modal contribution factor.

Similarly, if there are p sensors for the recording,

$$\varepsilon(z,t) = \sum_{i=1}^{p} C_i(t)\ \frac{\partial^2 \varphi_i(z)}{\partial z^2} + \underbrace{\sum_{i=p+1}^{\infty} C_i(t)\ \frac{\partial^2 \varphi_i(z)}{\partial z^2}}_{e_1(t)} \tag{2.14}$$

where, $e_1(t)$ is the truncation error due to higher order modes.

At this point, filters will be applied to isolate the targeted ith mode $\varepsilon_i(z,t)$, in a similar manner as shown in the processing of acceleration data,

$$\varepsilon_i(z,t) = C_i(t)\ \frac{\partial^2 \varphi_i(z)}{\partial z^2} + \underbrace{\sum_{i=1}^{p-1} [d_i(t)]\ \frac{\partial^2 \psi_i(z)}{\partial z^2}}_{e_2(t)} \tag{2.15}$$

where, $e_2(t)$ is the error due to filtering error and the residual error of $e_1(t)$, which consists of orthogonal noise curvature modes.

The formation of energy matrix is the same as in Section 2.1 for the matrix format $[\varepsilon_i(z,t)]$, followed by the SVD process for U and Ω. The U matrix now consists of mode shape curvature of the ith mode and noise mode shape curvatures, specifically,

$$U = [\frac{\partial^2 \varphi_i(z)}{\partial z^2}, \frac{\partial^2 \psi_1(z)}{\partial z^2}, \frac{\partial^2 \psi_2(z)}{\partial z^2}, ..., \frac{\partial^2 \psi_{p-1}(z)}{\partial z^2}] \tag{2.16}$$

A similar computation as Eq. 2.8 is then conducted to compute the curvature modal contribution factor $C_i(t)$. To obtain the modal contribution factor $c_i(t)$, the following procedure needs to be executed:

$$c_i(t) = \frac{C_i(t)}{R} \tag{2.17}$$

From here, Half-Power Bandwidth method will be adopted to give an estimate of the damping ratio with the time history of the modal contribution factor ξ_i.

In order to compute the displacement mode shapes, the double integration of the curvature mode shapes $\partial^2\varphi_i(z)/\partial z^2$ is required. The central differential method is used to recover the mode shapes from mode shape curvatures that were obtained by TDD with the appropriate boundary condition. The directly recovered curvature mode shape may be coarse and non-uniform due to the placement of sensors, thus spline curve fitting technique is used to construct a smooth mode shape with J points equally spaced. It follows then that a linear system of equations can be developed based upon the expression

$$\frac{\partial^2\varphi(j)}{\partial z^2} = \frac{\varphi(j-1)+\varphi(j+1)-2\varphi(j)}{\Delta h^2} \tag{2.18}$$

where, $j = 1, 2, \ldots J$, and Δh is the equal distance between two consecutive curvature mode shape points.

If the boundary condition is known, for example, both end clamped or pined,

$$\varphi_{x=0,\,L} = 0 \tag{2.19}$$

Then the mode shape deflections can be computed.

A flow chart of TDD with strain input is presented in Fig. 2.3.

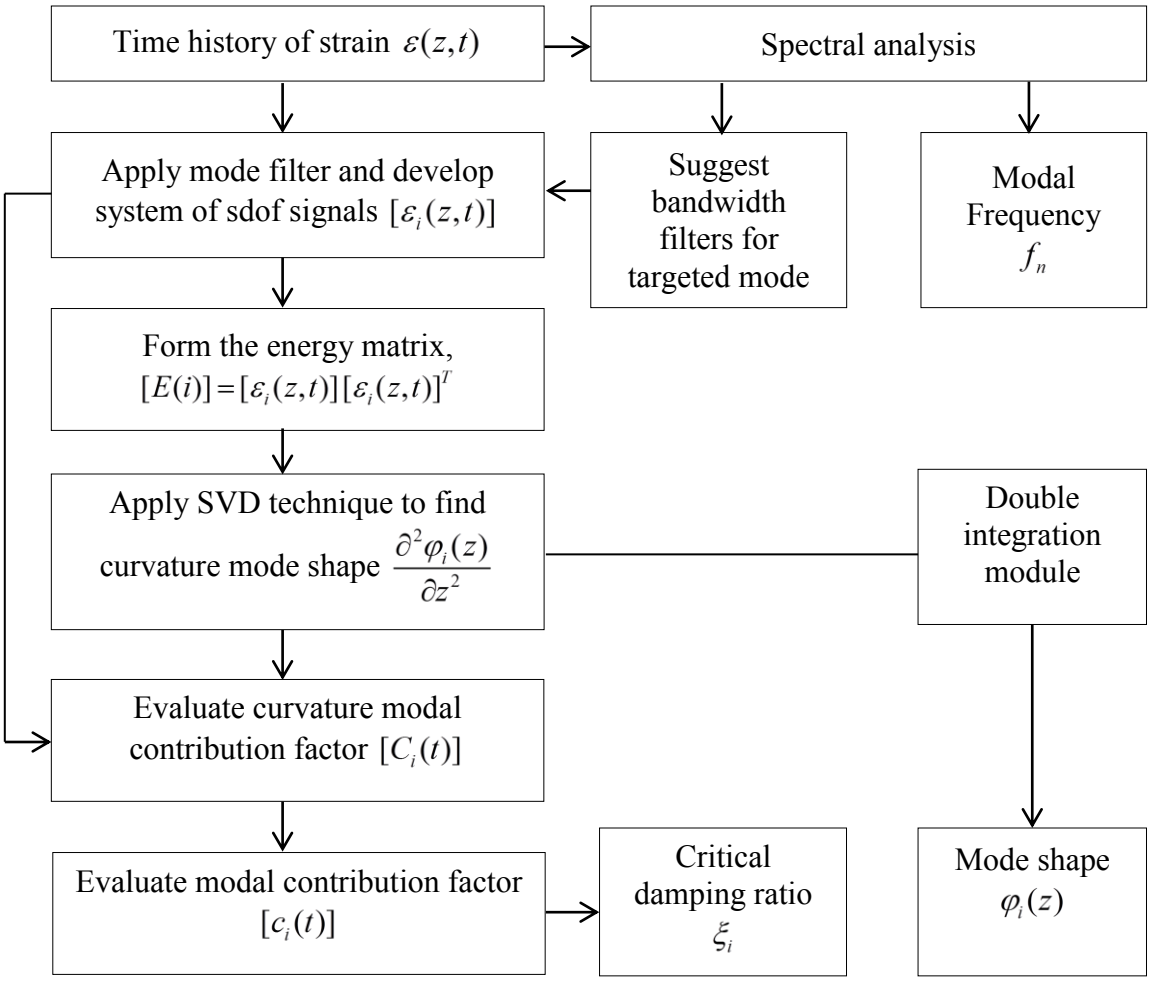

Fig. 2.3 Flow chart of TDD with strain input.

2.2 Damage Index Method

Vibration based damage detection of structures can be achieved via monitoring changes in mode shape curvatures, flexibility and stiffness information. Damage index method, proposed by Stubbs, Kim and Topole (1992), which originally detects damages of beam-like structures with changes of mode shape curvatures before and after damages assuming modal strain energy, can be expanded to cover more complex problems, such as offshore transmission pipelines or selected ice sheets. This section will review the

formulation of damage index method for beam-like structures, followed by the method for plate-like structures.

2.2.1 DIM for Beam-like Structures

A simple beam with length L before and after damage is proposed as the example of damage index method for beam-like structures, as shown in Fig. 2.4. The damage occurs at the i^{th} element among the total N elements, with the coordinates of a and b. Two assumptions are made upfront: one is the damage occurred primarily at a single sub-region, instead of spreading out; the other one is fractional strain energy at structural elements remains constant before and after the damage. The fractional strain energy is defined as strain energy stored in a local element divided by the total strain energy across the structure.

(a) Intact (b) Damaged

Fig. 2.4 An intact and damaged simple beam.

For the intact beam, the individual modal strain energy $U_{i,j}$ of a Bernoulli-Euler beam for element i at mode j is given by

$$U_{i,j} = \frac{1}{2}\int_a^b (EI)_i \left(\frac{\partial^2 \varphi_j}{\partial x^2}\right)^2 dx \tag{2.20}$$

where, $(EI)_i$ is the local bending stiffness, φ_j is the mode shape for mode j.

The total modal strain energy is then given by

$$U_{total,j} = \frac{1}{2}\int_0^L (EI) \left(\frac{\partial^2 \varphi_j}{\partial x^2}\right)^2 dx \tag{2.21}$$

where, (EI) is the general bending stiffness across the structure.

The fractional strain energy $F_{i,j}$ is therefore defined by

$$F_{i,j} = \frac{U_{i,j}}{U_{total,j}} \tag{2.22}$$

Clearly,

$$\sum_{i=1}^{N} F_{i,j} = 1 \tag{2.23}$$

Similarly for the damaged beam, the fractional strain energy $F_{i,j}^{*}$ is given by

$$F_{i,j}^{*} = \frac{U_{i,j}^{*}}{U_{total,j}^{*}} = \frac{\frac{1}{2}\int_{a}^{b} (EI)_{i}^{*} (\frac{\partial^2 \varphi_j^{*}}{\partial x^2})^2 \, dx}{\frac{1}{2}\int_{0}^{L} (EI)^{*} (\frac{\partial^2 \varphi_j^{*}}{\partial x^2})^2 \, dx} \tag{2.24}$$

where, $*$ denotes the damaged structure.

Assuming the fractional strain energy remains constant before and after damage

$$F_{i,j} = F_{i,j}^{*} \tag{2.25}$$

Following,

$$\frac{\frac{1}{2}\int_{a}^{b} (EI)_{i} (\frac{\partial^2 \varphi_j}{\partial x^2})^2 \, dx}{\frac{1}{2}\int_{0}^{L} (EI) (\frac{\partial^2 \varphi_j}{\partial x^2})^2 \, dx} = \frac{\frac{1}{2}\int_{a}^{b} (EI)_{i}^{*} (\frac{\partial^2 \varphi_j^{*}}{\partial x^2})^2 \, dx}{\frac{1}{2}\int_{0}^{L} (EI)^{*} (\frac{\partial^2 \varphi_j^{*}}{\partial x^2})^2 \, dx} \tag{2.26}$$

As stated early, if the damage occurs primarily at a local sub-region, and the general bending stiffness remains constant before and after the damage, the ratio of local bending stiffness before and after damage, noted as $\beta_{i,j}$, can be derived as

$$\beta_{i,j} = \frac{(EI)_i}{(EI)_i^{*}} = \frac{\int_{a}^{b} (\frac{\partial^2 \varphi_j^{*}}{\partial x^2})^2 \, dx \Big/ \int_{0}^{L} (\frac{\partial^2 \varphi_j^{*}}{\partial x^2})^2 \, dx}{\int_{a}^{b} (\frac{\partial^2 \varphi_j}{\partial x^2})^2 \, dx \Big/ \int_{0}^{L} (\frac{\partial^2 \varphi_j}{\partial x^2})^2 \, dx} \tag{2.27}$$

Here, $\beta_{i,j}$ is the damage index for mode j.

In order to obtain a general damage index β_i accounting for multiple modes, a few schemes have been proposed; a direct solution is equally weighted average if M modes are considered

$$\beta_i = \frac{\sum_{j=1}^{M} \beta_{i,j}}{M} \tag{2.28}$$

Damage index method in physical space, proposed and developed by Stubbs, Fang, Li (2012) estimates displacement using modal information and flexibility and further estimates the energy. The relationship between flexibility matrix and the mode shape, which was derived and proven by Zhao and Dewolf (1999), is given by

$$[F] = [\Phi][\Omega]^{-1}[\Phi]^T = \sum_{j=1}^{N} \frac{1}{\omega_j^2} \{\varphi_j\} \{\varphi_j\}^T \tag{2.29}$$

where the mode shapes need to be mass normalized.

In the same manner as stiffness matrix $[K]$ connecting displacement vector $\{v\}$ and load vector $\{L\}$, if the flexibility matrix $[F]$ is given, for a specified load vector $\{L\}$, the displacement vector $\{v\}$ is approximated as

$$\{v\} = [F]\{L\} \tag{2.30}$$

The displacement $\{v^*\}$ for the damage structure can be obtained in the same way.

At this point, the damage index in physical space can be derived as

$$\beta_i = \frac{\int_a^b (\frac{\partial^2 v^*}{\partial x^2})^2 \, dx \Big/ \int_0^L (\frac{\partial^2 v^*}{\partial x^2})^2 \, dx}{\int_a^b (\frac{\partial^2 v}{\partial x^2})^2 \, dx \Big/ \int_0^L (\frac{\partial^2 v}{\partial x^2})^2 \, dx} \tag{2.31}$$

Damage index method in physical space may have two advantages depending on the actual application. One potential advantage is that the damage index peak may be relatively narrow therefore it is easier to identify the damage. The other potential advantage is that it eliminates the effort of selecting modes in computing the damage index.

2.2.2 DIM for Plate-like Structures

The methodology can be extended to plate-like structures in the same manner except for additional complexity. Unlike beams, the strain energy for plate-like structures is computed using two-dimensional partial differential equations. The formulation of the method is illustrated with a simple isotropic and homogenous plate as shown in Fig. 2.5. The intact plate is shown in Fig. 2.5a. The planar dimensions of the plate are A and B. The damaged plate is shown in Fig. 2.5b, where the shaded area is location of the damage. The local damage is assumed to be confined in the element i, j.

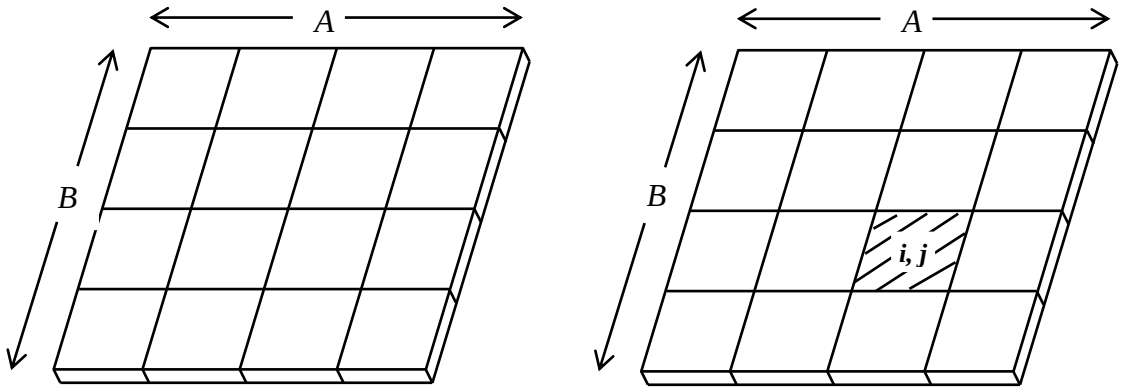

(a) Intact (b) Damaged

Fig. 2.5 An intact and damaged simple plate.

The governing equation of a plate in vibration subjected to an external force $f(x, y, t)$ is given by

$$D\nabla^4 w(x, y, t) + \rho h \frac{\partial^2 w(x, y, t)}{\partial t^2} = f(x, y, t) \tag{2.32}$$

where, w is deflection. D is the flexural rigidity of the plate, defined by Young's modulus E, plate thickness h, plate density ρ, Poisson's ratio ν, and is given by

$$D = \frac{Eh^3}{12(1-\nu^2)} \tag{2.33}$$

And the biharmonic operator $\nabla^4 w(x, y, t)$ is defined as

$$\nabla^4 w(x, y, t) = \frac{\partial^4 w}{\partial x^4} + 2\frac{\partial^4 w}{\partial x^2 \partial y^2} + \frac{\partial^4 w}{\partial y^4} \tag{2.34}$$

A detailed derivation of vibration of plate can be found in Rao, 2007.

The modal strain energy of a plate element i, j at mode k for the intact plate is given by

$$U_{i,j,k} = \frac{D_{i,j}}{2} \iint_{a_j, b_k} [(\frac{\partial^2 \varphi_k}{\partial x^2})^2 + (\frac{\partial^2 \varphi_k}{\partial y^2})^2 + 2\nu \frac{\partial^2 \varphi_k}{\partial x^2} \frac{\partial^2 \varphi_k}{\partial y^2} + 2(1-\nu)(\frac{\partial^2 \varphi_k}{\partial x \partial y})^2] dxdy \tag{2.35}$$

A two-step slicing technique is used to compute the ordinary and partial derivatives numerically for a given mode shape φ_k. First the first order derivatives, $\partial \varphi_k / \partial x$ and $\partial \varphi_k / \partial y$, are computed for each slice with respect to x and y coordinate resulting in two meshes of the first order derivatives in both coordinates. Then the slicing method is applied to the meshes of the first order derivatives to obtain the second order derivatives, specifically, applying slicing of $\partial \varphi_k / \partial x$ in x coordinate will result in the second order ordinary derivative $\partial^2 \varphi_k / \partial x^2$, applying slicing of $\partial \varphi_k / \partial y$ in y coordinate will result in the second order ordinary derivative $\partial^2 \varphi_k / \partial y^2$, and applying slicing of $\partial \varphi_k / \partial x$ in y coordinate will result in the second order partial derivative $\partial^2 \varphi_k / \partial x \partial y$. The modal strain energy can be computed with the second order ordinary and partial derivatives.

The total modal strain energy that accounts for all elements is

$$U_{total,k} = \frac{D}{2} \iint_{A,B} [(\frac{\partial^2 \varphi_k}{\partial x^2})^2 + (\frac{\partial^2 \varphi_k}{\partial y^2})^2 + 2\nu \frac{\partial^2 \varphi_k}{\partial x^2} \frac{\partial^2 \varphi_k}{\partial y^2} + 2(1-\nu)(\frac{\partial^2 \varphi_k}{\partial x \partial y})^2] dxdy \tag{2.36}$$

The fractional strain energy $F_{i,j,k}$ is defined similarly as that for beams,

$$F_{i,j,k} = \frac{U_{i,j,k}}{U_{total,k}} \tag{2.37}$$

The elementary strain energy $U^*_{i,j,k}$, total strain energy $U^*_{total,k}$ and fractional strain energy $F^*_{i,j,k}$ for the damaged plate are defined in the same manner, noted by * , and given by

$$U^*_{i,j,k} = \frac{D^*_{i,j}}{2} \iint_{a_j,b_k} [(\frac{\partial^2 \varphi^*_k}{\partial x^2})^2 + (\frac{\partial^2 \varphi^*_k}{\partial y^2})^2 + 2\,\nu\, \frac{\partial^2 \varphi^*_k}{\partial x^2} \frac{\partial^2 \varphi^*_k}{\partial y^2} + 2(1-\nu)\,(\frac{\partial^2 \varphi^*_k}{\partial x\,\partial y})^2]\, dxdy \quad (2.38)$$

$$U^*_{total,k} = \frac{D^*}{2} \iint_{A,B} [(\frac{\partial^2 \varphi^*_k}{\partial x^2})^2 + (\frac{\partial^2 \varphi^*_k}{\partial y^2})^2 + 2\,\nu\, \frac{\partial^2 \varphi^*_k}{\partial x^2} \frac{\partial^2 \varphi^*_k}{\partial y^2} + 2(1-\nu)\,(\frac{\partial^2 \varphi^*_k}{\partial x\,\partial y})^2]\, dxdy \quad (2.39)$$

$$F^*_{i,j,k} = \frac{U^*_{i,j,k}}{U^*_{total,k}} \quad (2.40)$$

Assuming the fractional strain energy is constant before and after damage,

$$F_{i,j,k} = F^*_{i,j,k} \quad (2.41)$$

The relationship between the stiffness, for plates, the flexural rigidity D, before and after damage can be constructed by associating Eq. 2.32-2.38. The damage index for plate-like structures at the element i, j and at mode k is defined by

$$\beta_{i,j,k} = \frac{D_{i,j}}{D^*_{i,j}} \quad (2.42)$$

and given by

$$\beta_{i,j,k} = \frac{\iint_{a_j,b_k} [(\frac{\partial^2 \varphi^*_k}{\partial x^2})^2 + (\frac{\partial^2 \varphi^*_k}{\partial y^2})^2 + 2\,\nu\, \frac{\partial^2 \varphi^*_k}{\partial x^2} \frac{\partial^2 \varphi^*_k}{\partial y^2} + 2(1-\nu)\,(\frac{\partial^2 \varphi^*_k}{\partial x\,\partial y})^2]\, dxdy}{\iint_{A,B} [(\frac{\partial^2 \varphi^*_k}{\partial x^2})^2 + (\frac{\partial^2 \varphi^*_k}{\partial y^2})^2 + 2\,\nu\, \frac{\partial^2 \varphi^*_k}{\partial x^2} \frac{\partial^2 \varphi^*_k}{\partial y^2} + 2(1-\nu)\,(\frac{\partial^2 \varphi^*_k}{\partial x\,\partial y})^2]\, dxdy} \Big/ \frac{\iint_{a_j,b_k} [(\frac{\partial^2 \varphi_k}{\partial x^2})^2 + (\frac{\partial^2 \varphi_k}{\partial y^2})^2 + 2\,\nu\, \frac{\partial^2 \varphi_k}{\partial x^2} \frac{\partial^2 \varphi_k}{\partial y^2} + 2(1-\nu)\,(\frac{\partial^2 \varphi_k}{\partial x\,\partial y})^2]\, dxdy}{\iint_{A,B} [(\frac{\partial^2 \varphi_k}{\partial x^2})^2 + (\frac{\partial^2 \varphi_k}{\partial y^2})^2 + 2\,\nu\, \frac{\partial^2 \varphi_k}{\partial x^2} \frac{\partial^2 \varphi_k}{\partial y^2} + 2(1-\nu)\,(\frac{\partial^2 \varphi_k}{\partial x\,\partial y})^2]\, dxdy} \quad (2.43)$$

To account for multiple modes associated, equally weighted average method is adopted to compute the general damage index at element i, j.

$$\beta_{i,j} = \frac{\sum_{k=1}^{M} \beta_{i,j,k}}{M} \tag{2.44}$$

2.3 Genetic Algorithm in Sensor Array Optimization

In this study, genetic algorithm will be used to find the optimized sensor arrays. Genetic algorithm is a method for solving optimization problems based on natural selection (Rechenberg, 1965). The fact that genetic algorithm can be applied on problems with objective functions being discontinuous, non-differentiable, random or nonlinear, makes it very suitable for the current task of sensor optimization. Specifically designed for this study, the genetic algorithm includes 3 main steps: initialization, reproduction, and evolution to the optimal solution. In the initialization phase, the following terms need to be defined: an individual sensor, a group of individual sensors, fitness function and population. An individual sensor is identified with the index of the sensor and its location on the structures, i.e. for a 1-D structure as $s_i(x)$ and for a 2-D structure as $s_i(x, y)$. A group of individual sensors, noted as the set of the sensors $[s_1(x), s_2(x)...s_I(x)]$ for 1-D or $[s_1(x, y),\ s_2(x, y)...s_I(x, y)]$ for 2-D. The group size I is the number of sensors used. It is noted that each group of sensors is evaluated with a fitness function. The fitness function and fitness value are keys to genetic algorithm for they quantify how good a group of the sensors is. For the problem of sensor optimization, the fitness function is typically the difference between the sensor recovered information and the true value, noted as $f(s_1(x), s_2(x)...s_I(x))$. The smaller the fitness value, the better performance the group of sensor is. It is noted the sensor optimization problem is discontinuous and nonlinear as the optimal depends on both the location of each individual sensor and the combination of sensors. Population of groups is defined as a set of grouped sensors. In the algorithm, populations are constantly updated through multiple generations, and evolve toward an optimal solution. The generation in the initialization step is set to be 1.

With the defined individual, group, fitness function and population, the sensor optimization problem can be framed in the format for genetic algorithm. Take a beam for example, the 1-D sensor array optimization is:

$$\begin{aligned} &\underset{x}{minimize} \quad f(s_1(x),\ s_2(x) \ldots s_I(x)) \\ &subjected\ to,\ \ s_i(x) \in [0, L],\ \ i = 1, 2 \ldots I \end{aligned} \tag{2.45}$$

where L is defined as the length of the beam.

In the case of an ice sheet, the 2-D sensor array optimization is:

$$\begin{aligned} &\underset{x}{minimize} \quad f(s_1(x, y),\ s_2(x, y) \ldots s_I(x, y)) \\ &subjected\ to,\ \ s_i(x, y) \in R \end{aligned} \tag{2.46}$$

where R is defined as the domain of the ice sheet.

In the reproduction phase, two questions are answered, how to select the best groups among the population, and how to reproduce the next generation? In order to select the best groups, the fitness values of each grouped sensors in the population is computed and ranked, while a small portion of the top best groups is selected as parents. However, being a parent solution doesn't necessarily mean the solution can yield children for the next generation. There are several ways to select the parents based on their favored fitness values. One way is to do a stochastic uniform selection where each parent solution is assigned a line of length proportional to its fitness value. Two random numbers are generated along the total length to select both parents and then children solutions can be generated. Another way is to conduct a tournament selection where tournament size solutions are selected randomly from the parent solutions and then the winner of the tournament guarantee a spot in generating children solutions. Another tournament will be held to find the other parent. Generally the tournament size is 4 which can be adjusted but no less than 2.

The operators of crossover and mutation are used to reproduce the next generation as illustrated in Fig. 2.6. From generation 1 to 2, group 1 experiences a mutation, where the location of the blue sensor is changed and in the meantime the red sensors remain unchanged. Group 2 and 3 are modified with crossover, where the blue

and red sensors in group 2 and 3 in generation 1 are reorganized to produce beams with all blue and red sensors in generation 2. Mutation and crossover are useful tools in generating better solutions.

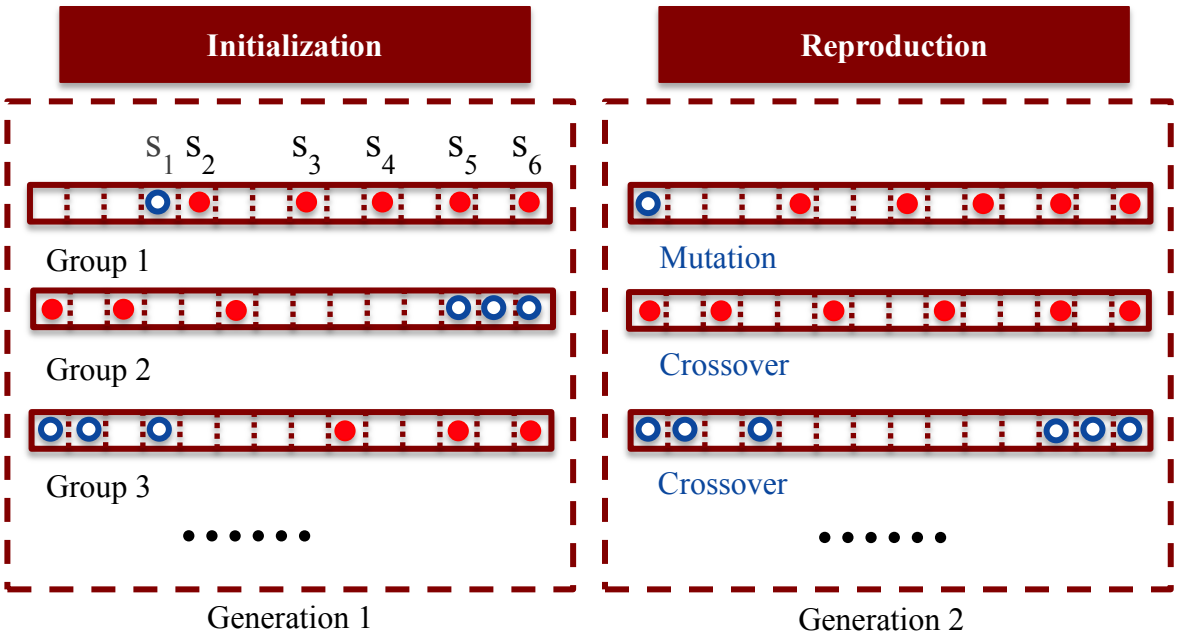

Fig. 2.6 Initialization and reproduction phases of a genetic algorithm.

Though sensor arrays according to the fitness in their top ranks are selected as parents to generate favorable children solutions, there is no guarantee that the children solution would outperform parents. A third operator that ensures the population of solutions to converge faster towards the optimal is elitism, which means to directly keep a number of the best sensor arrays into the next generation. The number of the best sensor arrays is noted as elites.

Convergence criteria or stopping criteria shall be considered in the implementation as well. Typically a tolerance of 10^{-6} is used for convergence. If the tolerance is not met, the algorithm stops at the largest generation. The evolution of

solutions continues as generation goes on until all the solutions are converged. Then the sensor array, with the optimal numbers and locations, is achieved from the algorithm.

Fig. 2.7 illustrates the flow chart of the genetic algorithm for sensor optimization.

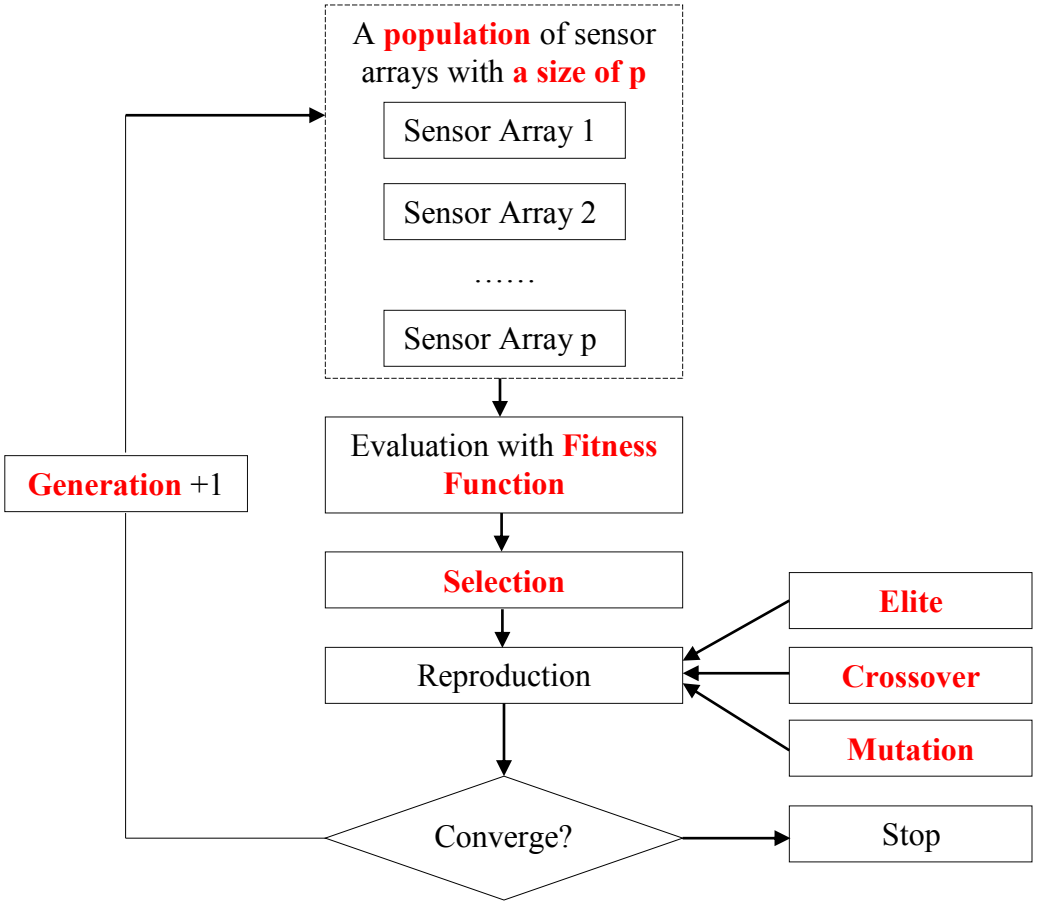

Fig. 2.7 Flow chart of the genetic algorithm for sensor optimization.

The successful execution of a genetic algorithm heavily relies on the parameters chosen, specifically the fraction of crossover/mutation in the population, the number of elite, the fitness function, the size of population, the number of generations and the stopping criteria. Genetic algorithm is stochastic global search and optimization model the goal of which is to converge into the right optimal as fast as possible. One important

feature genetic algorithm has a competitive advantage than derivative based optimization method is its ability to spread out enough to search the entire domain for the optimal without trapping into local maxima. Fig. 2.8 illustrates the relationship between fitness values with a range of sensor arrays where a derivative based optimization technique may try hard to find the optimal solution as sensor array C without realizing the true optimal away from the searching regions. Genetic algorithm has the possibility of securing the optimal solution but depends on its ability to be dynamic and active in spreading its population over the search domain. Adjusting the fraction of crossover and mutation can help sustain the spreading ability; specifically crossover tends to keep the comfortable solutions while mutation tends to explore new territories hence weighing the two factors appropriately can maneuver the direction of the searching. Elite solutions compensate the flaw of crossover in generating next generations but not fully able to keep the known best solution hence elitism is part of the stabilizing forces, the number of which must be determined by weighing the spreading and converging.

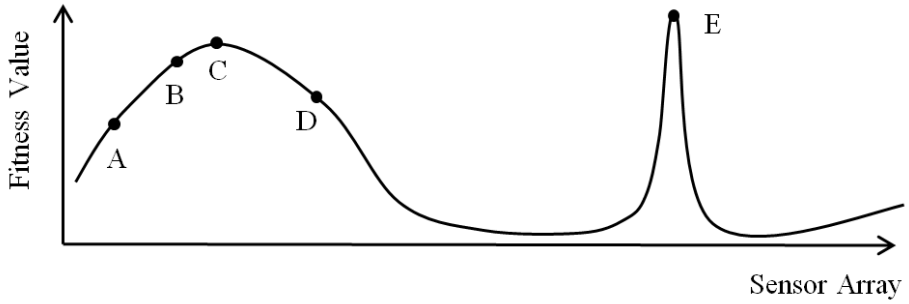

Fig. 2.8 An example of distant true optimal solution in sensor optimization.

The determination of the fitness function can affect the searching quality of the genetic algorithm. When sensor arrays are specifically utilized to extract mode shapes, modal assurance criterion (MAC) proposed by Allenmang and Brown (1982) can be a good fitness criterion, which is defined as

$$MAC(i,j)=\frac{\left|\{\varphi(i)\}^T\{\psi(j)\}\right|^2}{(\{\varphi(i)\}^T\{\varphi(i)\})(\{\psi(j)\}^T\{\psi(j)\})} \tag{2.47}$$

where, $\varphi(i)$ and $\psi(i)$ are the corresponding mode shape extracted from a sensor array and the theoretical mode shape. The modal assurance criterion quantifies the correlation of the mode shapes and values will vary between zero and one. If the value of the MAC for a particular mode is one or very close than the two modes of interest are virtually identical and for values that are small or approaching zero then the two modes are dissimilar. Depending on the requirement, the value of MAC should be overviewed carefully for it might be misleading. It can be close to one but still have recognizable differences from the optimal solutions.

Engineering judgment and available information sometimes can help improve the performance of MAC. Many mode shapes of a uniform and symmetric structure behave symmetry and that symmetric features can be built into the evaluation of MAC. Propose

$$MAC_{sym}(i,j)=\underbrace{\frac{\left|\{\varphi(i)\}^T\{\psi(j)\}\right|^2}{(\{\varphi(i)\}^T\{\varphi(i)\})(\{\psi(j)\}^T\{\psi(j)\})}}_{original\ MAC}+\underbrace{\frac{\left|\{\varphi(i)\}^T\{\varphi(i)_{flip}\}\right|^2}{(\{\varphi(i)\}^T\{\varphi(i)\})(\{\varphi(i)_{flip}\}^T\{\varphi(i)_{flip}\})}}_{MAC\ for\ symmetry}-1 \tag{2.48}$$

where, the first part is the original MAC, while the middle part is MAC between the obtained mode shape $\varphi(i)$ and flipped mode shape $\varphi(i)_{flip}$ to compensate the asymmetry.

Not all optimization problems are in search of one single value. In some problems, multiple objectives must be met. Lump summing all the objective values with weighted average can easily turn the multi-objective problem to a single-objective problem (Unger, Teughels and Roeck, 2006). However, it is not easy to assign the

weight factor without knowing the nature of the problem, what"s worse, a wrong assignment can easily distort the lengthy optimization resulting in false optimal.

The Pareto front is a methodology which does not search for one single optimal but a series of solutions, each one of which represents the best optimization result it can achieve. The Pareto front provides a framework and a platform to select a preferred optimal from the serial solutions. The Pareto front is determined by comparing dominancy of solutions as illustrated in Fig. 2.9. The optimization problem is set at minimization for both objective 1 and 2. Point A is dominating point B for if B moves to A both objectives can be improved. When point A moved to E where no further improvement can be made in one objective without undermining the other, a Pareto front point is identified. Point D and F are both identified as points on Pareto front. The Pareto front in this case is formed with point D, E and F.

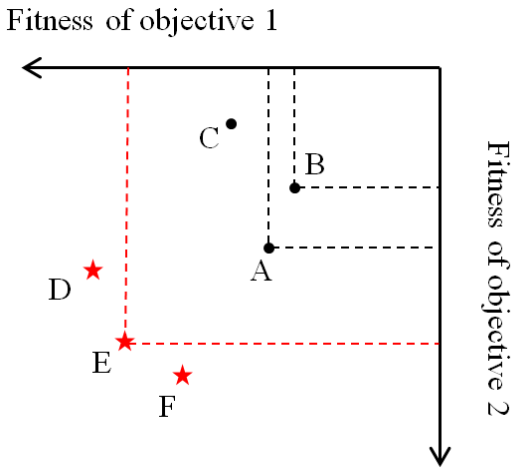

Fig. 2.9 Illustration of a Pareto front.

3. ANALYSIS AND INTERPRETATION OF FLOW-INDUCED VIBRATION*

Long and slender cylindrical marine structures such as pipelines and risers constantly suffer from flow-induced vibrations (FIV) due to vortices developed in the interaction with current and wave loads. In addition, devices for different engineering purposes typically installed on those structures add complexity into the analysis. Flow-induced vibration suppression concepts and devices such as airfoil firings, ribbon fairings and helical strakes were invented and tested to prevent or alleviate the undesired responses, see example Zdravkovich (1981), Every, King and Weaver (1982), Kumar, Sohn and Gowda (2008). Buoyancy elements are generally needed to balance the top tension and the weight due to the heavy weight of marine risers. Service lives of the structures are bounded by the dominant modes, scale of extreme responses and their locations, performance of FIV suppression devices, effect of environment loads, etc.

Of particular interest is the evaluation of modal responses including mode dominancy, modal frequencies, mode shapes and modal damping. In previous studies made by Kaasen (2001), Trim et al. (2005), and Li et al. (2011), sinusoidal mode shapes are typically assumed regardless of the complexity of the geometry and response behavior. Among many modal recognition techniques (Juang and Pappa, 1985, Ibrahim and Mikulcik, 1977), the Time Domain Decomposition technique (TDD) developed by Kim, Stubbs and Park (2005) to recover modal parameters from response time histories, is especially suitable in the study of FIV problems. The method utilizes ambient excitation for the modal analysis, which is essentially useful for analyzing vortex-induced vibrations where the excitation can hardly be fully known and may involve for example combined ocean wave and sheared current flows. Besides, the TDD technique

*Part of the data reported in section 3.1 of this chapter is reprinted with permission from "Comparison of airfoil and ribbon fairings for suppression of flow-induced vibrations" by Fang and Niedzwecki, 2013. International Journal of Computational Methods and Experimental Measurements, Volume 2, Issue 1, and "Suppression of flow-induced vibrations using ribbon fairings" by Niedzwecki and Fang, 2013. International Journal of Computational Methods and Experimental Measurements, Volume 1, Issue 4, Copyright (2013) by WIT Press.

requires no assumptions regarding modal information as it depends totally on the recorded data to identify modal characteristics. TDD has been validated by numerical models, and field tests such as King Storm Water Bridge in California (Kim, Stubbs and Park, 2005), Seohae cable-stayed bridge (Kim et al., 2008) and the Jitan bridge of Korean High-Speed Train system (Kim, Lee and Lee, 2010). However, the methodology has not been applied to a marine structure and sensor arrays used in above examples are all equally spaced with sufficient sampling frequency. In addition, the methodology was developed on either acceleration or displacement input.

Correctly recovered modal parameters are crucial to the analysis of long and flexible subsea transmission lines undergoing flow-induced vibrations. First, resonances may be avoided by shifting away the modal frequencies from the frequencies of external forces, (i.e. shedding frequency of FIV or wave frequency). Second, magnitudes and locations of extreme displacements and stresses might be predicted with recovered modal responses. Third, modal parameters may serve as indicators of damage detection. It is believed that when a structure is subjected to certain damage, there are changes in modal behavior. Oil and gas industry pioneered in the development of using changes in natural frequencies to detect damage dating back to 1970s (Vandiver 1975, 1977, Begg et al., 1976). Damage index method (DIM), developed by Stubbs, Kim and Topole (1992) which used fractional strain energy ratios before and after damage, is a robust technique in detecting, locating and sizing single occurrence, even multiple occurrences of damages. Strain energy as an indicator of damage is by far one of the best among all modal parameters (Farrar and Jauregui, 1998, Fan and Qiao, 2011). DIM has been validated with a field bridge I-40 (Stubbs et al., 1995). However, very few studies use DIM to analyze marine risers. Therefore this study utilizes DIM to numerically evaluate damages of marine transmission lines using modal response recovered by TDD.

Instrumentation on slender marine structures is important because the data collected from various sensors provide the basis of the analysis shown later on (Dai and Bai, 2011). The types of measurements include displacement, velocity, rotation, acceleration and strain, among which acceleration and strain are the most common ones.

Accelerometers, single axial, bi-axial and even tri-axial, are typically used to measure accelerations. Strain gages and fiber optic sensors are common devices to measure strains, especially the fiber optic sensors in recent years (Morikawa et al., 2008). There are both pros and cons of measuring accelerations and strains. Acceleration measurements are robust and cost effective, but when the data are manipulated to obtain displacements or stresses, errors may arise during the numerical integration and additional baseline information is typically needed to correctly account for the offset. Besides, the data might be influenced by gravity as shown in Kaasen (2001). Strain gages are sometimes preferred since the measurements can be readily converted to stresses or displacement curvatures, which in turn, may be beneficial in monitoring extreme conditions. In addition, strain gage data are not sensitive to gravity. However, strain measurements for structures with asymmetric sections might have issues due to the uncertainty of the neutral axes. Fiber optic sensor has a unique benefit since the sensor allows massive data collection of multiple parameters (sometimes even in the order of a thousand), for example temperature and strain at the same time, which is very attractive to the oil and gas industry in deep water operations (Inaudi and Glisic, 2006). Experimentalists working on Vortex-Induced Vibration (VIV) response in the laboratories or in the field use accelerometers to measure the response, e.g. Kaasen (2001), or the combination of accelerometers and strain gages, e.g. Frank et al. (2004) and Trim et al. (2005) as shown in Table 3.1. However, several new studies used fiber optic sensors densely distributed on the test cylinders, e.g. Li et al. (2011), Jaiswal and Vandiver (2007), and Wilde (2004). Jaiswal and Vandiver (2007) designed a Gulf Stream field test on a long composite pipe with a length of 152.4 m and a diameter of 36.3 mm, using the Research Vessel F. G. Walton Smith. Eight optical fiber cables, each containing thirty-five fiber optical sensors were attached onto the cylinder to measure the VIV response. Fiber Bragg Gratings (FBG) sensors were installed to measure the strain information in the experiment of Li et al. (2011). In light of previous findings that in-line (IL) responses usually had higher frequency components than cross-

flow (CF) responses (Blevins, 1990), 25 measurements were deployed in the IL direction and 19 in the CF direction.

The number and placement of sensor arrays is of great importance since the data collected provide the basis for the time domain decomposition and damage index method. Optimized sensor arrays in numbers and locations have both economic and technical benefits, especially for offshore industry. Considering the cost related to installation, maintenance and actually implementation of sensor arrays, the smaller the number of sensors, the more cost effective the sensor arrays are. Placement of sensor arrays needs to account for the variation of dominant modes due to the changing environment, intense arrangement for venerable regions due to excess loads or deformation, and access limitation due to physical conditions. In this study, a customized genetic algorithm will be adopted to find the optimal sensor array for implementation in marine transmission lines.

This study customized the TDD method in combination with spectral analysis techniques to use unequally spaced sensor arrays with coarse sampling frequency to recover modal parameters of two marine transmission line models, with length to diameter ratios of 760 and 263 respectively. More specifics of the experiments can be found in Chitwood (1998), Li et al. (2011), Niedzwecki and Fang (2013) and Fang et al. (2013). The first test used accelerometers mainly with acceleration as input. While the second test utilized fiber optic sensors with strain data as input. The second example with strain input will be used to conduct the sensor optimization work due to availability of sufficient data.

Table 3.1 Summary of experimental particulars of studies on buoyancy, strakes w/wo fiber-optic sensors.

Author	Year	L/D	Re	Current	Buoyancy Element				Strakes			Instrumentation	
					$\frac{D_B}{D}$	$\frac{L_G}{L_B}$	$\frac{L_B}{D}$	Coverage	$\frac{Pitch}{D}$	$\frac{Height}{D}$	Coverage	Accelero-meters	Strain
			10^3					%			%		
Jhingran et al.	2012	475, 1267	Up to 200	Uniform	2.67	1-3	13.7	25-50		/		Number unknown	Number unknown
Vandiver & Peoples	2003	230, 574	4-95	Uniform/ Sheared	2.50	0.1, 1, 3	25	15, 25, 50, 100		/		9 (CF)	/
Li et al.	2011	105, 263	6-195	Uniform	2.50	0.07, 3,	10	0, 25, 50, 91	17.5	0.25	50, 75	/	Fiber optic sensors (19 IL, 25 CF)
Jaiswal & Vandiver	2007	4198	/	Gulf stream		/			17.5	0.25	25-84	/	Fiber optic sensors (70 IL, 70 CF)
Wilde & Huijsmans	2004	788	8-48	Uniform								2 bi-axial	Fiber optic sensors (10 IL, 10 CF)
Vandiver et al.	2006	1839, 3670	10-37	Near uniform		/			17.5	0.25	100	6 tri-axial	/
Trim et al.	2005	1407	8-65	Uniform/ Sheared		/			17.5, 5.0	0.25, 0.14	41, 62, 82, 91	8 bi-axial	Strain gages (24 CF, 40 IL)
Allen et al.	2004	466	150-350	Sheared		/			17.5, 12	0.1, 0.15, 0.25	18, 37	4 bi-axial	/
Frank et al.	2004	480	4-48	Uniform/ Sheared		/			16	0.25	25, 50, 75, 100	8 bi-axial	Strain gages (17 CF, 35 IL)

Note:

1. D_B : the diameter of the buoyancy unit, D : the diameter of the cylinder, L : the length of the cylinder, L_G : the length between buoyancy elements, L_B : the length of the buoyancy element.
2. Flow regime: sub-critical, $\mathrm{Re} < 2*10^5$; critical, $2*10^5 < \mathrm{Re} < 6*10^5$; super-critical, $\mathrm{Re} > 6*10^5$
3. CF: cross-flow direction, IL: in-line direction.
4. Fiber optic sensors are generally installed in a group of 2 on the top and bottom to address CF responses, in another group of 2 on the fore and aft to address IL responses. Each group is considered as one measurement, e.g. Li et al., 38 fiber optic sensors at IL direction mean 19 measurements.

3.1 Analysis Based on Acceleration Input

An industrial scale experimental investigation into the flow-induced response behavior of a horizontally towed cylinder with varied fairing coverage was performed and some of that data were selected for the study reported here. The data of interest focuses on the flow-induced response behavior for model tests involving variable coverage of zip-on ribbon fairings and free-rotating airfoil fairings. Additional details regarding the original scope test program can be found in the report by Chitwood (1998). Fig. 3.1 presents a fairly detailed schematic of the test setup. The vertical I-beams shown in the figure were rigidly connected to the bridge structure and provided a means to pretension the cylinder model in order to target various modes of vibration. Load cells were incorporated in the design and were used to monitor the tension variations during towing. The figure also shows the location of the three wave gages and the six bi-axial accelerometers that were located inside the cylinder model. The cylinder ends were sealed and a slight pressure was maintained inside the cylinder in order to keep the bi-axial accelerometers dry. The cylinder support structure was designed so that the cylinder can be pre-tensioned so that the third mode would be the dominant mode of cylinder vibration. The composite cylinder had a length of 29.5m, an outside diameter of 38 mm, an inside diameter of 22 mm, a unit weight of 1.04 kg/m (0.698 #/ft) and a mass ratio of approximately 0.91. Given these dimensions the length to outer diameter, L/D, was estimated to be approximately 760. The cylinder depth of submergence was 0.61 m.

The towing speeds varied between 0.18 to 0.43 m/s and simulated uniform current conditions. For the combined uniform current and wave conditions tested, regular waves with the wave height 0.24 m and the peak period 3.2 s were introduced. Considering the maximum horizontal wave kinematic velocity, the Reynolds number was estimated to vary between $7*10^3$ and $2.3*10^4$, corresponding to sub-critical flow regime. As shown in Fig. 3.1, the six bi-axial acceleration pairs were unequally spaced. A string-potentiometer sensor, not shown in Fig. 3.1, was mounted on the bridge and connected to the cylinder at its mid-span in order to record the displacement. Those

measurements were later used to provide a comparison with the displacement estimates obtained by the double integration of the accelerometer data. Both transverse and in-line displacements were later estimated from the bi-axial acceleration data.

This experimental study focused on evaluating the performance of two different FIV suppression devices: airfoil and ribbon fairings. The performance of a suppression device implemented for marine subsea transmission lines is judged by its reduction in responses magnitudes, effect in changing dominant modes and reduction in drag forces. The majority of the devices attached will alter the system properties to some extent and change the natural frequencies, either closer to or further from the frequency of the external forces. Airfoil fairings function by streamlining the vortices to remove the alternative shedding forces and hence to suppress the response. Because of the streamlining effect, the drag forces applied on the structure were reduced as well (Allan and Henning, 2008). Ribbon fairings function via a combination effect of streamlining and disrupting the flow. Fig. 3.2 shows side-by-side photos of the airfoil and ribbon fairings used in the study. The airfoil fairings were made of Acrylonitrile Butadiene Styrene plastic (ABS), with a width of 304.8 mm (1 ft), a chord length of 165.1 mm (6.5 in) and a thickness of 44.5 mm (1.75 in) resulting in a c/t ratio of 3.7. The airfoil fairings were attached to the cylinder with zip-ties to ensure free rotation. The ribbon fairings were made of soft compliant vinyl, with the same width as the airfoil fairings, and trailing length of 127 mm (5 in). The faring length when attached was 3.3D long with a slit width of 0.67D at right angles to the cylinder. D was the diameter of the cylinder.

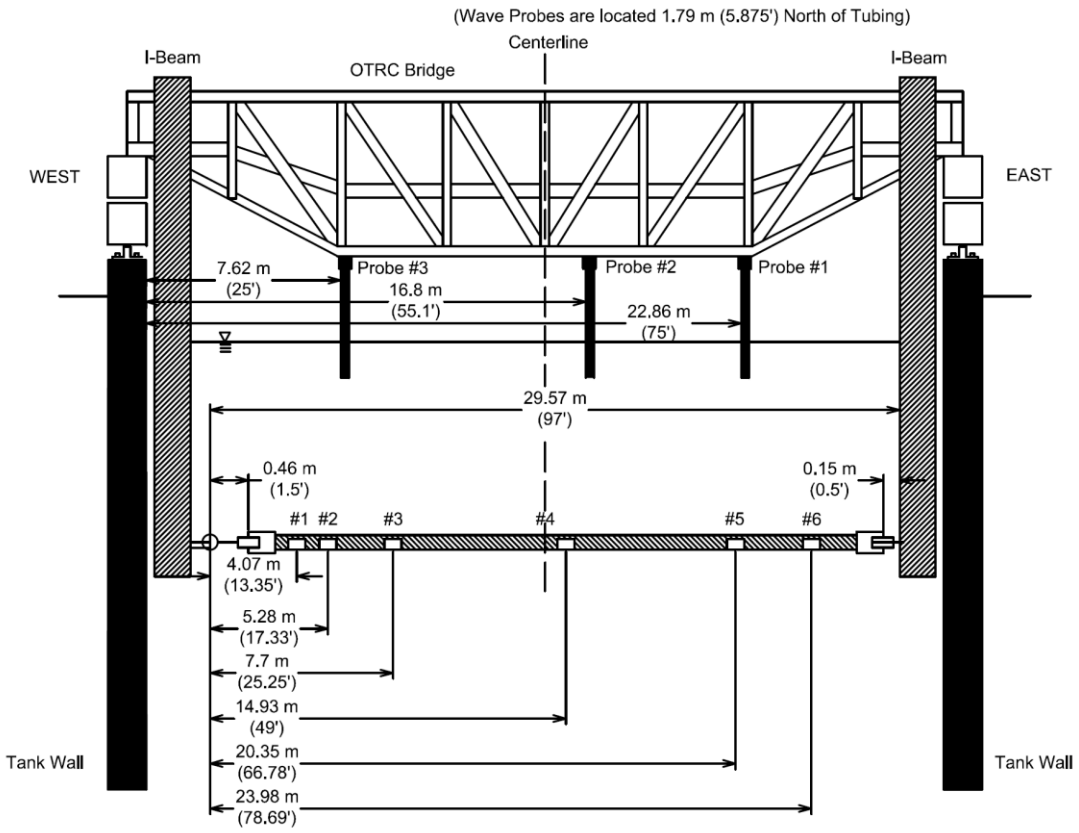

Fig. 3.1 Schematic of the model and instrumentation locations (Chitwood, 1998).

A detailed figure with configuration of the ribbon fairing is shown in Fig. 3.3. The ribbon fairings were secured around the cylinder by zippers on the leading edge. The unit weight of the airfoil and ribbon fairings in air was 5.925 N/m and 1.824 N/m respectively. Note that since the airfoil fairings were not watertight the water trapped inside needs to be accounted for when considering the total mass. The unit weight of the trapped water was estimated to be 21.680 N/m. The airfoil fairings were tested at 100 – 40% coverage in 10% decrements. The fairings were removed from the left end (accelerometer 6). The ribbon fairings had the same coverage range but the reduction from 100% coverage was conducted in 20% decrements.

Fig. 3.2 Photographs of the airfoil (left) and ribbon (right) fairings used in the test.

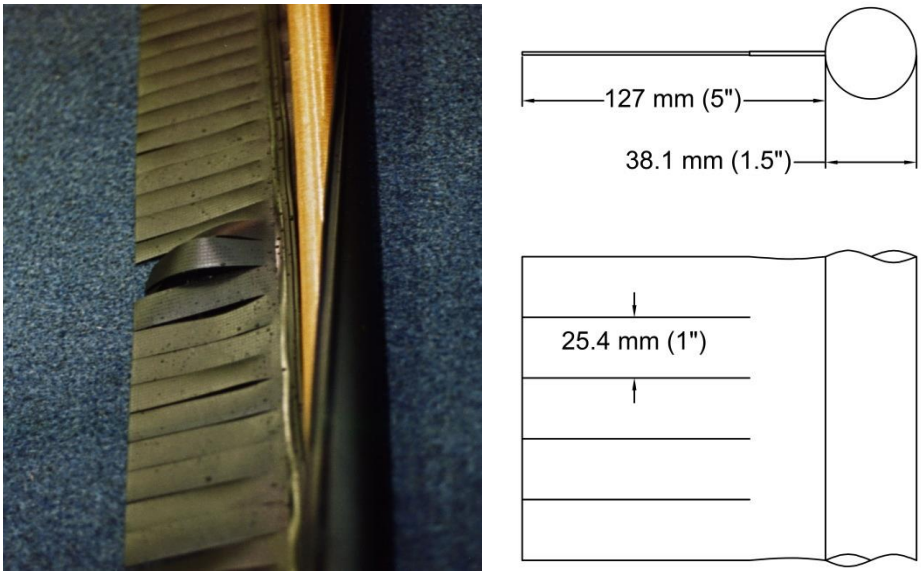

Fig. 3.3 Configurations of the ribbon fairing.

Table 3.2 Test matrix of the acceleration test.

Scenario	Suppression devices	Environmental conditions
1	Bare	Uniform current only, velocity = 0.18, 0.21, 0.24, 0.27, 0.30, 0.38, 0.43 m/s
2	Bare	Combined uniform current (0.38 m/s) plus regular wave (0.24 m wave height, 3.2 s period) condition
3	Full airfoil fairings	Uniform current only, velocity = 0.18, 0.21, 0.24, 0.27, 0.30, 0.38, 0.43 m/s
4	Full ribbon fairings	Uniform current only, velocity = 0.18, 0.21, 0.24, 0.27, 0.30, 0.38, 0.43 m/s
5	Partial airfoil fairings (40 - 90% with every 10% increase)	Uniform current only, velocity = 0.18, 0.21, 0.24, 0.27, 0.30, 0.38, 0.43 m/s
6	Partial ribbon fairings (40 - 80% with every 20% increase)	Uniform current only, velocity = 0.18, 0.21, 0.24, 0.27, 0.30, 0.38, 0.43 m/s
7	Partial airfoil fairings (40 - 90% with every 10% increase)	Combined uniform current (0.38 m/s) plus regular wave (0.24 m wave height, 3.2 s period) condition
8	Partial ribbon fairings (40 - 80% with every 20% increase)	Combined uniform current (0.38 m/s) plus regular wave (0.24 m wave height, 3.2 s period) condition

The test matrix analyzed in this study is summarized in Table 3.2. Scenarios of current only and current plus wave conditions are listed. The conditions of suppression devices included bare, full/partial coverage of airfoil fairings and ribbon fairings.

The analyses of the time series data from the towed composite cylinder experiments required a rethinking of the time domain decomposition technique implementation to address subtleties of the phenomena and recorded data. Consequently, the analyses of the data were divided into several interrelated well-defined tasks. First, the cross-flow and in-line displacements were obtained through double integration of the acceleration time series data measured using the bi-axial accelerometers. In addition, the statistical characteristics that included the maximum, minimum and standard deviations of the displacements, measured tension, and current and wave data were obtained. The next major task was to perform a modified time

domain decomposition of the displacement time series to recover information on the dominant modes that included the natural frequency, mode shape, modal contribution factor and modal damping.

A schematic diagram illustrating the relationship between the experimental measurements and the major aspects of the modified time domain decomposition (TTD) methodology as applied to the analysis of flow-induced vibration is presented in Fig. 3.4. Starting with the time history data obtained from a test run, the first step in the analysis procedure is to isolate single-degree-of-freedom signals $[Y(i,t)]$ at a specific mode through the application of a Butterworth filter. These vectors are then used to form an energy matrix E from which one extracts the ith mode shapes φ_i using singular value decomposition (SVD). With this information one can also recover the damping ratio ξ_i and the modal contribution factor $c(i,t)$. Note that the critical damping ratios reflect the summation of structural damping and hydrodynamic damping, as in multimodal responses of a long flexible cylinder, hydrodynamic damping can be several times larger than structural damping and cannot be neglected; see for example Vandiver (1993).

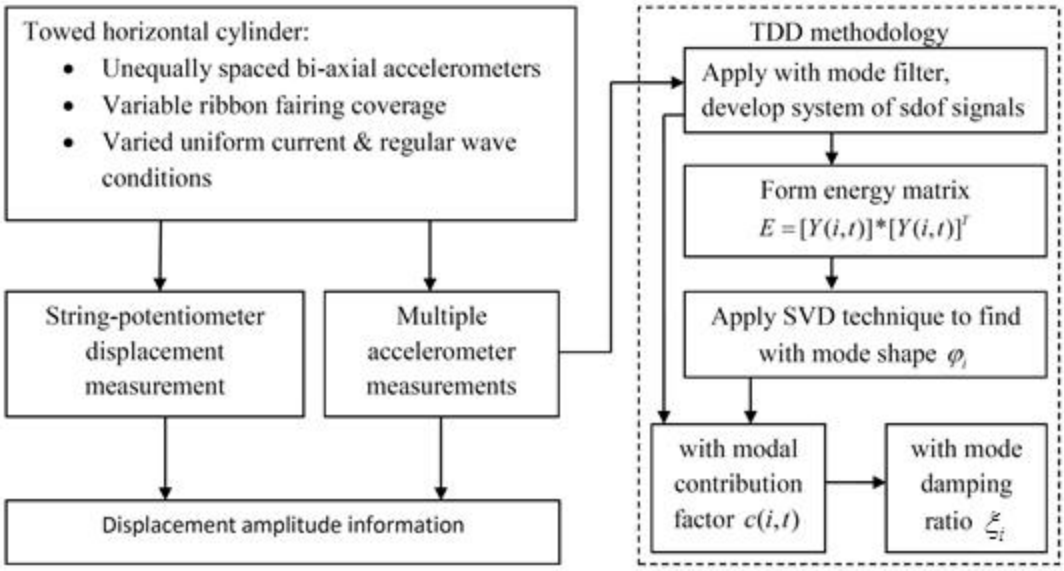

Fig. 3.4 Schematic illustrating the connection between the model tests and TDD method.

In evaluation of multi-modal vortex induced vibration behavior one needs to be careful as the various modes can have the same lock-in range, and the mode of interest may blend in with other possible modes and might not be correctly recognized. This was not an issue for single mode vortex induced vibration for within the lock-in range, only one mode would be excited hence the recognition was relatively easy. Chung (1987) analyzed experimental data from a variety of sources and demonstrated the lock-in range can vary significantly depending on the mass ratio; in particular cylinders with low mass ratios had a broader lock-in range than those with higher mass ratios. Fig. 3.5 shows data from this study illustrating the relationship between the mode number and the reduced velocity, which is defined as the ratio of the current velocity to the product of the cylinders natural frequency times its diameter. The figure presents information for the bare cylinder subjected to three different uniform current velocities (0.18, 0.27 and 0.43 m/s). The data suggests that as the uniform current velocities increase that the corresponding modes 1-3, 2-4, 3-7 might be excited. Fig. 3.5 provides some guidance

for the various configuration scenarios for the evaluation procedures regarding the expected mode behavior in this study.

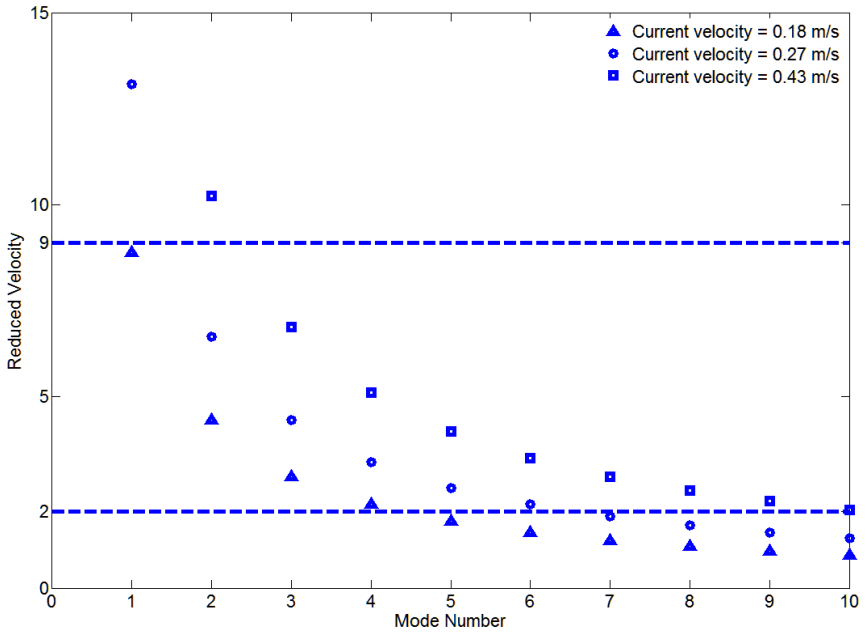

Fig. 3.5 Mode number versus Reduced velocity at varied current velocities for the bare cylinder.

It is of particular interest to study the conducted experiment in the following aspects: suppression effect of ribbon fairings and airfoil fairings in various coverage densities, effect of waves on flow-induced vibration of cylinders installed with suppression devices and effect of fairings, either full or partial coverage, on modal response. Specifically, what makes the experiment unique compared with similar tests is the considerable overall size of the test cylinder, the focus on multi-modal response behavior by targeted mode excitation and observation, the alternative suppression device – ribbon fairings, the combined current and wave condition, and the unequally spaced sensor arrays.

For the initial phase of the study the response of the towed cylinder was investigated without and with complete coverage by the ribbon fairing and airfoil fairing. The Reynolds number range for these tests was estimated to vary between $7*10^3$ and $1.6*10^4$, and corresponds to current velocities in the range of 0.18 and 0.43 m/s. For the cylinder without fairings tested at constant towing speeds corresponding to current velocities of 0.18, 0.24, 0.38 and 0.43 m/s, the RMS amplitude ratios at mid-span of the cylinder were determined to be 0.12D, 0.19D, 0.23D and 0.71D respectively. With the introduction of the 100% coverage of the ribbon fairings along the cylinder length, those ratios were reduced to 0.05D, 0.06D, 0.07D and 0.13D. By way of comparison, with the introduction of the 100% coverage of the airfoil fairings along the cylinder length, those ratios were reduced to 0.04D, 0.08D, 0.12D and 0.13D. These results indicate that for the bare cylinder that the RMS response increases as the uniform flow velocity increases and that both ribbon and airfoil fairings are effective in significantly reducing the RMS vibration for the current velocities tested. One must be careful in characterizing the overall response behavior of the flow-induced response of a flexible cylinder with a single RMS value.

The normalized minimum and maximum flow-induced response behavior of the model in uniform current velocities of 0.24 m/s and 0.38 m/s are presented in Fig. 3.6 and 3.7 respectively. These figures illustrate that as the velocity is increased the dominant mode can change. Specifically, in Fig. 3.6 the second mode dominates the response behavior while in Fig. 3.7 the third mode dominates the response behavior. In both cases it is evident that there is the influence of a higher mode contribution to each of the response envelopes near stations #1 and #2. At bi-axial station #5 in Fig. 3.6 for the ribbon faired case the signal was found to be erratic, so the response behavior in that region is approximate but appears to be drawn in a manner consistent with the response observed in Fig. 3.6. The third mode response in Fig. 3.7 was confirmed using the TDD method. The response envelopes again indicate a single RMS value is not enough and more information is needed to evaluate the overall responses for a cylinder undergoing

multi-modal vibrations. Both ribbon and airfoil fairings effectively reduced the vibrations.

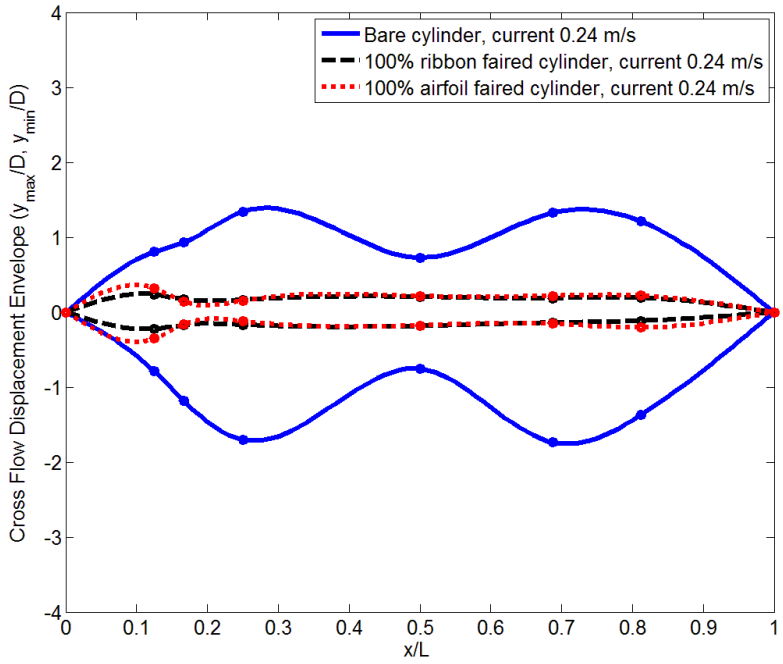

Fig. 3.6 Cylinder response in a uniform current of 0.24 m/s.

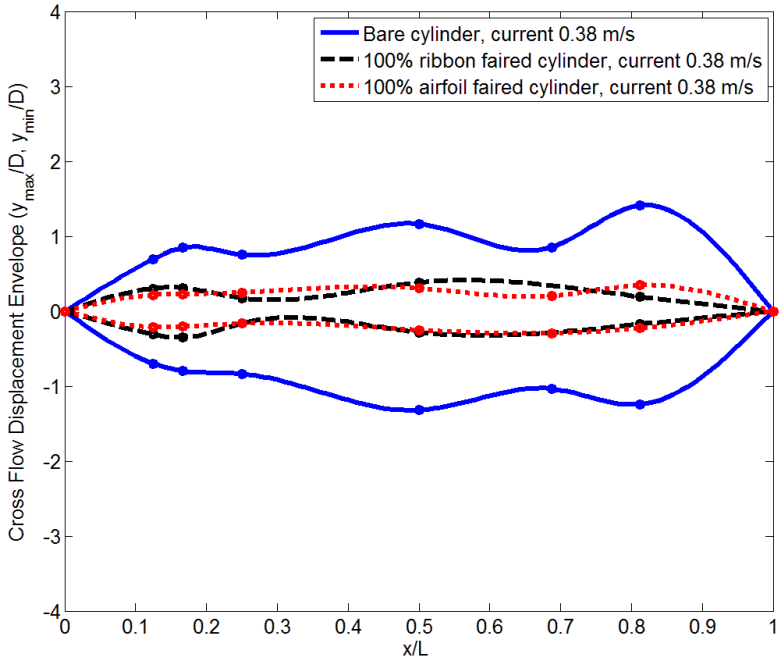

Fig. 3.7 Cylinder response in a uniform current of 0.38 m/s.

Information on the critical damping ratio, dominant frequency and mode of cylinder response for three uniform current velocities are presented in Table 3.3. The first grouping of three columns contains estimates obtained from spectral analyses for the bare cylinder cases and the second groupings of three columns contain information extracted using the TDD method for the 100% ribbon faired cylinder cases. Note that for the 100% airfoil faired cylinder cases, the vibrations were suppressed to an extent due to the streamlining effect that the modes can hardly be extracted with given sensor arrays. In the first grouping the damping ratios were computed using the Half-Power Bandwidth method and the frequency and mode were estimated through comparison with spectral information; see for example Bendat and Piersol (1980). More specifically the most dominant mode and the corresponding frequency were estimated by selecting the largest spectral peak in the corresponding power spectral density. For the bare cylinder cases, the excited modes were obtained by comparing the spectral peak frequencies with the natural frequency. The natural frequency was estimated based upon

the known mass per unit length and measured tension and the assumption that given that large L/D ratio that the bending stiffness was negligible compared with the tension. Added mass was assumed in the computation as well.

The 6th to the 10th natural frequencies computed for bare cylinder were 3.29, 3.84, 4.39, 4.94, 5.48 Hz. Thus, a mode excited at 4.7 Hz would indicate that the 8th or 9th mode would be dominant. In the TDD estimates it was not possible to identify all the modes present as the number of sensors used in the experiments limited the resolution of higher modes that can be determined from the experimental data. For the cylinder outfitted with zip-on ribbon fairing, the excited modes were confirmed by reconstructing the time series using the mode shapes and modal contribution information extracted by TDD method. The dominance of the modes is validated by comparing the modal contribution factors $c(i,t)$ for each mode excited with the help of TDD method. For example, in the case of 0.43 m/s, the RMS value of $c(i,t)$ for the most dominant mode at 1.4 Hz is 6 times bigger than that of the less dominant mode at 2.8 Hz. The modal responses listed show that for bare cylinders, the modes with the largest energy are typically excited at frequencies associated with higher modes, and for ribbon faired suppression the modes and frequencies are significantly shifted to lower frequencies modes. Damping ratios related without or with ribbon fairings is increased from 0.3-0.8% to 1.3-4.1% respectively.

Table 3.3 Modal information obtained using spectral analysis and the TDD method.

	Bare Cylinder			Full Ribbon Faired Cylinder		
Current Velocity m/s	ζ_i %	Excited Frequency Hz	Excited Mode	ζ_i %	Excited Frequency Hz	Excited Mode
0.27	0.4	3.4	6 or 7	4.1	0.8	2
0.38	0.3	4.7	8 or 9	2.5	1.3	3
0.43	0.8	5.4	10	1.3	1.4	3

One of the more interesting design aspects is the effect of partial coverage by the ribbon fairing on the flow-induced response in current only condition. Fig. 3.8 and 3.9 present a comparison of the 0%, 40%, 60%, 80% and 100% ribbon fairing coverage provide a dramatic evolutionary contrast in flow-induced response behavior. The ribbon fairing coverage was removed starting from the cylinder end near Station # 6 and was not a uniformly distributed reduction in suppression coverage. The tests were conducted with the same current velocity of 0.38 m/s. The root-mean-squared response amplitudes in the middle of cylinders at bare, 40%, 60%, 80% and 100% ribbon coverage were 0.23D, 0.50D, 0.36D, 0.26D and 0.07D. These values suggested that something dramatic was happening at the 40% and 60% coverage conditions and the cross-flow displacement envelopes shown in the figures further confirmed this. The 100% and the 80% coverage by the ribbon fairing were effective in reducing the amplitude of the response behavior when compared with the bare cylinder case.

However, in the 80% coverage case there begins to be an indication of the trends seen in the 60% and 40% ribbon coverage cases. Examination of the spectral density functions is consistent with these figures indicating that energy at the higher frequencies is indeed increased and that the multi-mode excitation begins to dominate the response behavior.

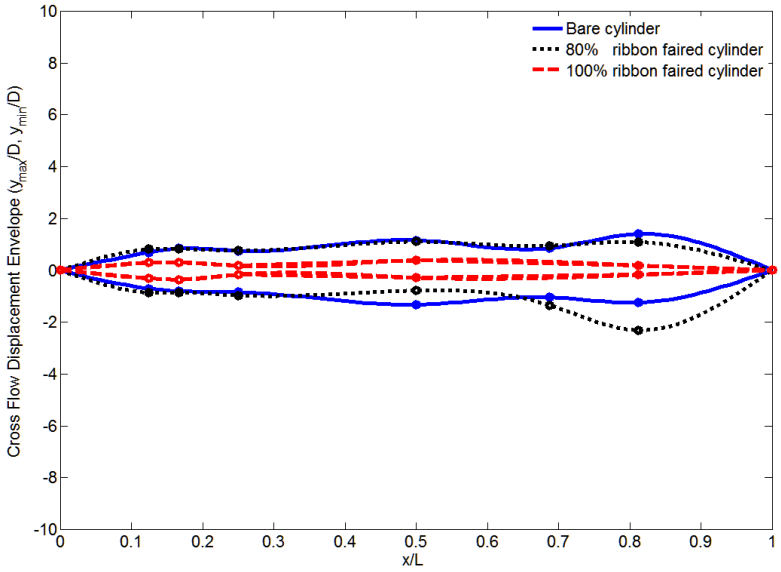

Fig. 3.8 Cylinder response behavior with 80% and 100% ribbon fairing coverage.

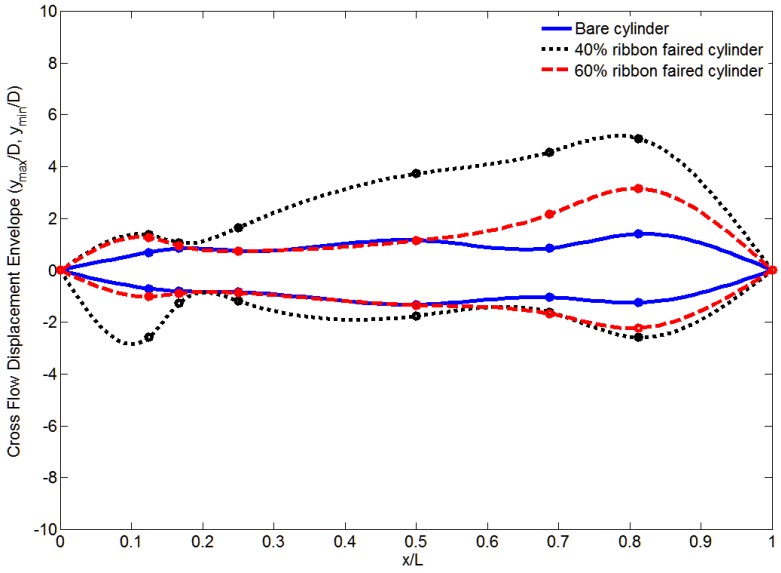

Fig. 3.9 Cylinder response behavior with 40% and 60% ribbon fairing coverage.

The combined wave and current conditions on top of a long cylinder with or without suppression devices undergoing multi-modal behavior adds value to the study of

complicated flow-induced vibrations. Effect of ribbon and airfoil fairings in either full or partial coverage will be the focus. Prior to the introduction of any fairings, bare cylinder tests were conducted first for a uniform current speed of 0.38 m/s, and then for the same current speed with the addition of regular waves with 0.24 m wave height and 3.2 s period. The normalized maximum and minimum cross-flow displacement envelopes for the cylinder under these conditions are presented in Fig. 3.10. Upon comparison of the envelopes it is quite evident that regular waves significantly amplify and dominate the bare cylinder response behavior. The targeted 3rd mode vibration behavior can be recognized for both environmental loading conditions. The results also indicate one possibility: the total responses in combined current and wave loads are composed of two components, a fundamental mode dominated by regular waves and a 3rd mode from the vortex shedding forces mainly due to current. Both components of the responses are significant for the bare cylinder cases.

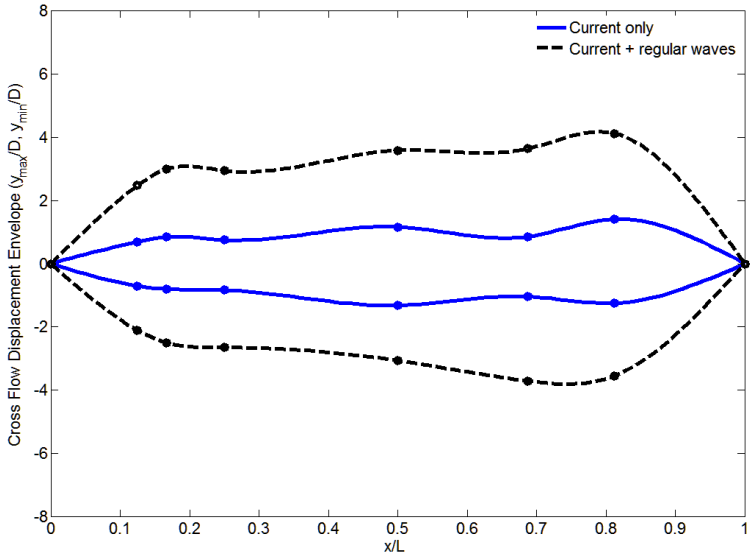

Fig. 3.10 Bare cylinder response in current only (0.38 m/s) and combined current (0.38 m/s) and waves (0.24 m wave height, 3.2 s wave period) conditions.

An example of the cross-flow response behavior for the cases of complete coverage by either airfoil or ribbon fairings when the regular waves were introduced is presented in Fig. 3.11. For comparison the corresponding bare cylinder case is included in the figure. Clearly the wave kinematics dominated the response behavior and neither fairing type was able to suppress motions. In fact the cylinder equipped with airfoil fairings significantly amplified the vibrations and the one with ribbon fairings somehow kept the responses in similar scale or slightly increased the responses compared with the bare cylinder. The airfoil fairings although free to rotate seemed to accentuate the motion as they followed the wave kinematic motion resulting in increased maximum and minimum RMS values especially at the mid-span of the test cylinder. The ribbon fairings were completely compliant and seemed to also respond to the fundamental mode induced by the wave motion, although one can observe the influence of an additional mode in the envelopes. The bare cylinder surface was not completely smooth as the surface reflected the construction of the composite material and had minor indentions and protrusions. Though the fairings tested were originally designed to mitigate flow-induced vibrations in current only situations, the results in Fig. 3.11 indicate the significantly reduced functionality of both fairings when regular waves were present.

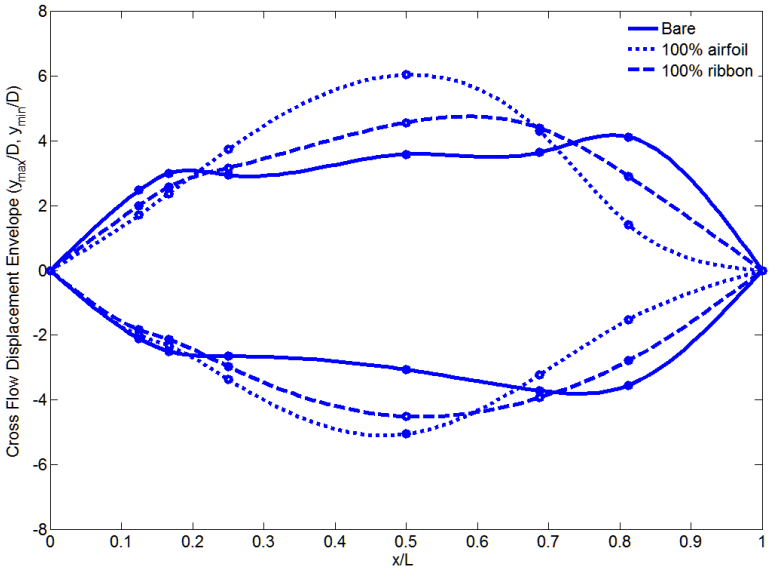

Fig. 3.11 Bare, full airfoil and ribbon faired cylinder response behavior in combined current and waves.

The amplification effect of airfoil and ribbon fairings can be partially explained by comparing the wave peak period and the natural period of the system. For a slightly damped system, the closer the excitation peak frequency approaches one of the natural periods within certain range, the larger the response will be. Considering structure mass, added mass and the mass of possibly trapped water especially for airfoil fairings, the natural periods of the 1st mode for full airfoil, ribbon faired and bare cylinders are estimated to be 2.8, 1.9 and 1.8 s respectively. Since the wave peak period in the current study is 3.2 s, airfoil faired cylinder has the closest natural period to the waves, followed by ribbon faired and bare cylinder. The rank of this closeness matches well with the actual response envelopes. The amplification effect is also verified by the wave-induced vibration simulated results. Assuming the cylinders with and without fairings are uniform, the wave-induced response amplitude ratios at mid-span were estimated to be 4.8D, 3.5D and 2.0D for full airfoil, ribbon faired and bare cylinders. By way of comparison the measured cross-flow total responses ratios were 5.5D, 4.5D and 3.3D as

shown in Fig. 3.11, confirming the dominance of the wave kinematics in the observed response behavior.

The power spectral densities for the three cylinder configurations are presented in Fig. 3.12. The bare cylinder is subject to energy over a large range of frequencies and the effectiveness of the both fairings in reducing this to a few frequencies can be observed. The first peak for each case is centered on the wave frequency with the sequence of peak values corresponding to the airfoil followed in reduced amplitudes of the ribbon fairing and bare cylinder cases. The few remaining higher frequencies clearly influenced the ribbon fairings envelope when compared with the airfoil fairings, which was even more effective in reducing the effects of higher frequency contributions.

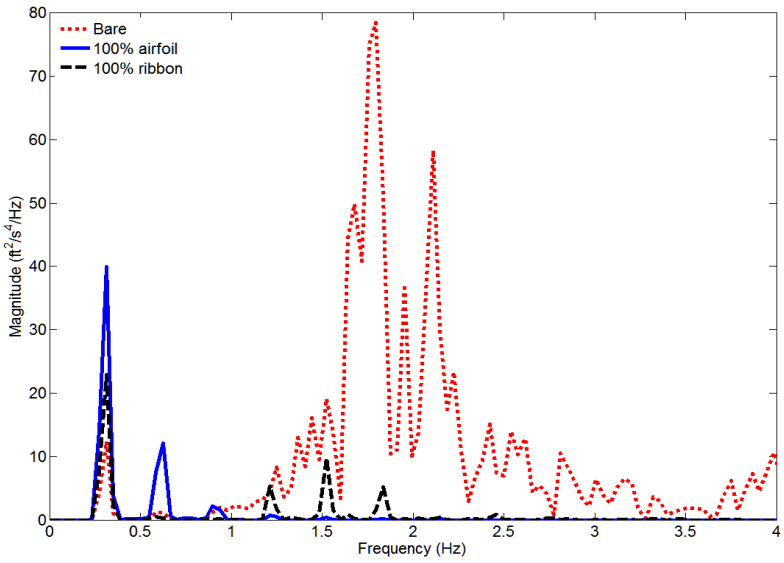

Fig. 3.12 PSDs of bare, fully airfoil and fully ribbon faired cylinders.

It is of interest to study the effect of partial coverage on cylinders subjected to combined current and wave condition. A comparison of 40% and 100% coverage was selected as being representative and is presented in Fig. 3.13. The results suggest in the combined loading condition, the response magnitudes are not sensitive to coverage, i.e.

neither suppression device is effective in mitigating the response behavior. This is consistent with the previous discussion, as the responses are dominated by waves and coverage of VIV suppression devices only affects the less important current-induced vibrations.

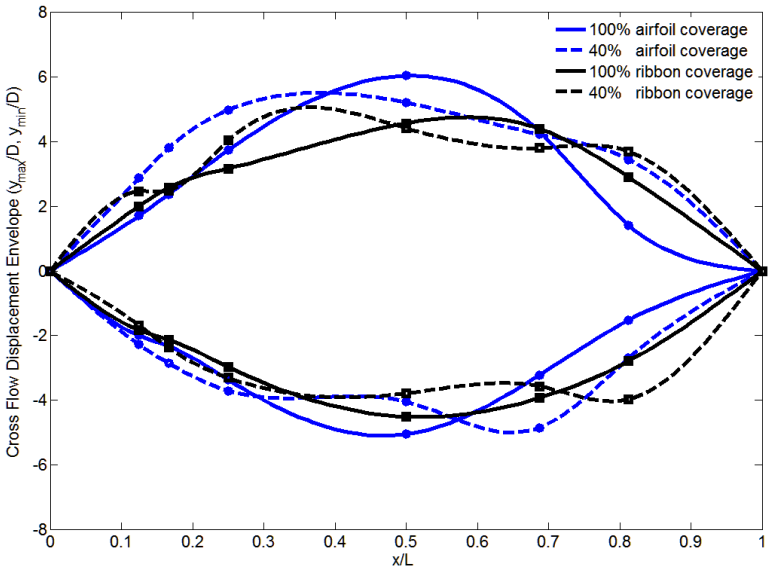

Fig. 3.13 Response envelopes for airfoil and ribbon faired cylinders with coverage of 100% and 40%.

The modal responses of partial coverage tests in the combined loading condition further explained the phenomena that though ineffective around the wave frequency, fairings can suppress the higher order modes. For illustrative purpose, power spectral densities of bare, 60% and 100% ribbon coverage at accelerometer 4 in the middle of the cylinder are presented in Fig. 3.14, which showed that the higher order mode components of the vibrations were gradually suppressed by the increased coverage while the responses near the wave frequency at 0.31 Hz remained significant. The total energy of the responses became smaller and moved toward lower frequencies as the coverage increased. The trend of energy shifting was similar in the case of airfoil faired cylinders.

The other indicator of the effect of partial coverage on the responses is the tension recorded at the ends of the cylinder. The mean values of tension being stable at 2300 N (520 pounds), the standard deviations of tension in coverage of 0%, 40%, 80% and 100% of ribbon fairings were 73, 68, 60 and 57 N respectively. The reduction of tension variation along with the increased ribbon coverage suggests that though ribbon can reduce the drag force in both cross-flow and in-line directions. The results are also in accordance with the conclusions of Kwon (2002) and Nakamura and Koterayama (1992), who demonstrated the drag reduction effect of ribbon fairings with experiments.

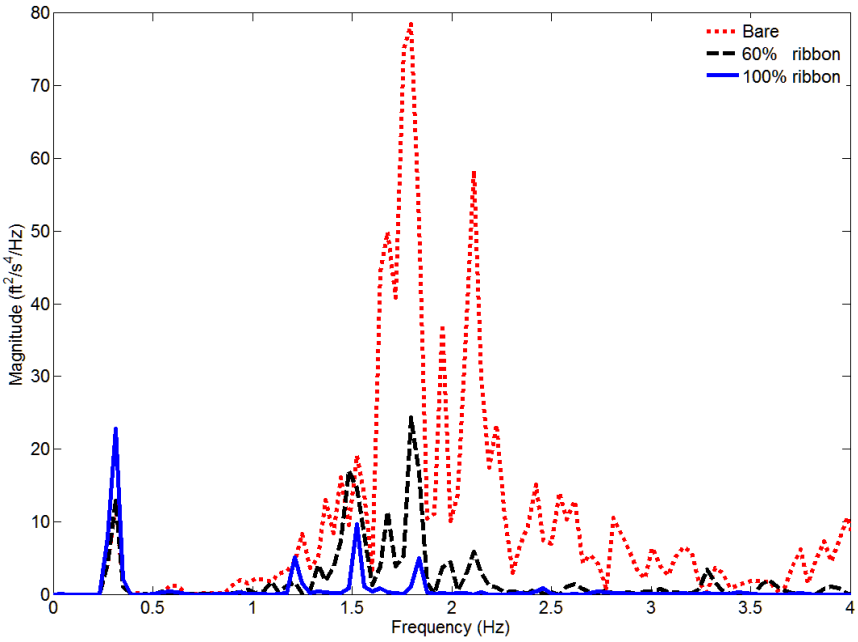

Fig. 3.14 PSDs of bare, 60%, 100% ribbon faired cylinders.

The first three dominant mode shapes of airfoil and ribbon fairings in combined current and wave conditions, extracted from measured data using the time domain decomposition technique are presented in Figs. 3.15a and 3.15b, and further validate the noted observations. In particular, the mode shapes corresponding to airfoil fairing

coverage appear to be strongly controlled by the fundamental mode, and meanwhile, the multiple mode shapes for the ribbon fairings are explicit and clear, corresponding to the 1st, 2nd and 3rd mode. This is another indicator that in ribbon faired cases, waves were not as dominant as that in airfoil cases, and vortex shedding forces were still significant to excite response in higher mode numbers. The damping ratios of the first three modes using non-destructive zoom technique and Half-Power Bandwidth method were estimated to be 8.4%, 4.4% and 3.2% for complete coverage by the airfoil fairings, and 7.7%, 2.4%, 2.3% for the comparable ribbon fairing case. These results illustrate that the airfoil fairings provide larger damping for the system when compared with the ribbon fairings.

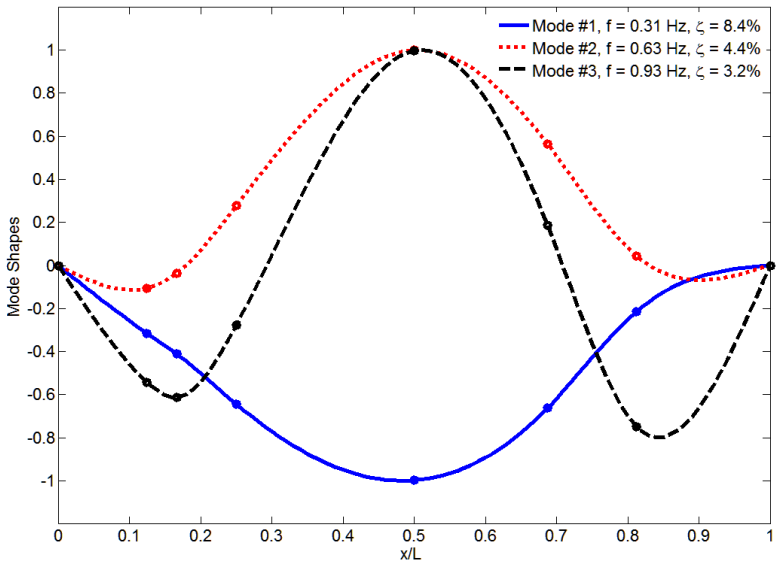

(a) Airfoil

Fig. 3.15 The three dominant modes for fully airfoil and ribbon faired cylinders.

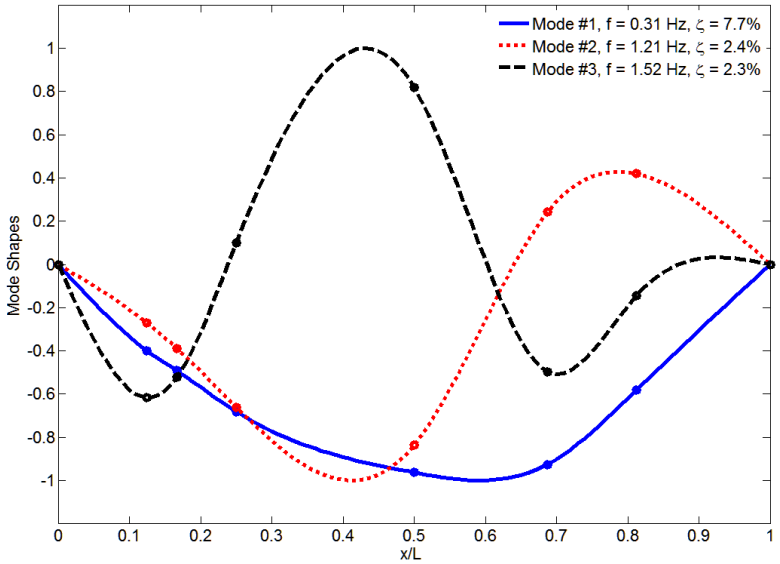

(b) Ribbon

Fig. 3.15 Continued.

The different behavior of the suppression devices at low and high frequencies was also reflected in the mode shapes, as shown in Fig. 3.16a for the fundamental modes of 0%, 60% and 100% ribbon coverage and Fig. 3.16b for the second modes of 40% airfoil and ribbon coverage. In Fig. 3.16a, the near symmetry of the mode shapes confirmed the insensitivities of coverage density in wave dominated responses. In Fig. 3.16b, both mode shapes at partial coverage were asymmetric and unbalanced, with larger values on the bare right end, which was similar to a normal 2nd mode shape, and with reduced values on the left faired end. Moreover, the reduction effect of the mode shape from the airfoil fairing seemed stronger than that from the ribbon fairing, which suggested the airfoil fairing may provide larger damping than the ribbon fairing. It was further confirmed by the estimations of the damping ratios of the excited modes, 2.3% for airfoil and 1.5% for ribbon. A possible explanation for the unbalanced mode shapes is partial coverage affected distribution of structural and added mass, as well as hydrodynamic damping across the cylinder.

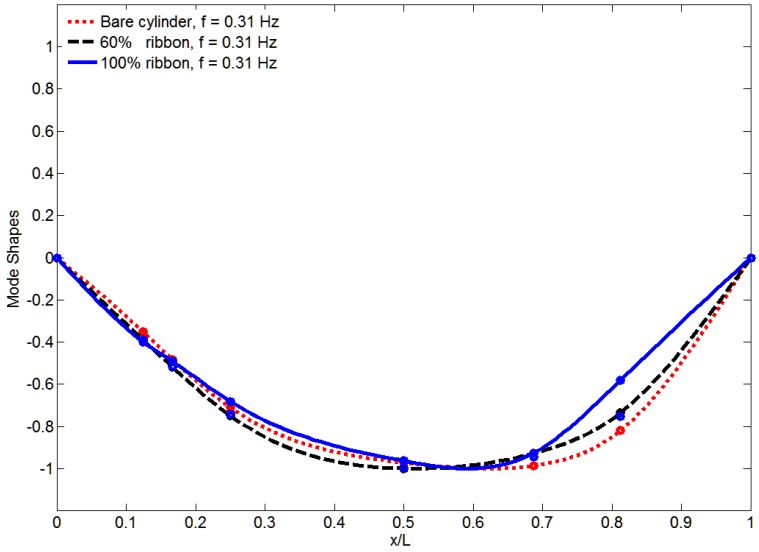

(a) 1st mode of bare, 60% and 100% ribbon coverage

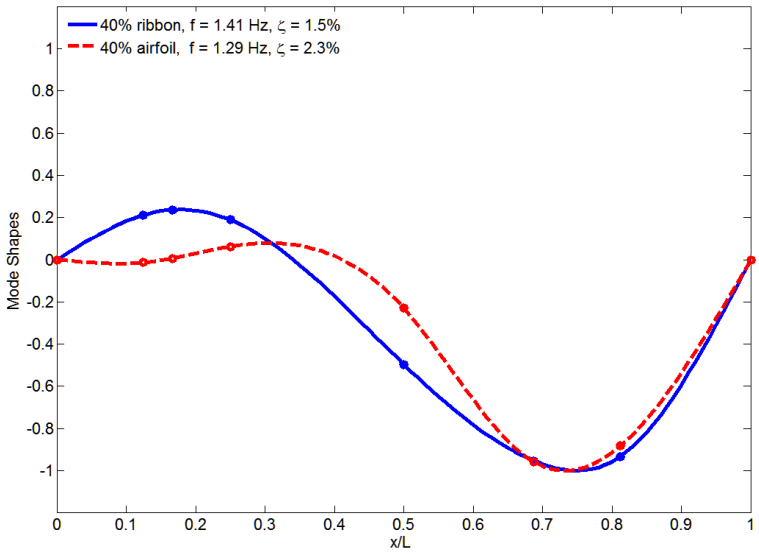

(b) 40% airfoil and ribbon coverage

Fig. 3.16 Recovered symmetric 1st mode shapes and asymmetric 2nd mode shapes with partial ribbon coverage.

In sum, the time domain decomposition (TDD) method in combination with spectral analysis techniques was used to interpret the flow-induced response behavior of a towed flexible horizontal cylinder with variable coverage of zip-on ribbon fairings and

free rotating airfoil fairings. The various cylinder configurations were towed at several different speeds to simulate uniform current velocities and for some cases regular wave conditions were superimposed. The VIV analysis program developed for this ongoing study was employed to conduct time series analysis, modal analysis and numerical simulation, and to extract useful response information in space and modal domain. First of all, with full coverage in uniform current conditions, both fairings can significantly suppress the flow-induced vibrations. As for partial coverage cases, take ribbon for example, when the fairing coverage was either 100% or 80% and subject to uniform current flows, the ribbon fairings were shown to be very effective in suppressing vortex-induced vibrations. As the fairing coverage was further reduced to 60% and then 40%, the dynamic response was changed significantly becoming increasingly asymmetric about the uncovered portion of the test cylinder. For cylinders with large L/D ratios, flexible cylinders are not dominated by bending stiffness, this finding raises some interesting questions about the dynamics of partial suppression coverage for some offshore applications.

For the experiments where regular waves were introduced as the test cylinder was being towed, the response behavior was dominated by the orbital nature of the wave kinematics and the functionality of both fairings types was greatly disturbed. The research findings serve to illustrate the challenges faced by offshore engineers when designing long flexible cylindrical offshore structures and flow-induced suppression devices when both currents and waves are present. Based upon the analysis of the data it was shown that the ribbon fairings provided less average damping compared to the airfoil fairings, and that the airfoil fairings had a strong affinity to amplify the horizontal response behavior when subject to the combined current and wave conditions. It should be noted that in design practice ribbon fairings are typically used to suppress the flow-induced vibration of long vertically oriented slender cylinders or cables. On the positive side for ribbon fairings, the minimal relative mass and negligible rigidity clearly does not amplify the motions as might be expected in passive airfoil suppression devices. The experiments also demonstrated the response behavior of test cylinder when subject to

combined loads was not as sensitive to coverage density of fairings as might be expected, though higher modes and unbalanced mode shapes were observed in the partial coverage cases. The lack of motion suppression was countered to some degree by the observed reduction in tension variation which begs further investigation.

Finally, the TDD method was shown to be effective in recovering mode shapes, damping characteristics and modal contribution factors for data obtained from unequally spaced sensors. The relationship between the number of sensors and the ability to resolve higher modal contributions using the TDD method suggests some optimization within practical constraints is possible.

3.2 Analysis Based on Strain Input

The focus of this study is to extend the TDD technique to be compatible with strain input with the experimental data described in Li et al. (2011), which will add up its complexity from a simple bare cylinder to a buoyancy element/strake partially covered cylinder which tempts to resemble the actual riser. Buoyancy elements are typically adopted to resolve the challenge drilling and production risers in deep and ultra-deep waters faces to handle the heavy structures with the rigs‟ limited capacity of top tension. Strain mode shapes and strain modal contribution factors in both IL (In-Line) and CF (Cross-Flow) directions will be recovered firstly with the strain data, and then be manipulated to obtain displacement mode shapes, modal contribution factors and damping ratios. Selected cases with controlled tension, current velocity and placement of buoyancy element/strake will be studied. Using the bare cylinder as the baseline, comparison in terms of modal parameters and energy distributions will be made with a full strake coverage cylinder and a 50% buoyancy element plus 50% strake non-uniformly distributed cylinder.

The experiment was conducted in a towing tank with the length, width and depth of 192 m, 10 m and 4.2 m respectively. The cylinder with a length of 7.9 m and a diameter of 30 mm was secured and hung underneath the carriage with the submergence depth of 1.5 m. The length-to-diameter ratio was 263. The cylinder was connected to

the end supports with constraints on torsion. The material of the cylinder was H65 brass, which was chosen to endure the tension of 1960 N and 2940 N, which was referred as the low tension and the high tension hereafter. Mass per unit length in the air of the cylinder was 1.2 Kg/m. Fig. 3.17 presents the schematic of the test setup.

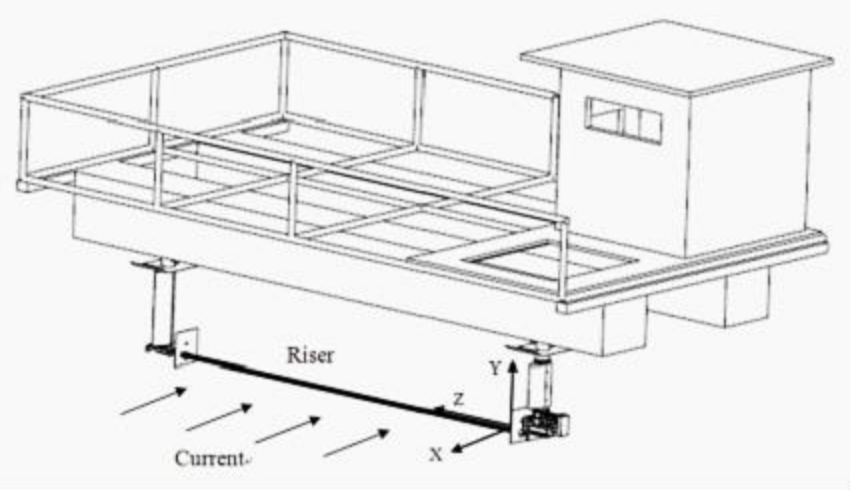

Fig. 3.17 Schematic of the test setup (Li et al., 2011).

Two symmetric and one asymmetric configuration were analyzed in the current study as shown in Fig. 3.18. The symmetric cases were a bare cylinder and a full strake covered cylinder. For the asymmetric case, continuous buoyancy elements were deployed on one side of the cylinder, while staggered buoyancy elements were on the other side. Strakes were arranged to fill in the gaps between those staggered buoyancy elements. The total coverage of buoyancy elements and strakes were both 50%. The buoyancy element had an outer diameter of 75 mm and a mass per unit length in the air of 4.37 Kg/m. The strake selected for the analysis had a pitch of 17.5 D and a height of 0.25 D. The strake configuration was discovered by Allen (1993) to be the most effective among other strakes in suppressing vortex induced vibrations. Note that both

the low and high tensions were applied in the bare cylinder cases while only the high tension was used when strakes and buoyancy elements were present.

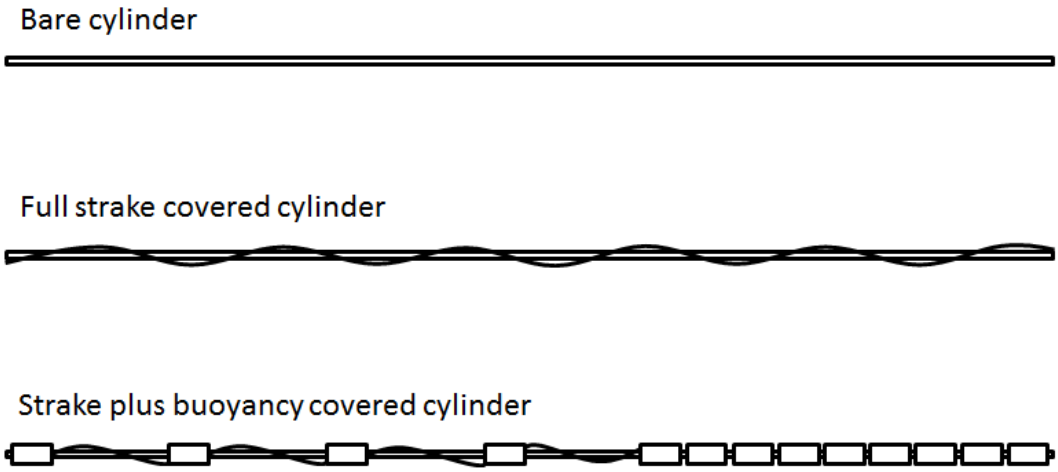

Fig. 3.18 Configurations of strakes and buoyancy elements.

The selected towing speeds in the analysis were 0.4, 0.8, 1.6 and 2.0 m/s. The Reynolds number was in the range of $1.2*10^4$ and $7.2*10^4$ for the bare cylinder and $3.0*10^4$ and $1.8*10^5$ for the buoyancy element. For additional information of the experimental setups, see Li et al. (2011).

Nineteen pairs of fiber optic sensors were installed on the top and bottom of the cylinder surface to measure CF responses and twenty-five pairs on the fore and aft of the cylinder surface to measure IL responses. The sensors were deployed between 0.17 m and 7.73 m along the cylinder equally spaced, with a gap of 0.42 m in the CF direction and a gap of 0.315 m in the IL direction. Note that due to the difference of the gaps, the sectional profile of the cylinder with four sensors installed only occurred at a few locations, at 0.17, 1.43, 2.69, 3.95, 5.21, 6.47 and 7.73 m. One example of the fiber optic sensor setup is presented in Fig. 3.19. The sampling frequency of the sensors was 125 Hz.

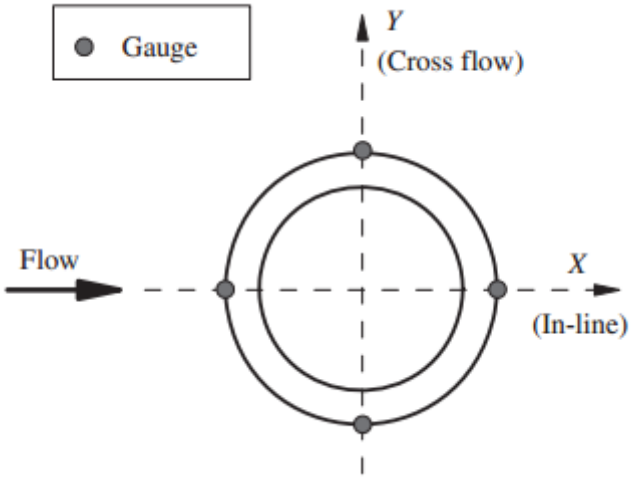

Fig. 3.19 Sketch of four fiber optic sensors on the cross section of test cylinder.

The reason why pairs of sensors in either direction were adopted for the measurement was because the recorded strains can result from both pretention and vortex-induced vibrations. Signals of the paired sensors will contain the pretension induced strains with the same signs, which will be both tension, but will contain the VIV induced strains with opposite signs, which will be tension and compression alternatively. Deducting the baseline strain of the fiber optic sensor itself, which can be done by averaging the still water measurements, the desired VIV induced strain components in the CF direction can be achieved by subtracting the paired sensor measurements from each other. The VIV induced strain components in the IL direction can be obtained in a similar manner but the process might be a bit more complicated due to the existence of drag induced tension, the strain of which unfortunately has the same signs as VIV induced strain. The strain from drag induced tension was removed by time averaging the signals based on an assumption that strain from VIV in IL direction have a zero mean over time but the strain from drag induced tension should have an offset.

As most experimental data do, the raw data collected in the current test contain some outliers, especially in the still water stage, as illustrated in an example below in Fig. 3.20. The outliers must be removed for they may shift the baseline values of the

FBG sensor. To remove the outlier, a basic mean and standard deviation is computed and any data outside a predefined confidence level are considered as outlier and removed from the measurements. The mean value after removing the outliers is computed again as the baseline of the measurement. Three confidence levels: 99.8%, 98% and 95%, reflected by 3 σ, 2.236 σ and 1.96 σ respectively, are compared in Fig. 3.21. The confidence levels of 98% and 95% are good for the purpose, which can be seen. After checking other channel‟s data, 98% is decided as the confidence level to remove outliers and retain the most available information.

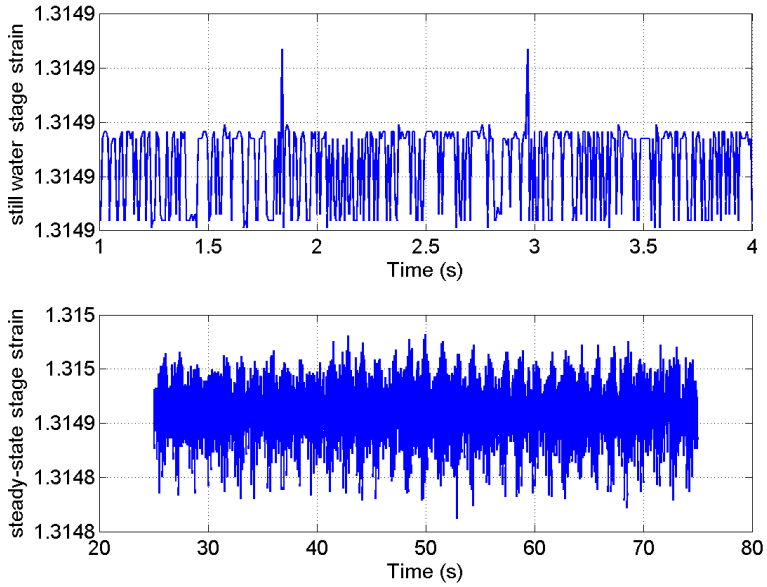

Fig. 3.20 Still water and steady state strain with outliers.

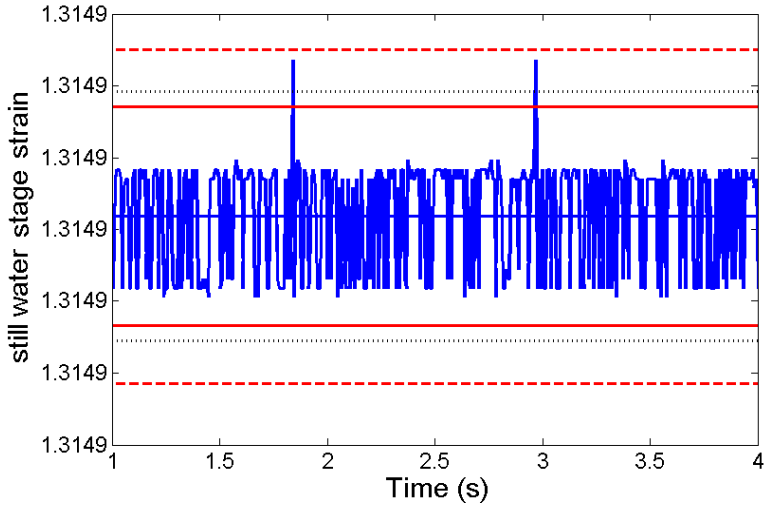

Fig. 3.21 Outlier removers with three confidence levels, 99.8%, dash line (3 σ); 98% dotted (2.236 σ), and 95%, solid line (1.96 σ).

Before applying the TDD algorithm with strain input on the analysis of strain data obtained in the towing tank experiment, two simple numerical examples of a uniform beam with pinned-pinned and fixed-fixed boundary conditions were constructed with finite element method codes Abaqus and used to test the algorithm. The results are shown in Fig. 3.22a and b. The first and second strain mode shapes were extracted with TDD via the strain input and then converted to displacement mode shapes, which was further validated by the displacement mode shapes computed by the FEM codes separately. The matching results were satisfactory.

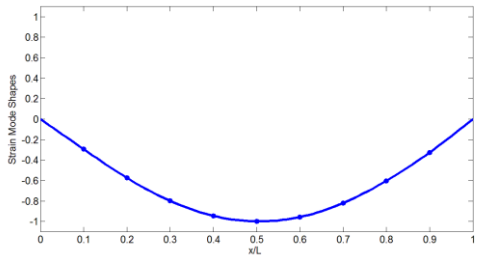

TDD recovered 1st mode shape curvature

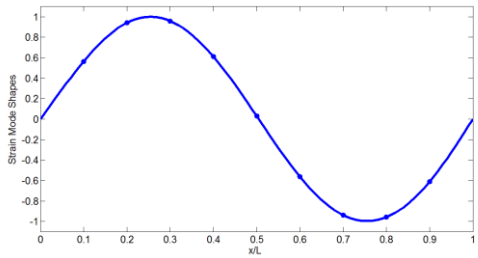

TDD recovered 2nd mode shape curvature

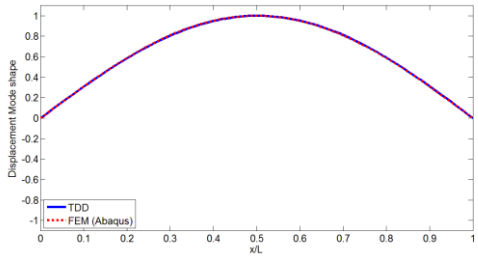

Integrated 1st displacement mode shape

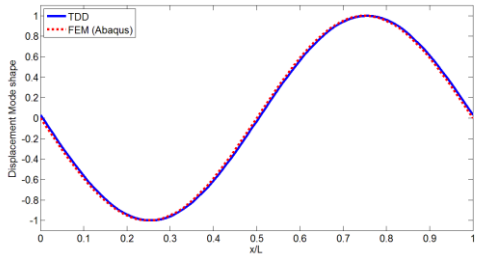

Integrated 2nd displacement mode shape

(a) Pinned-pinned beam

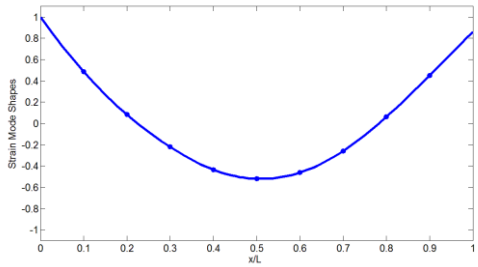

TDD recovered 1st mode shape curvature

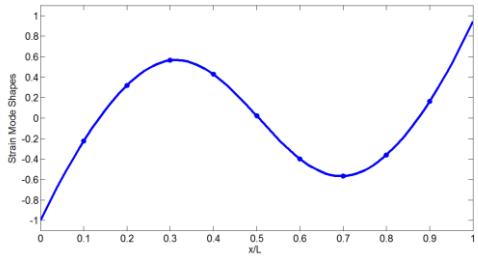

TDD recovered 2nd mode shape curvature

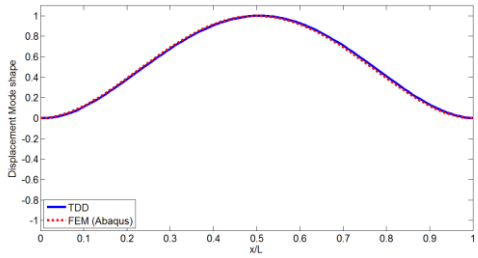

Integrated 1st displacement mode shape

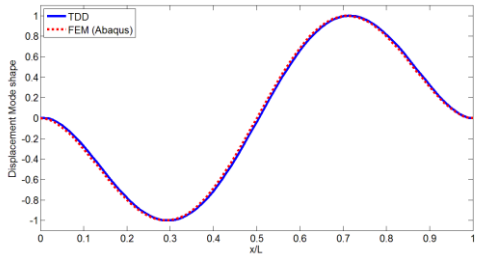

Integrated 2nd displacement mode shape

(b) Fixed-fixed beam

Fig. 3.22 The numerical example of TDD recovered strain mode shapes and double integrated displacement mode shapes.

Strain envelopes, power spectral densities and motion trajectories varied in both time and spatial domain are global response indicators of the test cylinder undergoing VIV. The indicators provide basis to compare and understand the effects of current velocity, tension and attached strakes and buoyancy elements on the VIV response behavior.

Increased current velocity affects the VIV response behavior in two aspects, to exert more energy into the system hence excite larger responses, and to increase the vortex shedding frequency hence excite responses in high order harmonics. Strain envelopes in response to current velocities of 0.4, 0.8, 1.6 and 2.0 m/s in both CF and IL directions are presented in Fig. 3.23a and b. The cylinder was tested in a low tension of 1960 N. As the current velocities increased in a multiple manner, the response envelopes in both directions increased and the dominant modes increased as well. The envelopes provided more comprehensive information of the total responses than a single point measurement, for example, if one only had the measurements of CF responses in the middle, false and incomplete judgment might be made that 0.4 and 0.8 m/s cases were equivalent while 1.6 m/s case was larger than 2.0 m/s. In comparing CF and IL responses, the magnitudes in CF direction were roughly 40-80% higher than that in IL direction. The excited frequencies in CF direction seemed lower than that in IL direction. From the patterns of the envelopes alone, in CF direction, at 0.4, 0.8, 1.6 and 2.0 m/s, mode 1, mode 2 and 4, mode 3 and 5, and mode 4 seemed dominant; in IL direction, at 0.4, 0.8, 1.6 and 2.0 m/s, mode 2, mode 3, mode 5, and mode 6 seemed dominant. Higher harmonics resulted from higher current velocities were not restricted to one mode, e.g. in CF responses at 0.8 m/s, both mode 2 and mode 4 were observable.

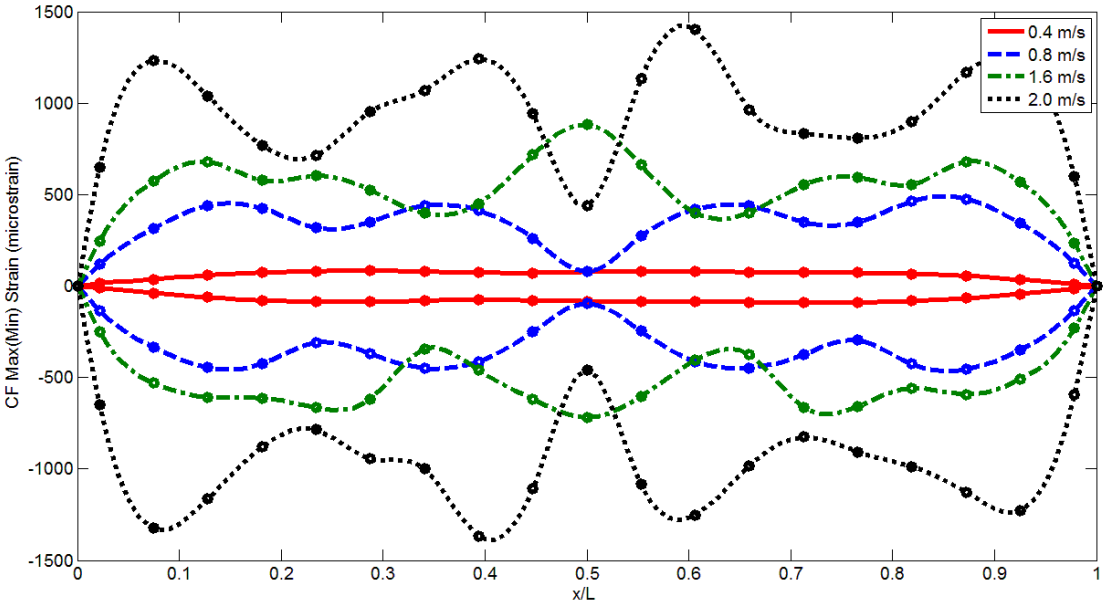

(a) CF

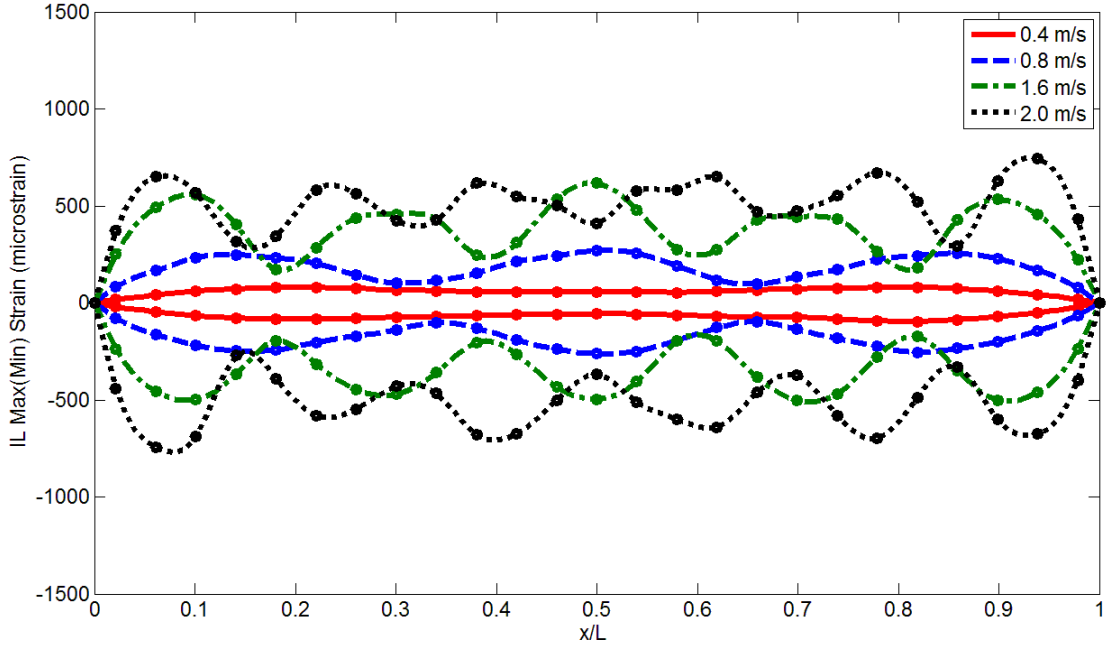

(b) IL

Fig. 3.23 Bare cylinder CF and IL strain envelopes at the low tension in varied current velocities.

A trend of energy shifting with the increasing current velocity can be clearly seen in strain power spectral densities (PSD) in both CF and IL directions, as shown in Fig. 3.24a and b. The energy shifting reflected the increasing vortex shedding frequency, which was defined as the ratio between the product of Strouhal number and current velocity, and the diameter of the cylinder. The primary peaks in CF direction at 0.4, 0.8, 1.6 and 2.0 m/s were 2.0, 4.0, 8.7 and 12.1 Hz respectively, while the primary peaks in IL direction were 4.3, 8.1, 17.5 and 24.2 Hz. The frequencies in IL direction roughly doubled that in CF direction which was reported by previous researchers (Blevins, 1990). In addition, other than the primary peaks, multiple minor peaks were also present. As shown in Fig. 3.22a, the secondary peaks at 0.8, 1.6 and 2.0 m/s in CF direction also followed the increasing trend, from 12.1, 17.5 to 24.2 Hz. The interaction between CF and IL responses can also be noted in the PSD plots. For example, at 1.6 m/s, two peaks were present in CF direction near 8 and 17 Hz with 8 Hz being dominant. The same two energy peaks were also present in IL direction except the 17 Hz frequency became dominant. This interaction can be validated by the envelopes where a 3rd mode seemed dominated the CF responses while a 5th mode seemed dominated the IL responses. The 5th mode was observable in CF responses.

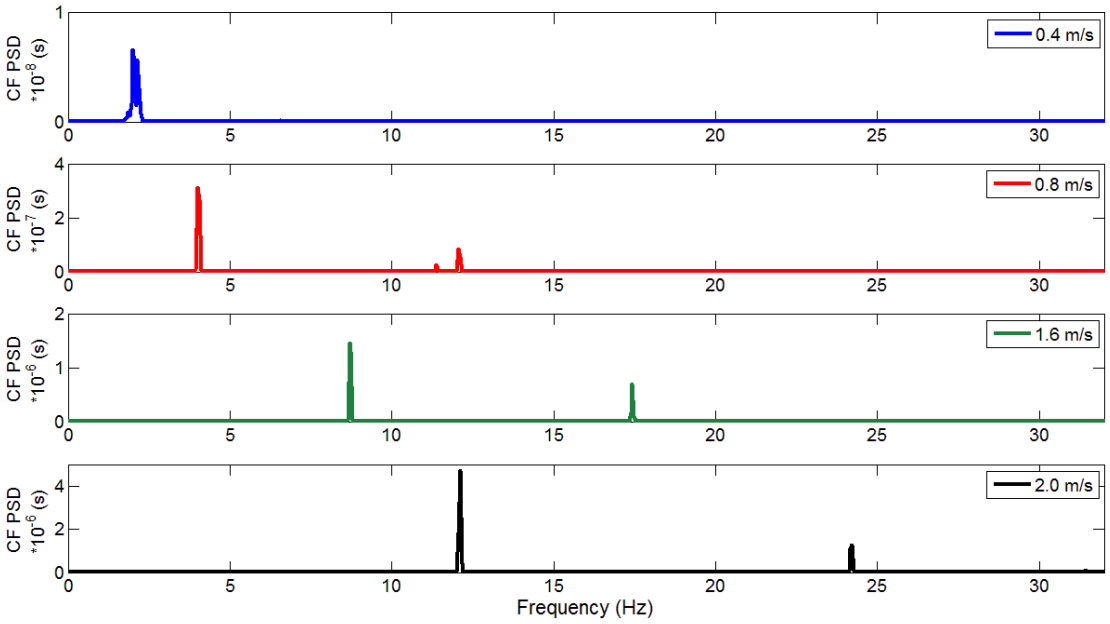

(a) CF

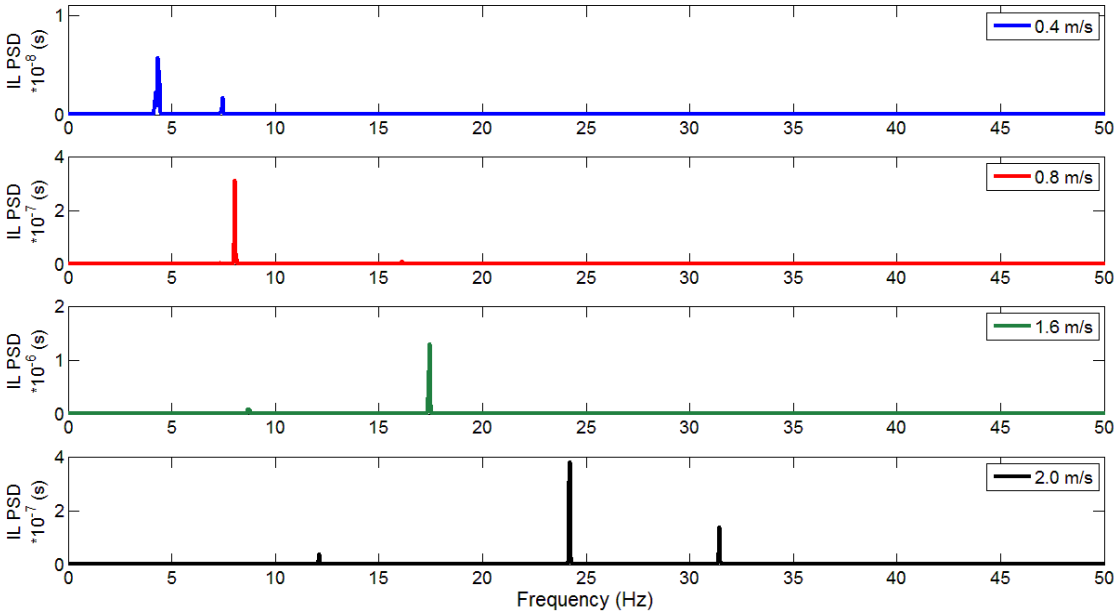

(b) IL

Fig. 3.24 Energy shifting of CF and IL power spectral densities at the low tension in varied current velocities.

Table 3.4 and 3.5 summarize the actual values of the excited modes in frequencies and in energy peak values of the PSD. The modal parameters especially mode shapes were extracted from the strain data.

Table 3.4 Excited multiple frequencies for the bare cylinder at the low tension.

	Mode 1 Hz	Mode 2 Hz	Mode 3 Hz	Mode 4 Hz	Mode 5 Hz	Mode 6 Hz	Mode 7 Hz	Mode 9 Hz
0.4CF	**2.0**	4.2	6.5					
0.8CF		**4.0**		11.4 /12.1				
1.6CF			**8.7**		17.5		26.1	
2.0CF				**12.1**		24.2	31.5	
0.4IL		**4.3**	7.4	11.7				
0.8IL			7.3 /**8.1**		15.4 /16.1			
1.6IL			8.8		**17.5**		26.1 /35	
2.0IL					16.9 /19.3	**24.2**	31.5 /36.3	48.3

Note:
1. 0.4, 0.8, 1.6, 2.0, current velocities in m/s; CF: cross-flow; IL: in-line response;
2. Red: the dominant frequency in CF; Blue: the dominant frequency in IL;
3. The same mode might be excited at two neighboring frequencies, e.g. 08CF.

Table 3.5 Energy peaks of excited modes for the bare cylinder at the low tension.

	Mode 1	Mode 2	Mode 3	Mode 4	Mode 5	Mode 6	Mode 7	Mode 9
0.4CF	**0.9e-8**	0.02e-8	0.01e-8					
0.8CF		**0.34e-6**		8.6e-8				
1.6CF			**1.5e-6**		0.7e-6		1.5e-8	
2.0CF				**4.7e-6**		1.3e-6	0.2e-6	
0.4IL		**0.6e-8**	0.5e-8	0.01e-8				
0.8IL			**0.3e-6**		1.3e-8			
1.6IL			9.0e-8		**1.3e-6**		0.9e-8	
2.0IL					0.6e-8	**0.85e-6**	0.3e-6	0.5e-8

Note:
1. Major peaks are of magnitude of e-6, minor peaks are of magnitude of e-8.
2. If multiple peaks existed for one mode, the higher energy peak was selected.

Fig. 3.25a and b present the CF and IL strain envelopes of the bare cylinder with the high tension, which can be compared with that of the low tension in Fig. 3.23a and b.

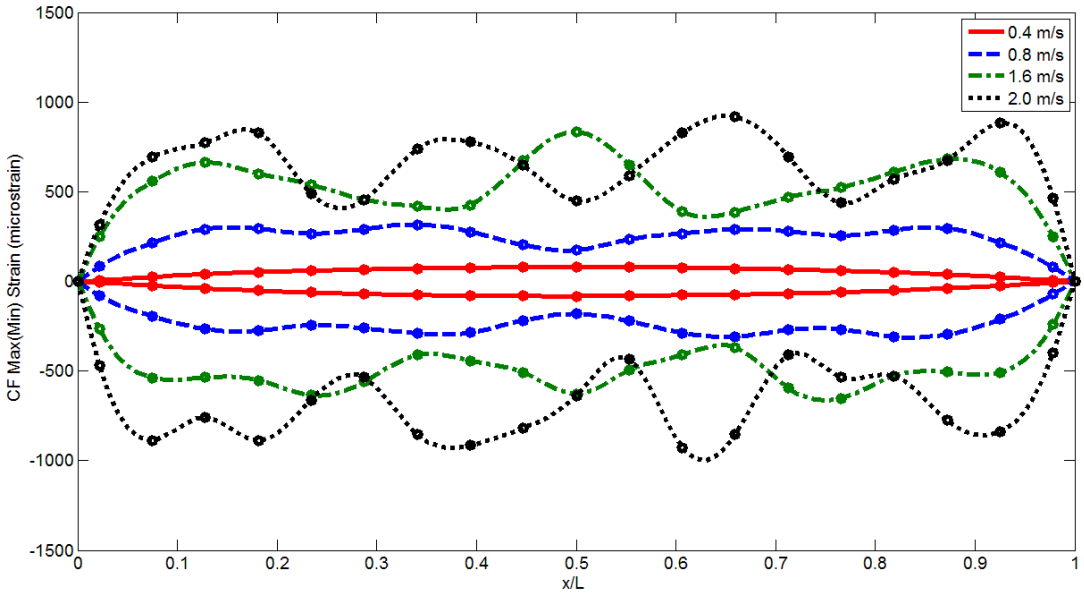

(a) CF

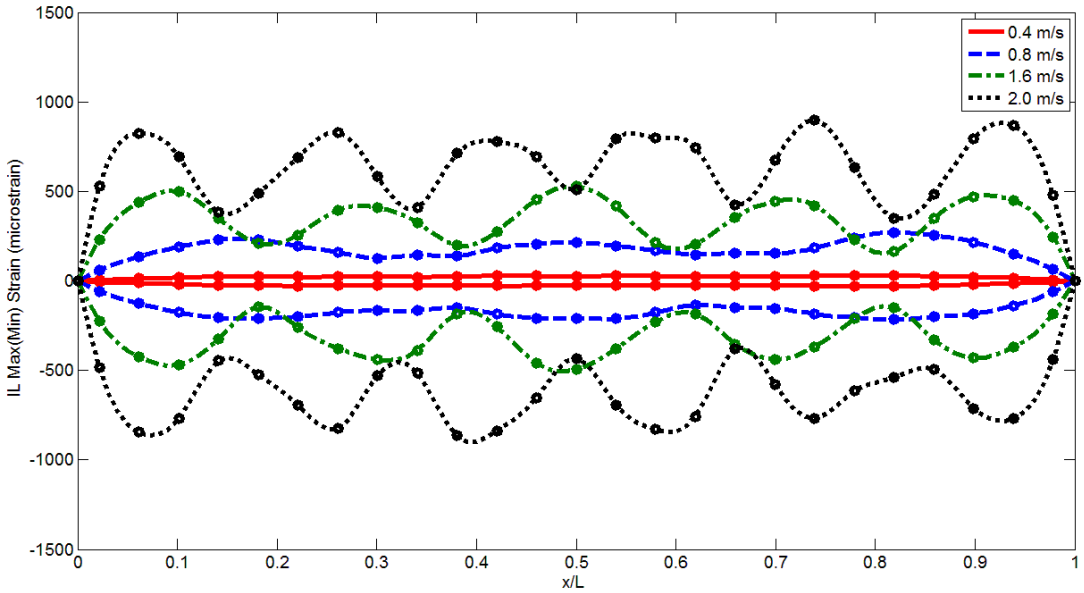

(b) IL

Fig. 3.25 Bare cylinder CF and IL strain envelopes at the high tension in varied current velocities.

Apparently the high tension reduced the CF responses in all velocities. However, in the IL direction, the responses at 2.0 m/s were much larger at the high tension than that at the low tension. The clearer presence of the 6^{th} mode in the high tension envelope indicated the increased tension made the 6^{th} natural frequency closer to the shedding frequency (corresponding to the alternate shedding of vortices), which resulted in a larger response.

Many studies have validated the effectiveness of helical strakes in suppressing VIV responses, however, not many have worked on the mixture of strakes and buoyancy elements. An attempt was made in this experimental work and the strain envelopes are presented in Fig. 3.26a and b, in both CF and IL directions at 0.4, 1.6 and 2.0 m/s. The results of 0.8 m/s were removed due to excessive noise. A few phenomena were observed in response magnitudes and dominant modes. Overall, the strains were greatly reduced in both directions, especially in the IL direction. The dominant modes were also pushed to lower ones, e.g. the 2^{nd} mode dominated the cases at 1.6 and 2.0 m/s. The reduction in maximum strains seemed to result from the dominance of the lower modes. Sometimes this is preferred as smaller curvatures of lower modes mean smaller extreme stresses. The reduction effect of mixed arrangement of strakes and buoyancy elements may come from both devices though the working mechanisms were different. The strakes were working possibly because the strakes disrupted the formation of vortices hence reduced the external force. The buoyancy elements were working because the larger diameter of the buoyancy elements made the Strouhal shedding frequency lower, therefore the dominant modes shifted from 4-6 in the CF direction for the bare cylinder to 2 for the strake + buoyancy covered cylinder. In the current situation, the staggered buoyancy and strakes on the left end seemed to have slightly bigger strain responses than the continuous coverage of buoyancy elements on the right end.

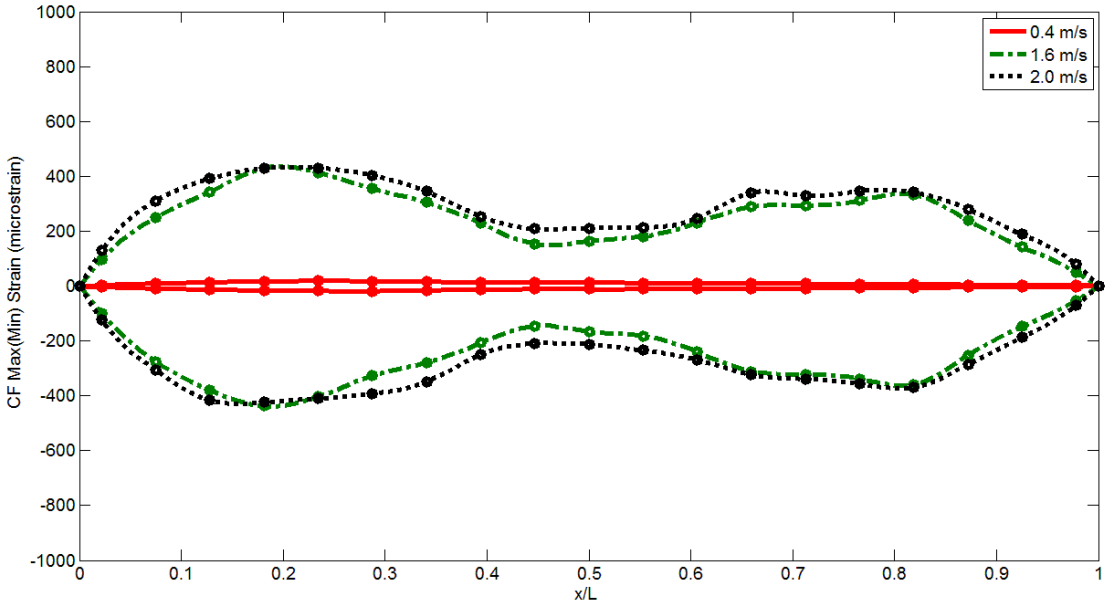

(a) CF

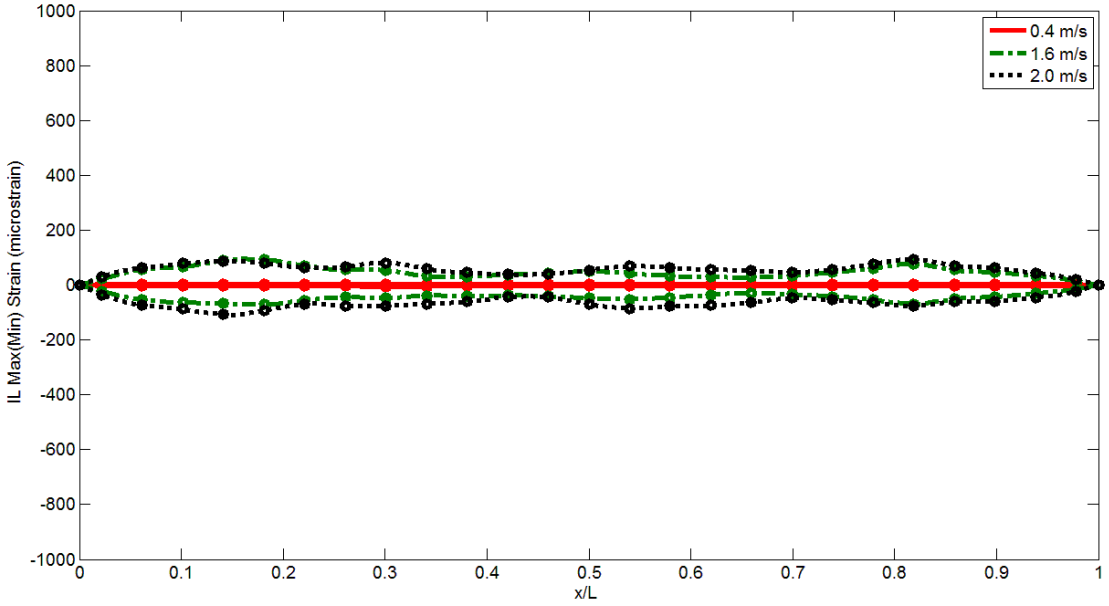

(b) IL

Fig. 3.26 50% buoyancy + 50 % strakes covered cylinder CF and IL strain envelopes at the high tension in varied current velocities.

A comparison of maximum root-mean-squared (RMS) CF curvature responses across the cylinder was made between low tension bare cylinder case and high tension bare, full strake, and 50% strake plus 50% buoyancy element covered cases. The results in Fig. 3.27 firstly showed the influence of tension in reducing the responses, and then indicated mixed coverage of buoyancy and strakes can reduce nearly 50% of the responses at the high tension. The full coverage of strakes almost suppressed all of the vibrations in all current velocities tested here, which provided additional confirmation of the effectiveness of strakes in the form of strains whereas most other studies were in the form of displacements. The results showed general consistency with Jhingran et al. (2012) with similar but different experimental setup, where the maximum RMS CF curvatures increased from 0 to 0.02 when the current velocity increased from 0 to 1.2 m/s. The interpolated value in the current study at 1.2 m/s was in the similar range. Moreover, the trend continued when the current velocity further increased to 2 m/s.

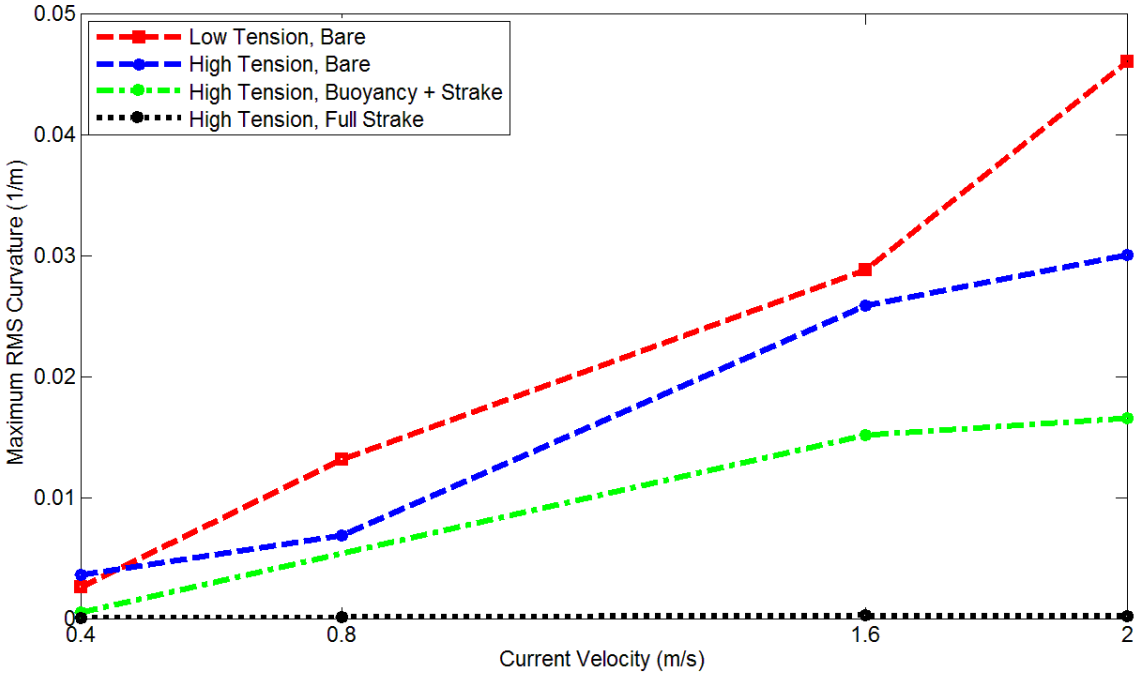

Fig. 3.27 Maximum RMS curvatures of bare, full strake covered and strake plus buoyancy covered cylinders.

Selected trajectory plots at current velocities of 0.4, 1.6 and 2.0 m/s are presented in Fig. 3.28. The plots are in 2 groups: bare and strake plus buoyancy element covered cylinders. The scale of the plots was set to be 100 micro-strain for the lower velocity at 0.4 m/s and 1000 for the higher velocities at 1.6 and 2.0 m/s. The measured stations were selected based on two concerns: the response motions were as large as possible, and four fiber optic sensors were all installed in both CF and IL directions. For the bare cylinder case, the classical "figure of eight" can be clearly recognized at 0.4 m/s, but was transformed to a complex shape at 1.6 m/s, indicating the possible existence of multiple high order harmonics. The trajectory plot at 2.0 m/s was very complicated though some repetition can still be seen. As to the case of 50% strakes plus 50% buoyancy elements, the responses in the CF direction were much larger than that in the IL direction. Moreover, the strains in both directions were largely suppressed compared with the bare cylinder case. A near "figure of eight" can be observed at 1.6 m/s, indicating the response was of single or a few lower harmonics. The plots for the full strake covered cylinder are not presented because the trajectories nearly shrank to dots, which indicates the effectiveness of the strakes.

Modal parameters including mode shapes, modal contribution factors and damping ratios estimated with time domain decomposition method are important variables in understanding the physics of a flexible cylinder"s VIV responses. As listed in Table 3.4, multiple modes up to the 9^{th} mode were excited and observable for the bare cylinder at the low tension. The strain mode shapes extracted from the measured strains with *no a priori* information can be used to validate the approximation of sinusoidal mode shapes. Assumption of sinusoidal mode shapes must be made carefully and is only possibly valid when the geometry of the structure and the environmental loads are symmetric. Moreover, the boundary conditions should be simply supported. Implementation of those requirements in an experiment is not easy and can only be achieved with good design. Comparison of the TDD extracted strain mode shapes and the assumed sinusoidal strain mode shapes can be made with modal assurance criterion (MAC) as defined in Eq. 2.44.

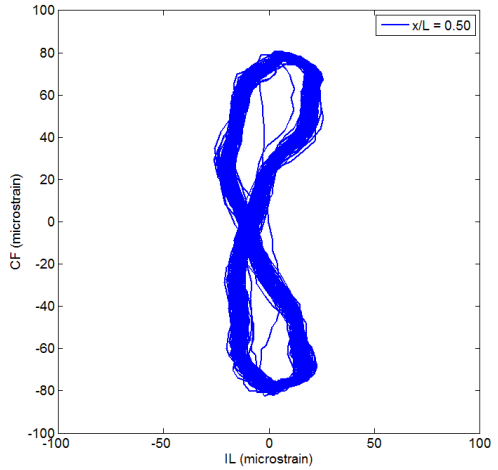

Bare, v = 0.4 m/s

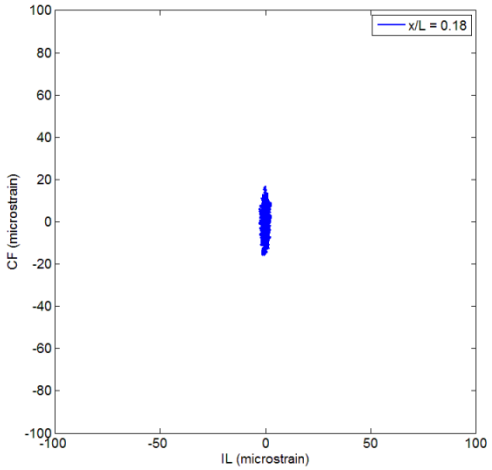

Strakes + buoyancy, v = 0.4 m/s

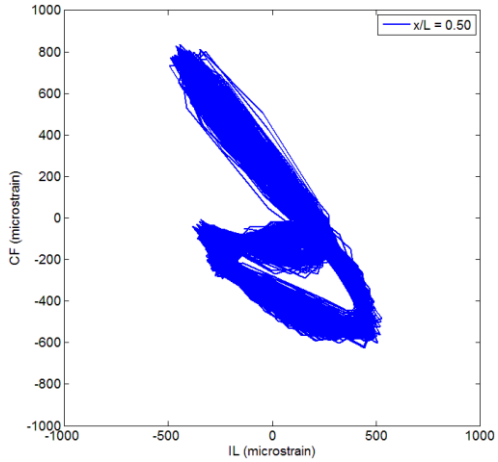

Bare, v = 1.6 m/s

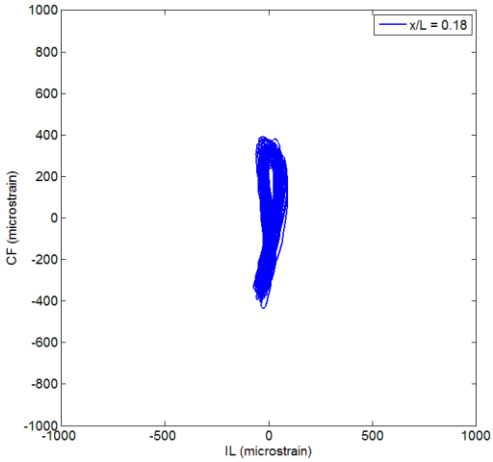

Strakes + buoyancy, v = 1.6 m/s

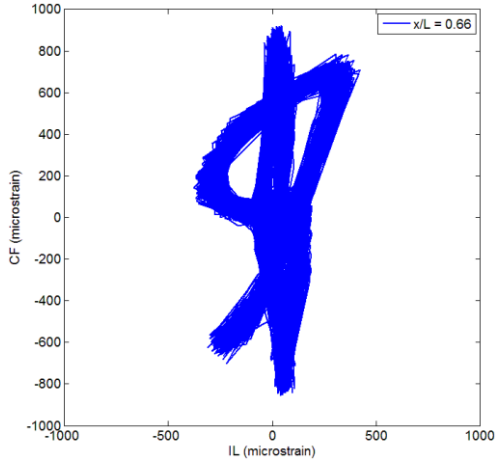

Bare, v = 2.0 m/s

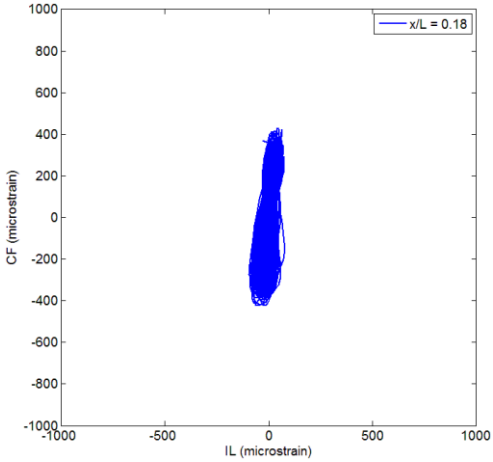

Strakes + buoyancy, v = 2.0 m/s

Fig. 3.28 Trajectory plots of bare, strake plus buoyancy covered cylinders at selected current velocities.

The value of MAC is between zero and one, which can quantify the correlation of two mode shapes. If MAC is approaching zero, the two modes are getting to be dissimilar. If MAC is approaching one, the two modes are getting to be identical. Previous studies indicated the threshold values of MAC need to be selected with attention. A value of 0.95 may suggest the two modes are fairly close but the differences are still recognizable. Table 3.6 presents the MACs of excited modes for the bare cylinder at the low tension. The selection of the threshold MAC depends on the required accuracy and available structural properties. In this case, 0.98 is used as the threshold value. In most bare cylinder cases, the strain mode shapes estimated with TDD match well with sinusoidal mode shapes.

Table 3.6 MAC of excited modes for the bare cylinder at the low tension.

	Mode 1	Mode 2	Mode 3	Mode 4	Mode 5	Mode 6	Mode 7	Mode 9
0.4CF	**0.9930**	**0.9996**	0.9682					
0.8CF		0.9961		0.9958				
				/**0.9978**				
1.6CF			0.9707		**0.9943**		0.8860	
2.0CF				0.9850		**0.9905**	0.9816	
0.4IL		0.9995	**0.9987**	**0.9985**				
0.8IL			0.9717		0.9650			
			/0.9963		/0.9723			
1.6IL			0.8657		0.9927		0.9553	
							/0.7551	
2.0IL					0.9018	0.9897	**0.9842**	**0.9025**
					/0.9309		/0.6183	

Note:
1. Red: the best estimated modes in each current velocity

The mode shapes of the bare cylinder behaved sinusoidally because of physical properties and hydrodynamics along the cylinder were uniform, however, the mode shapes may be distorted when the cylinder was fitted with helical strakes and buoyancy elements, which can be seen in the TDD extracted strain mode shapes in Fig. 3.29a and b. Mode 2 and 4 for the bare cylinder case and the buoyancy strake case were compared,

both subjected to the high tension. Obviously the introduction of strakes and buoyancy elements changed the geometry of the configuration resulting in asymmetric strain mode shapes. In order to achieve the same mode number as the bare cylinder case, a higher current velocity may be needed in the buoyancy strake case, resulting from the reduced shedding frequency with increased diameter. For the 2nd mode the bare cylinder was at 0.8 m/s while the strake plus buoyancy covered cylinder was 2.0 m/s. The 4th mode shapes were at the same velocity in both cases except they were in the IL direction. The modal frequencies were also smaller for the strake plus buoyancy case due to the physical mass and varied added mass of both devices. It was unknown how much influence the added mass exerted on the shifted modal frequencies and which one had a larger impact, whether the added physical mass or the added mass. But it was believed that the mode shapes at the same mode for bare cylinder excited at different velocities should have similar shapes, which can be partially confirmed by the MACs in Table 3.6. For example, mode 2 was excited in both CF and IL direction at 0.4 m/s, and excited in the CF direction at 0.8 m/s. The three different 2nd mode shapes had MACs of 0.9996, 0.9995 and 0.9961.

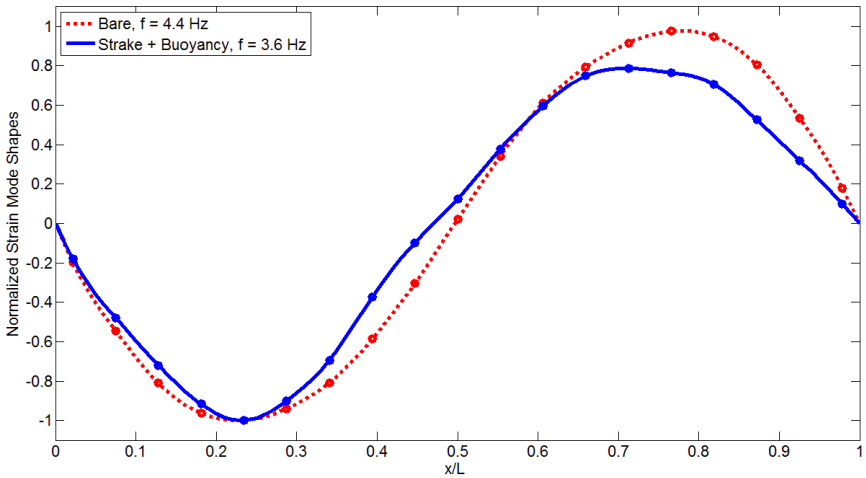

(a) Mode 2

Fig. 3.29 Strain mode shapes 2 and 4 for the bare and stake plus buoyancy covered cylinders.

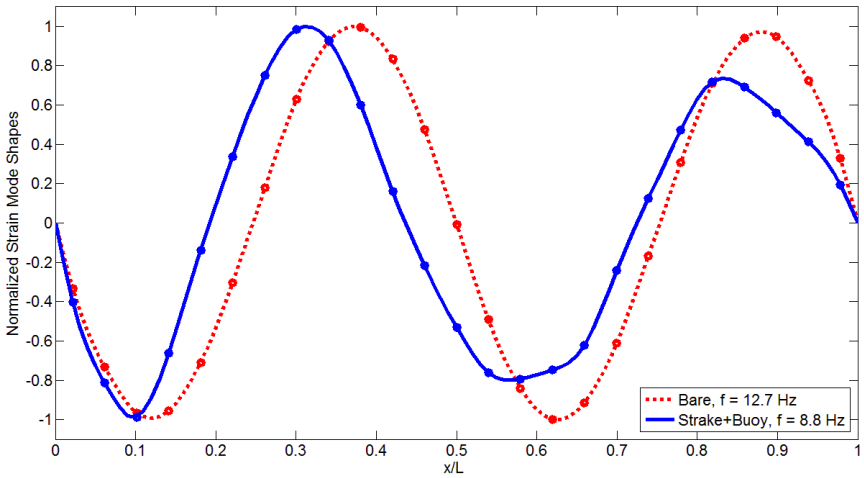

(b) Mode 4

Fig. 3.29 Continued.

The strain mode shapes were converted to displacement mode shapes via TDD with strain input as shown in Fig. 3.30 a and b. Again the displacement mode shapes for the buoyancy strake case were distorted compared to the bare cylinder case. In both cases, the normalized displacement mode shapes were 180 degree off with that of the strain mode shapes. In addition, for the buoyancy strake case, the maximum of displacement mode shapes happened at the smallest trough in strain mode shapes. Li et al. (2011) utilized finite element codes to estimate the displacement and strain mode shapes in which similar behavior was also observed. This perhaps was due to a small trough or crest in strain mode shapes allowed accumulation of a larger displacement response. For the bare cylinder case, the 2nd displacement mode shape was very regular with its node in the middle and the magnitudes of the crest and the trough were nearly the same. The regularity was slightly off in the 4th mode where the first crest was smaller than the second. This indicated that to obtain the best displacement mode shape, the strain mode shape must be recovered with high accuracy or else errors may arise during the numerical integration.

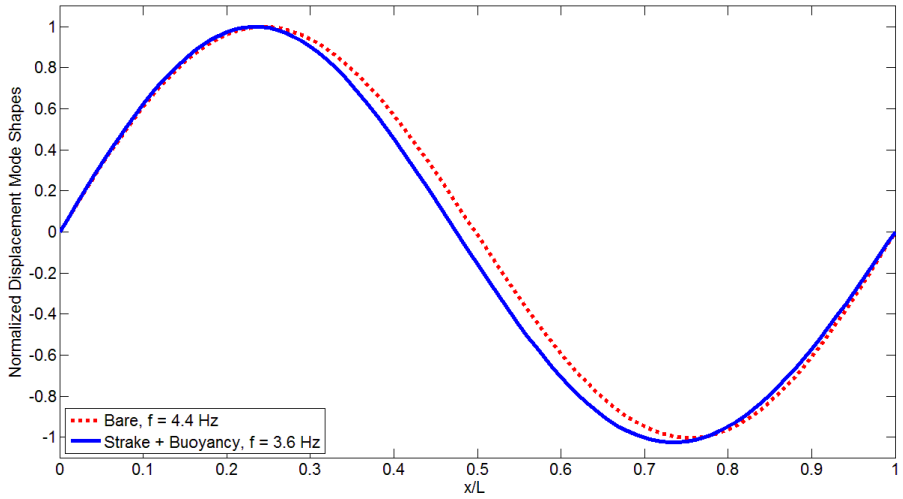

(a) Mode 2

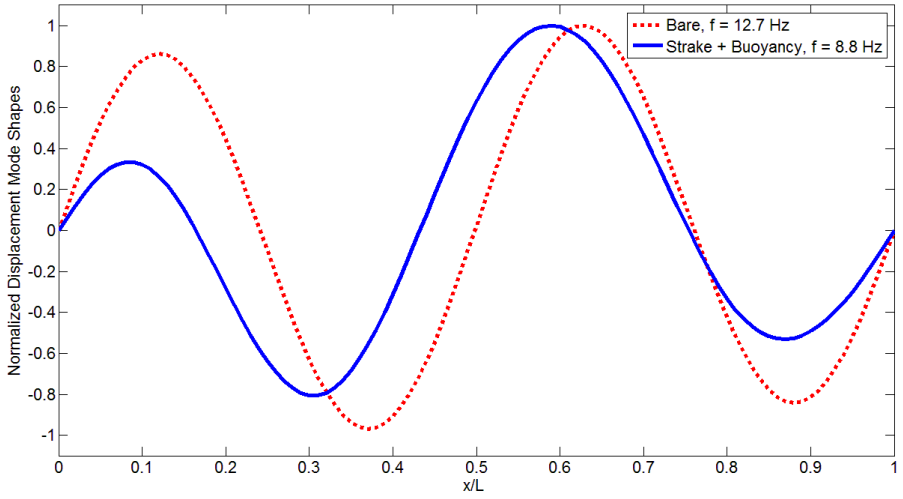

(b) Mode 4

Fig. 3.30 Computed displacement mode shapes 2 and 4 for the bare and stake plus buoyancy covered cylinders.

The damping ratios for the bare cylinder and the buoyancy strake cases are presented in Table 3.7 and 3.8 respectively. Fu et al. (2011) reported that decay tests conducted in still water of the bare cylinder showed the critical damping ratio was 0.3% in the air and 1.4% in the water. No decay experimental data was available for the buoyancy strake case. For the bare cylinder case, the estimated critical damping ratios of the dominant modes were 2.1%, 1.2%, 0.7% and 0.3% for modes 1, 2, 3 and 4 at 0.4,

0.8, 1.6 and 2.0 m/s respectively in the CF direction, while 0.7%, 0.3%, 0.2% and 0.2% for modes 1, 3, 5 and 6 respectively in the IL direction, which indicated a descending trend of the critical damping ratio as the velocity and mode number increased. It is believed that lower modes perhaps consumed more energy from the system. The critical damping ratios were much larger in the CF direction than that in the IL direction. For the buoyancy strake case, the critical damping ratios of the dominant modes were estimated as 5.3%, 4.4% and 0.8% for modes 1, 2 and 2 at 0.4, 1.6 and 2.0 m/s respectively in the CF direction, while 1.6%, 1.0% and 1.0% for modes 3, 3 and 2 respectively in the IL direction. Clearly the addition of the buoyancy and strakes dissipated more of the energy resulting in larger critical damping, which was favorable in suppressing the flow induced vibrations.

Table 3.7 Damping ratios of excited modes for the bare cylinder at the high tension.

	Mode 1 %	Mode 2 %	Mode 3 %	Mode 4 %	Mode 5 %	Mode 6 %	Mode 7 %	Mode 12 %
0.4CF	**2.1**		0. 3					
0.8CF		**1.2**		0. 6	0.2			
1.6CF			**0. 7**		0.3		0.2	
2.0CF				**0. 3**			0.2	
0.4IL	**0.7**	0.5	0. 4	0.2	0.2			
0.8IL			**0. 3**	0.8	0.1	0.4		
1.6IL					**0.2**	0.2	0.2	
2.0IL					0.6	**0.2**	0.2	0.2

Note:
1. Red: the best estimated modes

Table 3.8 Damping ratios of excited modes for the strake plus buoyancy cylinder at the high tension.

	Mode 1 %	Mode 2 %	Mode 3 %	Mode 4 %	Mode 5 %
0.4CF	**5.3**				0.5
1.6CF		**4.4**			
2.0CF		**0.8**	1.7		
0.4IL			**1.6**	1.1	0.7
1.6IL			**1.0**		
2.0IL		**1.0**	0.5	0.8	

Note:
1. Red: the best estimated modes

A unique phenomenon of two close energy peaks was observed in the power spectral density figure of the bare cylinder at the low tension at 0.8 m/s, as shown in Fig. 3.24a. The two peaks, at 11.38 Hz and 12.06 Hz were excited in a close range. TDD allowed extraction of the modal parameters of the targeted peaks. The results of the two close peaks presented in Fig. 3.31a demonstrated both peaks were the 4th mode. Similar behavior of two close peaks was also observed in Fig. 6 of Jhingran et al. (2012). One possible explanation regarding this odd behavior was that the oscillating added mass was stabilized to some extent to provide stable positive added inertia or negative added inertia. As a result, the 4th mode was excited in two close frequencies. A similar behavior was observed in the IL direction at the same velocity as well, as presented in Fig. 3.31b. Three energy peaks were excited between 15 Hz and 17 Hz with the center frequency being the largest and two sided frequencies smaller. The extracted mode shapes indicated 5th mode.

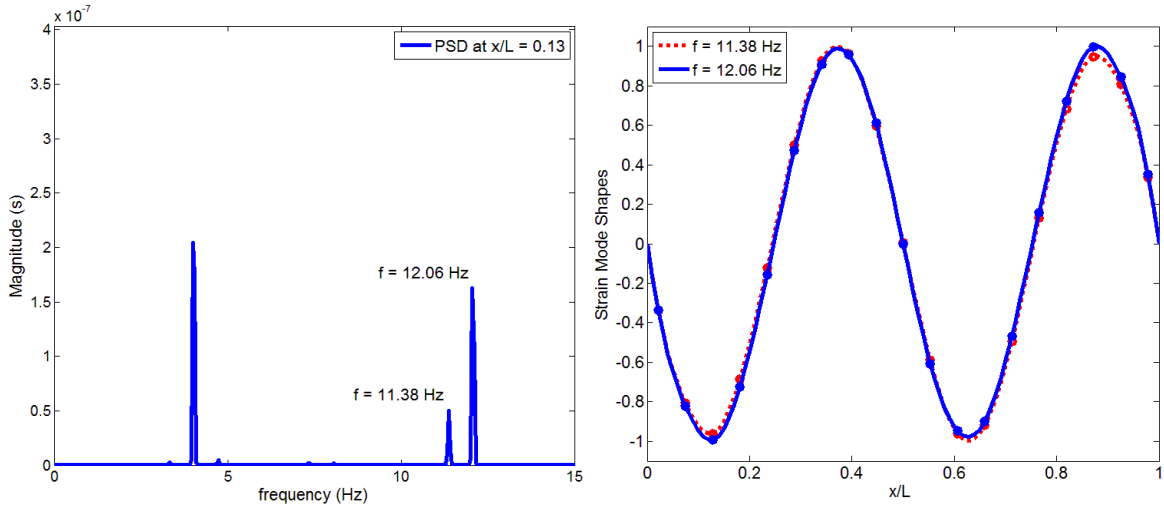

(a) Mode 4 in the CF direction

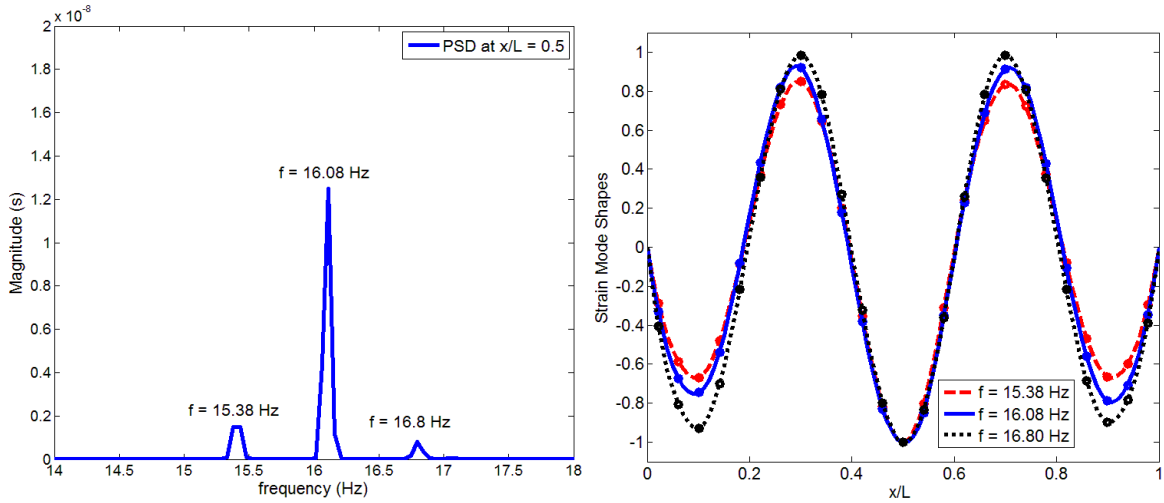

(b) Mode 5 in the IL direction

Fig. 3.31 Close peaks at the same modes.

3.3 1-D Sensor Array Optimization with Genetic Algorithm

To initiate the discussion, an example is introduced to illustrate the effect of sensor optimization. The 6 unequally spaced sensors used in Chitwood"s experiment (Chitwood, 1998) was adopted in Li"s experiment (Li et al., 2011) to recover the 4th mode shape in the in-line direction with TDD technique. The results are presented in

Fig. 3.32 to compare the mode shapes recovered with all the 25 sensors. Modal assurance criteria were computed against the assumed sinusoidal mode shapes, 0.907 and 0.998 respectively. Note that the 6 sensors originally were designed to recover the 3rd mode. Though theoretically speaking, the number of modes that can be extracted from a model test is bounded by the number of sensors therefore at first glance 6 sensors used in Chitwood experiment should be able to extract the 4th mode with ease. However, Fig. 3.32a shows the sensor array is not adequate and needs improvement despite having two additional sensors. In the meantime, a sensor combination targeted for one mode might be way off in estimating another mode within the theoretical bounds. A universal sensor combination that can recover more than one mode simultaneously is in need. In genetic algorithm, the former is classified as single-objective genetic algorithm (SOGA), and the latter as multi-objective genetic algorithm (MOGA).

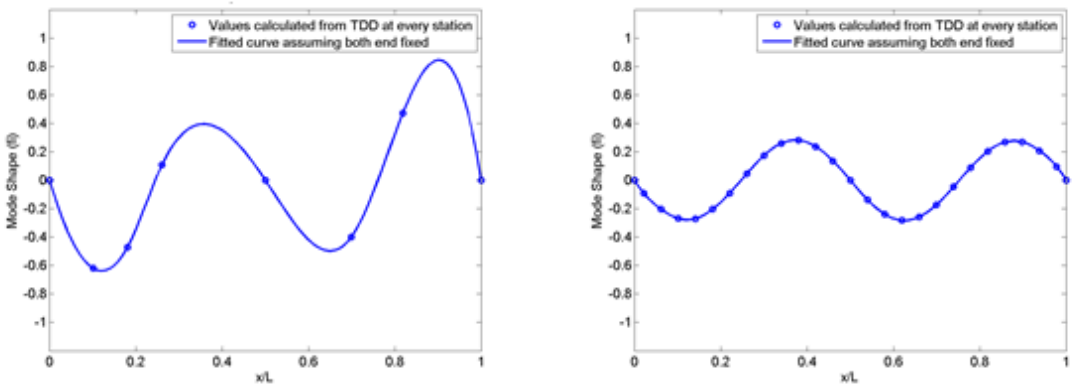

(a) 6 sensor s (Chitwood, 1998) (b) all 25 sensors

Fig. 3.32 Recovery of the IL 4th mode shape with 6 and 25 sensors.

The fine tuning process of a genetic algorithm is conducted with a numerical model constructed in a finite element code Abaqus (Abaqus, 2011), with the purpose of

excluding the imperfections of model test and possible irrelevant noise disturbance during the data collection. The varying tension, uneven added mass and added damping along the cylinder and irregularities that occur in flow-induced vibration can distort the modal parameters which might create trouble for the delicate fine tuning. After the fine tuning process, the algorithm with a preferred setting will be applied to recover strain mode shapes in FBG model conducted by Li et al. (2011).

The numerical model is a uniform beam with both ends simply supported. The length of the beam is 2 m. The cross section is rectangular with a width of 0.04 m and a height of 0.02 m. The finite element beam model consists of 100 elements (101 nodes including both ends). The material of the beam is steel, with a density of 7,800 kg/m^3 and a Young"s modulus of 200 GPa. 99 sensors were uniformly distributed on the beam to collect strain data. The finite element beam model is presented in Fig. 3.33. Periodic loads were applied near the left end and the 1st and 2nd modes were excited.

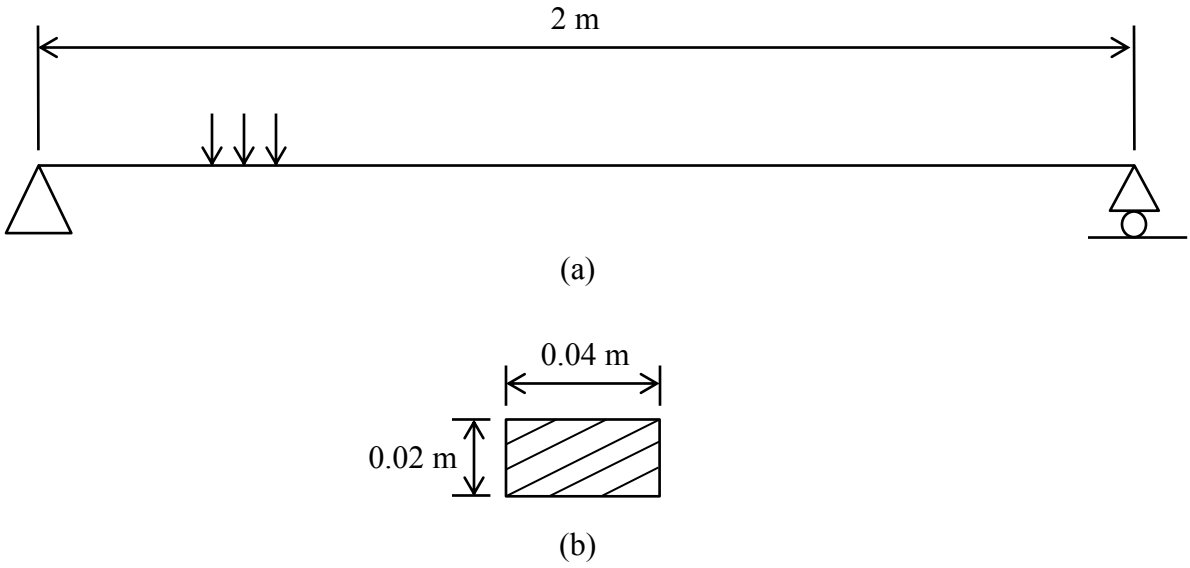

Fig. 3.33 A simply supported beam, (a) finite element model; (b) cross-section.

The natural frequencies and the mode shapes extracted from the finite element model were compared with theoretical values (Yang, 2005). Table 3.9 lists the comparison of natural frequencies up to the 5^{th} mode. Table 3.10 shows the MAC evaluations of FEM obtained mode shapes against the theoretical ones. Results indicate the numerical model was built with accuracy.

Table 3.9 Natural frequencies obtained via FEM and theoretical computation.

Mode	fn(FEM) Hz	Omega rad/s	fn/f1	fn(Theoretical) Hz	Off by
1	11.48	72.13	1	11.48	0.00%
2	45.89	288.52	4	45.92	0.07%
3	103.18	649.24	9	103.33	0.15%
4	183.23	1154.16	16	183.69	0.25%
5	285.89	1803.50	25	287.02	0.39%

Table 3.10 MAC between FEM obtained mode shapes and theoretical mode shapes.

		Finite Element Beam Model				
		fi1	fi2	fi3	fi4	fi5
Theoretical	fi1	1.00	0.00	0.00	0.00	0.00
	fi2	0.00	1.00	0.00	0.00	0.00
	fi3	0.00	0.00	1.00	0.00	0.00
	fi4	0.00	0.00	0.00	1.00	0.00
	fi5	0.00	0.00	0.00	0.00	1.00

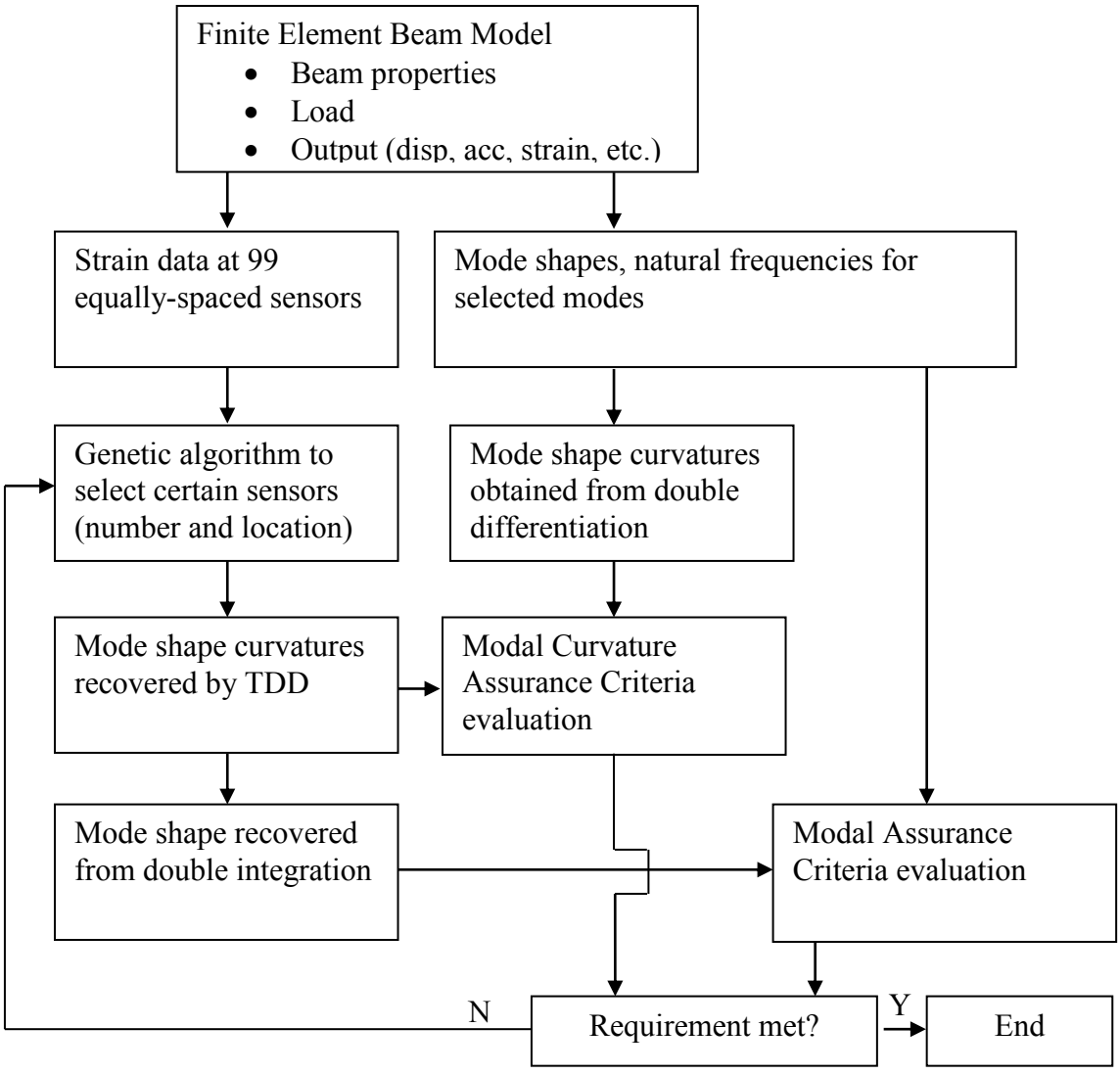

Fig. 3.34 Flow chart illustrating how genetic algorithm and TDD are applied in search of optimal sensor arrays.

The first step in developing an effective genetic algorithm is to obtain a satisfactory parameter setting. The parametric study was demonstrated with an example: to find the optimal sensor array to recover the 2^{nd} mode of the simply supported beam with 3 sensors. Every sensor has 99 possibilities in position. For a given number of available sensors, the variables of population size, the selection function, the elite count, the crossover rate, the mutation rate and the generation number, are varied to obtain a

preferred setting. It is possible to search the best setting from all the combination, but typically such exploration is not necessary because the balance must be made between the time spent on fine tuning the algorithm and the time spent on the actual optimization work. In addition, a genetic algorithm with good settings might not necessarily to be the fastest one. Flow chart of using the genetic algorithm, TDD and the finite element model was shown in Fig. 3.34.

The parametric study starts by determining the population size of sensor arrays. All other parameters are fixed while the population size is varied from 5 to 100, as shown in Table 3.11. Note the best MAC estimation that can possibly be obtained is 0.9870.

Due to the uncertainty involved in GA computation, each trial case was computed 10 times. The 10 running results for population size of 5 are presented in Table 3.12. The best MAC estimations were scattered and none of the tests found the true optimum.

Table 3.11 Parametric study of population size.

Trial case	**Population size**	Elite count	Selection type	Crossover fraction	Generation size
1	**5**	0	Tournament	80%	10
2	**20**	0	Tournament	80%	10
3	**50**	0	Tournament	80%	10
4	**100**	0	Tournament	80%	10

Table 3.12 10 computation cases with a population size of 5.

Trial case	Population size	Best MAC estimation	Obtained best sensor array
1.1	5	0.9830	26 50 74
1.2	5	0.9869	19 87 93
1.3	5	0.9837	19 84 93
1.4	5	0.9865	54 86 87
1.5	5	0.9830	42 43 60
1.6	5	0.9868	51 88 93
1.7	5	0.9867	9 12 49
1.8	5	0.9856	26 81 95
1.9	5	0.9833	35 58 61
1.10	5	0.9826	24 53 75

The 10 best estimations were averaged and taken as the performance of the population size of 5. Though the variation of MAC was fairly small, the best sensor array was highly variable. In each case, the averaged best MAC refers to the mean value of best MAC for the 10 test runs, and the overall best MAC refers to the best of all 10 test runs.

Table 3.13 Results of population size study.

Trial case	Population size	Averaged Best MAC	Overall Best MAC
1	5	0.9853	0.9869
2	20	0.9864	0.9870
3	50	0.9868	0.9870
4	100	0.9868	0.9870

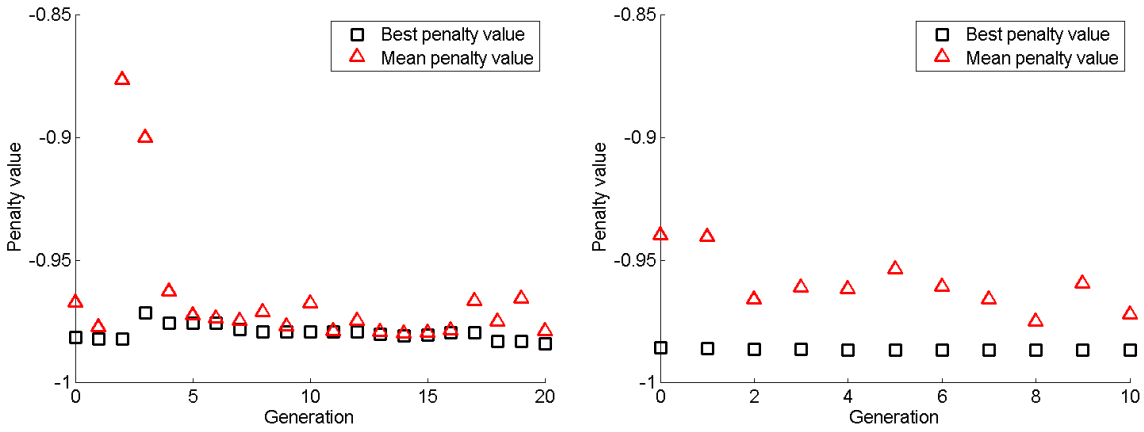

(a) with population size of 5 (b) with population size of 100

Fig. 3.35 Convergence of GA as population size increases.

The results in Table 3.13 and Fig. 3.35 show that as the population size increases, the performance of genetic algorithm improves though the improvement is not very significant. Penalty value in Fig. 3.35 means the fitness value, which is referred to as "penalty" because the problem is minimization and the negative value of MAC is used.

This is attributed to the nature of over simplifications in the example problem. Even though, a population size of 5 failed to find the optimal. Fig. 3.35 illustrates that a smaller population has the tendency of premature convergence as shown from the mean penalty value, which can be adjusted by using a larger size.

The parametric study was conducted to determine a suitable crossover fraction, and the results are presented in Tables 3.14, 3.15 and Fig. 3.36. The crossover operator selects a pair of good solutions in one generation as parents, and then exchanges their information exclusively and reproduces the children solutions for the next generation. Therefore the process of crossover is to pass the current „good" genes to the next generation without creating much spreading in contrast to the mutation operator. Crossover is a controlled and stabilized process. Results in Table 3.15 show that as the crossover fraction was increased, the 10 test run averaged best MAC decreased gradually. In addition, the overall best MAC was close to the optimal when crossover fraction was between 20% and 80%. The case of 100% crossover fraction produced a best MAC that was far from the true best. Considering the simplicity of the example, the results show 100% crossover was unsuitable. A test run example of the best, worst and averaged MAC versus generation with 40% and 100% crossover fraction is presented in Fig. 3.36. The solution with the 40% crossover obviously show more scatter than that of the 100% crossover. At first the case with 100% crossover seemed better because the results converged better, however, Table 3.15 reveals the premature convergence can be misleading and may even prevent the algorithm from finding the optimal. The more scattered results in the 40% cases are actually more attractive. The comparison results in tables and figures demonstrate a general property that all genetic algorithms follow, which is to spread the solution in the domain as wide as possible and in the meantime, to quickly converge to the global optimal and avoid the false solutions.

Table 3.14 Parametric study of crossover fraction.

Trial case	Population size	Elite count	Selection type	**Crossover fraction**	Generation size
1	20	2	Tournament	**20%**	20
2	20	2	Tournament	**40%**	20
3	20	2	Tournament	**60%**	20
4	20	2	Tournament	**80%**	20
5	20	2	Tournament	**100%**	20

Table 3.15 Results of crossover fraction study.

Trial case	Crossover fraction	Averaged Best MAC	Overall Best MAC
1	20%	0.9859	0.9869
2	40%	0.9855	0.9870
3	60%	0.9851	0.9869
4	80%	0.9842	0.9869
5	100%	0.9840	0.9865

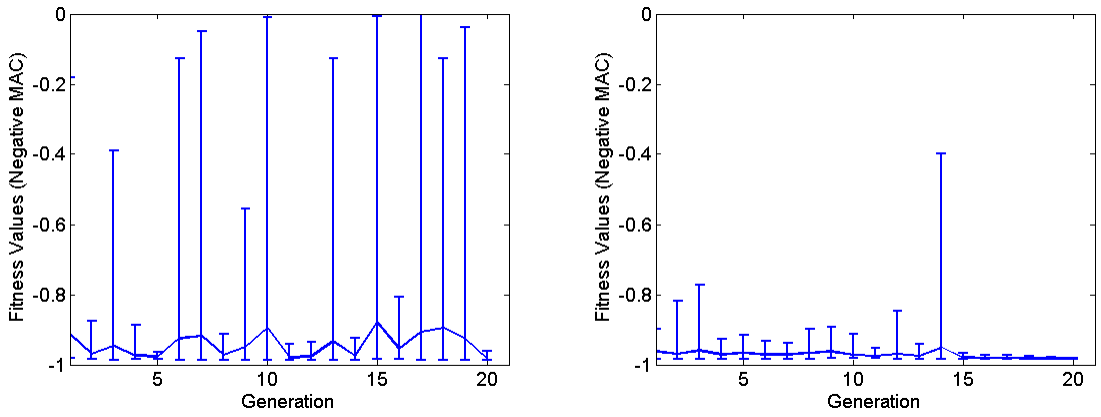

(a) 40% (b) 100%

Fig. 3.36 Best, worst and averaged MAC of 40% and 100% crossover fraction.

Parametric studies for elite count and generation number were conducted and the results are shown in Tables 3.16, 3.17, 3.18 and 3.19. The best result for elite count was 4 among a population of 20, which is reasonable for elite solutions help the algorithm

converge faster; however, a high elite parameter will limit the spreading. The parametric study of the generation parameter shows that a larger generation has better results, which may also result in a longer computation time.

Table 3.16 Parametric study of elite count.

Trial case	Population size	**Elite count**	Selection type	Crossover fraction	Generation size
1	20	**0**	Tournament	80%	10
2	20	**4**	Tournament	80%	10
3	20	**10**	Tournament	80%	10

Table 3.17 Results of elite count study.

Trial case	Elite count	Averaged Best MAC	Overall Best MAC
1	0	0.9864	0.9870
2	4	0.9868	0.9870
3	10	0.9862	0.9870

Table 3.18 Parametric study of generation size.

Trial case	Population size	Elite count	Selection type	Crossover fraction	**Generation size**
1	20	2	Tournament	80%	**5**
2	20	2	Tournament	80%	**20**
3	20	2	Tournament	80%	**50**

Table 3.19 Results of generation size study.

Trial case	Generation size	Averaged Best MAC	Overall Best MAC
1	5	0.9843	0.9863
2	20	0.9851	0.9869
3	50	0.9854	0.9869

From the parametric studies, one can see the GA results improve as sizes of population and generation increase. Elite count helps stabilize the results by ensuring

that good solutions pass through to future generations. The crossover operator, together with the mutation operator, affects the results by spreading the solutions throughout the entire domain and preventing premature convergence. As a result of the parametric study, a suitable parameter combination was determined for the sensor optimization work of the strain experiment as shown in Table 3.20.

Two questions are of particular interest in the analysis of sensor optimization for the strain experiment: what is the effect of number of available sensors in recovering a targeted mode? And what if the sensor placement is subjected to certain limitations? The study started with the 4th mode shape recovery of the bare cylinder case at 0.4 m/s as described in the beginning of this section, and then followed with more modes. Note that 25 sensors were available for selection, as shown in Fig. 3.37.

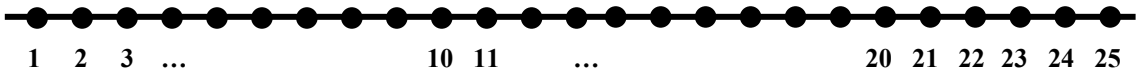

Fig. 3.37 Indices of sensors along the 7.9 m cylinder.

Table 3.20 Genetic algorithm parameters for strain data.

Parameter	Value	Parameter	Value
Population size	20	Initial range	[1, 25]
Number of Variable	Varied in [2, 25]	Elite count	2
Lower bound	1	Selection function	Tournament
Upper bound	25	Max generation	100
Crossover function	Scattered	Stall generation	50
Crossover rate	60%	Tolerance	1.0e-6

An example of the computation using genetic algorithm is shown in Fig. 3.38. The number of sensors was set at 4. The algorithm stopped at generation 50 because no improvement in best fitness was observed. Penalty value conveys similar meaning as fitness value in the genetic algorithms used here since the problem was converted into a

minimization problem from maximization. The mean fitness value has some oscillations as expected. The oscillations show that the mutation operator is spreading solutions in order to cover more areas of the domain. The best fitness value was determined as 0.9862.

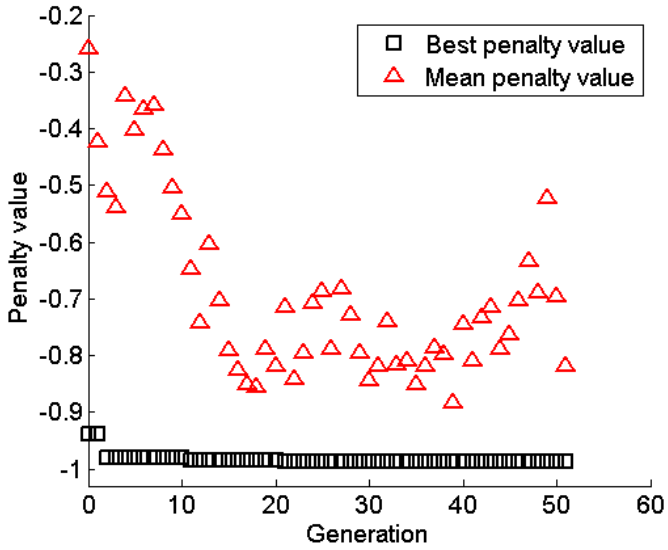

(a) Convergence of the genetic algorithm

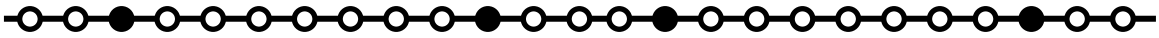

(b) Best sensor arrangement at [3, 11, 15, 23]

Fig. 3.38 Genetic algorithm of sensor optimization for the 4th mode with 4 sensors.

The relationship between best MAC estimation and the number of sensor adopted in presented in Fig. 3.39. Obviously when sensors are more than 4, the MAC approaches 1. Though subtle, when the number of sensors was increased beyond 4, the MAC still improved. The mode shape curvatures in Fig. 3.40 further confirm this phenomenon, where convergence was observed when sensor number exceeded 10. Note that the MAC is 0.986 with 4 optimal sensors, and 0.992 with 10 optimal sensors, a small difference of 0.006 is still recognizable as illustrated by the mode shape curvatures

presented in Fig. 3.40. This shows that the value of MAC can be misleading. Two mode shapes with very close MAC values can still be visually recognizable. Visualization of the mode shapes are needed to compensate for the imperfection of MAC.

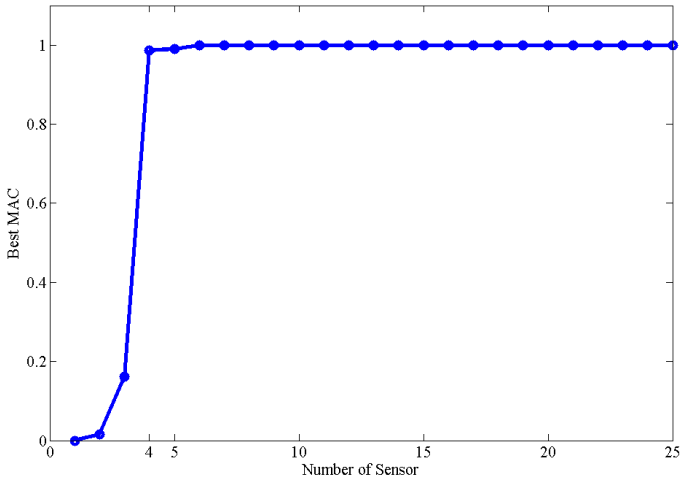

Fig. 3.39 MAC versus sensor number.

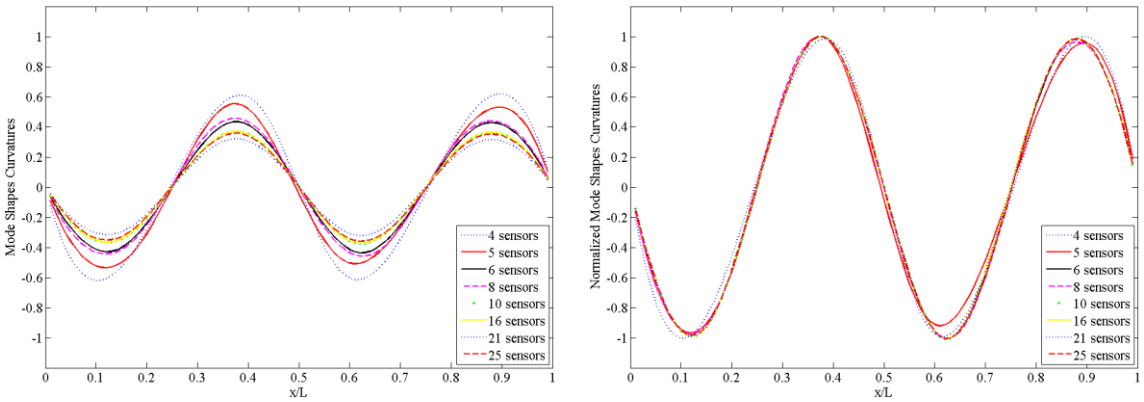

(a) before normalization (b) after normalization

Fig. 3.40 Mode shape curvatures recovered using optimal sensors of varied number.

Mode shape curvatures recovered with selected sensor numbers of more than 10 are overlapped and presented in Fig. 3.41. The convergence shows no significant improvement can be made when the number of sensors is sufficient, validating the stabilized MAC values in Fig. 3.39.

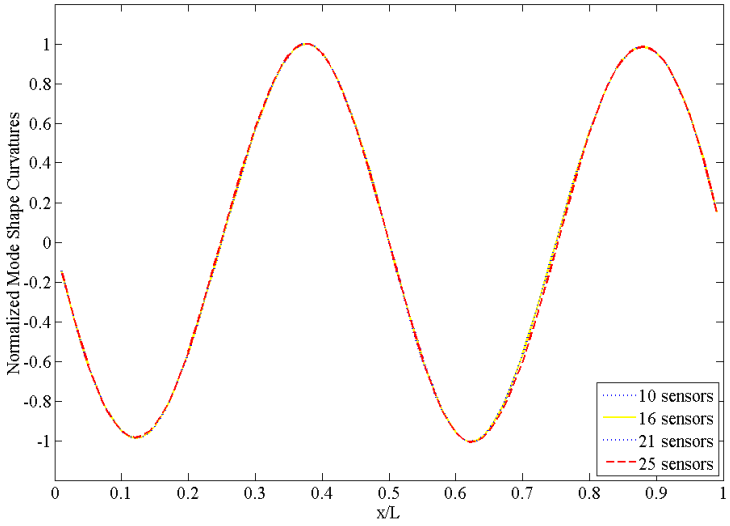

Fig. 3.41 Converged mode shape curvatures with more than 10 sensors.

It is typical that sensor placement has many restrictions and limitation due to technical difficulty or economic concern. In this study, an artificial restriction was applied to the analysis where placing sensors near the right end at $x/L > 0.82$ was not available. The reason of the restriction may be due to excessive marine growth. Consequently the original sensors 22-25 cannot be selected for sensor optimization, as shown in Fig. 3.42.

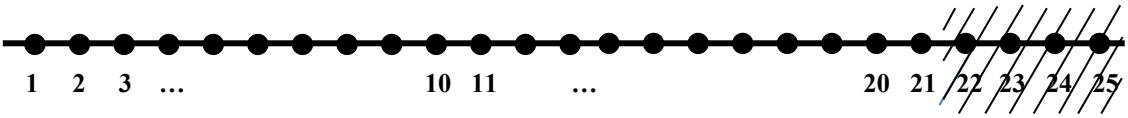

Fig. 3.42 Sensor placement with restriction on the right end.

The result of using restricted sensor arrays to recover the 4th mode is presented in Fig. 3.43 in comparison of the unrestricted sensor arrays. First, the best estimate that a restricted sensor array can achieve was downgraded compared with the unrestricted case. Second, the MAC estimate improved as the number of sensors available increased. Third, both sensor arrays show a small trough during the stabilization. For unrestricted sensor arrays, a combination of 6 sensors outperformed ones with higher number of sensors (7, 8). There are two possible reasons, the first is that GA at 7 or 8 sensors did not converge to the optimal after the 100 generations; the second is that by introducing more sensors, information upon an already optimized sensor array may introduce errors and noise, making the higher number of sensor combinations not necessarily better than their lower counterpart.

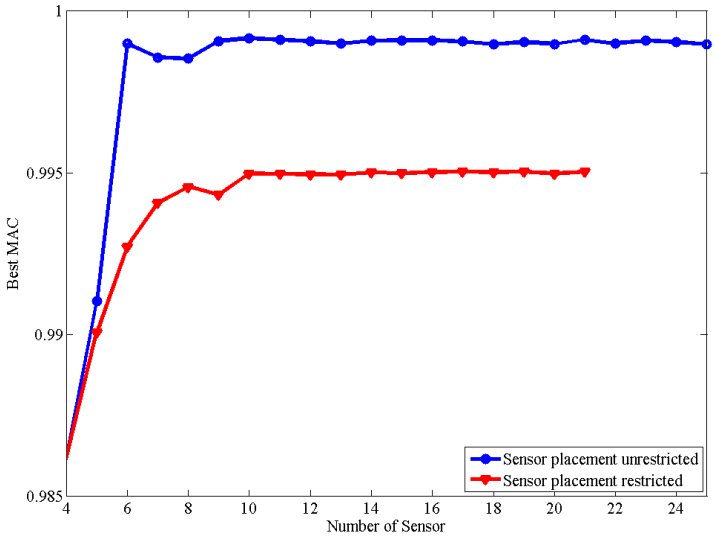

Fig. 3.43 MAC versus sensor number with and without placement restriction.

Similar to unrestricted sensor arrays, normalized and converged mode shape curvatures of restricted sensor arrays are presented in Fig. 3.44.

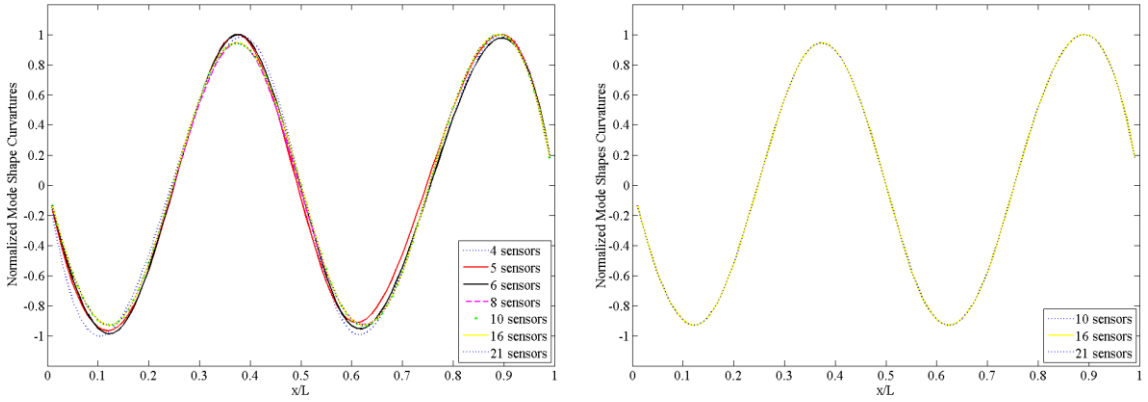

(a) normalized (b) converged

Fig. 3.44 Mode shape curvatures recovered using optimal sensors of varied number.

It is of interest to compare the stabilized and converged mode shapes without and with the placement restriction. Fig. 3.45 shows the direct results from TDD. The sensor placement without restriction is shown in Fig. 3.45a and the one with restriction in Fig. 3.45b. The red dash line is where the restriction was placed. In the case without the restriction, the best MAC estimation was 0.9862 and the best sensor array was [3, 11, 15, 23] in number, which was placed at [0.8, 3.32, 4.58, 7.1] m of the 7.9 m long cylinder. With the restriction on the right end, the best MAC estimation was 0.9861 and the best sensor array was [3, 11, 15, 19] in number, which was placed at [0.8, 3.32, 4.58, 5.84] m of the 7.9 m long cylinder.

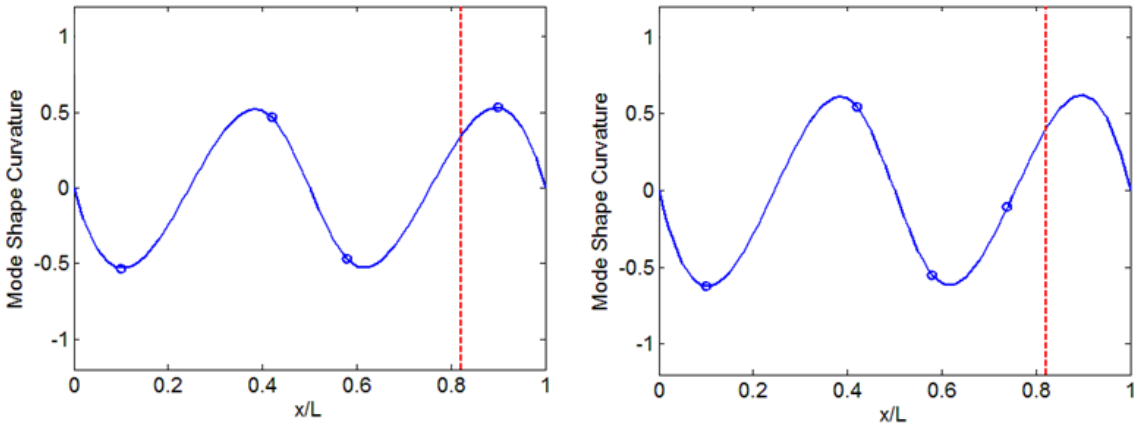

(a) without restriction (b) without restriction

Fig. 3.45 TDD recovered mode shape curvatures without and with restrictions.

It is important to highlight that an exhaustive search was conducted to compute every possible combination of placing 4 sensors out of 25 positions. Even for this simply problem, the total combination comes to an immense number of 303600 (25*24*23*22), which takes 4 hours for a very advanced computer with 3.06 GHz Inter Core Due CPU and 4 GB of RAM to finish. The optimal sensor array found by the exhaustive search was [3, 11, 15, 23]. In comparison, genetic algorithm found the same or a very close answer in roughly 3 minutes.

A similar comparative study was conducted on the 5th mode in the cross-flow direction at 1.6 m/s. The converged mode shape curvatures without and with restriction are presented in Fig. 3.46 and compared with results of the 4th mode. The results for the 5th mode were more affected by the restriction compared to those of the 4th mode. It is believed that the effect will continue to grow as the mode number increases.

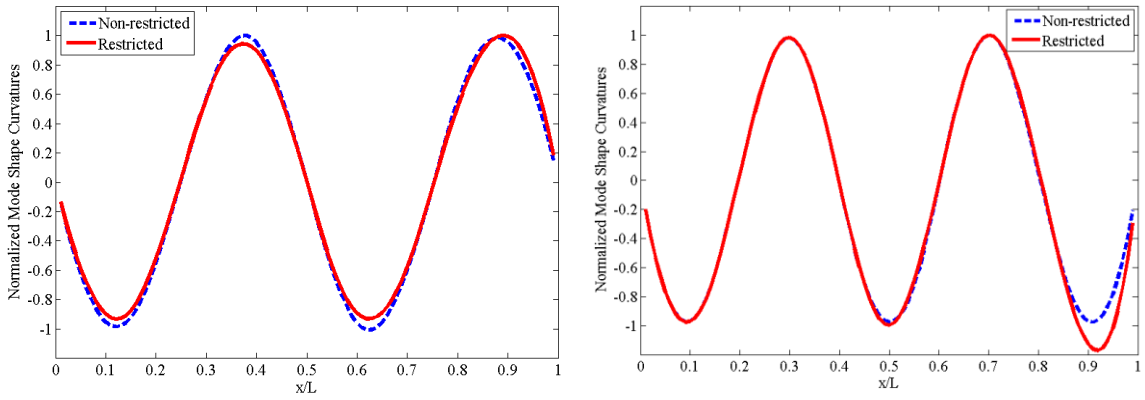

(a) 4th mode (b) 5th mode

Fig. 3.46 The 4th and 5th mode shape curvatures.

It is noted that for the 5th mode case, the restriction of the sensor placement resulted in a distorted recovery of the mode shape near the right end, which potentially may create fallacious impression of the pipe"s actual response after modal summation with an inaccurate asymmetric mode shape.

A way of improving the estimation was proposed considering the symmetry of mode shapes. Starting from Eq. 2.47 with the TDD obtained mode shape $\varphi(i)$ and assumed sinusoidal mode shape $\psi(j)$, considering the symmetry of the system, $MAC_{sym}(i, j)$ defined in Eq. 2.48 will be used to compensate the asymmetry brought by loss of information due to the restriction. Fig. 3.47 illustrates the mode shape recovered with modified MAC. Apparently the new MAC improved the symmetry of the recovered mode shape with the same amount of information. Without the full information due to the restriction, it is essentially very difficult to determine the exact true solution, mode shapes recovered with guidance from the original MAC and the modified symmetric MAC both deviated from the exact shapes, however, the modified symmetric MAC did not create similar misleading information near the right end, which is an advantage.

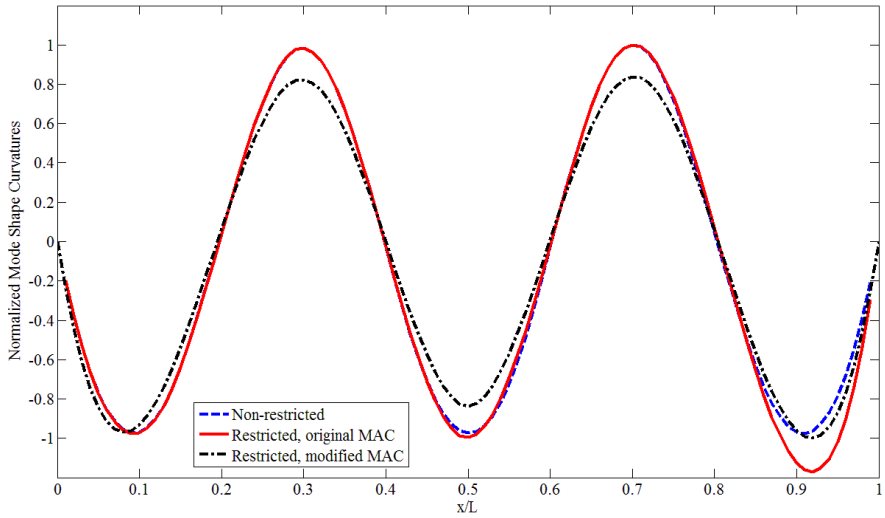

Fig. 3.47 Obtained 5th mode shape with the modified MAC index.

In the case of a marine riser, one sensor array originally designed for monitoring mode i can be ordered to monitor mode j, in other words, the dominant mode of the vibration can vary due to the change of environment, and that the phenomenon requires the same sensor array to multitask and meet multiple objectives. Because of the complexity of flow-induced vibration, dominant mode can even "jump" to another mode under the same environment condition. Lie et al. (1997) reported the lock-in mode changed from the 2nd mode to the 3rd mode while the vortex shedding frequency remained unchanged. Multi-objective genetic algorithm fits the purpose of searching one solution that best fit more than one goal. The Pareto front method is typically used to measure the performance of a solution in multi-objective problems, where the two objectives are plotted against each other and a convex curve on which the solutions cannot be further improved may be observed on the fitness domain. The convex curve is noted as a Pareto front, and solutions inside the Pareto front are dominated by those on the front.

The application of Pareto front can be demonstrated with a MOGA case where the goal was to effectively extract the 7th mode and the 9th mode for the bare cylinder case in the in-line direction at the same time. Sequentially the number of sensors

increased from 7 to 25 and the Pareto front plots were computed. Two examples are presented in Fig. 3.47 where 9 sensors and 17 sensors were selected out of 25 to extract the mode shape curvatures at the 7th mode, represented by Objective 1 in the horizontal axis, and the 9th mode, represented by Objective 2 in the vertical axis. Again the maximization problem of MAC evaluation was converted to a minimization problem in Matlab thus the smaller the value of the negative MAC, the better the estimation was. The GA generated solutions were either plotted on the Pareto front, or hidden because the solution was inferior to the ones on the Pareto front. Three inferior solutions are given in red as examples and shown in Figure 3.48. The results are interesting that though GA recovered sensors were able to adequately estimate the 7th mode in most cases (MAC > 0.93), they were not satisfactory for the 9th mode. The results were reasonable because many good combinations of 9 sensors can be found to estimate the 7th mode but the information was barely enough to estimate the 9th mode. The issue of incomplete information was solved by adding enough and even redundant sensors, for example, the Pareto front in the case of 17 sensors was much better where the estimation of the 7th mode continued to improve and in the meantime, the estimation of the 9th mode became more acceptable. By adding more sensors, the Pareto front for both the 7th and the 9th mode expanded toward better solutions.

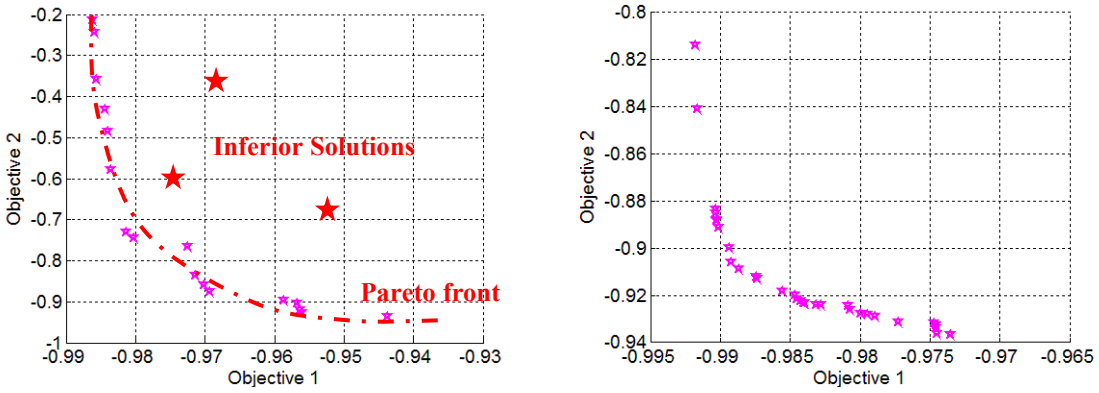

(a) use 9 sensors out of 25 (b) use 17 sensors out of 25

Fig. 3.48 Examples of Pareto front (objective 1: 7th mode, objective 2: 9th mode).

3.4 Damage Detection on Cylindrical Structures

The finite element beam model described in Fig. 3.33 of Section 3.3 was imposed with different levels of damage and used as an example for damage detection analysis. Considering the application of the methodology in the marine risers and subsea pipelines, two questions are of particular interest: can the methodology be improved in sizing different levels of damage to be more robust for field application? And, taking into account of the stiffness variation due to locally strengthened structures, is the methodology still applicable? This section will investigate damage detection on beam-like structures with those focuses.

The damage imposed was loss of stiffness in Young‟s modulus of the 17th out of 100 elements from 10% to 90% with every 20% increase. The natural frequencies of the intact and damaged beam up to the 10th mode are presented in Table 3.21. The mode shapes up to the 6th mode are shown in Fig. 3.49. The differences in both natural frequencies and mode shapes are minor. Though recognizable, the information of changes in natural frequencies and mode shapes is insufficient to directly locate the damages. The method of using mode shape deviation to detect damage obviously does not apply here (Fayyadh and Razak, 2011). At most, the two modal parameters can be used as indicator of damage occurrence. In addition, the effect of variation in mass can hardly be ruled out.

Table 3.21 Natural frequencies of the intact and the damaged beams (Hz).

Mode	Intact	Damaged beam in Young‟s module losses at the 17th element				
		10%	30%	50%	70%	90%
1	11.48	11.48	11.47	11.45	11.41	11.23
2	45.89	45.86	45.75	45.56	45.12	43.11
3	103.2	103.1	102.7	102.2	100.9	95.97
4	183.2	183.1	182.6	181.9	180.3	174.9
5	285.9	285.8	285.6	285.2	284.3	281.4
6	411.0	411.0	411.0	410.9	410.9	410.6
7	558.3	558.1	557.7	557.0	555.5	549.0
8	727.5	726.9	725.3	722.5	716.4	694.0
9	918.3	917.3	914.6	910.0	900.7	874.0
10	1130	1130	1127	1123	1115	1095

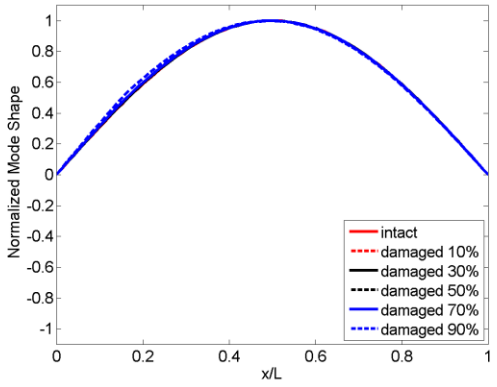

Mode 1

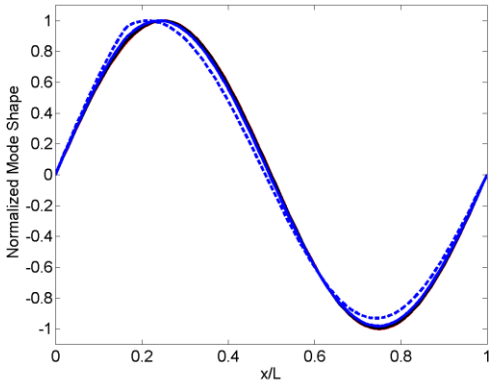

Mode 2

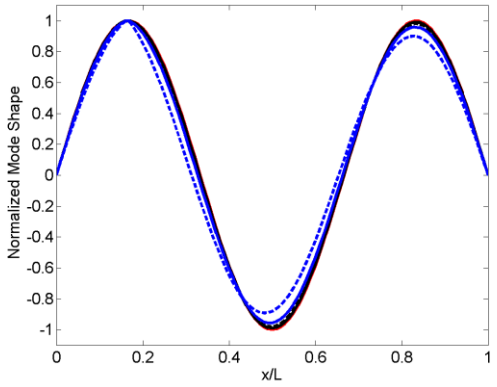

Mode 3

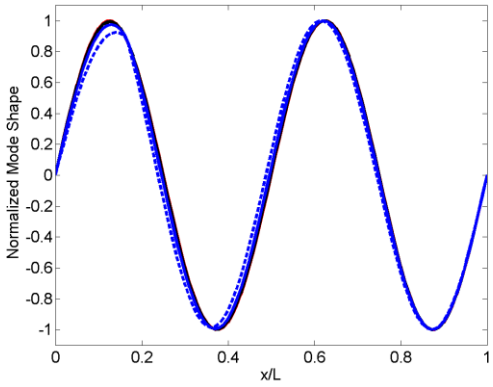

Mode 4

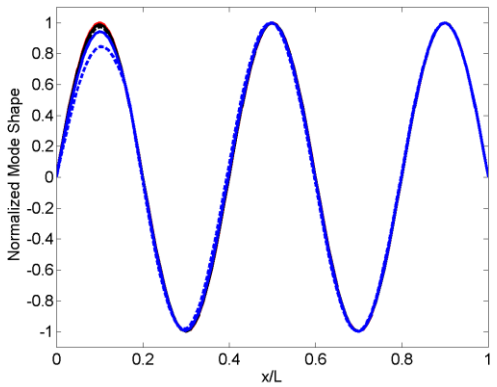

Mode 5

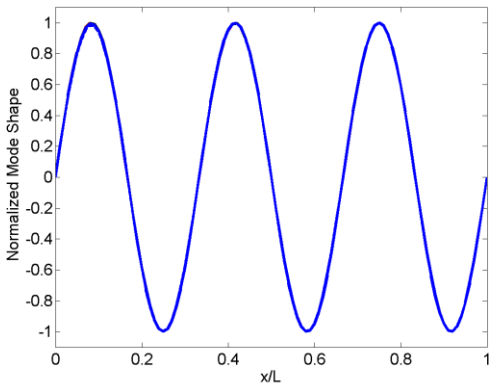

Mode 6

Fig. 3.49 Mode shapes of mode 1-6 of the intact and damaged beams.

The original damage index method was utilized and 10 modes were used to evaluate the damages. The results are shown in Fig. 3.50. In the current study, the original damage index method is denoted as DIM1. As can be seen, DIM1 performed well in locating the damage at x/L = 0.17 at the 17^{th} element and sizing the damage with its degree of stiffness loss. The damage index peaks were computed as 1.0011, 1.0046, 1.0114, 1.0293 and 1.1162 for damages in stiffness loss of 10%, 30%, 50%, 70% and 90%. For original damage index method, the following Eq. 3.1 can be used to size the damage with α. α was computed as -0.1%, -0.5%, -1.1%, -2.8% and -10.4%, which can size the damages qualitatively according to severity but not quantitatively.

$$\alpha = \frac{(EI(x))^{*} - (EI(x))}{(EI(x))} = \frac{1}{\beta} - 1 \tag{3.1}$$

Damage index method in physical space was utilized in this problem as well, denoted as DIMp. Results shown in Fig. 3.51 at first indicate that with damage index method in physical space, peaks are slightly more pronounced in the most severe case. Damage index method detected the damaged location.

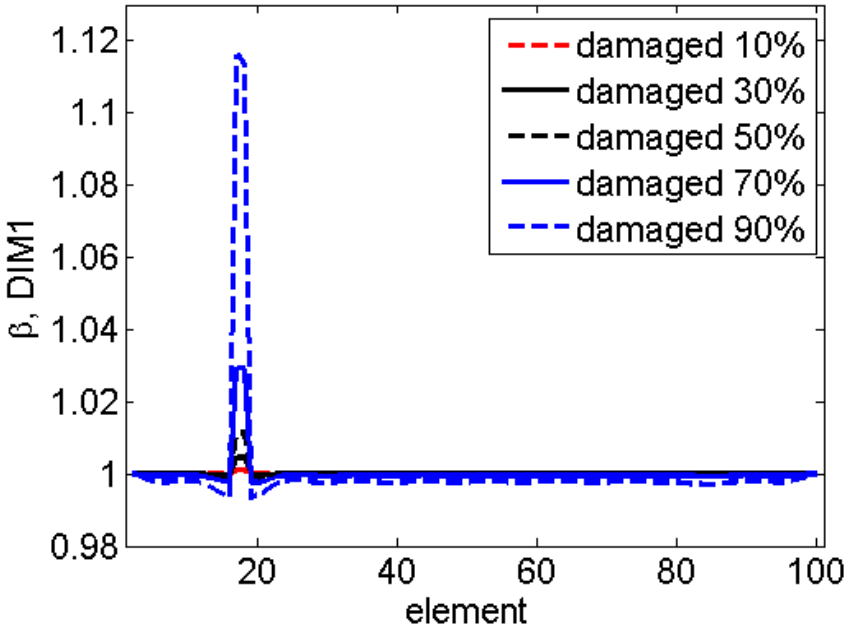

Fig. 3.50 The original damage index method, DIM1 .

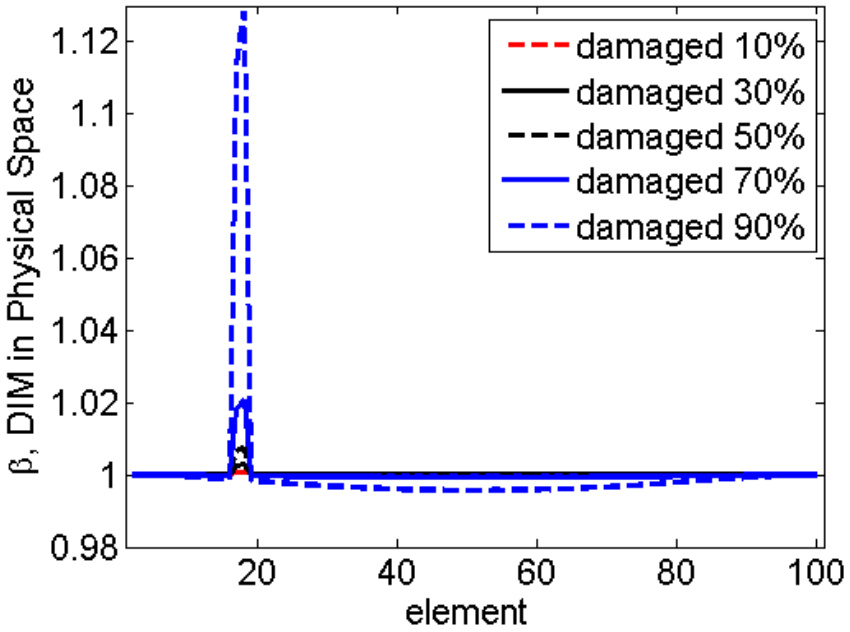

Fig. 3.51 Damage index method in physical space, DIMp.

When summarizing all the available modes for damage detection, the original damage index method DIM1 uses equal weight average, which might not be the case. The weight can be modified according to the observability of each mode for a specific damage. DIM2 is proposed as a two stage damage detection technique, where in the first stage, DIM1 is used to locate the damage, and in the meantime, specific weight factors are assigned for each mode; in the second stage, DIM2 uses the weight factor to evaluate the extent of damage. It is believed that the weight factors can be beneficial in ruling out the noise of some irrelevant modes. For example in Fig. 3.49, the damage has nearly no effect on the 6th mode because the damage occurs near a nodal point of the 6th mode. The weight factor may reduce some noise from irrelevant modes such as the 6th mode. In sum, 3 different variations of damage index method are investigated here, DIM1, the original damage index method, DIMp, the damage index method in physical space and DIM2, the weighted damage index method.

In DIM2, the weight factor for the ith mode $w(i)$ is defined as

$$w(i) = \frac{|\varphi(i, j)|}{\max(|\varphi(i)|)} \tag{3.2}$$

where, $\varphi(i)$ is the mode shape, $\varphi(i, j)$ is the value of the jth element of the ith mode. The damage location is determined at the jth element in the first stage of DIM2. For example, if the damage occurs at an anti-node of the 2nd mode, $x / L = 0.25$, the weight factor for the 1st mode $w(1)$ is 0.707, and for the 2nd mode $w(2)$ is 1.000.

The evaluation results of DIM2 are presented in Fig. 3.52. A different index δ is used here to distinguish DIM2 from DIM1 β which uses as the damage index.

$$\delta(j) = \sum_{i}^{N} \frac{w(i)\,\beta(i, j)}{N} \tag{3.3}$$

where, $\delta(j)$ is the DIM2 damage index at the jth element, $w(i)$ is the weight factor for the ith mode, $\beta(i, j)$ is the damage index for the jth element of the ith mode and N is the total number of the modes.

Table 3.22 Weight factor for computing DIM2.

Mode	1	2	3	4	5	6	7	8	9	10
Weight	0.482	0.844	0.998	0.907	0.588	0.125	0.368	0.772	0.982	0.951

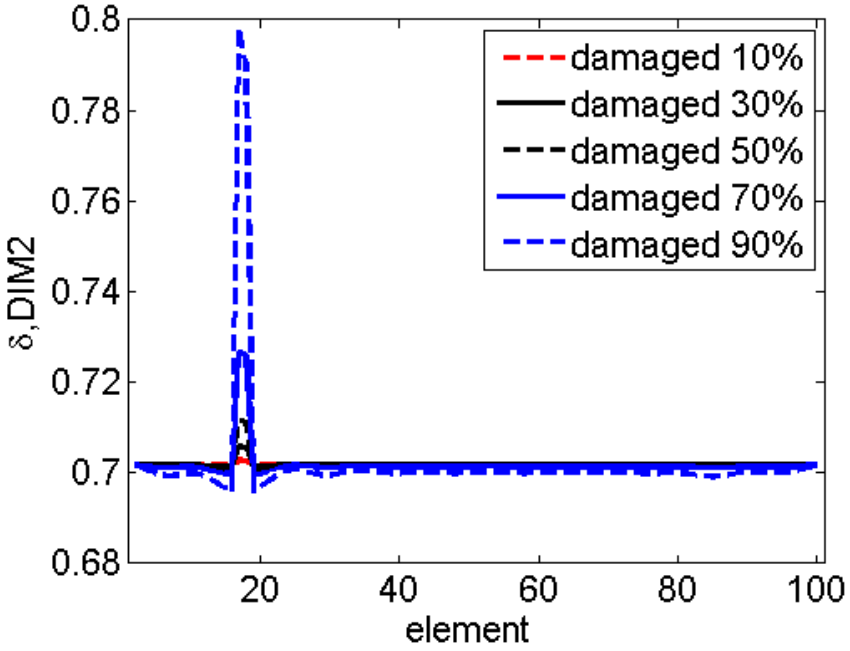

Fig. 3.52 The weighted damage index method, DIM2.

Peak values of the damage indices of DIM1 and DIM2 are presented in Table 3.23. Note that the index scales are different for DIM1 β and DIM2 δ due to the weighting process which might make the direct comparison of the two methods difficult. In order to address this issue, the damage index at 10% stiffness loss is used to normalize damage indices at other percentages. The normalized damage indices for DIM1 and DIM2 are presented in Table 3.24 and in Fig. 3.53. The comparison shows that DIM2 can give a better estimation than DIM1 by reducing some noises during the estimation. One example is the six mode illustrated in Fig. 3.49 which would generate some noise in DIM1 because of its low observability in the specific damage.

Table 3.23 DIM1 and DIM2 before normalization.

Damage in stiffness loss	DIM1, β_{peak}	DIM2, δ_{peak}
10%	1.0011	0.7027
30%	1.0046	0.7057
50%	1.0114	0.7115
70%	1.0293	0.7268
90%	1.1162	0.7982

Table 3.24 DIM1 and DIM2 after normalization.

Damage in stiffness loss	DIM1, $\beta_{peak} / \beta_{peak}(10\%)$	DIM2, $\delta_{peak} / \delta_{peak}(10\%)$
10%	1.0000	1.0000
30%	1.0035	1.0043
50%	1.0103	1.0125
70%	1.0282	1.0343
90%	1.1150	1.1359

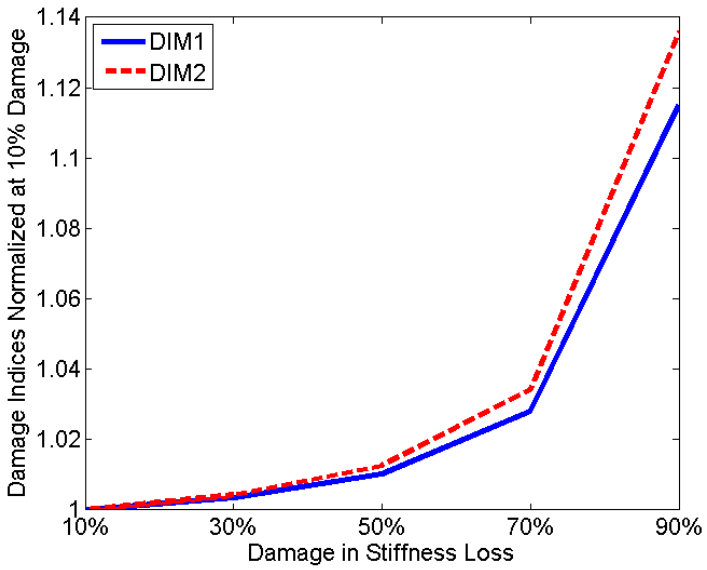

Fig. 3.53 DIM1 versus DIM2.

The flexible structures might have continuous strengthened stiffness portions due to design concerns or functionality concerns, e.g. helical strakes installed on risers

mitigated VIV and in the meantime, might increase stiffness. Another example would be a drilling riser might be strengthened near the waterline to take on the additional stresses induced by vessel motion. An illustration of a simple non-uniform beam is shown in Fig. 3.54.

Eq. 3.2 and Eq. 3.3 listed below are describing structures with uniform stiffness and non-uniform stiffness. The previous study in this research used Eq. 3.2 to detect damage. Compared with Eq. 3.2, the term $EI(x)$ cannot be cancelled in Eq. 3.3 if the stiffness is not uniform. In this case, a simple stepped non-uniform beam will be analyzed utilizing Eq. 3.3 and attempts will be made to understand damage detection upon this condition.

$$\beta_{i,j} = \frac{(EI)_i}{(EI)_i^*} = \frac{\int_a^b (\frac{\partial^2 \varphi_j^*}{\partial x^2})^2 \, dx \Big/ \int_0^L (\frac{\partial^2 \varphi_j^*}{\partial x^2})^2 \, dx}{\int_a^b (\frac{\partial^2 \varphi_j}{\partial x^2})^2 \, dx \Big/ \int_0^L (\frac{\partial^2 \varphi_j}{\partial x^2})^2 \, dx} \tag{3.4}$$

$$\beta_{i,j} = \frac{(EI)_i}{(EI)_i^*} = \frac{\int_a^b (\frac{\partial^2 \varphi_j^*}{\partial x^2})^2 \, dx \Big/ \int_0^L (EI(x))^* (\frac{\partial^2 \varphi_j^*}{\partial x^2})^2 \, dx}{\int_a^b (\frac{\partial^2 \varphi_j}{\partial x^2})^2 \, dx \Big/ \int_0^L (EI(x)) (\frac{\partial^2 \varphi_j}{\partial x^2})^2 \, dx} \tag{3.5}$$

(a) Uniform beam (b) Non-uniform beam

Fig. 3.54 Uniform and non-uniform beams.

The same 5 different levels of damage were imposed to the non-uniform beam at the 17th element, 40% of which were covered with stiffened materials. The natural frequencies of the intact and damaged beam up to the 10th mode are presented in Table 3.25. The mode shapes up to the 4th mode are shown in Fig. 3.55. Obviously the

strengthened regions on the left end increased the natural frequencies and distorted the mode shapes.

Table 3.25 Natural frequencies of the intact and the damaged non-uniform beams (Hz).

Mode	Intact	Damaged beam in Young"s module losses at the 17th element				
		10%	30%	50%	70%	90%
1	12.99	12.20	12.19	12.19	12.17	12.09
2	54.55	54.53	54.44	54.30	53.96	52.30
3	121.8	121.0	120.7	120.0	118.4	111.8
4	209.3	209.1	208.6	207.7	205.7	198.7
5	336.6	336.4	336.0	335.2	333.5	327.9
6	477.4	477.3	477.1	476.7	475.8	472.8
7	642.9	642.9	642.8	642.8	642.6	641.7
8	851.8	851.6	851.0	849.9	847.4	836.5
9	1061	1060	1058	1054	1045	1014
10	1304	1303	1300	1296	1286	1256

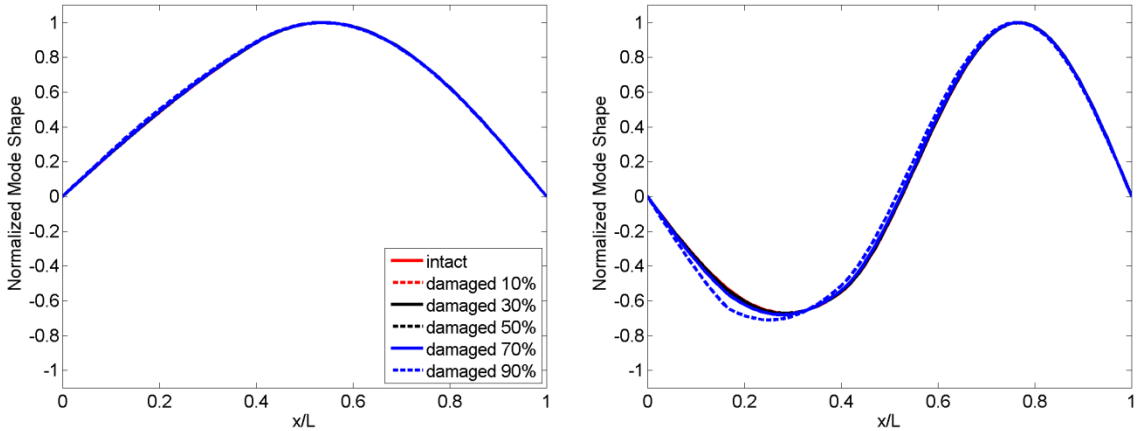

Fig. 3.55 Mode shapes of mode 1-6 of the intact and damaged non-uniform beams.

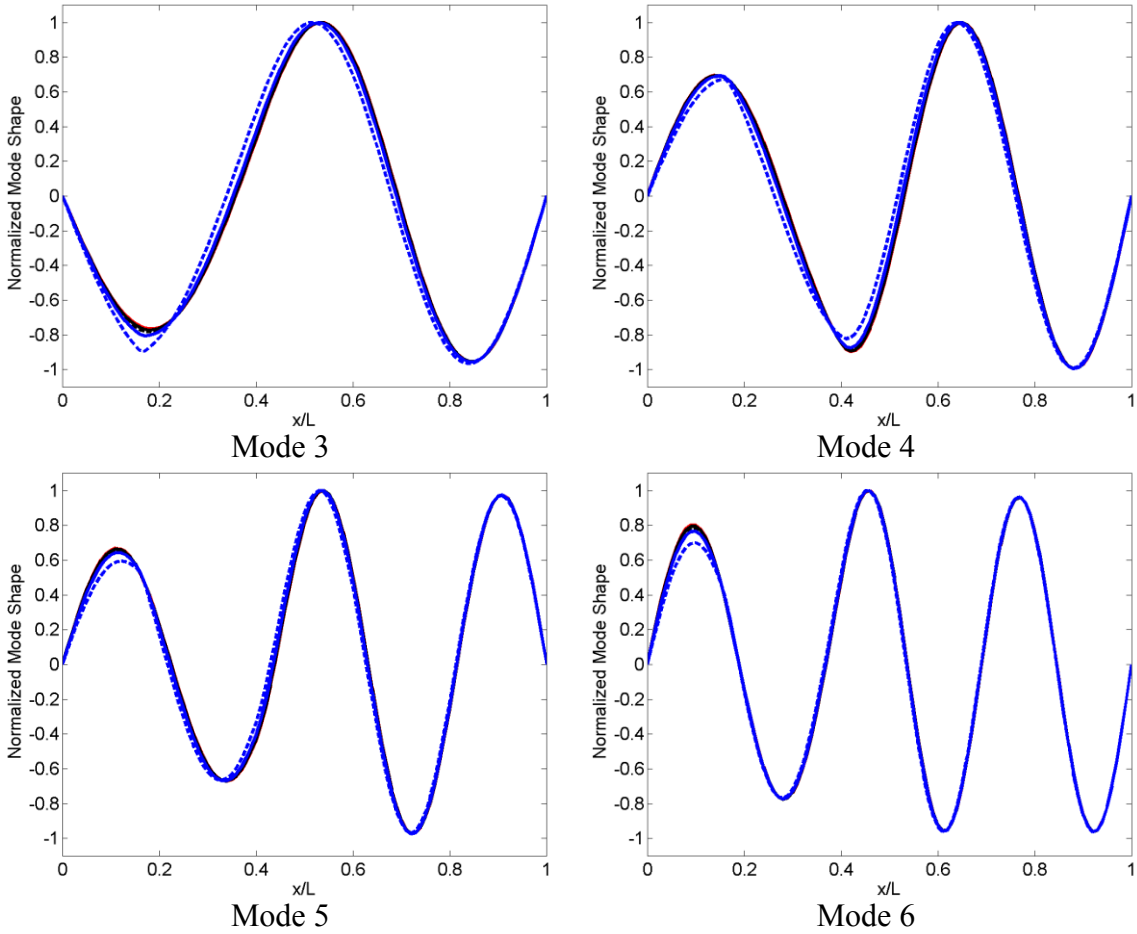

Fig. 3.55 Continued.

At this point, damage index methods using Eq. 3.2 assuming the actual stiffness profile remains unknown and using Eq. 3.3 considering the non-uniform stiffness profile in the computation for the indices are utilized to detect the damage of the 5 degrees. DIM1 and DIM2 were computed in both cases and presented in Fig. 3.56 and Fig. 3.57.

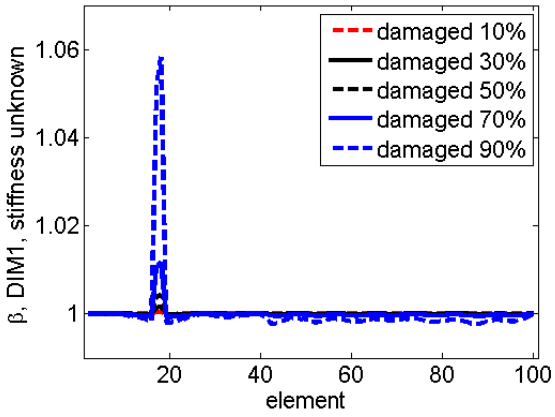

with unknown stiffness prifle

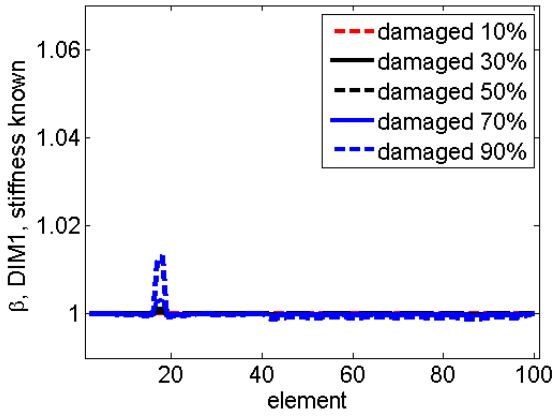

with known stiffness prifle

Fig. 3.56 DIM1 with unknown and known stiffness profiles.

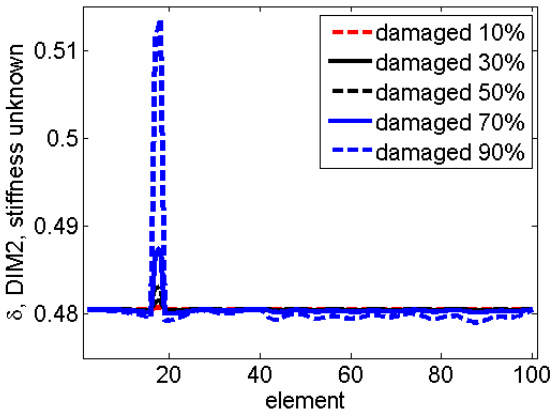

with unknown stiffness prifle

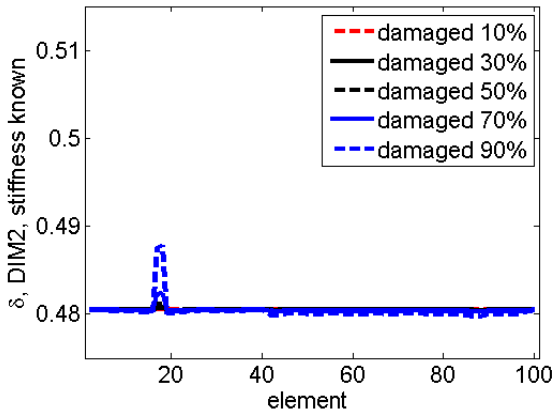

with known stiffness prifle

Fig. 3.57 DIM2 with unknown and known stiffness profiles.

When using Eq. 3.3 instead of Eq. 3.2 to compute the damage indices, both DIM1 and DIM2 become smaller with correct recognition of the damage location. Similar comparative analysis was conducted using DIM1 and DIM2 methods and results are presented in Fig. 3.58. In the situation of a non-uniform beam, DIM2 still outperforms DIM1.

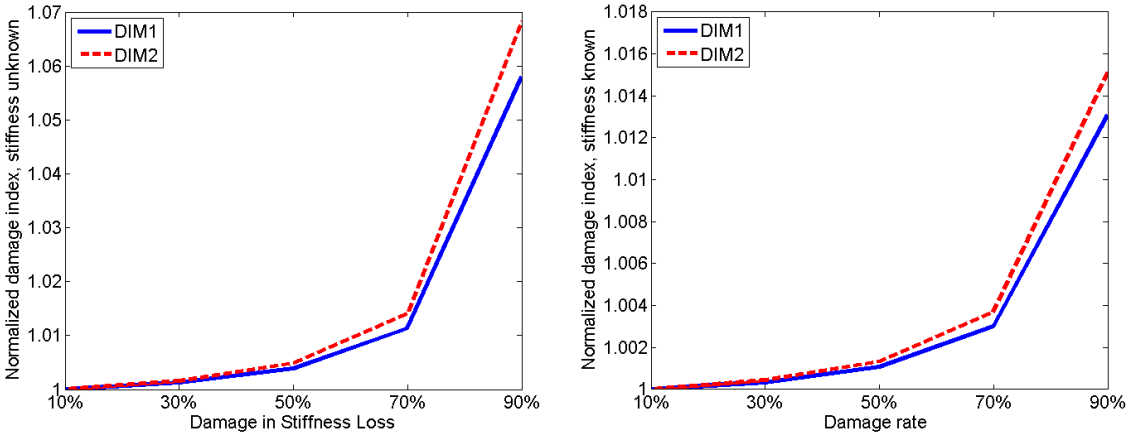

with unknown stiffness prifle with known stiffness prifle

Fig. 3.58 DIM1 versus DIM2 with unknown and known stiffness profiles.

The following numerical study focuses on analyzing the effect of marine growth on the performance of damage detection for a free spanning pipeline. Marine growth, or biofouling, is the accumulation of algae, barnacles, animals or other microorganisms that develop and attach on wetted surfaces. This phenomenon is very common on offshore structures as illustrated in Fig. 3.59. The thickness of the marine growth depends on age, water depth, geographical location, spices composition, etc. and can go from several centimeters to tens of centimeters (Page, Dugan and Piltz, 2010). In a sensitivity study conducted by Heaf (1979), thicknesses of 5, 15 and 25 cm were used to study the effect of marine growth on the statics and dynamics of a fixed platform in the North Sea. The mass of the marine growth can be considerable, e.g. Culwell (1997) reported when decommissioning platforms Helen and Herman in 1988, a total of 907 tons marine growth were removed from the two steel platforms with a weight of 2721 tons.

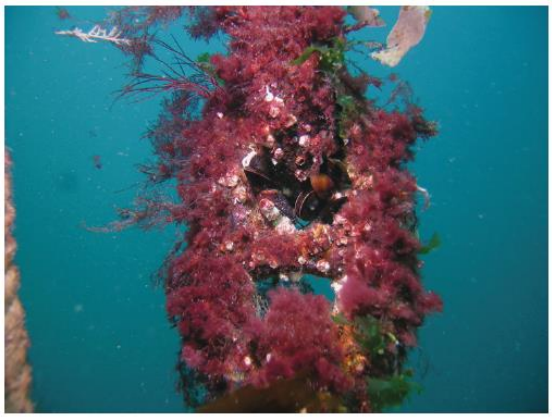

(a) Marine growth of marine chains at 5 m depth (Dürr and Thomason, 2010)

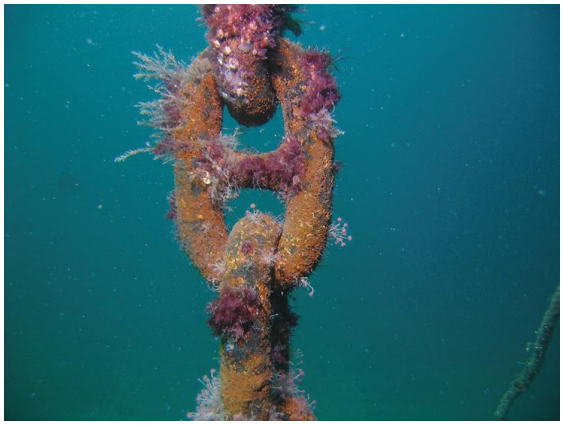

(b) Marine growth of marine chains at 10 m depth (Dürr and Thomason, 2010)

(c) Long term growth of a marine line (Brown et al., 2005)

(d) Light marine growth of a free-spanning pipeline (courtesy of Richard Whitcombe)

(e) A diver doing repair work on a marine structure with marine growth (Subsea Explore Services, 2013)

(f) An offshore diver doing inspection (Offshorediver, 2013)

Fig. 3.59 Marine growth on offshore structures.

Various types and extents of marine growth on the surface of offshore marine structures, especially on risers, mooring lines and subsea pipelines, pose challenges on strength design, monitoring and inspection. First, moderate and severe marine growth can change the geometries, physical masses, mass distributions and hydrodynamics, resulting in different dynamic behavior. More specifically, the hydrodynamics have a bigger impact on changing the dynamics, e.g. the drag coefficient may change significantly due to the increased surface roughness resulted from the marine growth, or the added mass may increase greatly due to a greater cross section. Second, the coating of the structures may be damaged by the marine growth, resulting in an accelerated corrosion rate. Third, the marine growth may block the reference points for ROV operation or interfere with the routing inspection by divers thus it needs to be removed periodically.

The free spanning pipeline used here for the numerical study has a span of 194.6 m and an outside diameter of 556 mm (22 inch), which references an actual case study of the Ormen Lange field (Nielsen, Soreide and Kvarme, 2002). The physical properties of the spanning pipeline are listed in Table 3.26. The average density of the marine growth, which was important for the dynamic analysis, can vary significantly according to location of the subsea structure, season, water depth, etc. Heaf (1979) reported that the marine growth in the waters of North Sea had a mean specific gravity of approximately 1.3, which was adopted here. In this study, marine growth was assumed to contribute to the mass of the structure but not the stiffness.

The existence of marine growth will affect the unit mass, diameter and added mass of the pipe. An example with 5 cm of marine growth is listed in Table 3.27. As can be seen, the total mass per unit length of the free spanning pipe considering added mass increased by 39%, with merely 5 cm marine growth.

Table 3.26 Physical properties of the free spanning pipe.

Item	Nomenclature	Value	Unit
Length of span	L	194.6	m
Outside diameter of the pipe	D_o	0.556	m
Wall thickness	t	24.4	mm
Young‟s modulus	E	2.07E+11	N/m^2
Bending stiffness	EI	2.99E+08	Nm^2
Mass of steel per unit length	m	318	kg/m
Added mass per unit length	m_a	249	kg/m
Total mass per unit length	m_t	567	kg/m

Table 3.27 Increased physical properties due to 5 cm marine growth.

Item	Nomenclature	Value	Unit
Thickness of marine growth	t_{mg}	0.05	m
Mass density of marine growth	ρ_{mg}	1300	kg/m^3
Mass of marine growth per unit length	m_{mg}	124	kg/m
Outside diameter of the pipe considering marine growth	D_{o_mg}	0.656	m
Added mass per unit length considering marine growth	m_{a_mg}	346	kg/m
Total mass per unit length considering marine growth	m_{t_mg}	788	kg/m

A sketch of the numerical model for the free-spanning pipeline before and after marine growth on 41% of its surface from the left end is illustrated in Fig. 3.60. The free spanning pipe with no marine growth is the reference model used for damage detection serving as the intact structure. The numerical model used 100 quadratic beam elements with simply supported boundary conditions. Natural frequencies of the free spanning pipeline with no marine growth were computed both numerically and theoretically as illustrated in Table 3.28, the results of which indicated the model was well calibrated. Natural frequencies with and without marine growth are listed in Table 3.29. With the increased mass due to the marine growth, the natural frequencies decreased by approximately 6-7%.

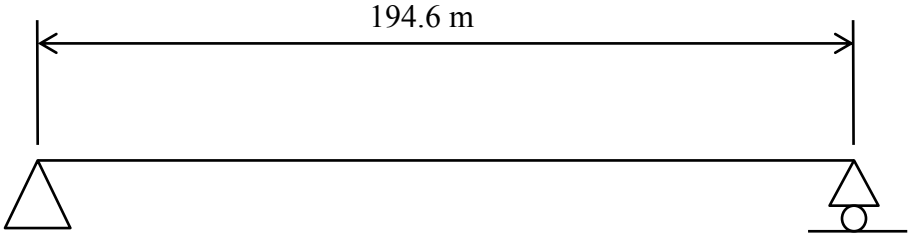

(a) A free spanning pipe simply supported, with no marine growth

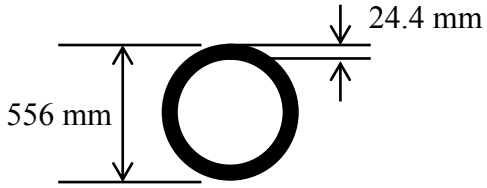

(b) Cross section of the pipe

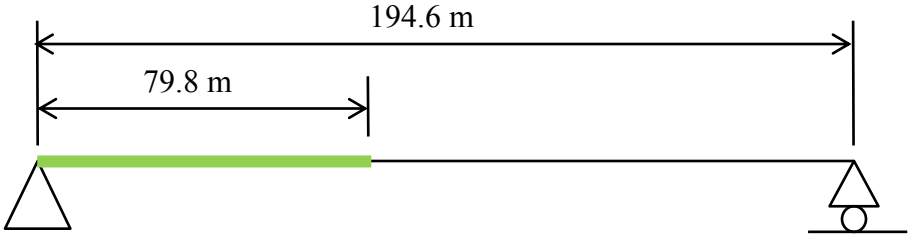

(c) A free spanning pipe simply supported, with marine growth on the left portion

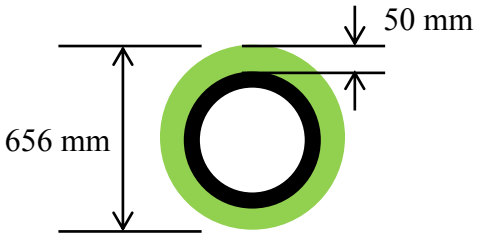

(d) Cross section of the pipe in the marine growth portion

Fig. 3.60 Sketch of the pipe before and after marine growth.

Table 3.28 Natural frequencies computed numerically and theoretically.

Mode	Modal frequency (Hz)		
	Numerical	Theoretical	Difference
1	0.0301	0.0301	-0.11%
2	0.1203	0.1204	-0.08%
3	0.2706	0.2710	-0.14%
4	0.4810	0.4817	-0.25%
5	0.7514	0.7527	-0.17%

Table 3.29 Natural frequencies with/without marine growth.

Mode	Modal frequency (Hz)		
	Pipe with no marine growth	Pipe with marine growth	Difference
1	0.0301	0.0282	-6.15%
2	0.1203	0.1112	-7.56%
3	0.2706	0.2540	-6.13%
4	0.4810	0.4452	-7.44%
5	0.7514	0.7036	-6.36%

A damage of stiffness loss was imposed on the free spanning pipe at the 17th element as in the previous studies at x = 31.1 ~ 33.1 m of the 194.6 m long pipe. Considering the fact that detecting a devastating damage was of less value than an early damage, the extent of the stiffness loss was set at 20%. The thickness of the marine growth increased from 5 cm, to 10, 15 and 20 cm.

Table 3.30 Sensitivity study of marine growth thickness.

	t_{mg}	D_{o_mg}	m_{mg}	m_{a_mg}	m_{t_mg}
	m	m	kg/m	kg/m	kg/m
Case 1	0.05	0.656	124	346	788
Case 2	0.10	0.756	268	460	1046
Case 3	0.15	0.856	433	590	1340
Case 4	0.20	0.956	618	736	1671

The modal parameters for the intact case and the four cases with 20% stiffness loss were extracted from the numerical models, specifically the natural frequencies in Table 3.31 and the mode shapes in Fig. 3.61. For each mode excited, the natural frequencies decreases as the marine growth became thicker, which was reasonable as increased marine growth increased the total mass. The mode shapes showed a trend of smaller response near the left end with marine growth due to the increased unit mass and the behavior became more apparent as the marine growth increased.

Table 3.31 Natural frequencies of intact and pipes with various marine growths.

Mode	Natural frequencies (Hz)				
	Intact	$t_{mg} = 0.05\ m$	$t_{mg} = 0.10\ m$	$t_{mg} = 0.15\ m$	$t_{mg} = 0.20\ m$
1	0.0301	0.0282	0.0264	0.0247	0.0232
2	0.1203	0.1109	0.1042	0.099	0.0948
3	0.2706	0.2533	0.2389	0.2252	0.2124
4	0.4810	0.4444	0.4165	0.3943	0.3765
5	0.7514	0.7033	0.6628	0.6251	0.5896

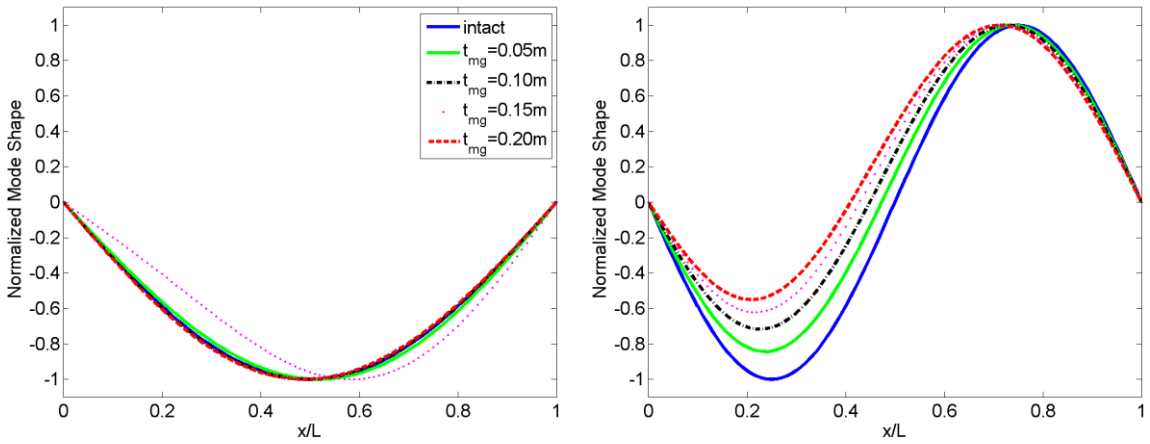

(a) Mode 1 (b) Mode 2

Fig. 3.61 Mode shapes up the 5th mode

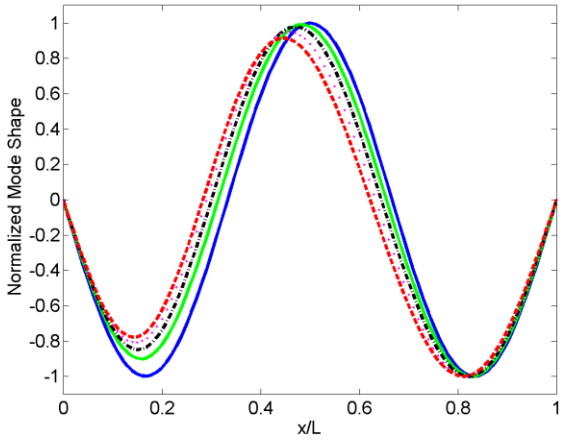

(c) Mode 3

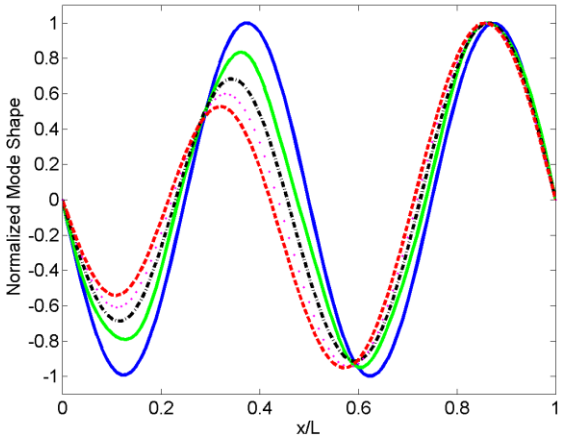

(d) Mode 4

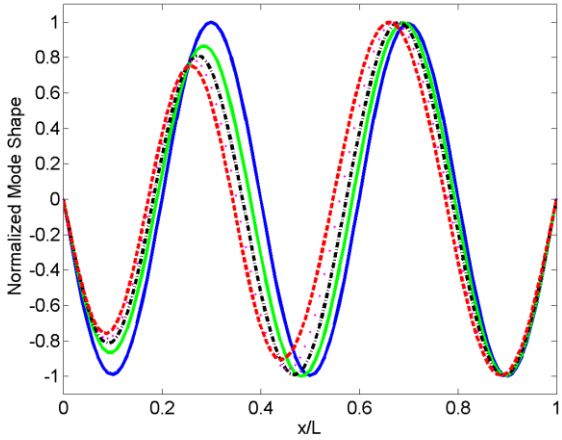

(e) Mode 5

Fig. 3.61 Continued.

The damage detection was firstly conducted with the mode shapes from all the information collected in the 100 elements, 99 nodes excluding both ends, or in other words, using 99 equally spaced sensors. Results are presented in Fig. 3.62.

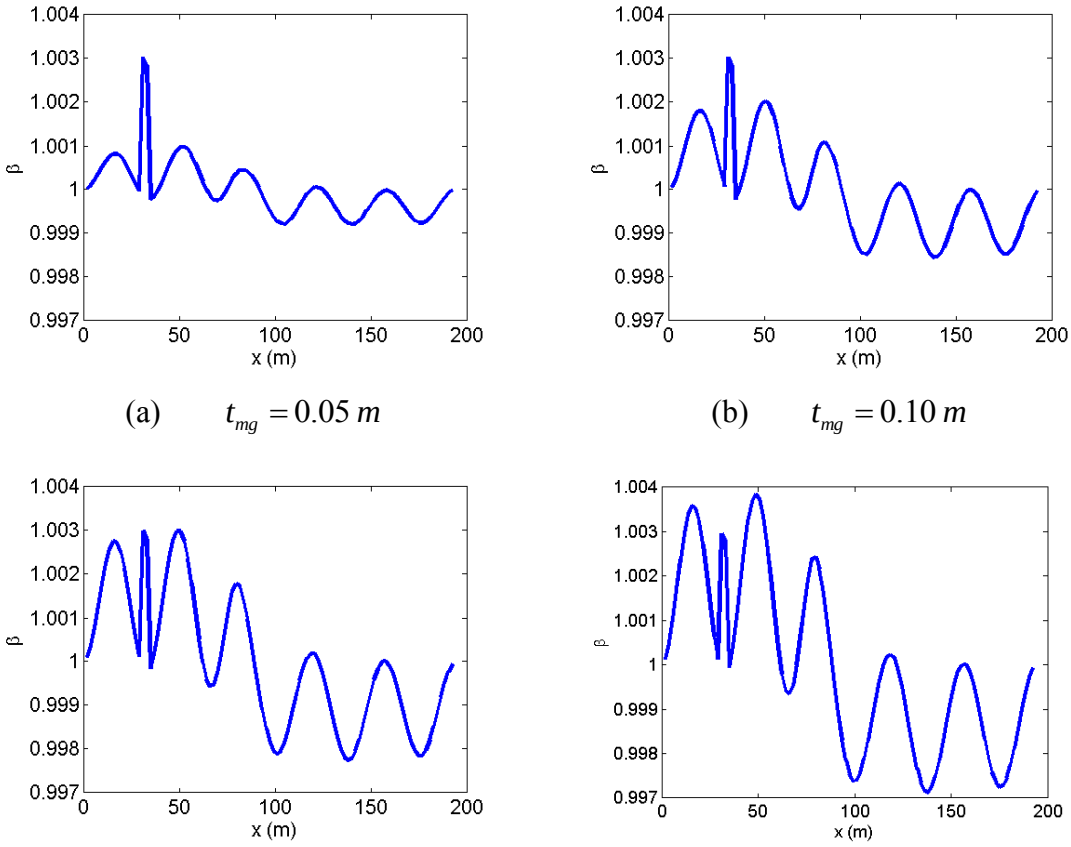

(a) $t_{mg} = 0.05\ m$ (b) $t_{mg} = 0.10\ m$

(c) $t_{mg} = 0.15\ m$ (d) $t_{mg} = 0.20\ m$

Fig. 3.62 Damage detection with varied marine growth with 99 sensors.

Damage indices in Fig. 3.62 show that when the marine growth was moderate, an early damage of 20% stiffness loss can be recognized with clear peaks, as indicated in Fig. 3.62a and b where marine growth had a thickness of 5 cm and 10 cm. The damage was correctly located at 31.1 m. However, when the thickness increased to 15 cm as presented in Fig. 3.62c, two peaks were identified in the detection procedure, considering only one damage was imposed to the structure, a false identification was made, which was undesirable. Damage index method was not able to correctly detect the damage when the marine growth was significant with a thickness of 20 cm.

The damage detection analysis conducted above was based on all available sensors, however, in a practical situation, only limited number of sensors can be placed on the structures. Genetic algorithms were applied in section 3.3 to search for optimal sensor arrays of a vibrating beam to best recover targeted mode shapes. A similar approach as shown earlier was used in the current study to firstly effectively recover the mode shapes and then detect possible damage.

Considering damage index method relied on the quality of the recovered modes, the sensor numbers used in this study were determined to be 5, 10, 15 and 20, though technically speaking 5 sensors should be enough for the 5^{th} mode. However, what may attribute to the complexity of the problem was all the modes from 1 to 5 were used in the computation for the damage index, i.e. the optimal sensor array for mode 5 may vary significantly with mode 4, and therefore more than 5 sensors should be used to conduct the damage detection. A third issue involved in the damage detection analysis was that a mode shape recovered with high MAC values compared with FEM recovered mode shape may not necessarily lead to a successful recognition of the damage or failure.

To simplify the problem, for a given number of sensors, a multi-objective genetic algorithm was utilized to locate the optimal sensor array that can best recover the highest two harmonics. It was assumed the sensor that fit the purpose of the top two modes should automatically work well with lower modes. A flow chart of the procedure is presented in Fig. 3.63.

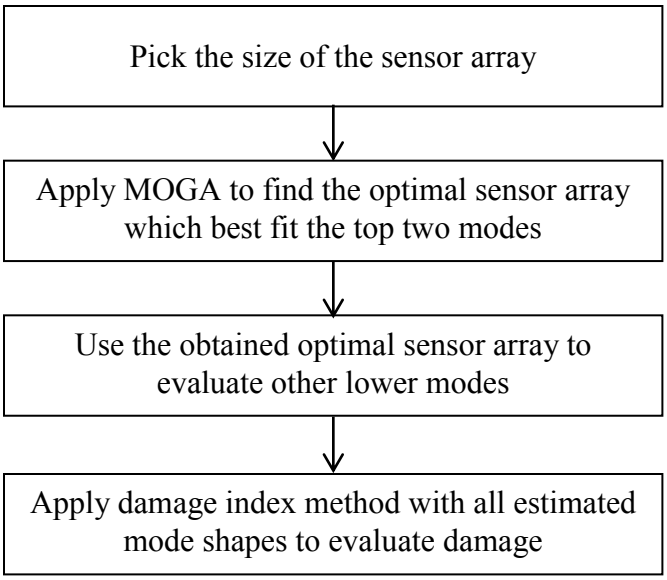

Fig. 3.63 Flow chart of damage detection with the optimal sensor array.

An example of the multi-objective genetic algorithm is provided in Fig. 3.64 for the 5 sensor case in recovering mode 4 and mode 5. Note that a series of optimal solutions was located on the Pareto front, therefore engineering judgment need to be applied here to pick the most suitable solution. Similar studies were conducted to find the optimal sensor array with higher numbers. The selected sensor arrays are presented in Fig. 3.65.

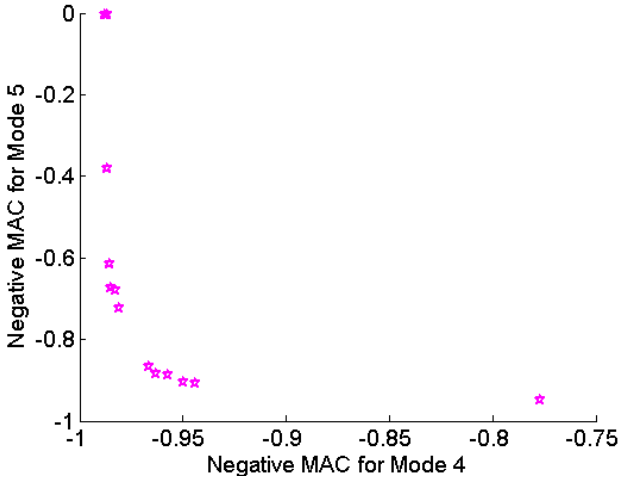

Fig. 3.64 Multi-objective genetic algorithm in search of sensor arrays with 5 sensors.

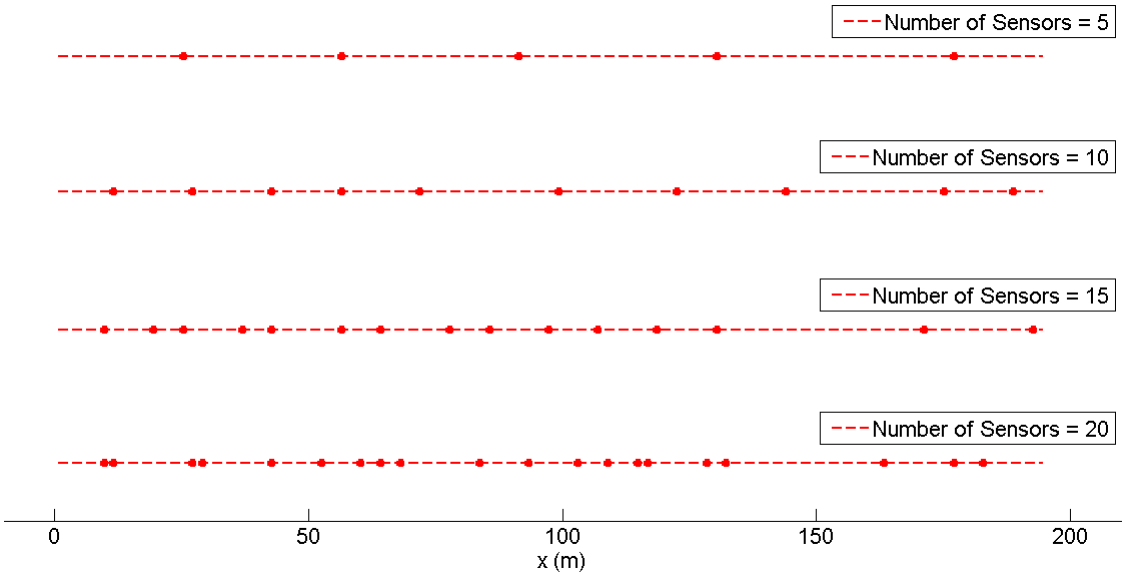

Fig. 3.65 Optimal sensor arrays with number of 5, 10. 15 and 20.

The optimal sensor arrays obtained with the multi-objective genetic algorithm targeting mode 4 and 5 had very good MAC values for the lower 3 modes, as indicated in Table 3.32 in the example of marine growth thickness of 5 cm, and in Fig. 3.66 of

mode shapes at mode 1 and 5 with increased sensor numbers. The visual display of mode shapes compensates the ineffectiveness of MAC in evaluating the differences. Though the MAC values for all modes were fairly high, differences can still be recognized, especially at mode 3 through 5. Another observation is that mode shapes with 10, 15 and 20 sensors seemed to reach agreement and distinguish from the one evaluated with 5 sensors.

Table 3.32 MAC of varied numbers of sensors for pipe with 5 cm marine growth.

Mode	Sensor			
	5	10	15	20
1	1.000	1.000	0.999	1.000
2	1.000	1.000	1.000	1.000
3	0.994	1.000	1.000	1.000
4	0.910	0.977	0.952	0.978
5	0.980	0.998	0.997	1.000

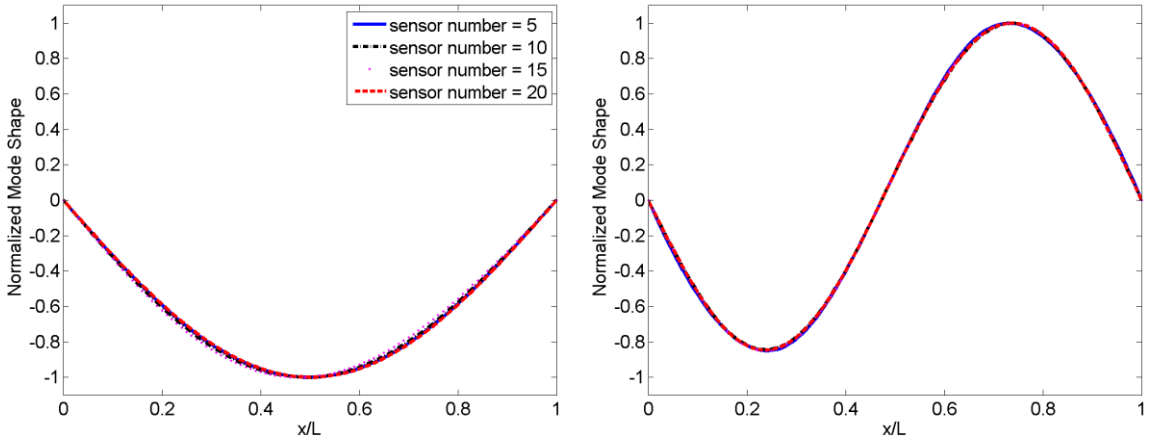

(a) Mode 1 (b) Mode 2

Fig. 3.66 Mode shapes with increased numbers of sensors with 5 cm marine growth.

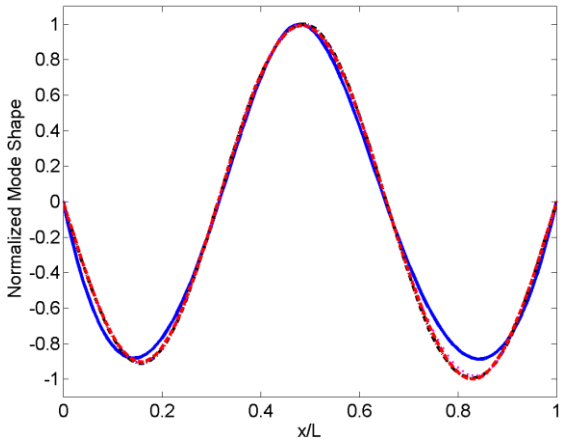

(c) Mode 3

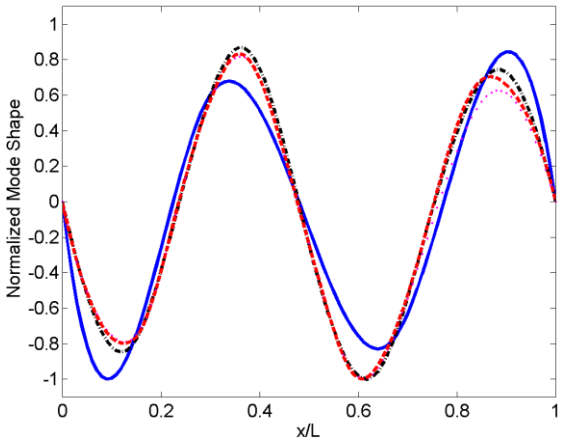

(d) Mode 4

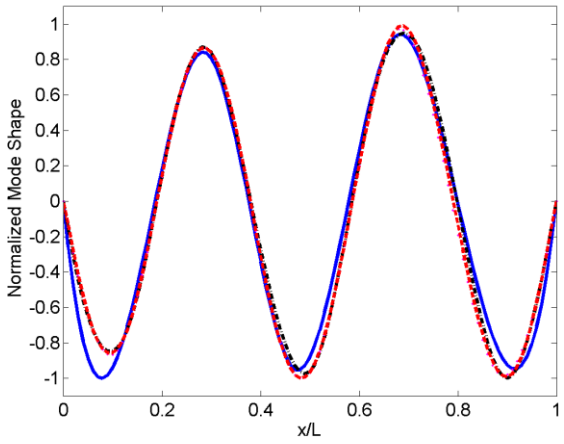

(e) Mode 5

Fig. 3.66 Continued.

The damage detection results using best available 5, 10, 15 and 20 sensors with marine growth of 5, 10, 15 and 20 cm are listed in Fig. 3.67 to 3.70. Damage indices computed with 5 sensors failed to detect the damage at all the four levels of marine growth. When the number increased to 10, it seemed that the damage indices with the least severe marine growth of 5 cm detect some damage but the location was incorrect and thus considered a failure. With 15 sensors, the damage indices at marine growth of 5 cm successfully detected the damage though the location was slightly off to the right. The damage indices were not able to detect damage for cases of severe marine growth.

With 20 sensors, the damage indices correctly detected and located the damage between 29.2 ~ 31.1 m at 5 cm marine growth, and seemed to detect the damage at 10 cm marine growth even though two other damage index peaks were also present to the left and right of the damaged area. The methodology failed to detect damage at marine growth with 15 and 20 cm of thicknesses. Specifically in this situation, damage index method was shown to work well with large number of sensors, 99 in this case, but its performance declined with fewer sensors though the mode shapes evaluated were in good qualities with optimal sensors arrays achieved with multi-objective genetic algorithms. In the framework of sensor optimization, the damage analysis using modal parameters posed more challenges on the sensor array selections due to higher requirements, which indicated more sensors should be used in the damage detection situation.

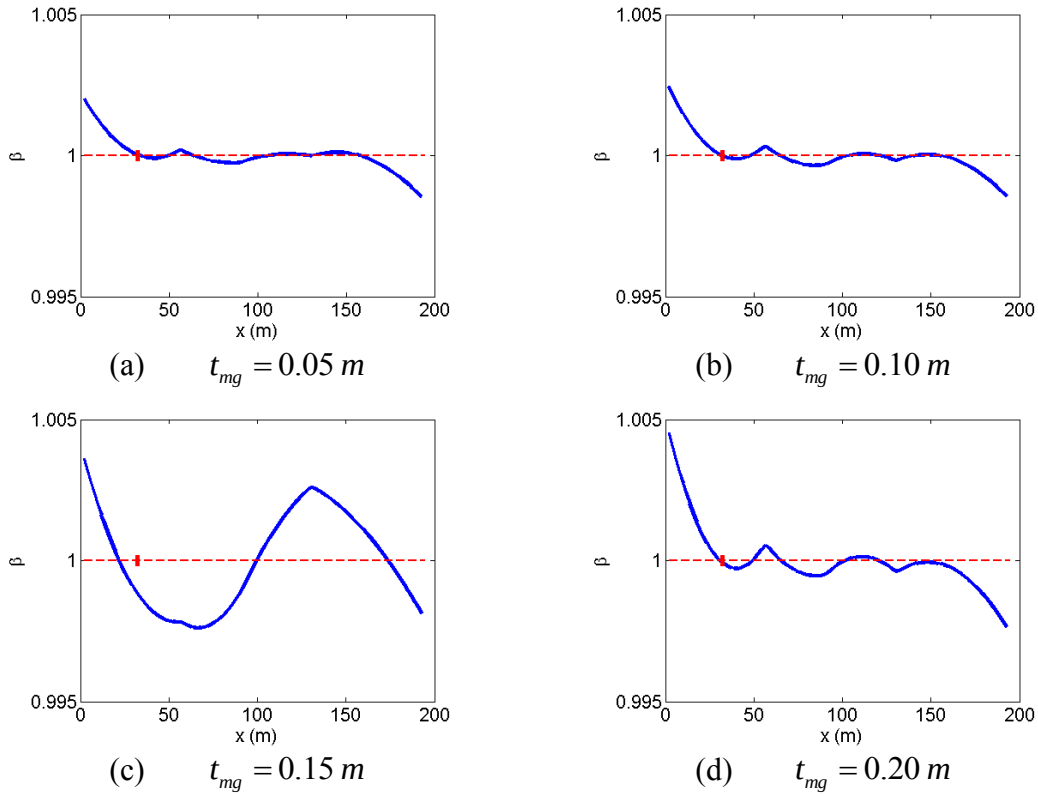

(a) $t_{mg} = 0.05\ m$ (b) $t_{mg} = 0.10\ m$

(c) $t_{mg} = 0.15\ m$ (d) $t_{mg} = 0.20\ m$

Fig. 3.67 Damage indices using the best available 5 sensors.

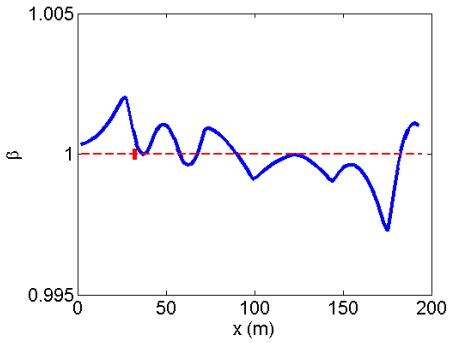

(a) $t_{mg} = 0.05\ m$

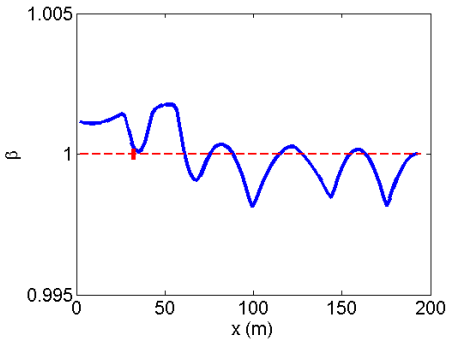

(b) $t_{mg} = 0.10\ m$

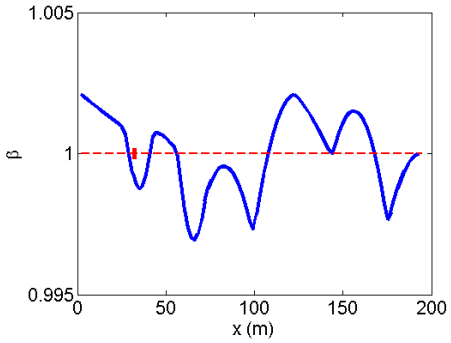

(c) $t_{mg} = 0.15\ m$

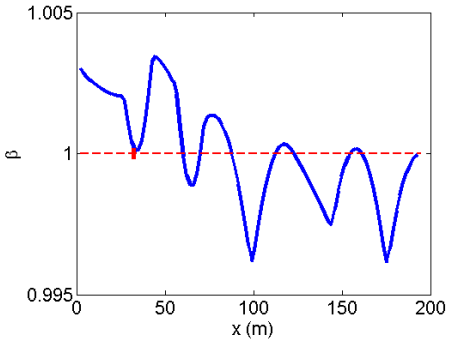

(d) $t_{mg} = 0.20\ m$

Fig. 3.68 Damage indices using the best available 10 sensors.

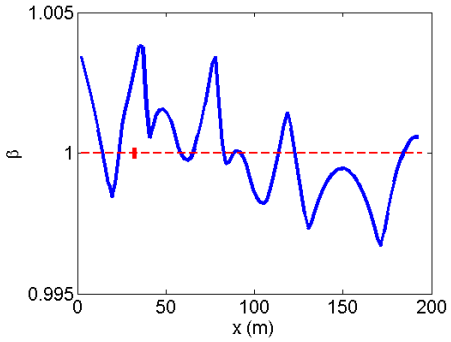

(a) $t_{mg} = 0.05\ m$

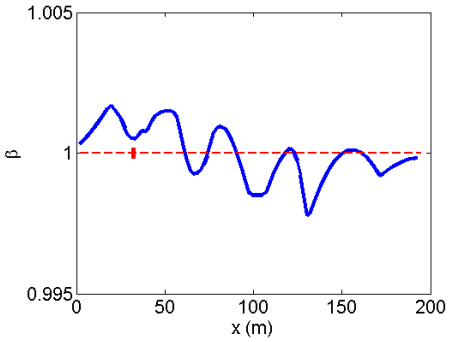

(b) $t_{mg} = 0.10\ m$

Fig. 3.69 Damage indices using the best available 15 sensors.

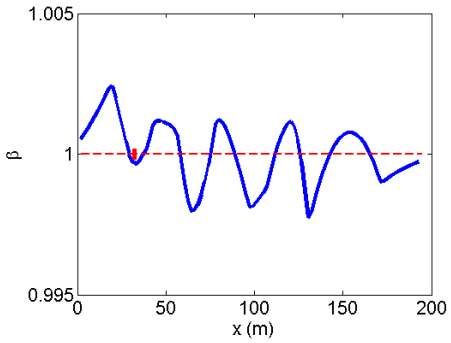

(c) $t_{mg} = 0.15\ m$

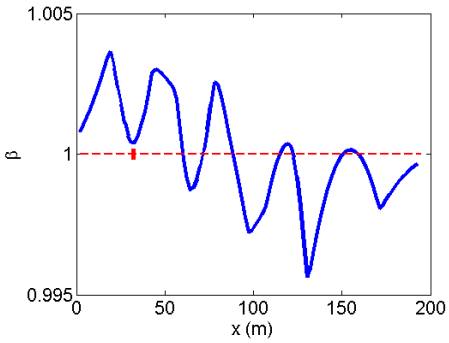

(d) $t_{mg} = 0.20\ m$

Fig. 3.69 Continued.

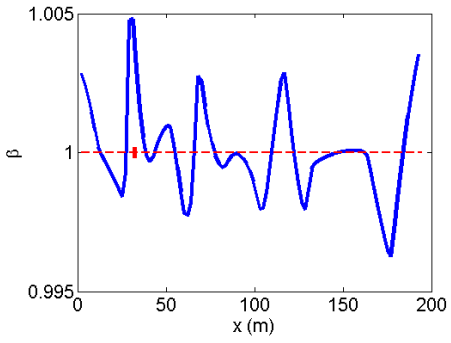

(a) $t_{mg} = 0.05\ m$

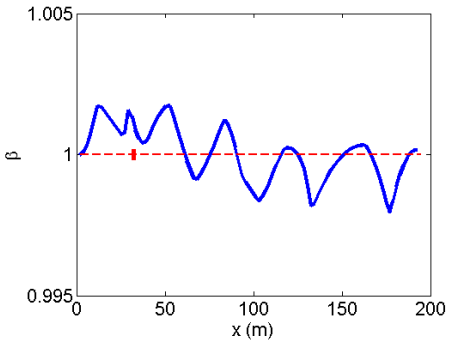

(b) $t_{mg} = 0.10\ m$

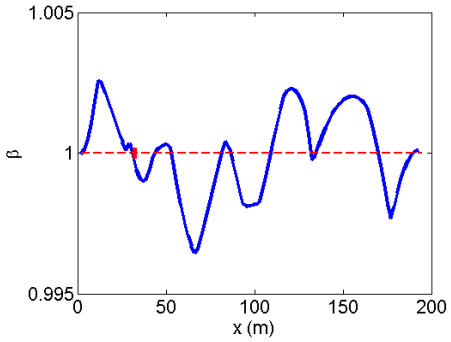

(c) $t_{mg} = 0.15\ m$

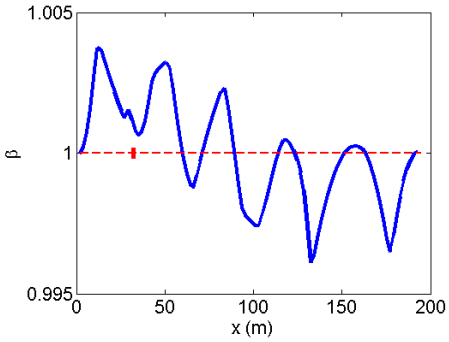

(d) $t_{mg} = 0.20\ m$

Fig. 3.70 Damage indices using the best available 20 sensors.

A statistical analysis was conducted using the normalized damage indicator $Z(j)$ for the j[th] element (Stubbs, Kim and Farrar 1995), as shown below:

$$Z(j) = \frac{\beta(j) - \mu_\beta}{\sigma_\beta} \tag{3.6}$$

where μ_β and σ_β are the mean and standard deviation of the damage index along the structure. The normalized damage indicators for the least severe case, marine growth = 0.05 m, at sensor number = 5, 10, 15 and 20, are presented in Fig. 3.71. Note the normalization used for the statistical analysis is different than the previous normalization presented in Table 3.24 and Fig. 3.53 which was conducted in order to compare DIM1 and DIM2.

As suggested by Stubbs, Kim and Farrar (1995), hypothesis testing was adopted to classify damage. Set up a threshold value Z_K for the normalized damage index Z. If $Z < Z_K$, choose the null hypothesis H_0 which rejects the identification of damage; otherwise, choose the alternative hypothesis H_1 which identifies the damage. The threshold value in this study was determined as 2.2. As the result of the hypothesis testing, the damaged area was located at 0 ~ 9.7 m with data collected from 5 sensors, at 27.2 m with data collected from 10 sensors, 35 ~ 37 m with data collected from 15 sensors, and 29.2 ~ 31.1 m with data collected from 20 sensors. Considering the actual location was assigned at 31.1 ~ 33.1 m, the analysis with 20 sensors generally identified and located the damage; the analysis with 10 and 15 sensors identified and located with offsets the damage; and the analysis with 5 sensors failed the damage detection.

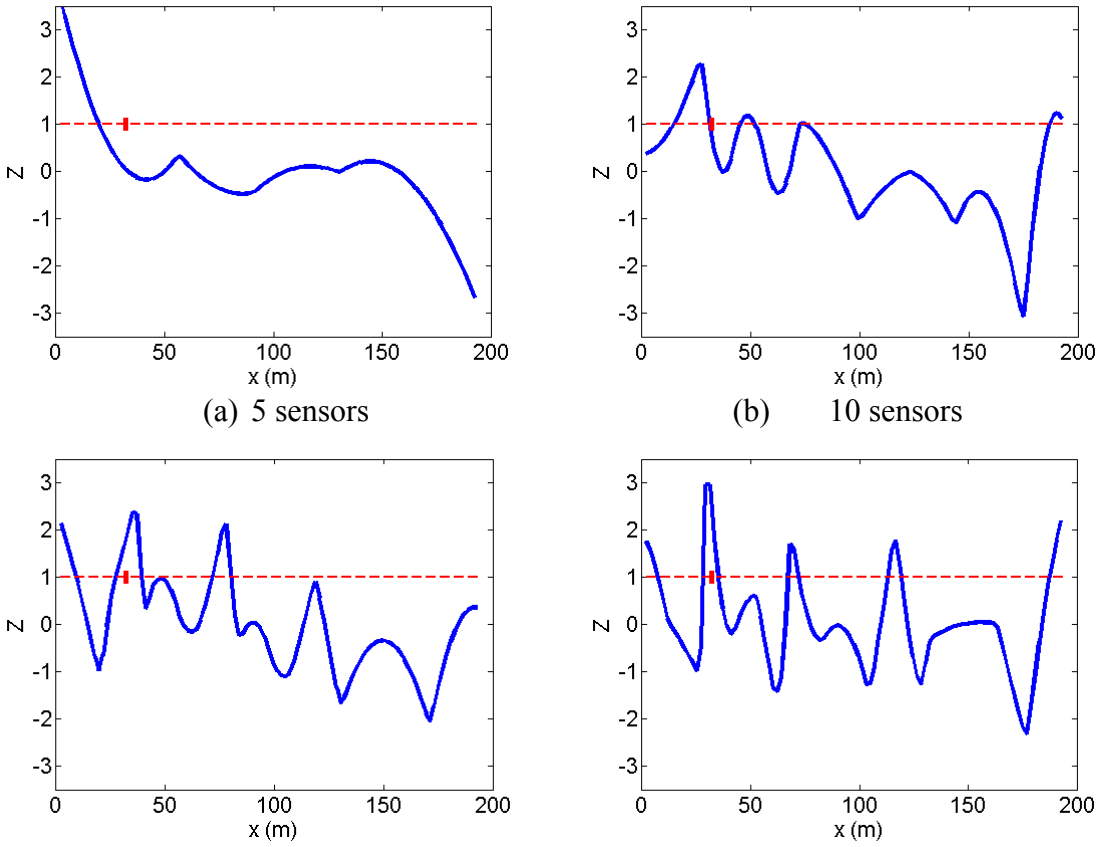

(a) 5 sensors (b) 10 sensors

(c) 15 sensors (d) 20 sensors

Fig. 3.71 Normalized damage indices with 0.05 m marine growth using various numbers of sensors.

4. STRENGTH ANALYSIS OF SELECTED ICE SHEET FORMATIONS

The exploration and production activities in arctic regions for hydrocarbon resources require an in-depth understanding of the strength properties of sea ice. Sea ice can be very complicated and its physical properties are affected by multiple factors that include temperature, brine volume, age, pressure, etc. In addition, sea ice can be categorized by its geometric features as iceberg and pack ice. For an offshore platform operating in Arctic waters, the aged moving pack ices with various ridges are of particular risk and sometimes are capable of exerting enormous damage. The magnitude of sea ice and its threat can be explained by the following example of a drillship Kulluk, which was in service and operated by Gulf Canada Resources Ltd at the Akpak locations in the Canadian Beaufort Sea in 1983-1986. The square shaped drillship Kulluk shown in Fig. 4.1 has general dimensions of 80 m which is comparable to the size of a football field. On June 16, 1985, an ice floe with a size of 14 km was observed moving towards the drillship. With the help of a fleet of ice breakers, the drillship initially managed to break through the large ice floe but immediately called for an emergency disconnection due to the sharp turn of the ice floe, resulting in loss of the well (Fardy, 1985).

Fig. 4.1 The drillship Kulluk facing vast pack ice (MXAK, 2013).

The veteran drillship Kulluk is now in service for Shell Oil Company in the exploration of Chukchi Sea of US waters after a long period of waiting of two decades since the offshore activities were halted due to the oil crisis in the late 1980s. However, the same threats from sea ice described above still exist. It is of importance to adequately understand ice strength and conduct efficient ice management, for example to break the dangerous large pack ice at its weak spots before it makes contact with the offshore facility.

Vibration based strength analysis of sea ice with data collected from sensor arrays can be a good alternative approach to traditional methods for its convenience and economic incentives. Traditionally the mechanical properties of sea ice are measured in field surveys. Samples of sea ice are drilled and extracted. Compression strength, bending strength and other properties are measured with specific equipment as shown in Fig. 4.2 (Palmer and Croasdale, 2012). Sometimes, underwater ADCP and ice profilers are deployed on the seabed to collect the velocity and thickness profile data, as shown in Fig. 4.3 (Fissel, Marko and Melling, 2008). The surveys are time-consuming and measurement stations are generally expensive. By contrast, vibration based strength analysis of sea ice uses sensor arrays to collect displacement or acceleration information and conduct modal analysis. Damage detection techniques originally developed for civil structures from changes in modal behavior can be utilized to study the strength distribution of the ice sheet.

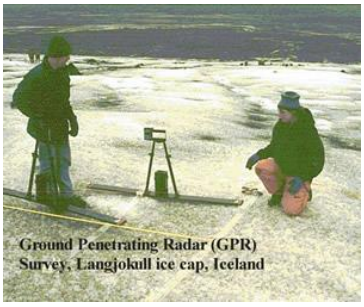

Source: UCL, 2013

Source: NOAA, 2013

Fig. 4.2 Ice survey using a variety of site specific equipment (Palmer and Croasdale, 2012).

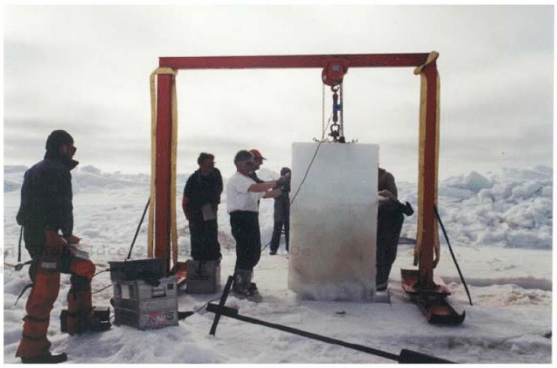

Apparatus used for load test of the ice rubble below – Sakhalin Island 1997, 1998 (KRCA)

Thermal drill (KRCA)

Direct shear test (KRCA)

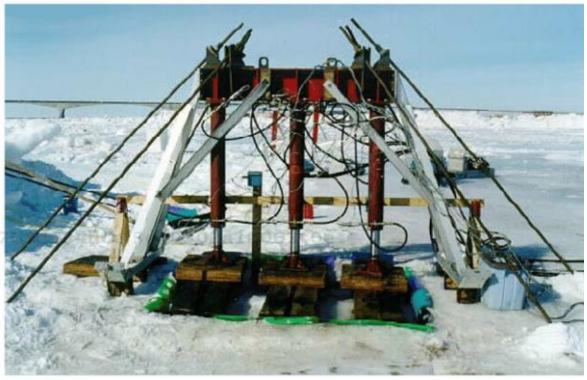

Punch shear test apparatus used in Canada in 1998 (KRCA)

Fig. 4.2 Continued.

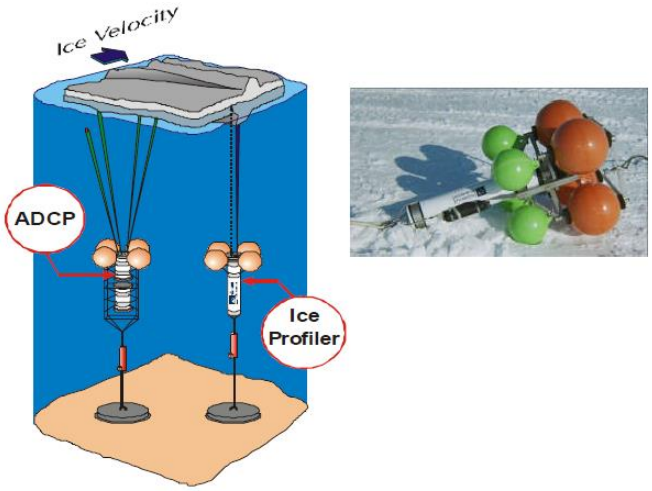

Fig. 4.3 ADCP and ice profiler deployed at seabed (Fissel, Marko and Melling, 2008).

Though promising, the development of vibration based strength analysis of sea ice needs to resolve the following challenges. First, the approach must address the complexity of sea ice features. Compared with typical materials such as steel or concrete, sea ice is not uniform but typically anisotropic and laminar. In addition, the ice sheets of the same age and area are roughly uniform, but can contain many strengthened regions such as ridges, and many weakened regions such as loosely compiled rubbles under the ice sheet and brine induced water ponds on the surface. The shapes of sea ice can be elliptical or in general irregular. Second, the modal parameter estimation technique, time domain decomposition method, utilized in Chapter 3 for beam-like structures will be extended to work for plate-like structures such as an ice sheet. Moreover, the optimization of sensor arrays will be more difficult since the computational volume increases exponentially. Finally, when searching for weakness of a given ice sheet, the damage detection technique Damage Index Method will need to study the effect of buoyancy provided by additional stiffness and the influence of ice sheet shapes. This chapter will focus on the challenges of modal recognition, sensor optimization and damage detection in the development of vibration-based strength analysis for selected sea ice formations.

4.1 A Sea Ice Numerical Model

The focus of this work is to build an approximate ice plate numerical model which takes into account the depth dependent mechanical properties of ice, such as salinity, brine volume, Young‟s modulus and Poisson ratio.

The mechanical properties of sea ice in the Arctic and sub-Artic regions may vary significantly according to its depth. For a typical first year ice plate with a thickness of 2 m, the temperature on the top of the ice can be as low as -30 ^{o}C due to the cold air, and drops rapidly to -2 ^{o}C at the bottom. Fig. 4.4 shows an ice plate example, with salinity, brine volume, Young‟s modulus and Poisson ratio varying with depth. Eq. 1.1, 1.4, 1.6 and 1.7 (Frankenstein and Garner, 1967, ISO 19906, 2010, Weeks and Assur, 1967) were used to calculate the mechanical properties.

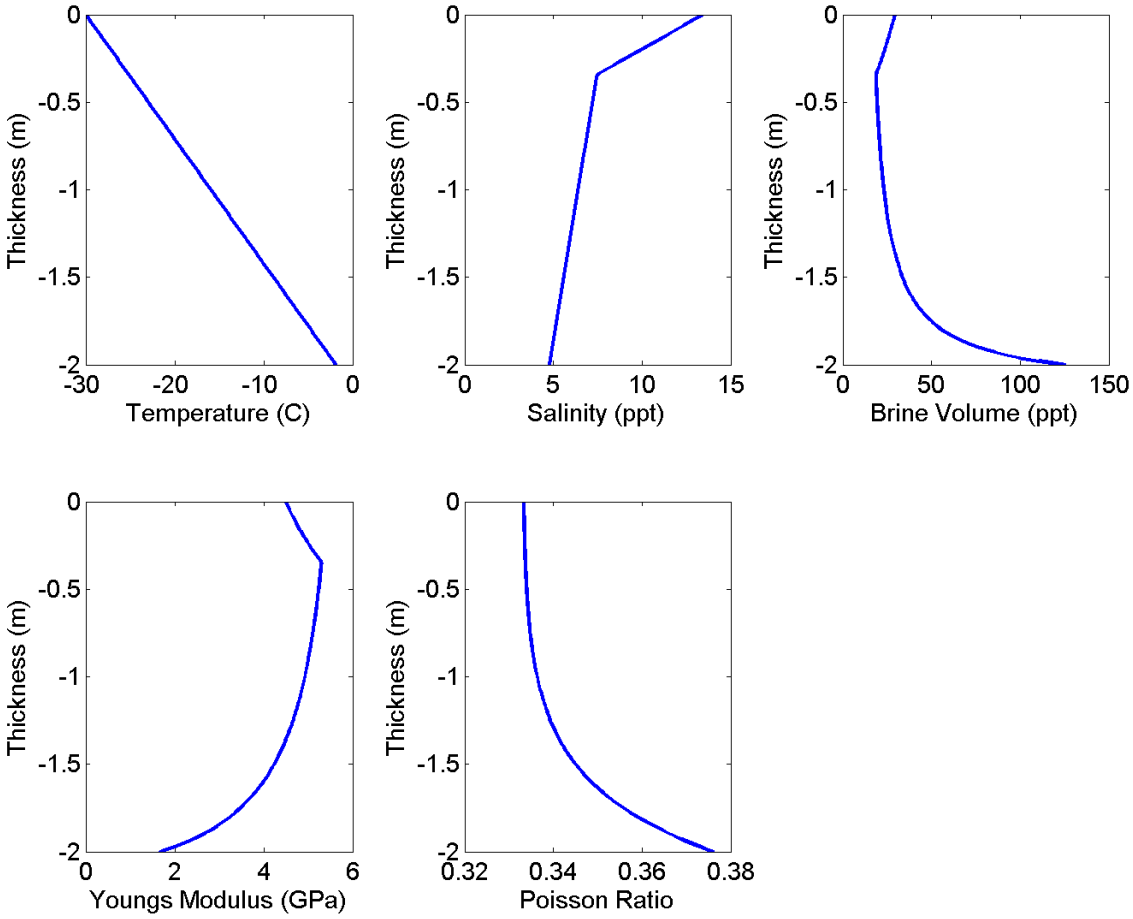

Fig. 4.4 Depth profiles of ice sheet mechanical properties.

A laminar ice sheet with a size of 40 m by 20 m and a depth of 2 m was built in the finite element code Abaqus using composite material. The ice sheet was divided to 10 layers with each layer assigned proper a Young‟s modulus and Poisson ratio according to the property profile illustrated in Fig. 4.4. The specific values are presented in Table 4.1.

Floating ice sheets in Arctic waters generally can have fixed or free boundary conditions depending on the local situation. The boundary conditions in this illustrative case were fixed at all four edges.

Table 4.1 Young's modulus and Poisson ratio of the laminar ice sheet.

Layer	Depth m	Young's modulus GPa	Poisson ratio
1	-0.10	4.68	0.33
2	-0.30	5.17	0.33
3	-0.50	5.23	0.33
4	-0.70	5.13	0.33
5	-0.90	5.00	0.34
6	-1.10	4.82	0.34
7	-1.30	4.58	0.34
8	-1.50	4.22	0.35
9	-1.70	3.66	0.35
10	-1.90	2.62	0.37

The ice sheet was firstly constructed with linear shell element S4R and then with quadratic shell element S8R. All elements were rectangular shaped. Typical mode shapes extracted from the finite element ice sheet model are presented in Fig. 4.5. Two naming conventions for the 2-D mode shapes are used here. One convention is mode (m1, m2), where m1 is the 1-D mode number on the longer side and m2 is the 1-D mode number on the shorter side. The other convention is to name the mode according to the order of the natural frequencies from lower to higher modes. Both naming conventions will be used based on convenience and the actual condition under consideration.

The numerical convergence of the model was verified by gradually increasing the size of the mesh, from 32 to 3200. The natural frequencies for mode (1, 0), (2, 0) and (0, 1) are listed in Table 4.2. The results indicate that the quadratic shell element S8R performs better than the linear shell element S4R by converging faster with fewer mesh sizes. Models using the quadratic element numerically stabilized when the mesh size reached 800 while ones using the linear element obtained similar results using a very fine mesh with size of 204800, which is 256 times larger.

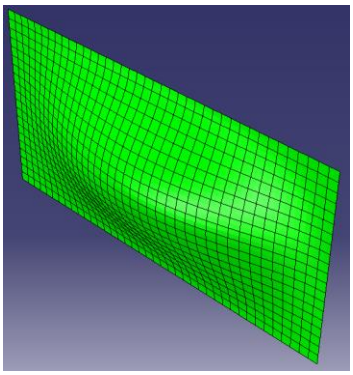

Mode (1, 1)

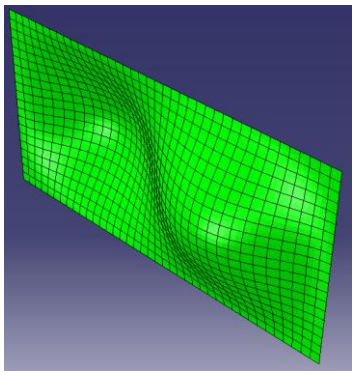

Mode (2, 1)

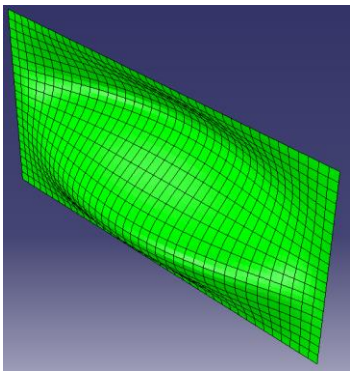

Mode (1, 2)

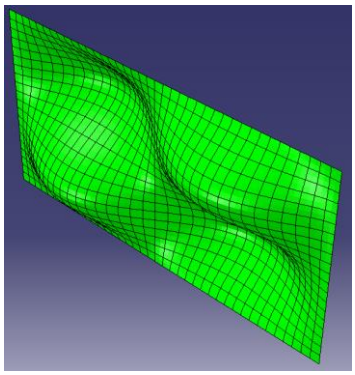

Mode (2, 2)

Fig. 4.5 Selected modes of the fixed-fixed ice plate.

Table 4.2 Natural frequencies of the free-free ice sheet with increased mesh sizes.

Element Type	Mesh Size	Mode (1, 1) (Hz)	Mode (2, 1) (Hz)	Mode (1, 2) (Hz)	Mode (2, 2) (Hz)
S4R	32	13.750	16.811	44.982	49.902
S4R	50	13.035	16.387	37.767	39.976
S4R	200	12.068	15.338	29.856	33.108
S4R	800	11.866	15.151	29.040	31.841
S4R	3200	11.817	15.105	28.699	31.540
S4R	12800	11.805	15.904	28.614	31.466
S4R	51200	11.801	15.901	28.593	31.447
S4R	204800	11.801	15.090	28.588	31.442
S8R	32	11.836	15.133	29.209	32.048
S8R	50	11.814	15.103	28.840	31.673
S8R	200	11.801	15.091	28.603	31.455
S8R	800	11.801	15.090	28.587	31.442
S8R	3200	11.801	15.090	28.587	31.442

Note the flexural rigidity of a plate considering a constant Poisson ratio is defined as:

$$D = \frac{1}{1-\upsilon^2}\int_{z_0-h}^{z_0} E(z)\, z^2\, dz \tag{4.1}$$

where, z_0 is the neutral axis, h is the ice thickness, υ is the Poisson ratio and $E(z)$ is the Young‟s modulus at coordinate z.

When Young‟s modulus is constant and neutral axis is in the middle, the flexural rigidity of the plate is:

$$D = \frac{1}{1-\upsilon^2}\int_{-0.5h}^{0.5h} E\, z^2\, dz = \frac{1}{1-\upsilon^2}\frac{h^3}{12}E \tag{4.2}$$

For cases where Young‟s modulus varies with depth of ice and assuming the neutral axis is similar to that of a uniform plate, which is in the middle of the plate, an Equivalent Young‟s modulus can be computed via

$$E_{equivalent} = \frac{\int_{z_0-h}^{z_0} E(z)\, z^2\, dz}{h^3/12} \tag{4.3}$$

Using Eq. 4.3, the equivalent Young‟s modulus for the laminar ice sheet is 4.07 GPa.

4.2 Recovery of Modal Parameters with TDD Using Uniformly and Non-Uniformly Distributed Sensor Arrays

The Time Domain Decomposition (TDD) technique was extended from 1-D beam-like structures to accommodate the 2-D surface data. Both coarse and fine mesh ice models built with the quadratic shell element were used to illustrate the methodology as illustrated in Fig. 4.6. Response data, in the format of accelerations, were collected and fed into TDD as the input. The reason for using accelerations instead of strains is because for a plate-like structure, the strains have 6 components in total and they can all be derived from displacement or acceleration data associated with geometries. External loads were applied onto the ice plate to specifically excite mode (1, 1) and mode (2, 1) around frequencies of 11.7 Hz and 15.2 Hz respectively. The methodology was firstly

applied to the coarse mesh data for the convenience of simplicity then to the fine mesh data.

Each node of the finite element ice plate model was considered as a sensor collecting acceleration data. Because of the regular rectangular mesh, the full sensor sets for both coarse and fine mesh are uniformly distributed. Non-uniformly distributed sensor arrays were created by selecting certain sensors from the total set.

The acceleration time histories and power spectral densities at selected nodes are presented in Fig. 4.7. The beginning part was truncated and only stabilized steady-state data were used for analysis. Using accelerations collected from the full sensor set, the response envelopes can be obtained for the coarse model, as shown in Fig. 4.8.

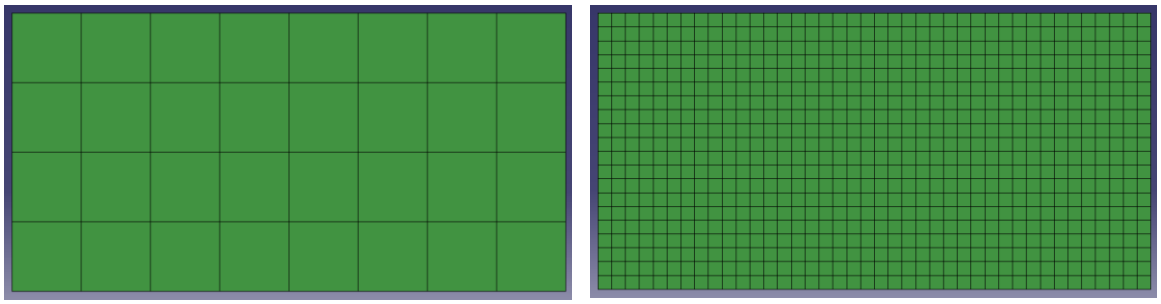

The coarse mesh, 4 by 8 (32) The fine mesh, 20 by 40 (800)

Fig. 4.6 The ice plate models with the coarse and the fine mesh.

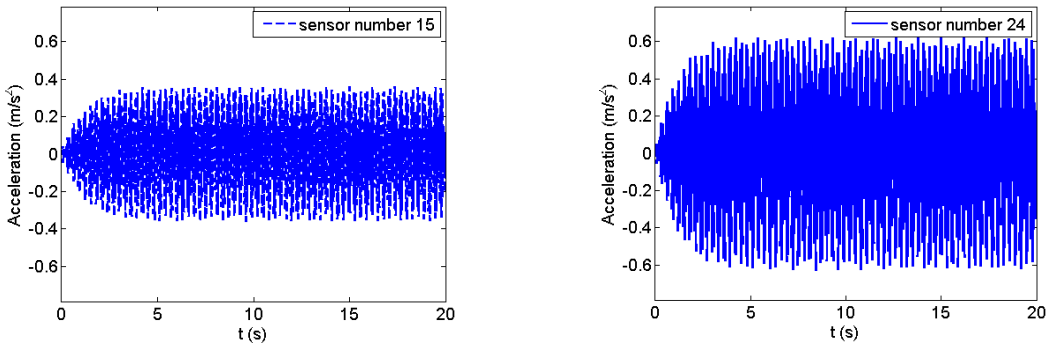

Fig. 4.7 Time Series and PSD at selected stations placed on the ice plate.

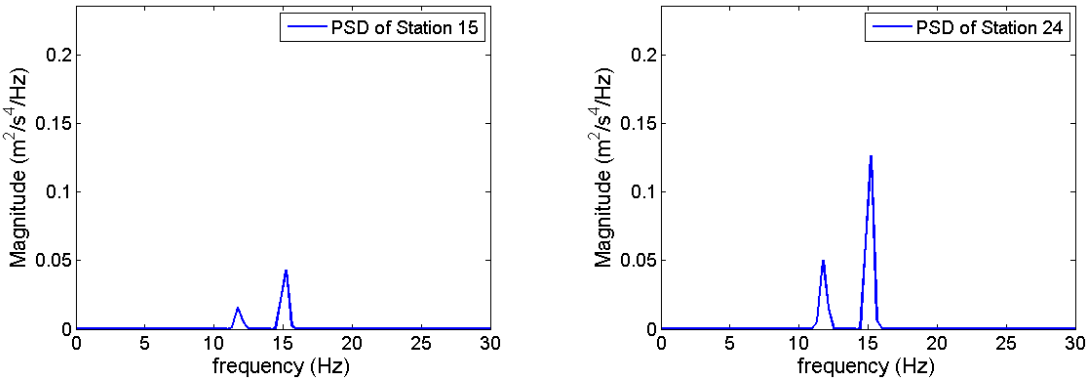

Fig. 4.7 Continued.

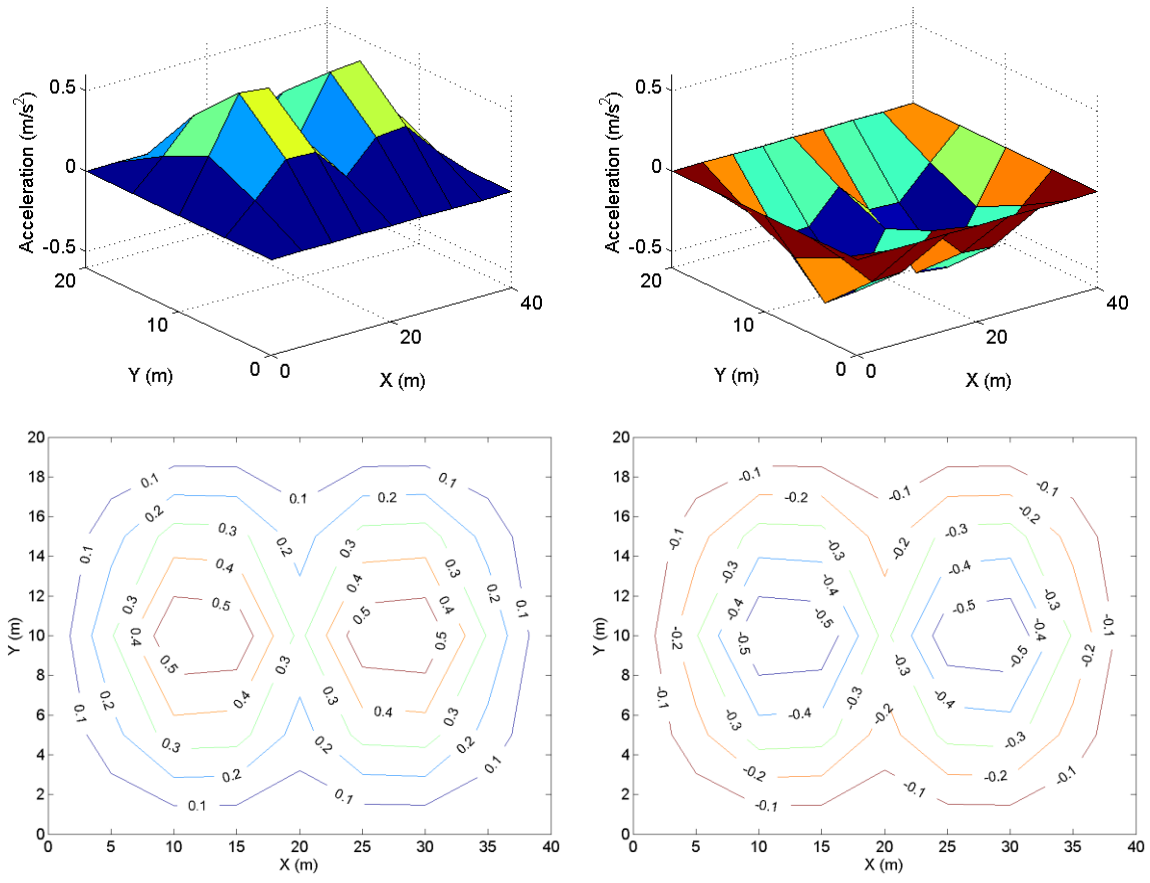

Max Min

Fig. 4.8 Response envelopes using the coarse model.

Mode shapes for mode (1, 1) and mode (2, 1) were computed with surface meshes and contours for better visualization.

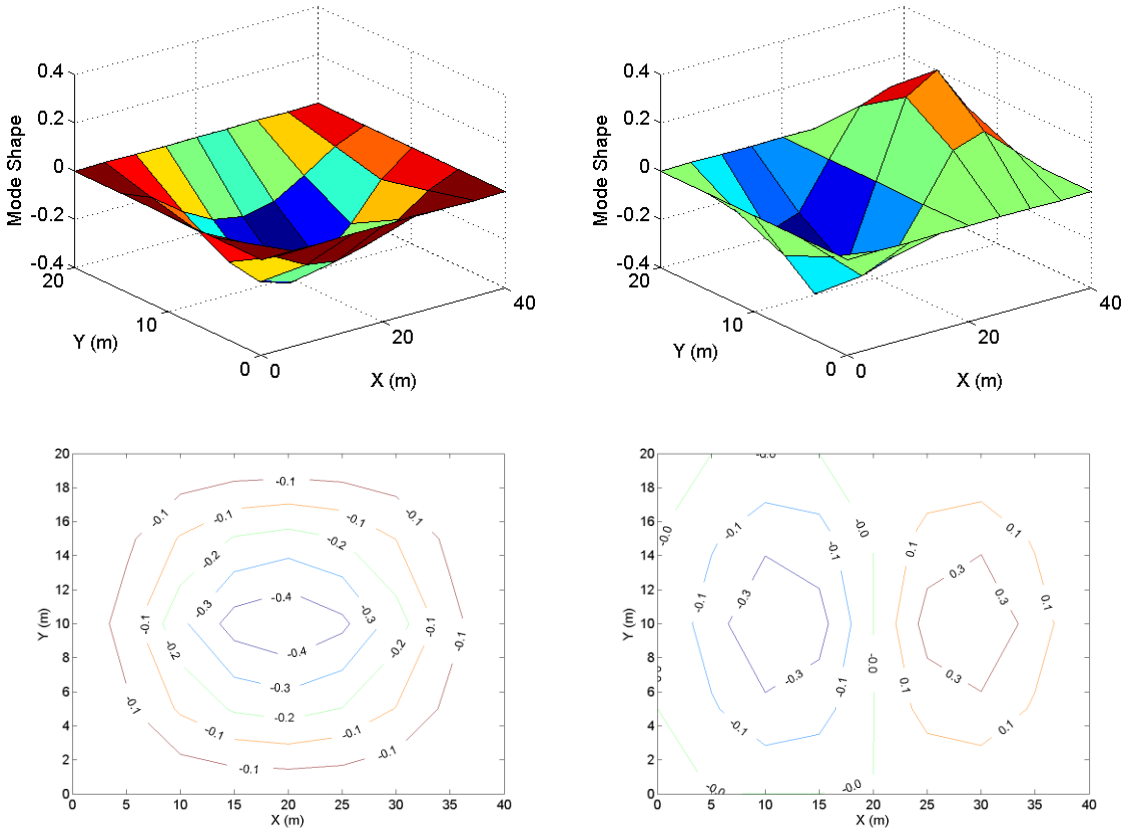

Fig. 4.9 Mode shapes for mode (1, 1) and (2, 1) using the coarse model.

The same procedure was applied to the fine mesh data set. The surface meshes and contours of response envelopes are presented in Fig. 4.10. The surface meshes and contours of mode (1, 1) and (2, 1) are presented in Fig. 4.11. The direct comparison between the coarse model and the fine model demonstrates that with sufficient sensors the estimation of response envelopes and mode shapes can both be greatly improved.

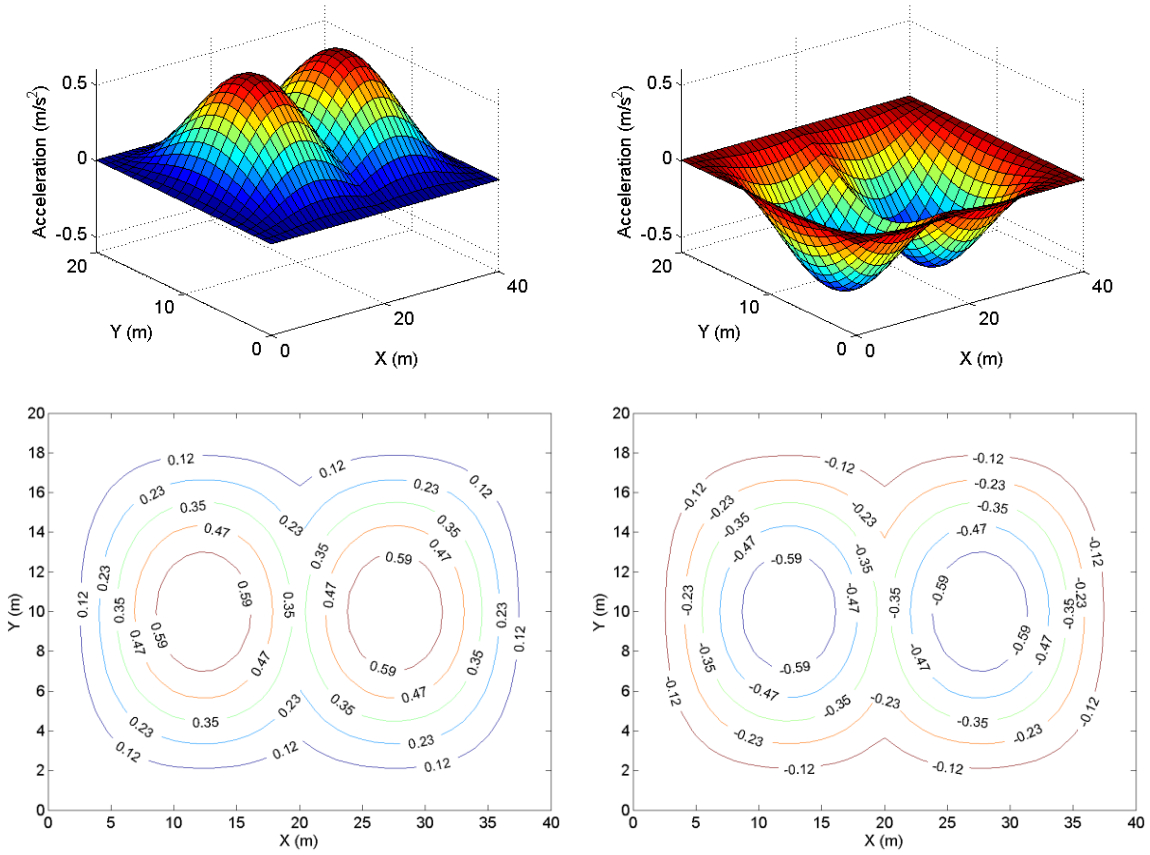

Max Min

Fig. 4.10 Response envelopes using the fine model.

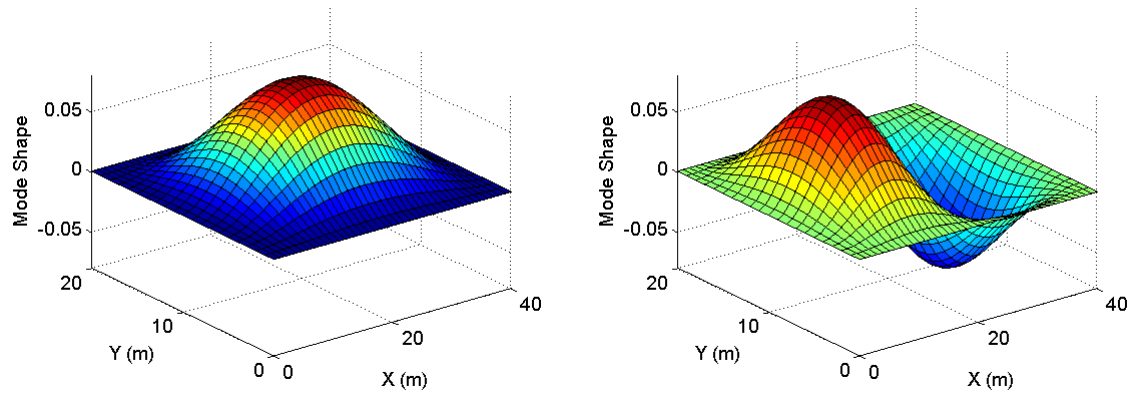

Fig. 4.11 Mode shapes for mode (1, 1) and (2, 1) using the fine model.

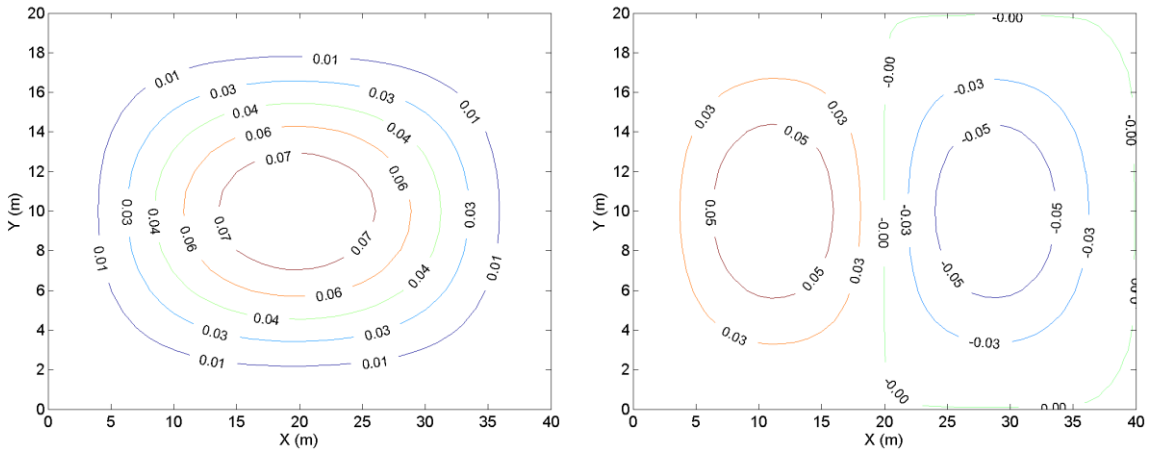

Fig. 4.11 Continued.

However, in the actual data collection, it is not common to have such a luxury of using dense and uniformly distributed sensor arrays. In most of the cases, the number of sensors is limited; the distribution of the sensor arrays can be non-uniform. It is of great interest to develop interpolation and curve fitting techniques to improve the quality of a given coarse data set.

Investigation into the performance of linear, spline, cubic 2-D interpolation methods and Matlab built in griddata technique indicate that spline fit and cubic fit perform better than the linear griddata technique when interpolating a finer dataset from the coarse 2-D data, as shown in Fig. 4.12. The normalized mode shape for mode (1, 1) was used for the investigation. Note in this interpolation procedure, the data distribution was always uniform. The interpolation for mode (2, 1) using either spline fit or cubic fit is also satisfactory as shown in Fig. 4.13. Modal Assurance Criteria (MAC) of the interpolated mode shapes with different methods was computed using the fine mesh model in order to quantify the difference between interpolation methods. The spline fit method performed slightly better than the cubic fit method.

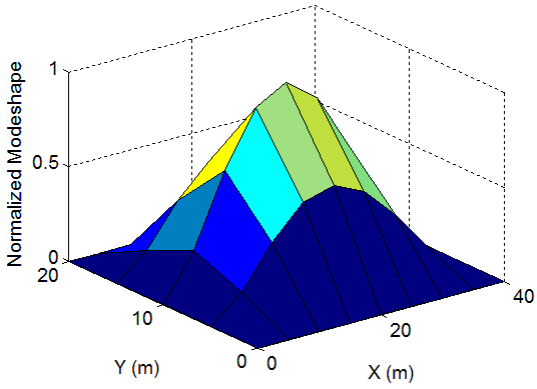

The original coarse mode shape

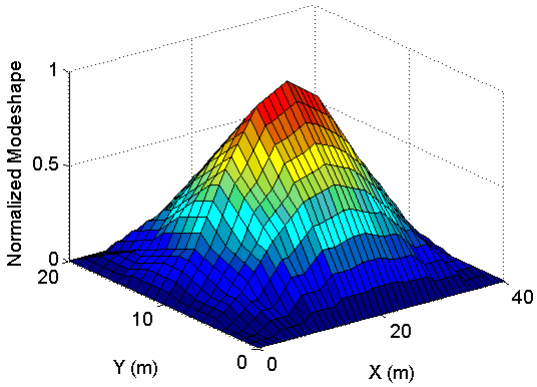

Using Matlab function: griddata (linear)

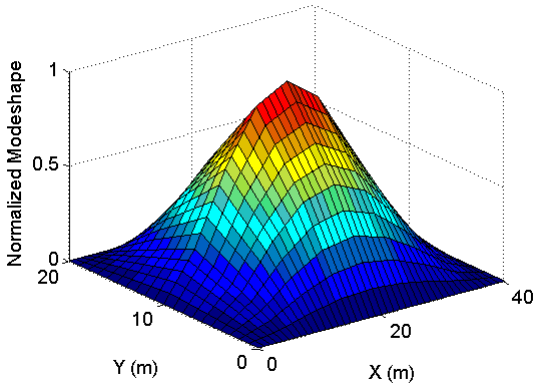

Linear fit

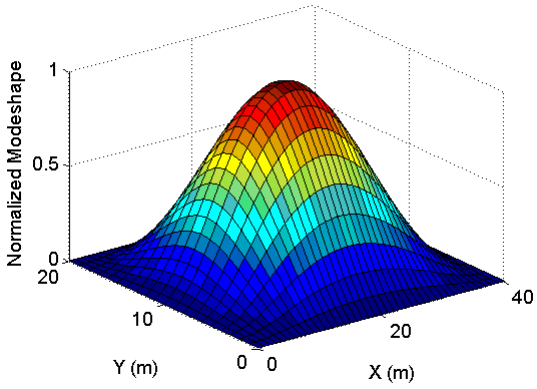

Spline fit

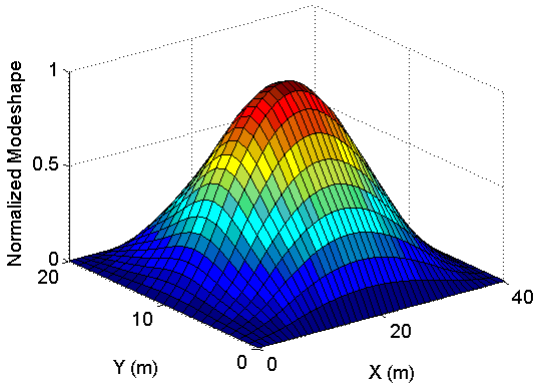

Cubic fit

Fig. 4.12 Interpolated mode shape with various fitting methods for mode (1, 1).

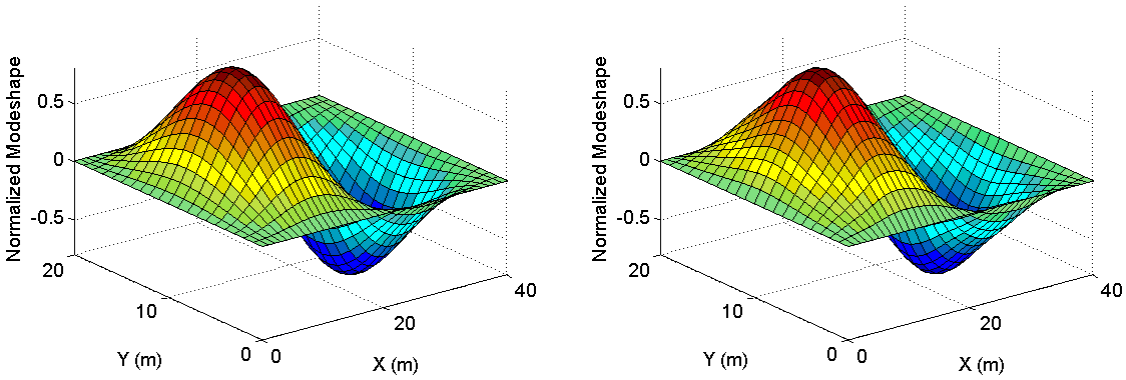

Spline fit Cubic fit

Fig. 4.13 Interpolated mode shape with spline and cubic fit for mode (2, 1).

Table 4.3 MAC of interpolated mode shapes.

Interpolation methods	MAC of mode (1, 1)	MAC of mode (2, 1)
Matlab griddata (linear)	0.9896	0.9831
Linear fit	0.9909	0.9888
Spline fit	0.9993	0.9988
Cubic fit	0.9927	0.9913

The implementation of non-uniformly distributed sensor arrays is of importance. As stated in previous discussion, spline fit works well when smoothing a uniformly distributed coarse data to a fine mesh; however the fitting method has problems when used to interpolate a non-uniformly distributed data set due to the lack of information. A three-step procedure is adopted to address this problem. First, TDD is applied to recover the non-uniform mode shape data; second, the non-uniform mode shape is interpolated to a uniformly distributed coarse mode shape; finally, the coarse mode shape is smoothed to a finer mode shape with spline fit method. The methodology is illustrated using four levels of coarse data as shown in Fig. 4.14 where the number of sensors increases from 3, to 5, 9 and 15.

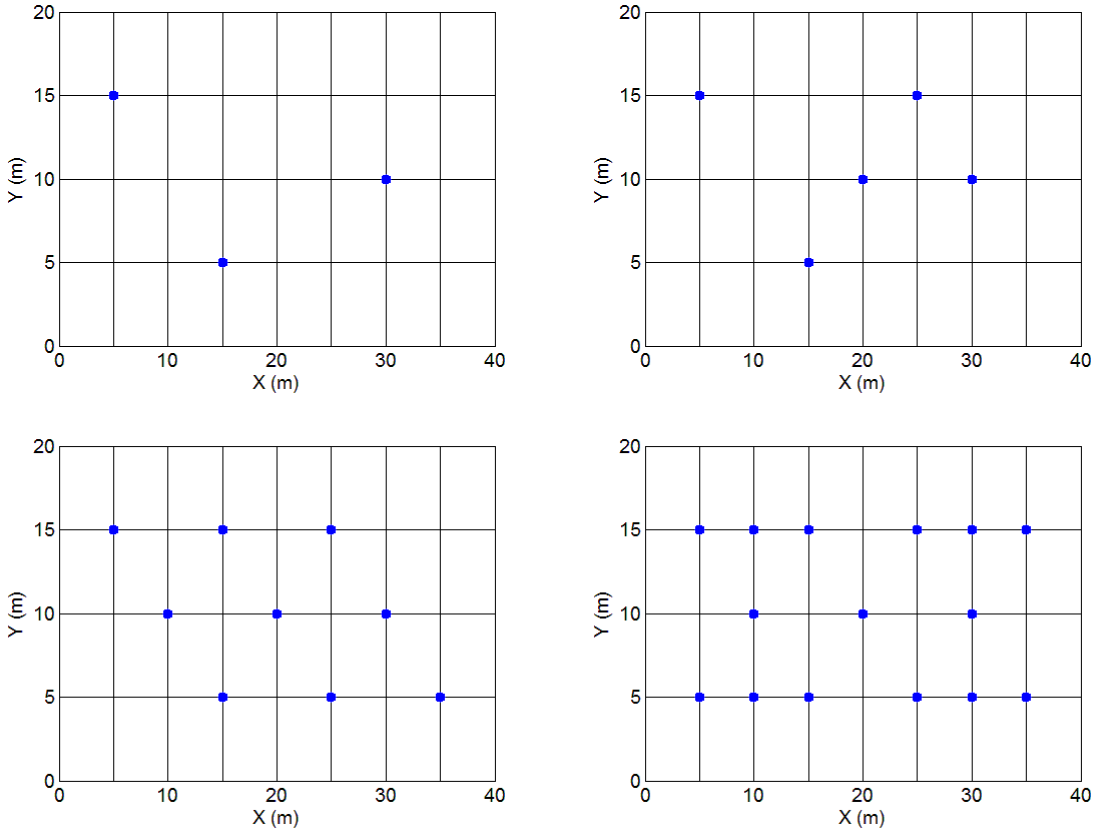

Fig. 4.14 Examples of non-uniformly distributed sensor arrays (in blue dots).

Linear, cubic interpolation and a Matlab developed „v4" interpolation technique were investigated in the second step to fit the non-uniform data to a uniformly distributed coarse data. Fig. 4.15, 4.16 and 4.17 present the results of mode (1, 1) recovery using linear, cubic and Matlab „v4" interpolation method for each test sensor array. Note that 3, 5, 9 and 15 non-uniform sensors were highlighted with solid dots and only measurements form the sensors were used in extracting the mode shape (1, 0). The fitted coarse mode shapes in blue meshes are presented on the bottom of each figure, on top of which overlay the spline fit smoothed fine mode shapes in red meshes. Generally the larger the number of the sensors used, the better recovery of the mode shape. Note that in the case of linear fit, the example with 15 sensors ended up with many unnecessary bumps indicating that redundant information can result in worse mode

shape recovery. Matlab „v4“ interpolation method performed the best among the three methods described here.

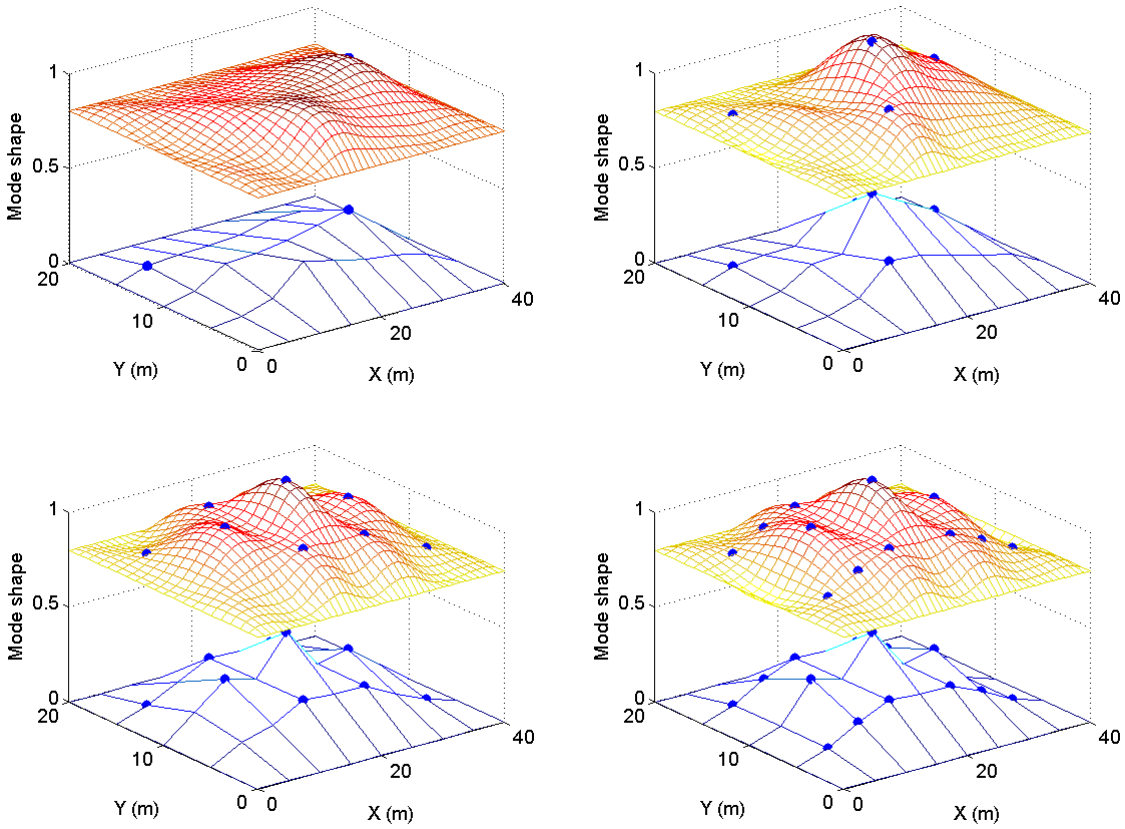

Fig. 4.15 Linear fit based on the coarse data.

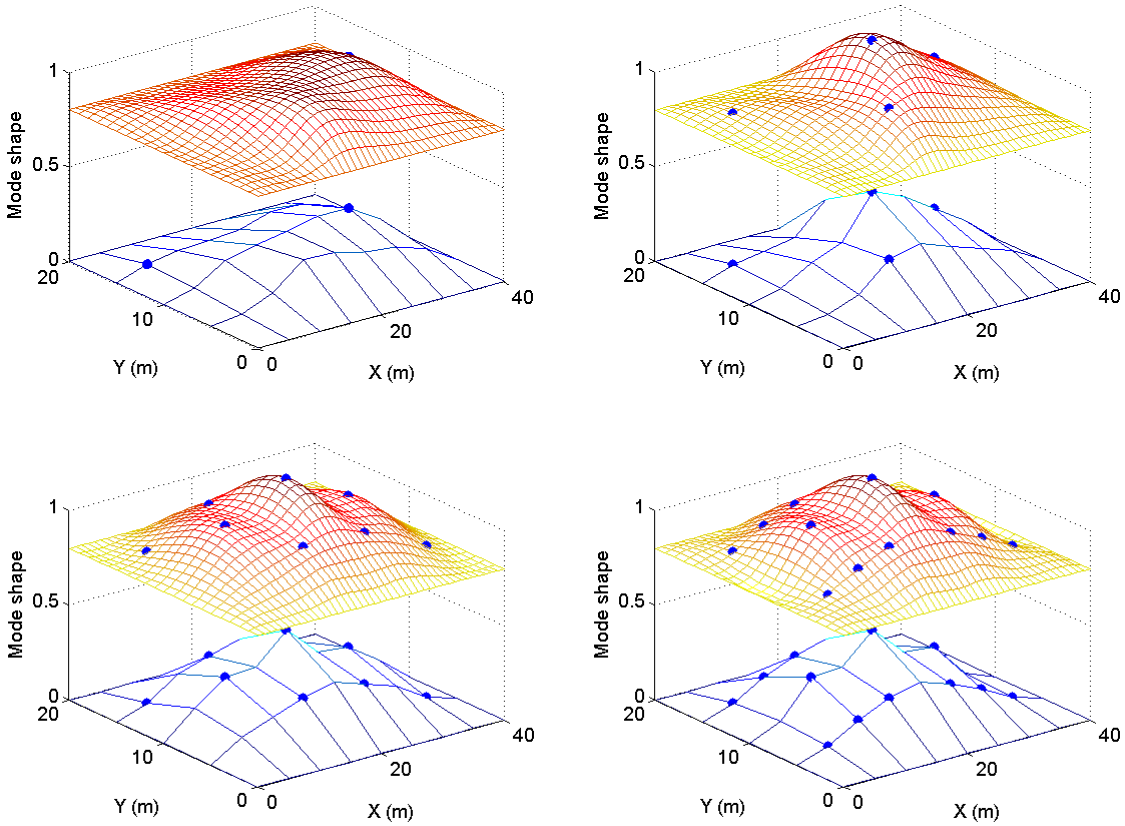

Fig. 4.16 Cubic fit based on the coarse data.

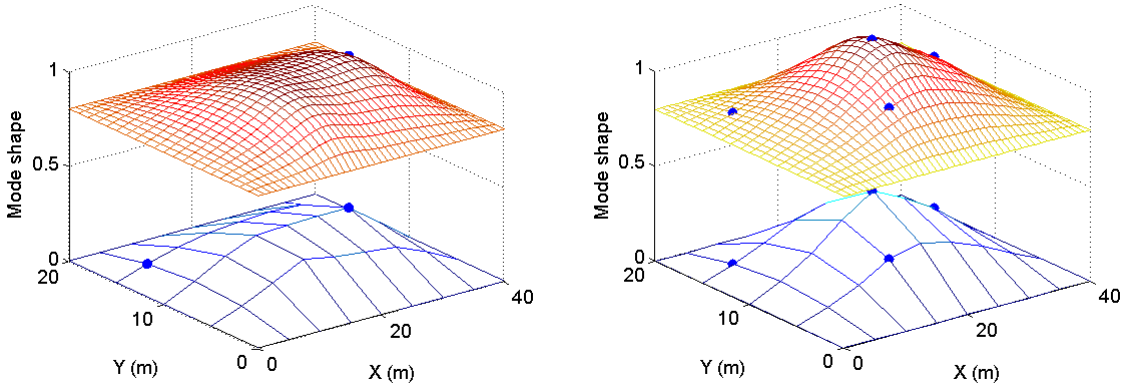

Fig. 4.17 Matlab „v4" fit based on the coarse data.

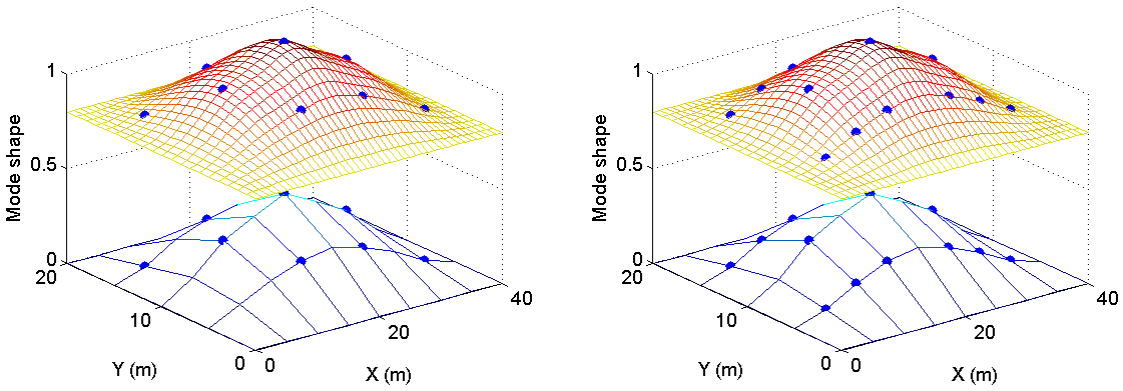

Fig. 4.17 Continued.

4.3 2-D Sensor Array Optimization with Genetic Algorithm

Prior to the discussion of sensor array optimization, the performances of two different sensor arrays with the same number of sensors were compared to illustrate the effect of sensor placement. Each sensor was named according to the nodal number in the finite element ice model and was labeled sequentially from bottom left to up right. In the case of the fine model with nodal numbers 21 and 41 on the short side and long side, each sensor had 741 spatial location possibilities after subtracting 120 nodal points on the four edges from 861 total nodal points. The configurations of the sensor arrays with 5 sensors are shown in Fig. 4.18 in which sensor array A was at [46 102 126 387 791] and sensor array B was at [257 359 472 542 687]. Note sensor array A was randomly selected and sensor array B was selected with engineering judgment. The recovered response envelopes and mode shapes for mode (1, 1) and mode (2, 1) using sensor array A are presented in Fig. 4.19. The recovered response envelopes and mode shapes for mode (1, 1) and mode (2, 1) using sensor array B are presented in Fig. 4.20. MACs of the two modes using sensor array A were 0.9588 and 0.1679, while using sensor array B were 0.9957 and 0.9905. The comparison indicates that even with the same number of sensors, the spatial placement of the sensors can greatly affect the quality of the response information recovered.

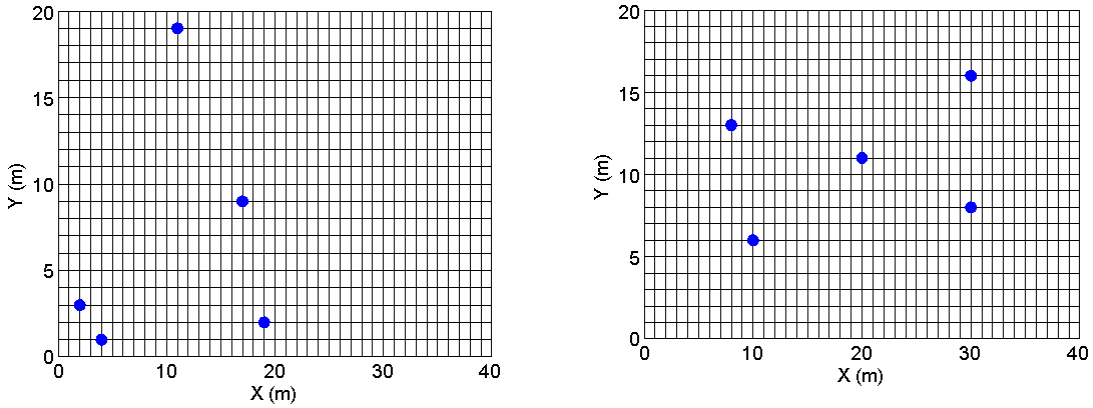

Fig. 4.18 Sensor array A (left) and B (right).

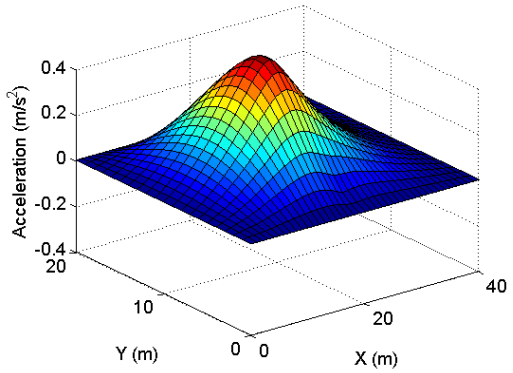

Max Envelope

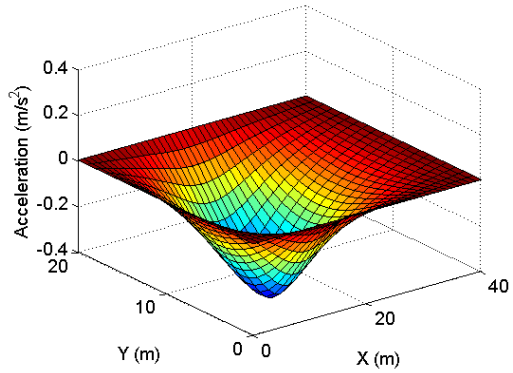

Min Envelope

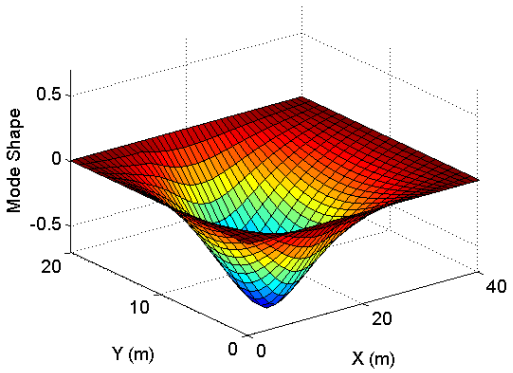

Recovered mode shape (1, 1)

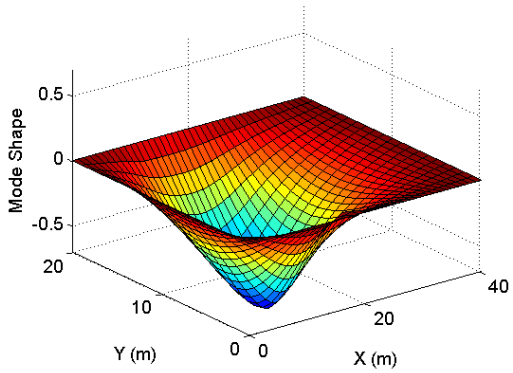

Recovered mode shape (2, 1)

Fig. 4.19 TDD using sensor array A.

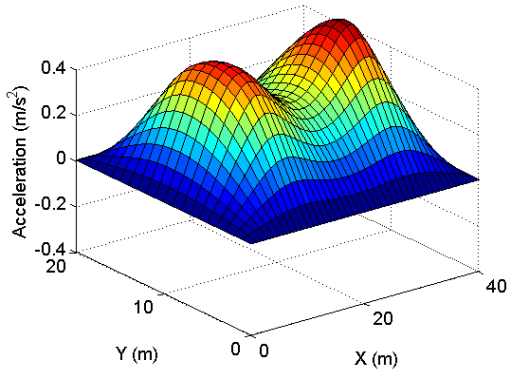

Max Envelope

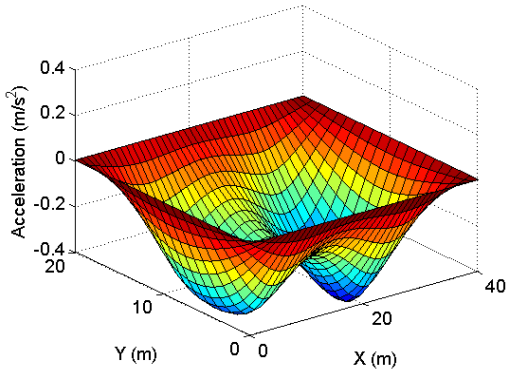

Min Envelope

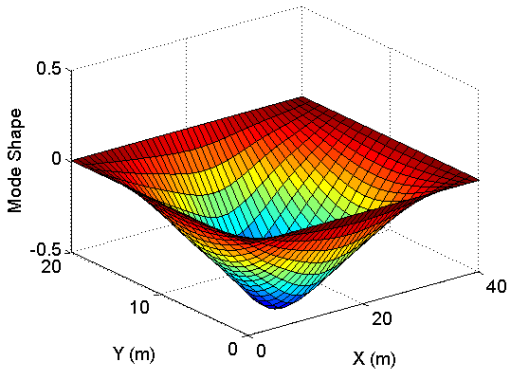

Recovered mode shape (1, 1)

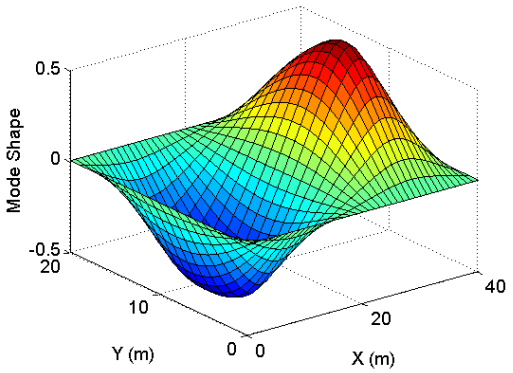

Recovered mode shape (2, 1)

Fig. 4.20 TDD using sensor array B.

The genetic algorithm is suitable for the problem of finding the optimal sensor array with a given number to best recover a specific mode. The optimization problem is nonlinear and involves massive computation considering each sensor has more than 700 possible positions deducting the edges. For example, the exhaustive search for 5 best sensors in the all the 741 possibility has to compute a number of cases up to $2.2*10^{14}$ (741*740*739*738*737). Remember in the previous chapter an exhaustive search of 4 sensors out of 25 possible positions computed $3.0*10^{5}$ cases using a relatively simple 1-D fitness function and the computation time was 4 hours. Assuming the computation of

the fitness function of the 2-D case occurs at the same speed, the exhaustive search for this case will take 33145 years.

The parameters of the genetic algorithm are presented in Table 4.4 after fine tuning and selecting appropriate parameter combinations using similar techniques utilized in Chapter 3. The computational load increased exponentially, due to a larger sensor array and lower selection probability, compared with a 1-D bean-like structure. It was harder to converge to the optimal solution hence the population size and generation number was determined to be sufficiently large. The fitness function was set to be a negative modal assurance criterion (MAC) using the finite element ice model to recover mode shapes.

Examples of optimized sensor array using the genetic algorithm with the goal of recovering the mode shape of mode (2, 1) are listed in Fig 4.21. The sensor array with 5 sensors had a scattered mean fitness values in every population while one with 50 sensors had a narrowed distribution. The best achievable MACs with increased number of sensor arrays are presented in Table 4.5. As the number of available sensors increases, the performance of the sensor array improves significantly. Another important observation is, when the number of available sensors is small, the performance variation of the population is large after some optimization work. When the number of available sensors is large, the performance variation is small. This phenomena means a relatively good sensor array with a small number of sensors is much harder to find in comparison to one with a large number. In other words, the probability of using a bad sensor array with small number of sensors is higher.

Table 4.4 Parameters used in the genetic algorithms.

Parameter	Value	Parameter	Value
Population size	50	Initial range	[1, 741]
Number of variable	5, 10, 30, 50	Elite count	4
Lower bound	1	Selection method	Tournament
Upper bound	741	Max generation	50
Crossover function	Scattered	Stall generation	30
Crossover rate	50%	Tolerance	1.0e-6

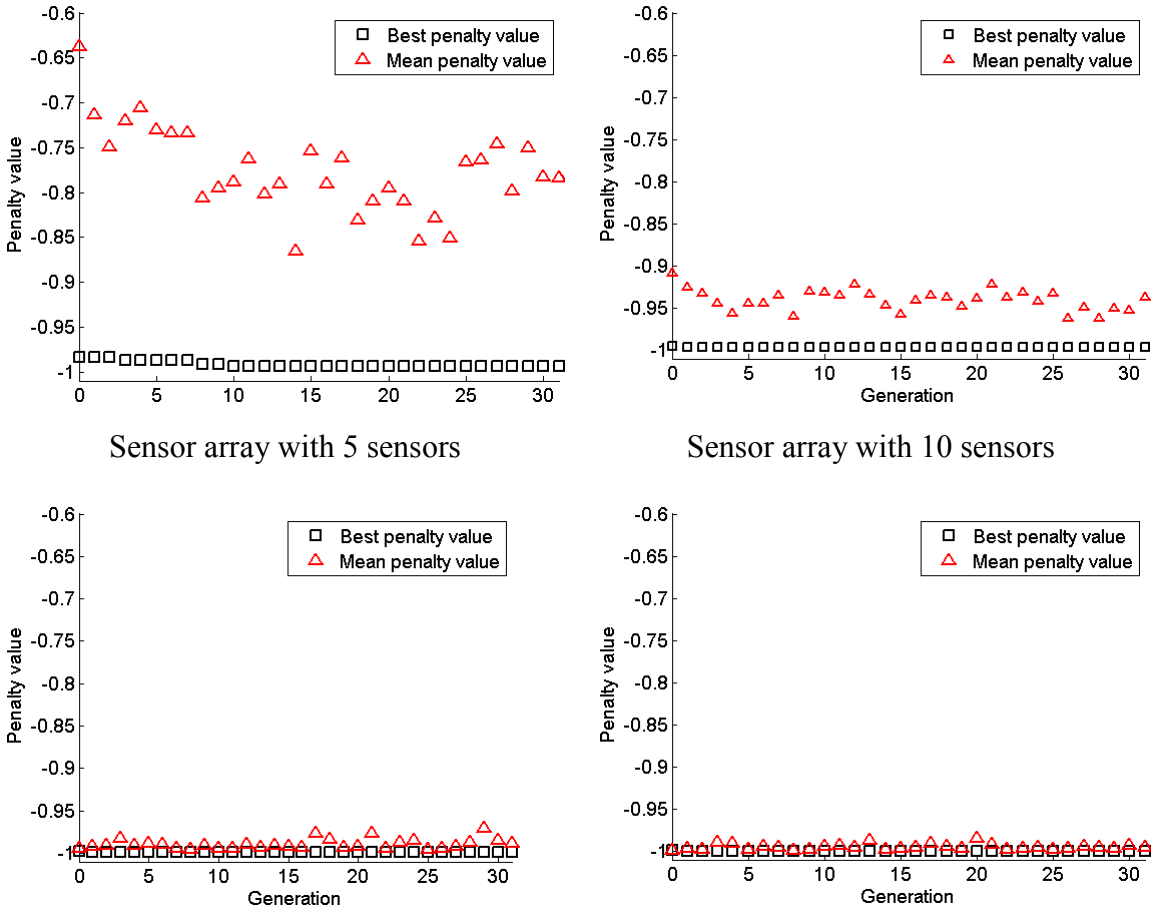

Sensor array with 5 sensors

Sensor array with 10 sensors

Sensor array with 30 sensors

Sensor array with 50 sensors

Fig. 4.21 Effect of generation size on convergence of the genetic algorithm.

Table 4.5 Best and mean MAC of optimized mode (2, 1).

Number of Optimal Sensor Arrays	Best MAC	Mean MAC
5 sensors	0.9934	0.7841
10 sensors	0.9964	0.9370
30 sensors	0.9989	0.9882
50 sensors	0.9995	0.9948

The best sensor placements for 5, 10, 30 and 50 sensor arrays are presented in Fig. 4.22.

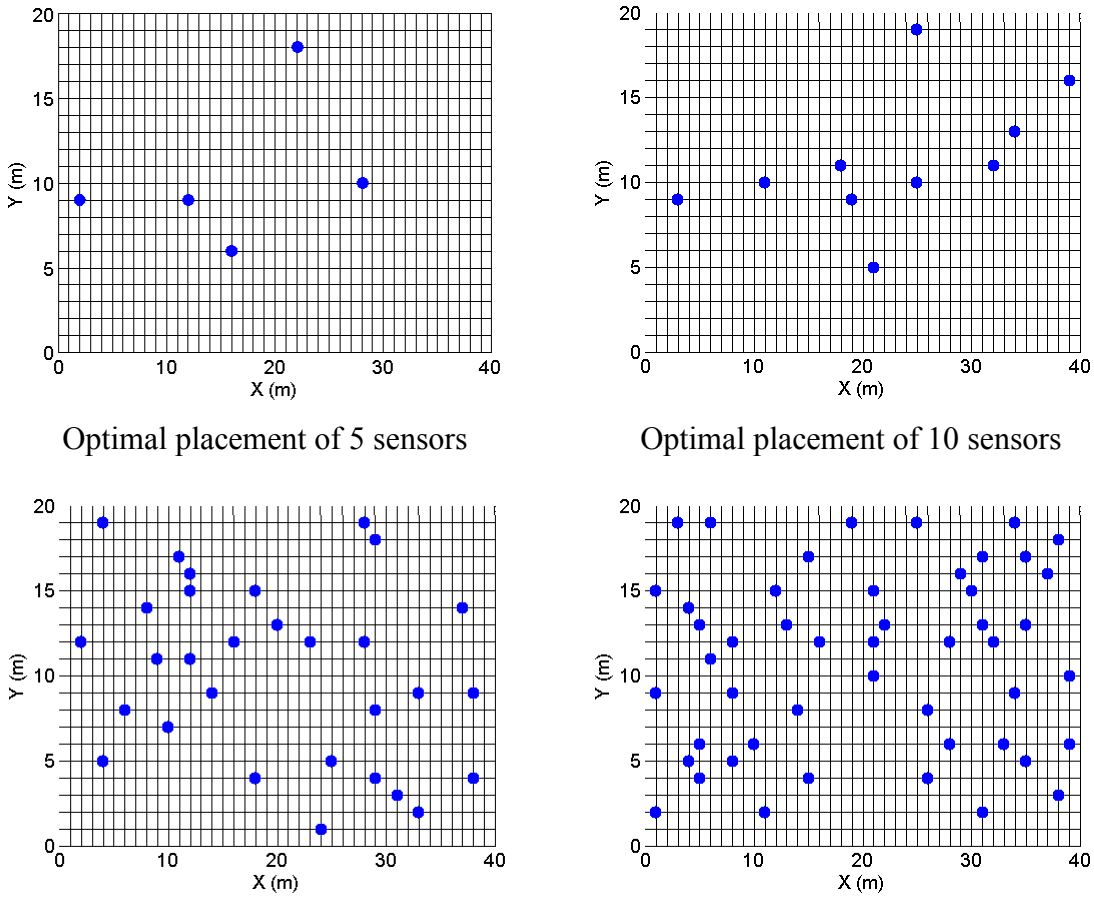

Optimal placement of 5 sensors

Optimal placement of 10 sensors

Optimal placement of 30 sensors

Optimal placement of 50 sensors

Fig. 4.22 Optimal placement of sensors used for recovering mode (2, 1).

The harsh and varying environment in the arctic regions poses great challenges in data collection and sensor placement. Sensor arrays are typically subjected to many limitations and restrictions in the placement, for example, the brine water ponds on the pack ice surface that develop due to the salt expelling process can prevent sensors from being deployed, as shown in Fig. 4.23 and 4.24.

Fig. 4.23 Ice sheets with multiple water ponds (photo courtesy of Stefan Hendricks, Alfred Wegener Institute, source: Huffingtonpost, 2013).

Fig. 4.24 An ice floe with a brine water pond in Russian waters (Voice of Russia, 2013).

Sensor optimization with the restriction in sensor placement is demonstrated using an example and the results are presented in Fig. 4.25. The irregular polygon is the restricted area that sensors cannot be placed.

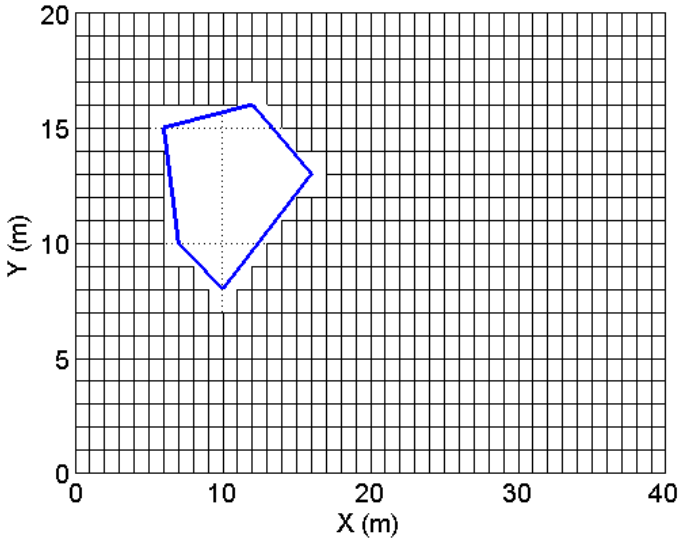

Fig. 4.25 Illustration of sensor placement with restrictions.

The optimization scheme was first verified in order to ensure that the genetic algorithm is able to identify the brine water pond by virtually selecting all possible sensors. The recovered mode shape for mode (2, 2) excited in the numerical model in Fig. 4.26.

Sensor optimization with and without restriction in search of the best estimated mode shapes for mode (2, 2) was conducted. Results are presented in Fig. 4.27. Clearly the existence of the brine water pond affected the extraction of mode shapes reflecting smaller values in red than that in blue. However, this effect seemed to be alleviated with the increase in number of sensors. The differences became smaller as the number of sensors increases.

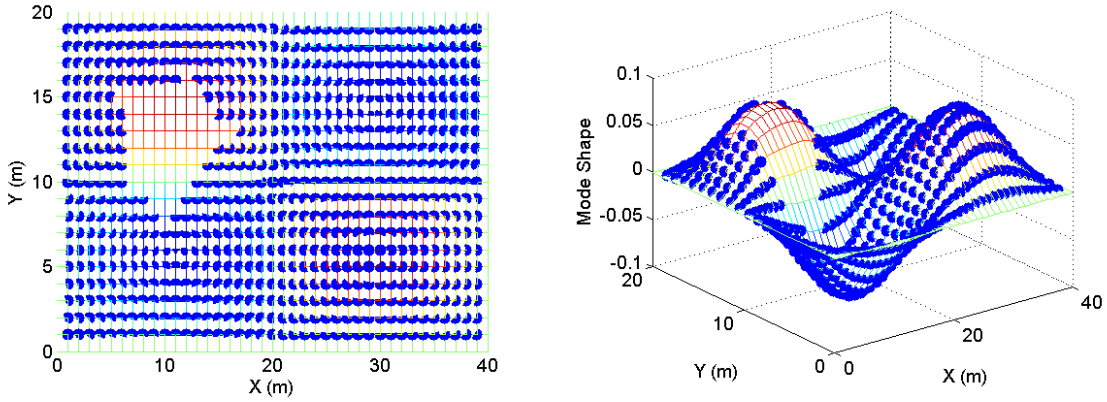

(a) Sensor placement (b) Recovered mode shape (2, 2)

Fig. 4.26 Verification of sensor optimization under restrictions.

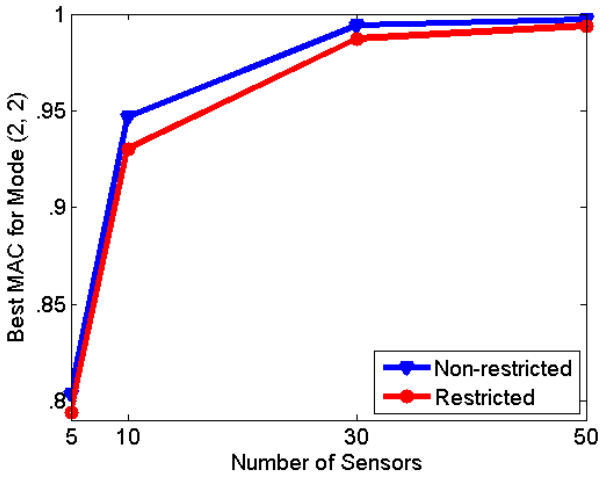

Fig. 4.27 Comparison of MACs recovered with non-restricted and restricted sensor arrays for mode (2, 2).

A single MAC value alone is not adequate to fully understand the effect of restriction in sensor placement. If possible, visual inspection of the recovered mode shapes should be conducted to verify that the algorithm provides correct optimized sensor analyses. For example, with 10 sensors, the MAC computed for the non-restricted case was 0.9468 while for the restricted case 0.9304. The mode shapes in X-Z

view and Y-Z view for these two cases are presented in Fig. 4.28. The fact that mode shapes recovered are not perfect suggests that there is room for improvement. However, the mode shape recovered with restricted sensor placement obviously had difficulty in the water pond area, which shows unbalanced shape in the left trough. It seems that for the two peaks and the right trough, the restricted sensor array performed slightly better than the non-restricted sensor array. The observation is reasonable because the restriction allows the optimization algorithm to deploy more sensors in other areas. The mode shape recovery was greatly improved when more sensors were available, as indicated in Fig. 4. 29 in which 30 and 50 sensors were used. However, the effect of sensor placement restriction on mode shape was still evident.

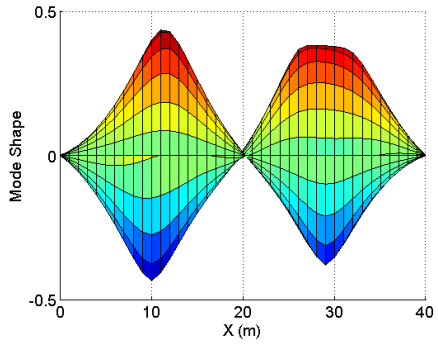

X-Z view, non-restricted

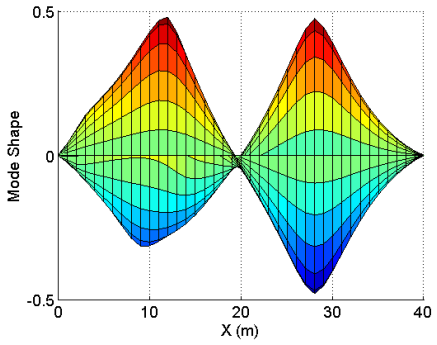

X-Z view, restricted

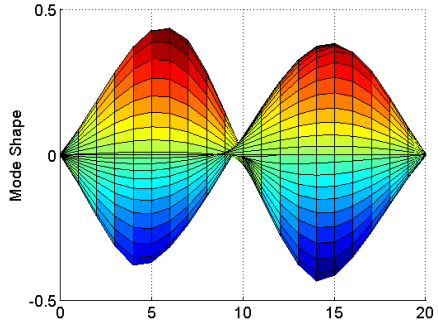

Y-Z view, non-restricted

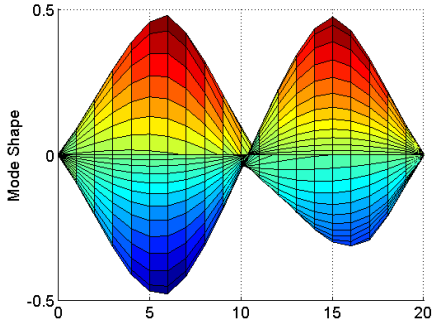

Y-Z view, restricted

Fig. 4.28 Mode shape (2, 2) recovered with 10 sensors w/wo restrictions.

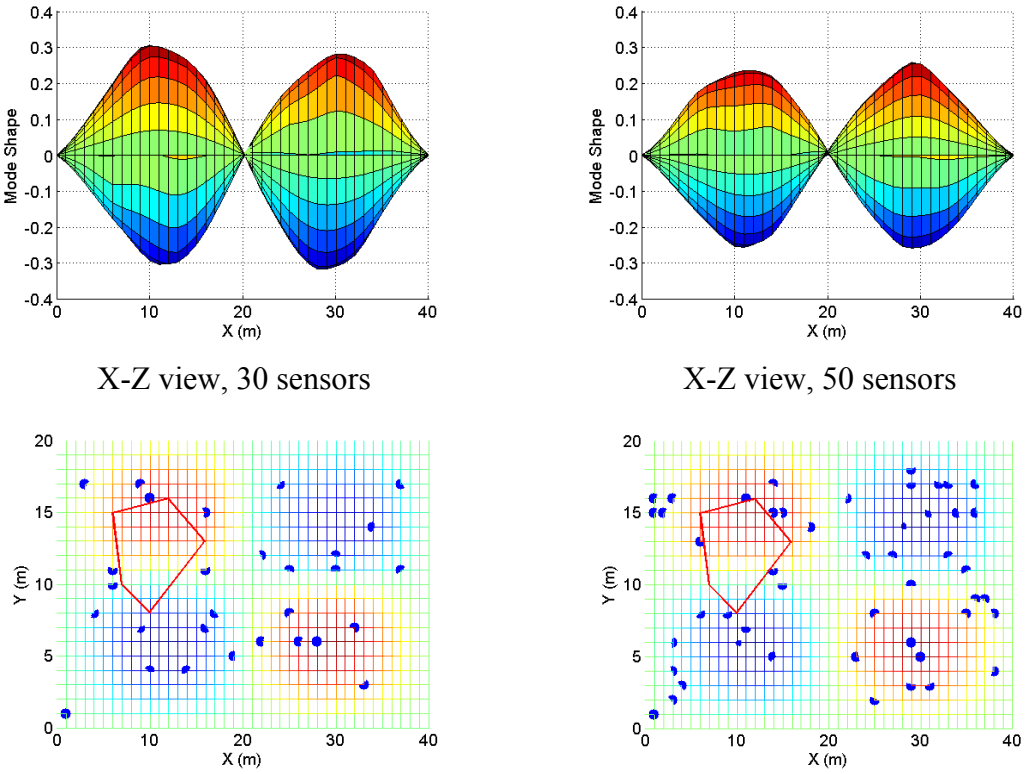

X-Z view, 30 sensors

X-Z view, 50 sensors

Sensor placement

Sensor placement

Fig. 4.29 Mode shape (2, 2) recovered with 30 and 50 sensors with restriction and resulted sensor placements.

An important measure of the quality of a specific sensor array is whether it can derive the modal information of multiple modes with recorded vibration response. Though it seems troublesome, recovery of multiple modes at the same time is worthwhile because the modal information would be concurrent in both time and spatial domain, and subjected to the same environmental loads, i.e. added mass of a floating pack ice in vibration can be the same for the estimated multiple modes. In addition, better evaluation of vibration response, damage detection and strength analysis of the ice features can achieve highly accurate multiple modes.

Pareto front method was adopted to resolve the challenge of sensor optimization under the requirement of recovering multiple modes simultaneously. For the sake of

illustration, 2 modes were chosen to be optimized at the same time. The complexity of the problem for 2-D ice plates is higher than that of the 1-D beam-like structures due to an additional spatial degree. Some patterns have be discovered for the optimal sensor arrays for 2-D mode shapes and these patterns are mixed in order to generate the best results. The advantage of a good Pareto front is that it provides a frame work to evaluate the best trade-offs between two competing modes. Moreover, the inherent disadvantage of some sensor arrays can be identified, i.e. a sensor array with limited number might never be able to recover two modes at an acceptable level. In addition, an instance where one mode is adequately recovered while the second mode is not implies a failure. The degree of failure can be demonstrated as well, which should be valuable information in the process of decision making.

The example used here to illustrate Pareto front method of multi-objective genetic algorithm (MOGA) for 2-D plate-like structures is a simply supported ice sheet, with mechanical properties presented in Table 4.1. The two objectives are to recover the mode shape of mode (1, 1) and mode (2, 1) simultaneously, which are very much similar to the mode shapes illustrated in Fig. 4.11 though the boundary conditions were fixed-fixed. The number of sensors increased gradually resulting in different levels of Pareto fronts. Fig. 4.30 illustrates four Pareto fronts corresponding to 5, 20, 50 and 100 sensors. The stars on the figures are dominant sensor arrays in the multi-objective solution domain which are close to the Pareto optimal frontiers. Note that the scale of each figure is not unified rather, is set to best accommodate the Pareto front. As the number of available sensors in the sensor arrays increased, Pareto fronts demonstrated better performances. Overall, sensor arrays can achieve a better estimation for mode (1, 1) in the vertical axes than that for mode (2, 1).

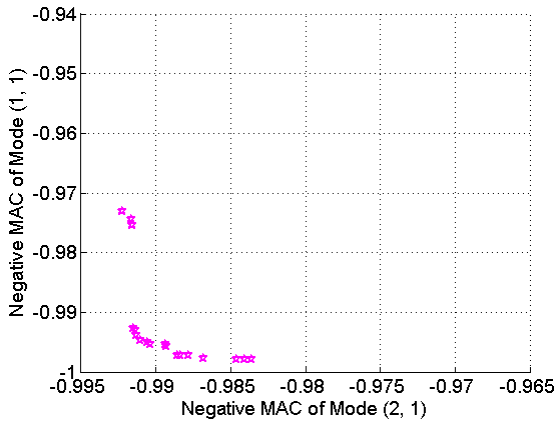

5 sensors

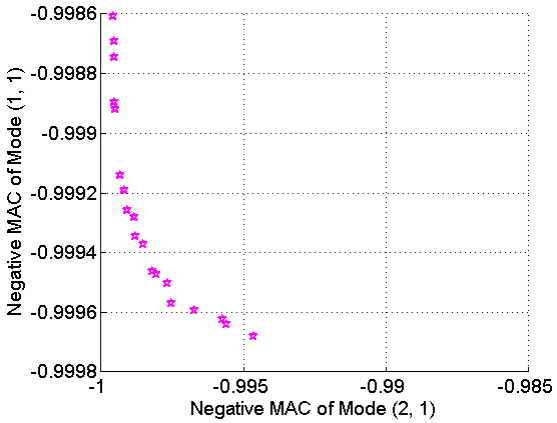

20 sensors

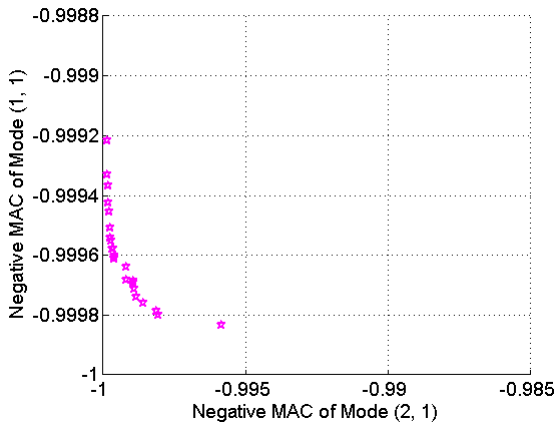

50 sensors

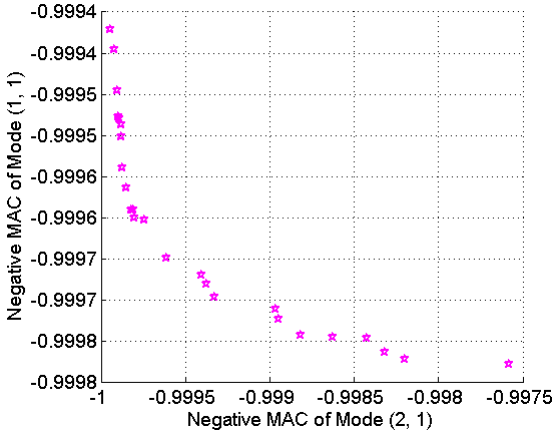

100 sensors

Fig. 4.30 Pareto fronts for sensor arrays with 5, 20, 50 and 100 sensors.

Curve fitting techniques were implemented to fit a parametric function to the data. Denote the negative MAC of mode (2, 1) as MAC_x and the negative MAC of mode (1, 1) as MAC_y. The results show that the vectors of $1+MAC\_x$ and $1+MAC\_y$ follow an exponential function. A two-term exponential model with four coefficients: a, b, c and d was used to fit the Pareto front data:

$$(1+MAC\_y) = a\,e^{b\,(1+MAC\_x)} + c\,e^{d\,(1+MAC\_x)} \tag{4.4}$$

The coefficients were derived with the least square method. Two examples of fitted results are shown in Fig. 4.31. The two term exponential models work well for the existing data.

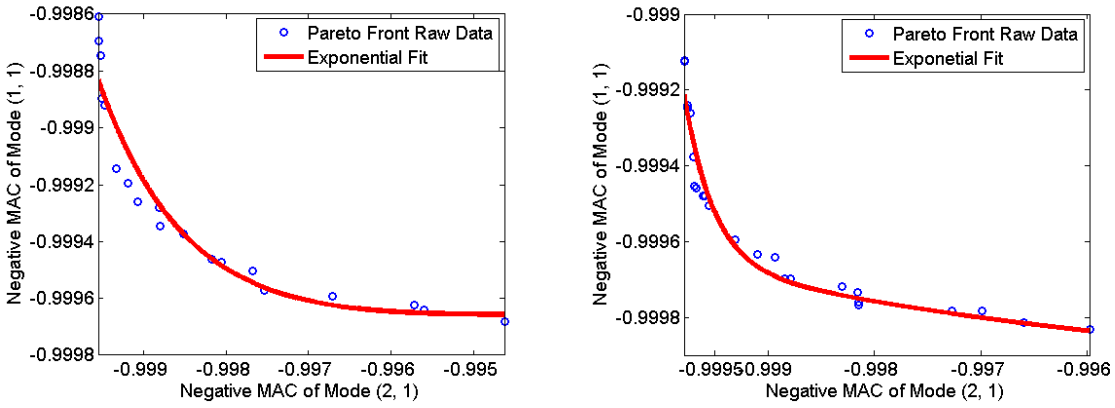

20 sensors 40 sensors

Fig. 4.31 Examples of two-term exponential fit for the Pareto front.

The overall Pareto fronts with selected sensor numbers are presented in Fig. 4.32. As can be seen, as the number of employed sensor increased, Pareto front shifted towards better estimations of both modes.

Six examples with 10 sensors on the Pareto front are presented in Fig. 4.33. Some consensus can be noticed between the solutions. The convergence and diversity of the sensor arrays are both favored in the sensor optimization process.

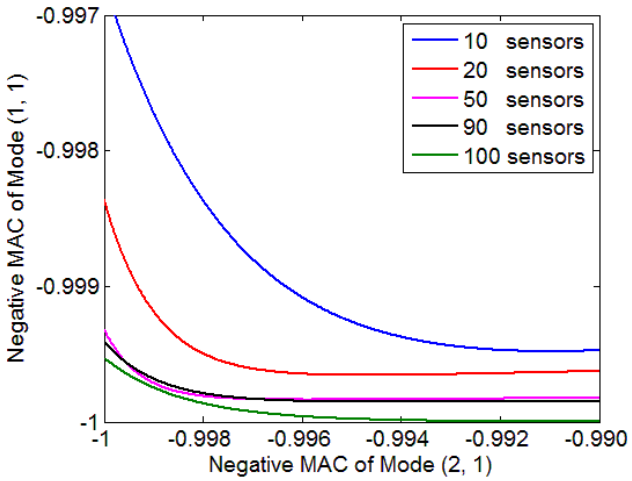

Fig. 4.32 Pareto front summary for mode (1, 1) and (2, 1) for the simply supported ice plate.

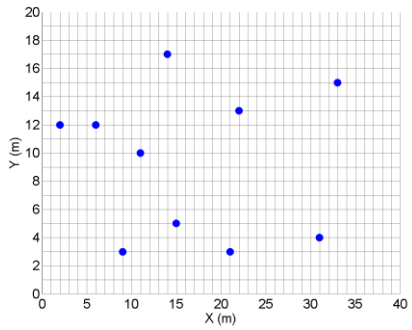

Combination 1

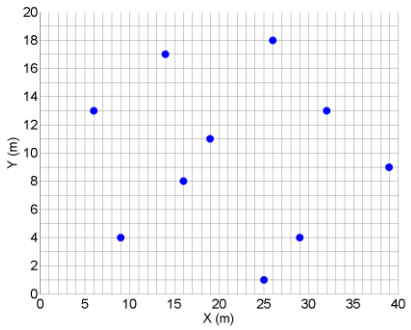

Combination 2

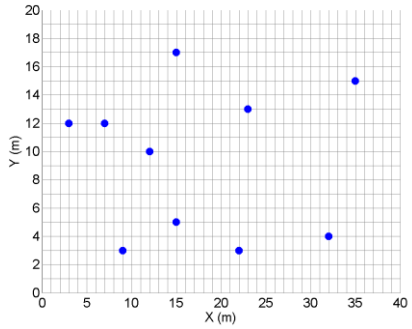

Combination 3

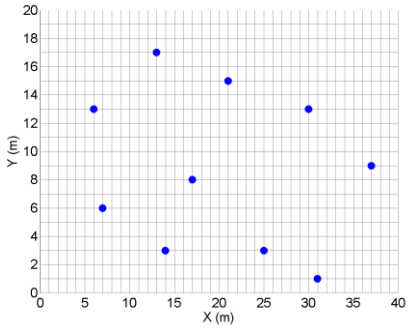

Combination 4

Fig. 4.33 Six example combinations of 10 sensors on the Pareto front for the simply supported ice plate.

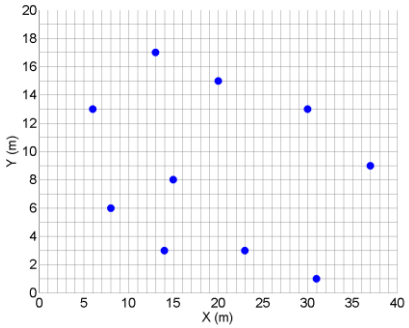

Combination 5

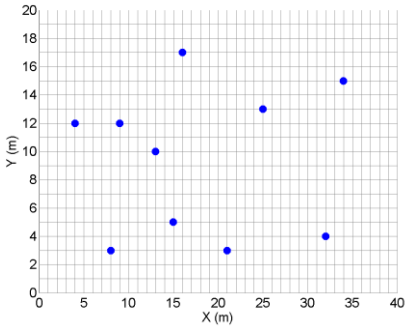

Combination 6

Fig. 4.33 Continued.

The MOGA approach was applied to the same ice plate with fixed-fixed boundary conditions in search of the optimal solutions for mode (1, 1) and (2, 1). The curves of the fitted Pareto fronts in Fig. 4.34 appear different but the trend shown by the Pareto front as the number of sensors increases is similar to the case of the simply supported ice sheet shown earlier.

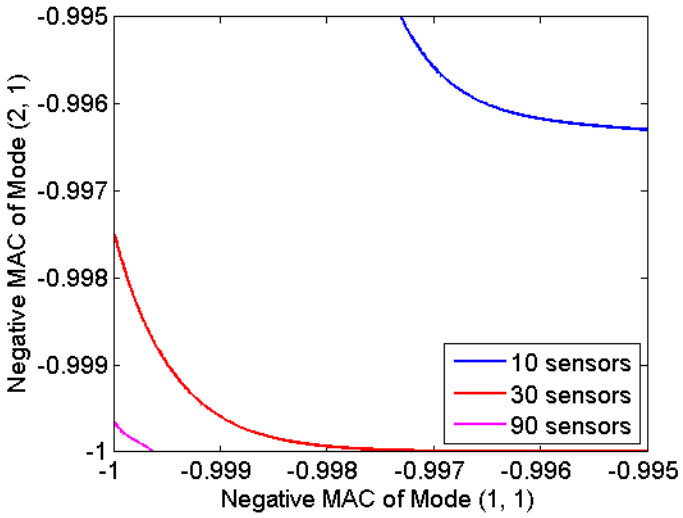

Fig. 4.34 Pareto front summary for mode (1, 1) and (2, 1) for the fixed ice sheet.

Six examples with 10 sensors on the Pareto front for the fixed-fixed ice sheet are presented in Fig. 4.35. The solutions seem to converge with some variation after sensor optimization.

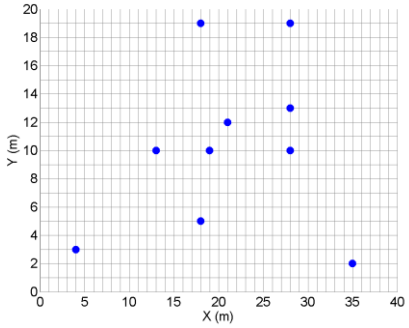

Combination 1

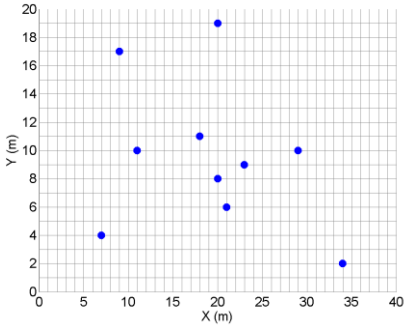

Combination 2

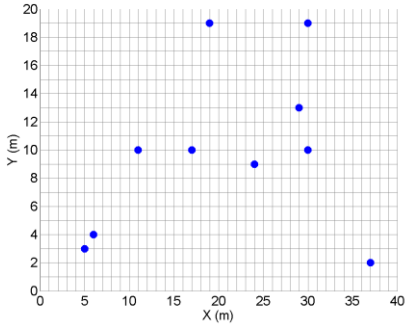

Combination 3

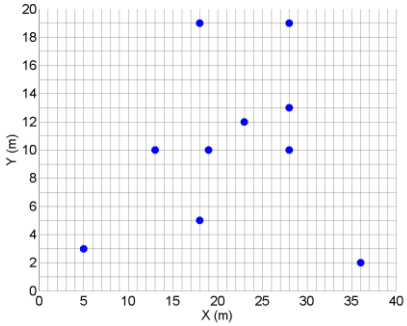

Combination 4

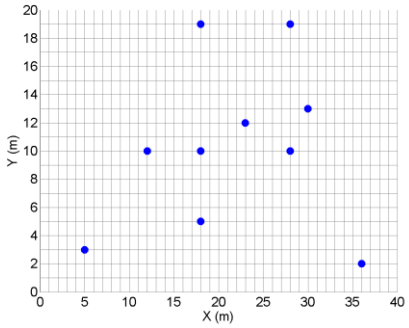

Combination 5

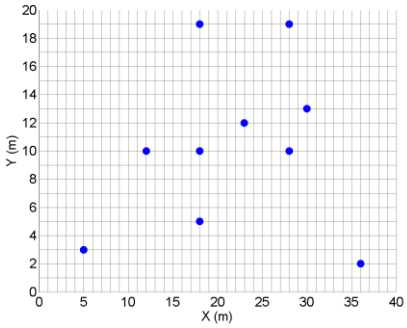

Combination 6

Fig. 4.35 Six example combinations of 10 sensors on the Pareto front for the fixed ice sheet.

The same approach of MOGA was applied to a free-free ice plate in search of the optimal solutions for mode (1,0) and (2, 0) excited around 2.7 Hz and 7.4 Hz as listed in Fig. 4.36, which were recovered with all available sensors. The overall Pareto fronts with selected sensor numbers are presented in Fig. 4.37. The results show a similar trend as seen in the previous study, that performance improves as the number of sensors increases.

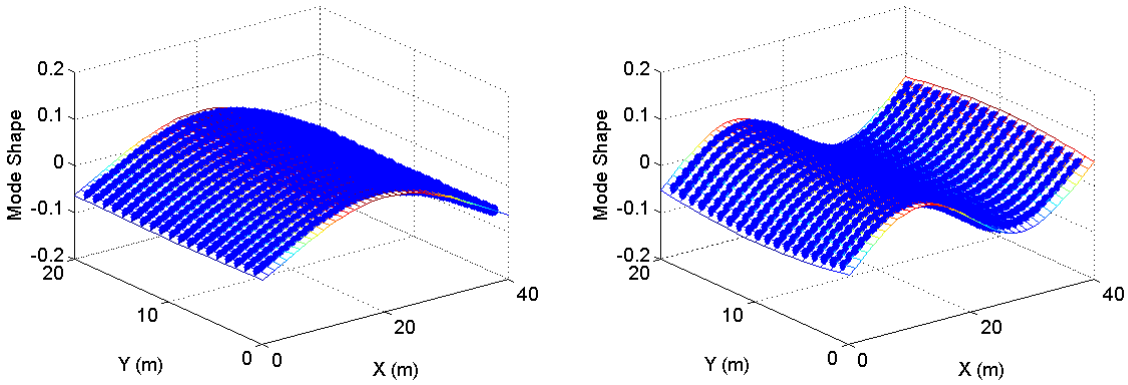

Mode (1, 0) Mode (2, 0)

Fig. 4.36 Mode shapes (1, 0) and (2, 0) of the free-free ice plate with all available sensors.

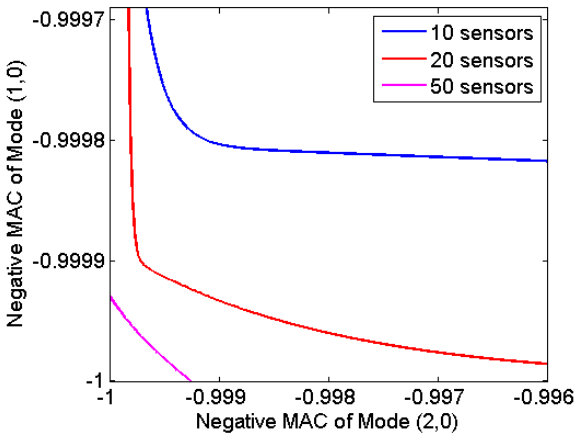

Fig. 4.37 Pareto front summary for mode (1,0) and (2, 0) for the free-free ice sheet.

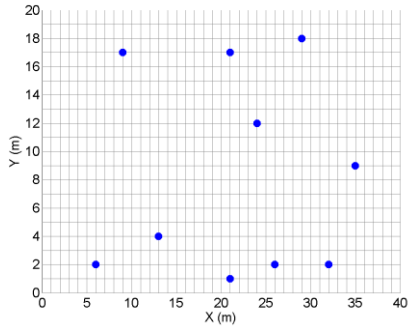

Combination 1

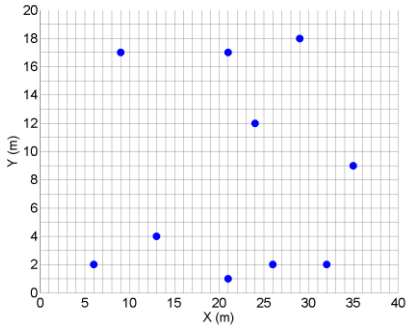

Combination 2

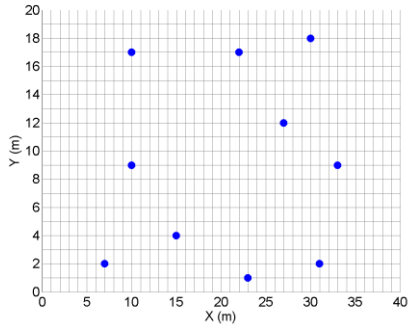

Combination 3

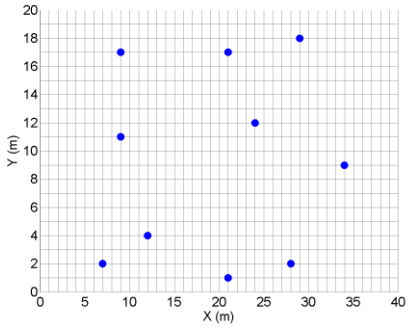

Combination 4

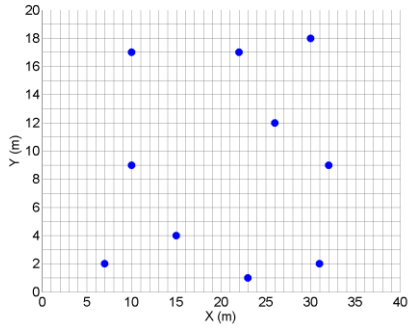

Combination 5

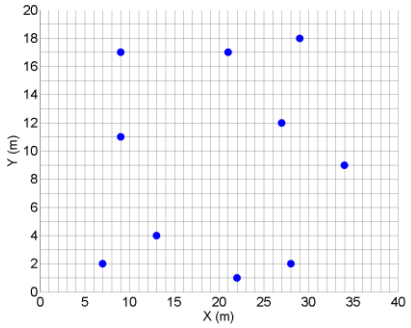

Combination 6

Fig. 4.38 Six example combinations of 10 sensors on the Pareto front for the free-free ice plate in search of optimal for mode (1, 0) and mode (2, 0).

It is of interest to investigate the performance of MOGA with higher harmonics. Two modes, 6 and 8 excited at 12.1 Hz and 14.4 Hz respectively, were used to demonstrate the performance of MOGA for sensor optimization. The mode numbers 6

and 8 were named after the order of the exciting frequency. The mode shapes recovered with all available sensors are presented in Fig. 4.39 and the overall Pareto fronts with selected sensor numbers are presented in Fig. 4.40. Compared to the lower modes, the best achievable MACs were not as high but still fairly high. Six sensor combinations on the Pareto front with 10 sensors are presented in Fig. 4.41. Note that two distinctive patterns of sensor combinations, combination 1, 2, 3 5 and combination 4, 6, can be recognized, which are believed to be the results of the competition between the two modes.

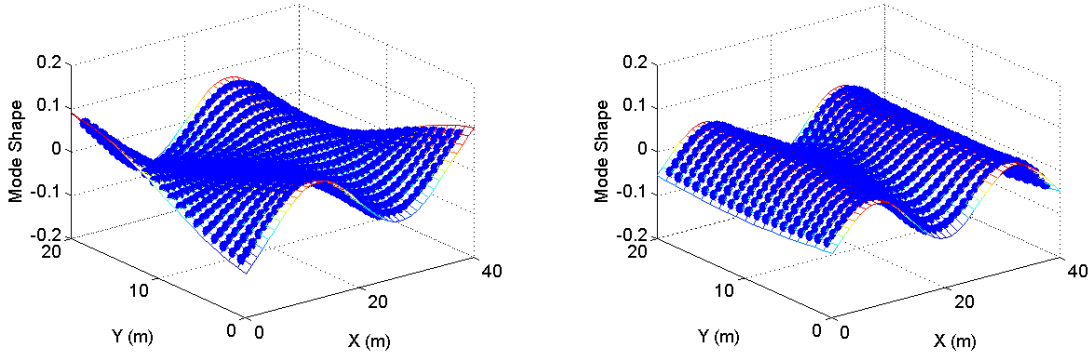

Mode 6 Mode 8

Fig. 4.39 Mode shapes 6 and 8 of the free-free ice plate with all available sensors.

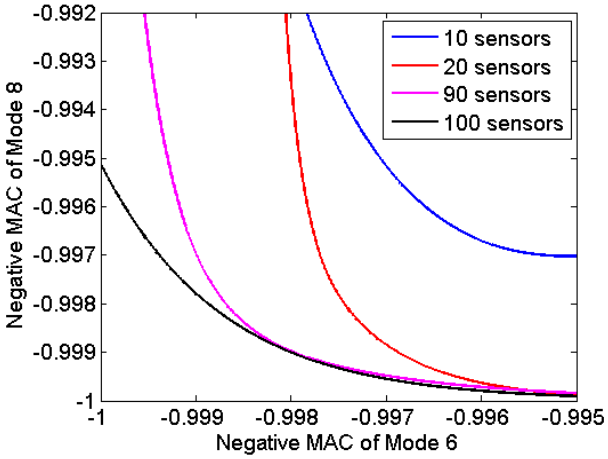

Fig. 4.40 Pareto front summary for mode 6 and 8 for the free-free ice sheet.

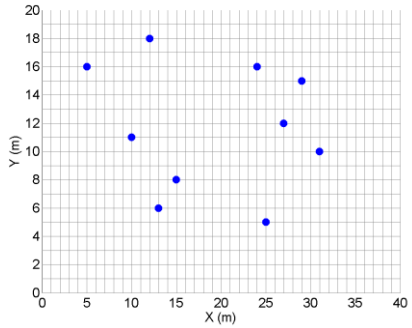

Combination 1

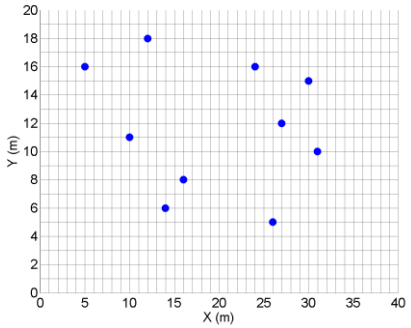

Combination 2

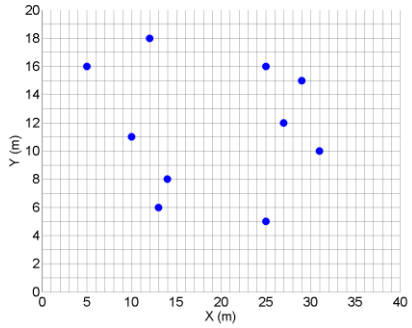

Combination 3

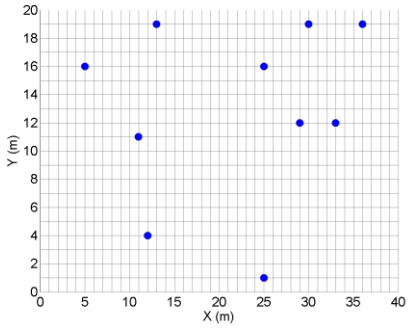

Combination 4

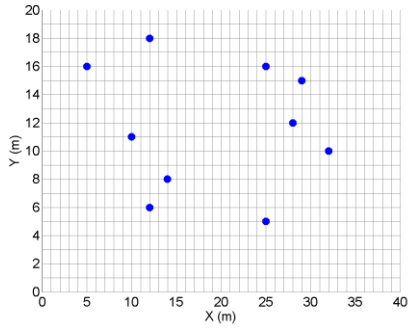

Combination 5

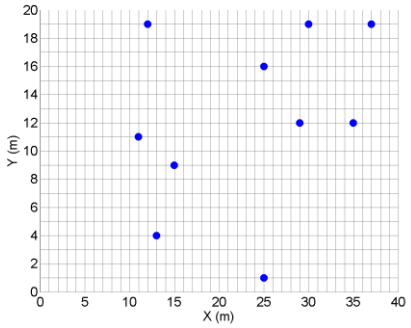

Combination 6

Fig. 4.41 Six example combinations of 10 sensors on the Pareto front for the free-free ice plate searching for optimal for mode 6 and mode 8.

4.4 Damage Detection of an Ice Plate

Both rectangular and elliptical uniform ice plates were used in the strength analysis. In the case of the rectangular shaped ice place, the boundary condition was set to be free at all the four edges, which was a prevailing situation for most of the free floating pack ices. A small area of the plate was assigned with different values of uniform Young‟s modulus to simulate the damage. As discussed earlier, the equivalent Young‟s modulus of the layered up plate was 4.07 GPa, based on which the Young‟s modulus was assigned between 0.20 GPa to 6 GPa, specifically, 0.2, 0.5, 1, 2, 4 and 6 GPa. The first five conditions were varied damages while the last one was actually a strengthened case.

Before conducting the damage detection analysis, selected natural frequencies and mode shapes in the free-free boundary condition were computed with increasing sizes of mesh, as shown in Table 4.6 and Fig. 4.42. The element type used was quadratic shell. The results indicate that the computation converged for mesh size greater than 800.

Table 4.6 Natural frequencies of the free-free ice sheet with increased mesh sizes.

Element type	Mesh Size	Mode (1, 0) (Hz)	Mode (2, 0) (Hz)	Mode (0, 1) (Hz)
S8R	32	2.698	7.382	10.902
S8R	200	2.698	7.370	10.864
S8R	800	2.698	7.370	10.863
S8R	3200	2.698	7.370	10.863

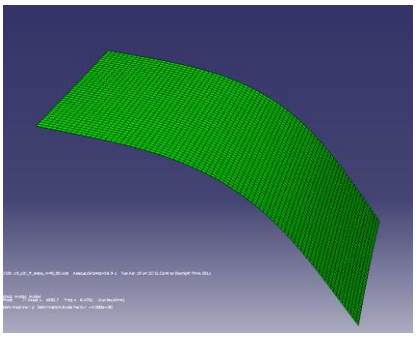

Mode (1, 0)

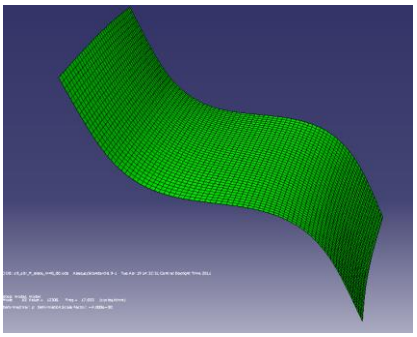

Mode (2, 0)

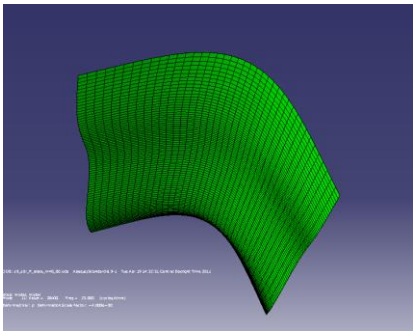

Mode (0, 1)

Fig. 4.42 Selected modes of the free-free ice plate.

The intact ice plate and damaged ice plate are illustrated in Fig. 4.43. Note that the damaged area was located at x = 7-8 and y = 14.5-15.5.

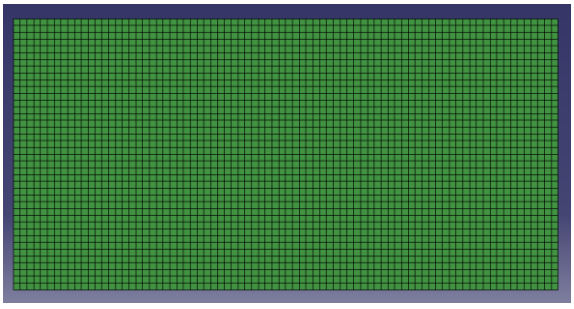

The Intact Ice Plate

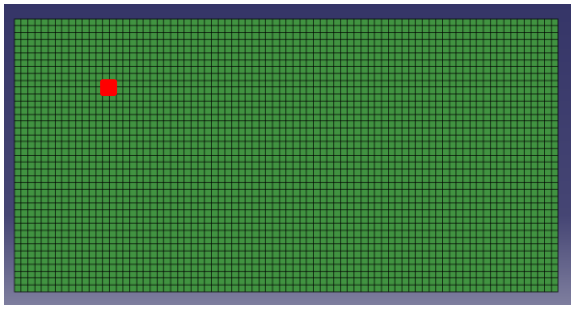

The Damaged Ice Plate

Fig. 4.43 The intact and damaged rectangular ice plate.

The excited frequencies for mode (2, 0) at varied damaged conditions are presented in Fig. 4.44. The red dash line is a reference line for the excited frequency of the intact plate. It is reasonable to find that as the Young‟s modulus assigned in the damaged area decreases, the excited frequency for the 1st mode decreases or vice versa. Note the x-axis was reversed to demonstrate the trend of damage.

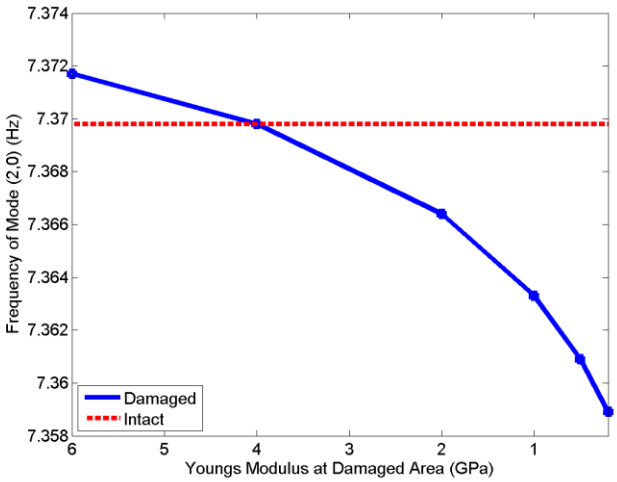

Fig. 4.44 Excited frequencies of the ice sheet with varied Young‟s modulus.

Damage detection was applied in each case and the damage indices were computed and plotted using the 0.5 GPa case as an example as shown in Fig. 4.45. The first 8 modes were used in the computation. Clearly the spike in the figure identifies the location of the damage. The same technique was applied on 6 GPa case, where the Young‟s modulus was actually stiffer than elsewhere. The downwards spike in the damage area in Fig. 4.46 shows that the change in stiffness is also identified, even it is not a damage. The application of damage index method on a strengthened ice sheet indicates that the methodology has the potential application for strength analysis in addition to damage detection.

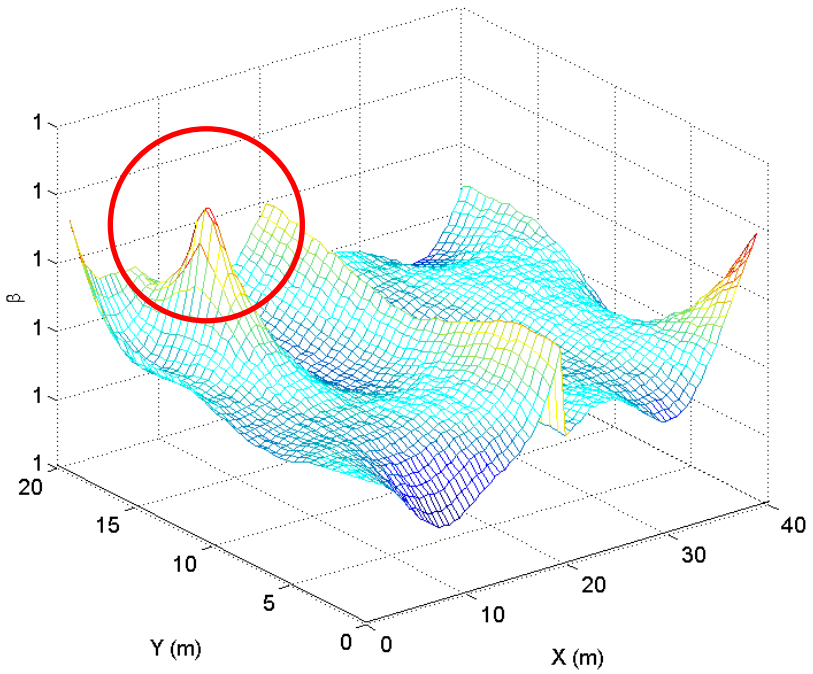

Fig. 4.45 Damage indices for 0.5 GPa case.

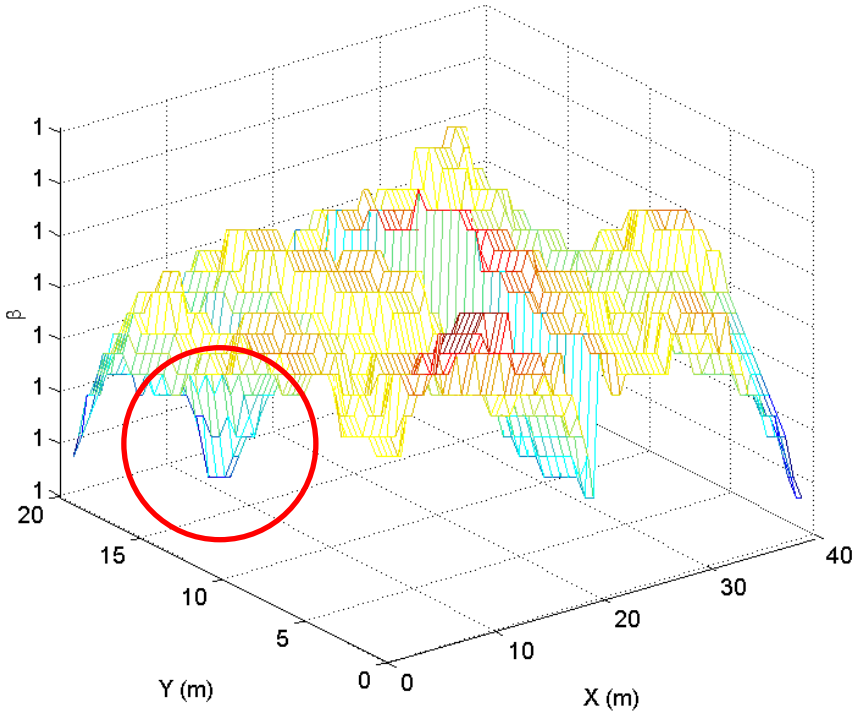

Fig. 4.46 Damage indices for 6 GPa case.

Fig. 4.47a shows the damage indices according to different levels of damage, from 0.2 GPa (the most severe) to 6 GPa (stiffer). 4 GPa corresponds to the intact case with an equivalent stiffness. The trend in damage index indicates that when the damage increases, the beta value increases as well. The results demonstrate damage index method is a level 3 damage detection method for it can size the damage properly. The magnitudes of the beta values were very small thus the values on y-axis show as 1 in all cases. To demonstrate the differences between various damage cases, the damage indices were deducted by 1 and plotted again in Fig. 4.47b. The damage index value at 6 GPa became negative after the deduction, which indicates that the area is strengthened instead of damaged. The locations of the damaged area are presented in Table 4.7, which are accurate in all cases with slight variation.

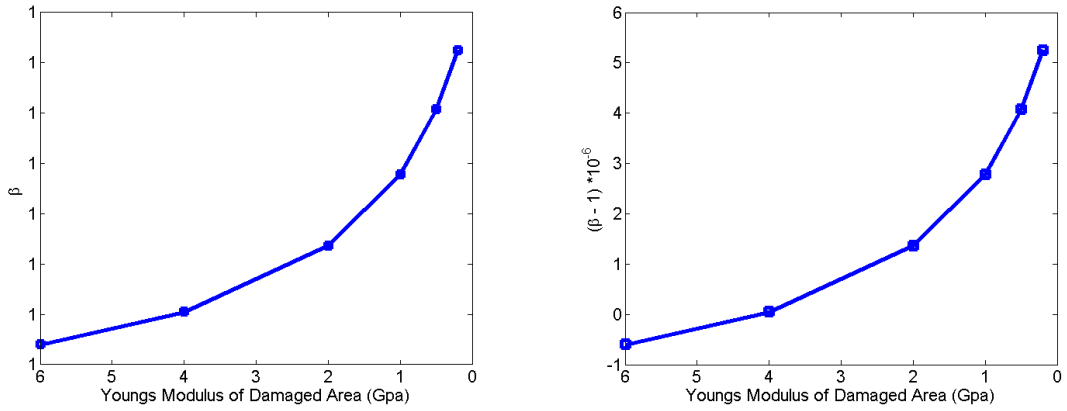

(a) β (b) $\beta - 1$

Fig. 4.47 Damage indices versus severities of damage.

Table 4.7 Identification of damaged area of the rectangular ice sheet.

Cases of damaged E GPa	X coordinate m	Y coordinate m
0.2	7	15
0.5	7	15
1	7	15
2	7.5	15
4	8	15
6	7.5	15

Damage index in 2 phases, denoted as DIM2, was designed to improve the results of DIM by acknowledging the first round identification of damaged location, and then assigning weights for each relevant mode. The results of DIM2 used for sizing the damages are presented in Fig. 4.48. Again δ was used as the weighted damage index for DIM2 to differentiate β for DIM1.

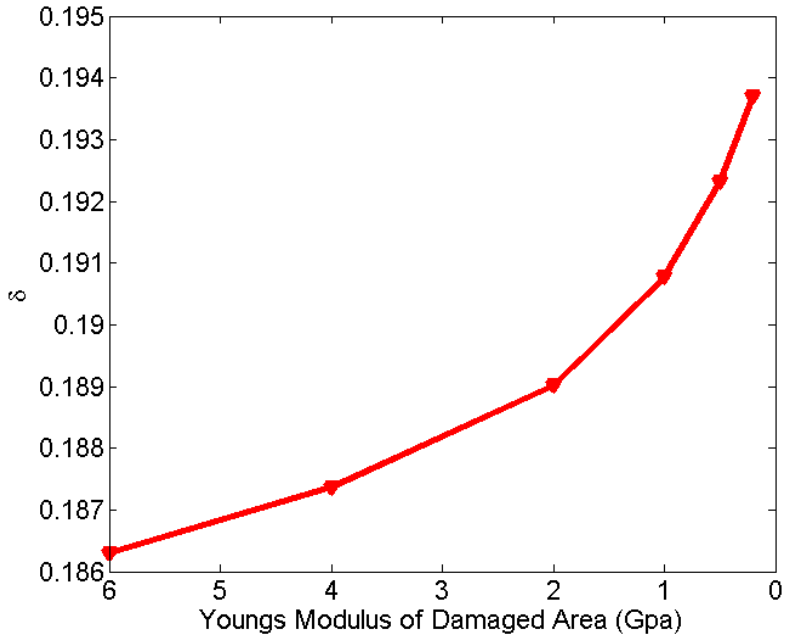

Fig. 4.48 Damage indices computed with DIM2.

The results are more spread out compared with DIM1 as indicated in Fig. 4.49. Taking the damage index value at 4.0 GPa as the normalization reference, DIM1 and DIM2 can be compared. For example, the normalized damage indices at 0.2 Gpa for DIM1 and DIM2 were both divided by the damage indices at 4.0 Gpa and listed as the normalized indices at 0.2 Gpa. Clearly DIM2 amplifies the difference while DIM1 show no significant variations.

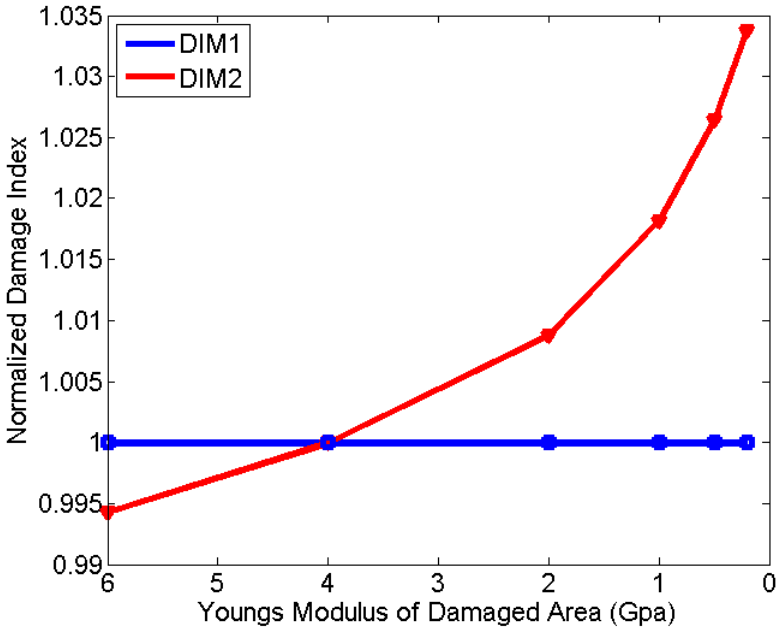

Fig. 4.49 DIM1 versus DIM2 in increased damage.

A direct comparison of DIM1 and DIM2 is presented in Fig. 4.50. It seems DIM2 performs better than DIM1 by removing the additional noises due to irrelevant modes in the damage detection analysis.

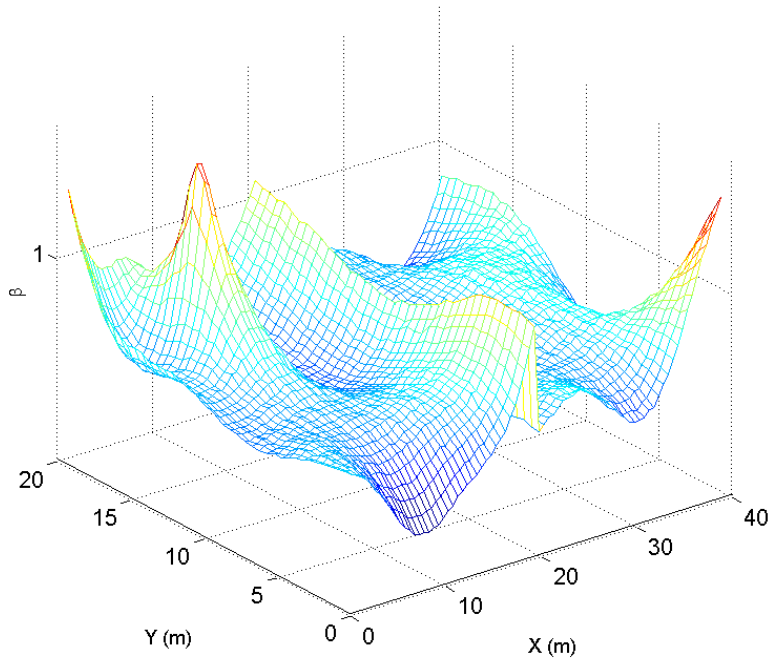

(a) DIM1

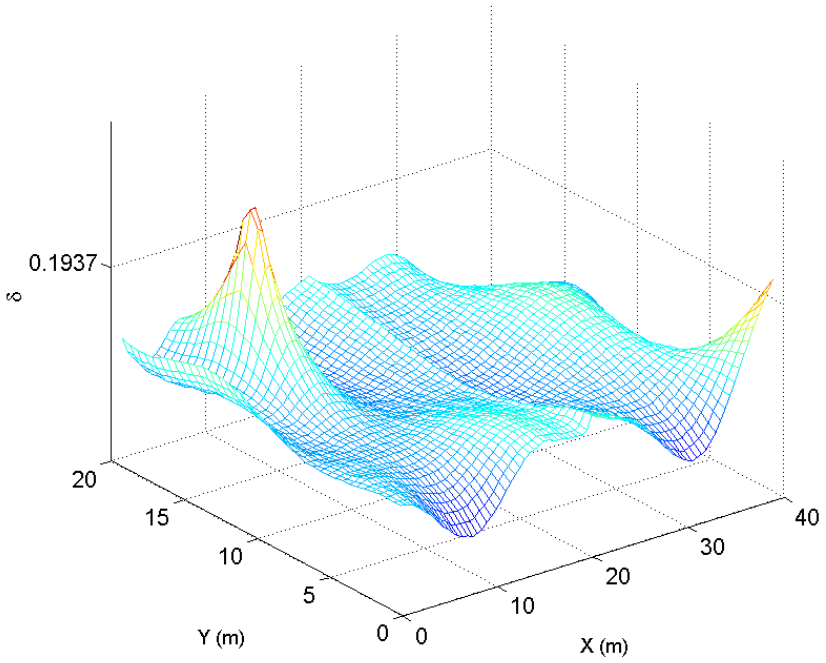

(b) DIM2

Fig. 4.50 DIM1 versus DIM2 in detecting 0.2 GPa case.

When an ice plate floats and vibrates on sea water, buoyancy force acts as a spring and provides additional stiffness. The question is, will this additional stiffness affect the responses and further, will it affect the ability to detect damage? Here a composite ice model considering buoyancy stiffness is built, and then is used to analyze modal response and damage detection process.

The buoyancy elasticity provided by water can be considered as arrays of springs uniformly distributed underneath the plate, as shown in Fig. 4.51.

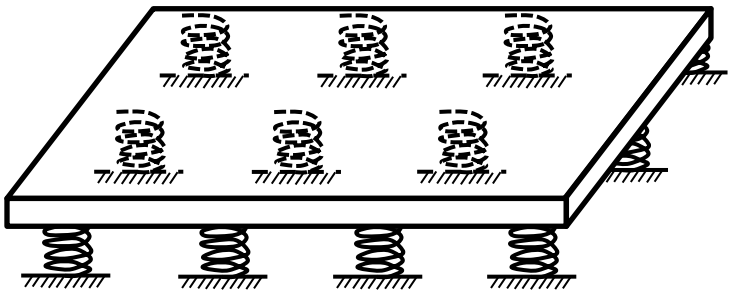

Fig. 4.51 Ice plate with uniform buoyancy stiffness.

The spring stiffness $K_{buoyancy}$ is calculated using the following equations considering additional buoyancy force from an increase in submergence depth Δh:

$$\rho_{sea\ water}\, g A \Delta h = K_{buoyancy}\, \Delta h \tag{4.5}$$

Therefore,

$$K_{buoyancy} = \rho_{sea\ water}\, g A \tag{4.6}$$

In the numerical model, the total stiffness was distributed uniformly onto the nodes of number N. Each spring had the following stiffness property:

$$K_{buoyancy\ individual} = \rho_{sea\ water}\, g A / N \tag{4.7}$$

Modal responses including mode shapes and modal frequencies were extracted from the numerical model. It seems that the mode shapes were not affected by the additional stiffness, as illustrated in Fig. 4.52. However, the natural frequencies were

higher due to the increase in system stiffness, in both intact and damaged conditions, for example mode (2, 0) in Fig. 4.53.

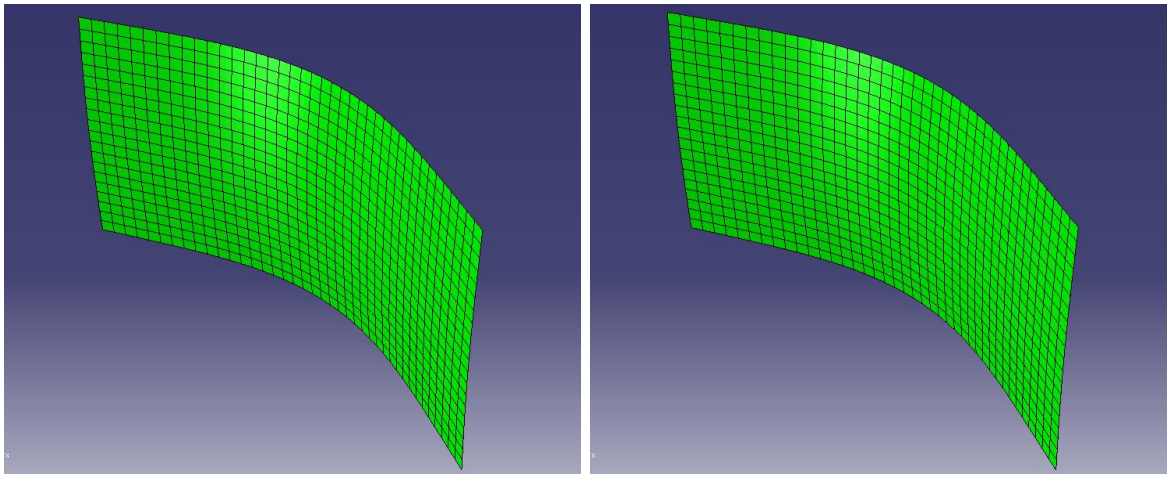

Without buoyancy stiffness With buoyancy stiffness

Fig. 4.52 Mode shape (1,0) w/wo buoyancy stiffness.

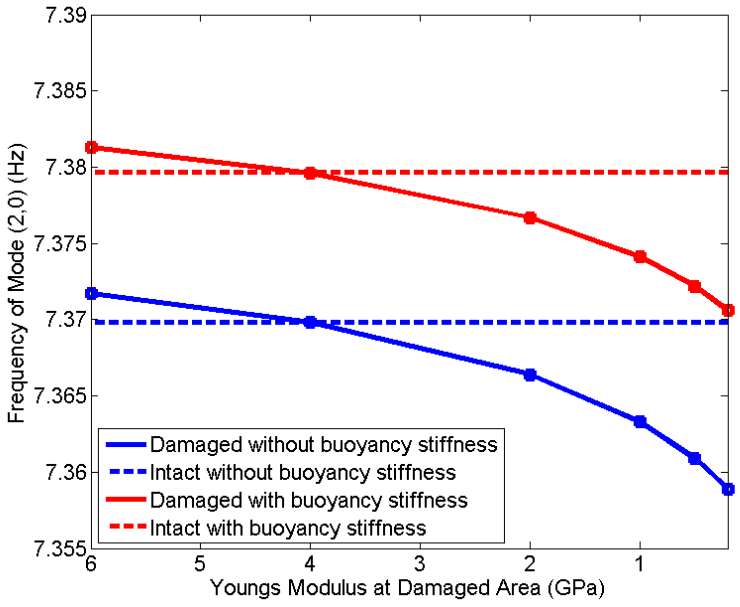

Fig. 4.53 Excited frequency versus Young‟s modulus.

Both DIM1 and DIM2 methods were used to detect the damage in this situation. Fig. 4.54 illustrates the damage detection indices for the two test cases. Compared to the damage index at 0.2 GPa case without buoyancy stiffness in Fig. 4.50, the indices seems noisier and less likely to identify the correct damage. A false peak in the middle of the ice sheet occurs in addition to the peak corresponding to the actual damage.

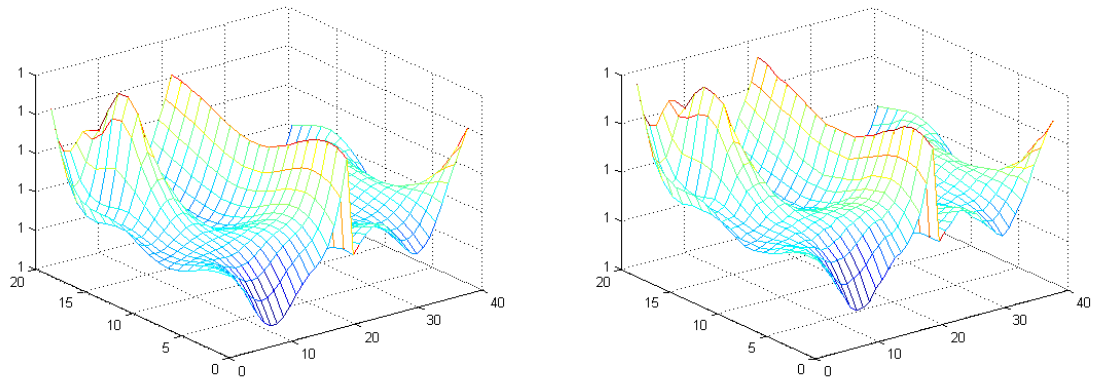

Damaged area, 0.2 GPa Damaged area, 2.0 GPa

Fig. 4.54 DIM1 for 0.2 GPa and 2 GPa cases.

DIM2 clearly removed the additional noise and enhanced the peaks around the actual damage area as indicated in Fig. 4.55. The false peak was almost completely removed. However, in DIM2, the highest damage index peaks were not at the actual location of the damage but at the right corner of the ice plate. The actual damage was identified by the secondary peaks.

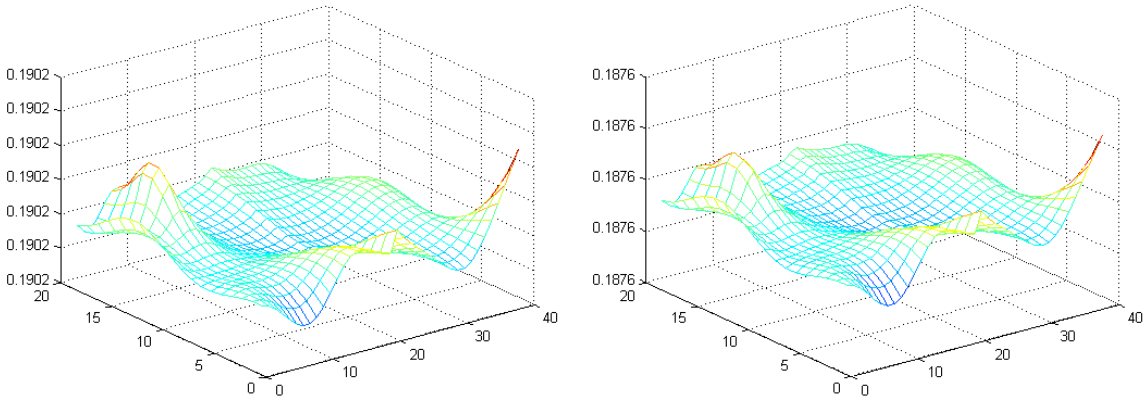

Damaged area, 0.2 GPa Damaged area, 2.0 GPa

Fig. 4.55 DIM2 for 0.2 GPa and 2 GPa cases.

The damage indices can be plotted against Young‟s modulus of damaged area, and compared with the cases without buoyancy effects. As illustrated in Fig. 4.56, the damage indices compared with DIM2 considering buoyancy effects were less sensitive than those without buoyancy stiffness.

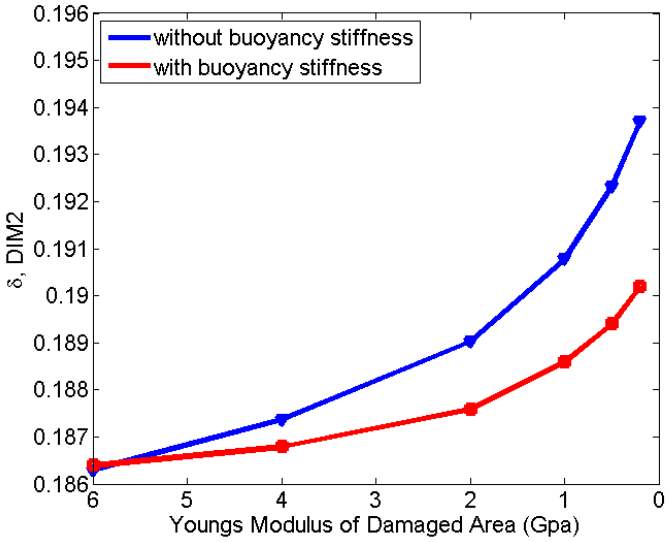

Fig. 4.56 DIM2 versus damage severities w/wo buoyancy stiffness.

The analysis above was conducted on rectangular shaped pack ice; however, actual shapes of a floating pack ice are hardly rectangular in shape. Some typical shapes of floating pack ices are shown in Fig. 4.57. The shape of a pack ice can be wedge, quadrangle, ellipse or some other arbitrary shape.

Sea ice in Beaufort Sea (NASA)

Antarctica Pack Ice (courtesy of Thomas Pickard)

Polar ice (courtesy by Thorsten Milse)

Polar Ice (courtesy by Thorsten Milse)

Fig. 4.57 Typical floating pack ices.

An elliptical ice sheet was analyzed for modal recognition and damage detection. The numerical ice model was built in the same composite manner. However, the

element used was not rectangular anymore but rather arbitrarily quadrangular shaped. The finite element elliptical ice model and nodal distribution is shown in Fig. 4.58. The origin of the coordinates was set to be the center of the ellipse.

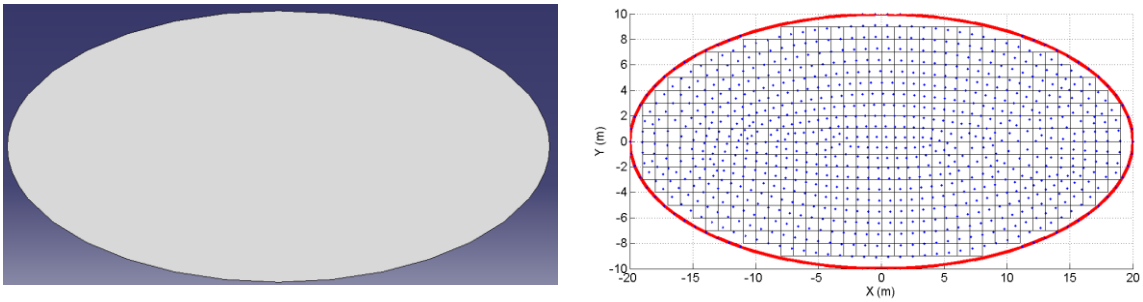

(a) The finite element elliptical ice model (b) The model with nodal points

Fig. 4.58 The finite element elliptical ice model.

The damaged area was determined between x = [-11.3, -10.1], y = [3.68, 4.7]. Young modulus varied from 0.2, to 0.5, 1, 2, 4 to 6 GPa, as in the previous analysis. The intact and damaged ice sheets are illustrated in Fig. 4.59.

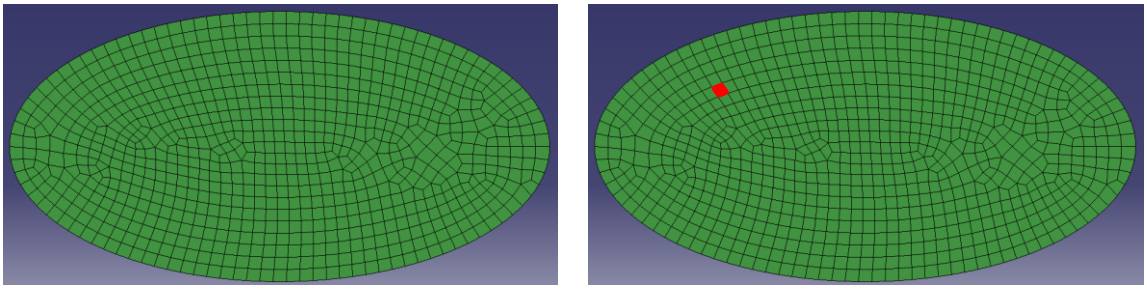

(a) The intact elliptical ice sheet (b) The damaged elliptical ice sheet

Fig. 4.59 The intact and damaged elliptical ice sheet.

The irregularly distributed nodal points were firstly fitted to a uniform and regular mesh, and then mode shapes were reconstructed onto a uniform mesh. The damage detection procedure was then conducted. Mode shapes up to the first 8 modes are presented in Fig. 4.60.

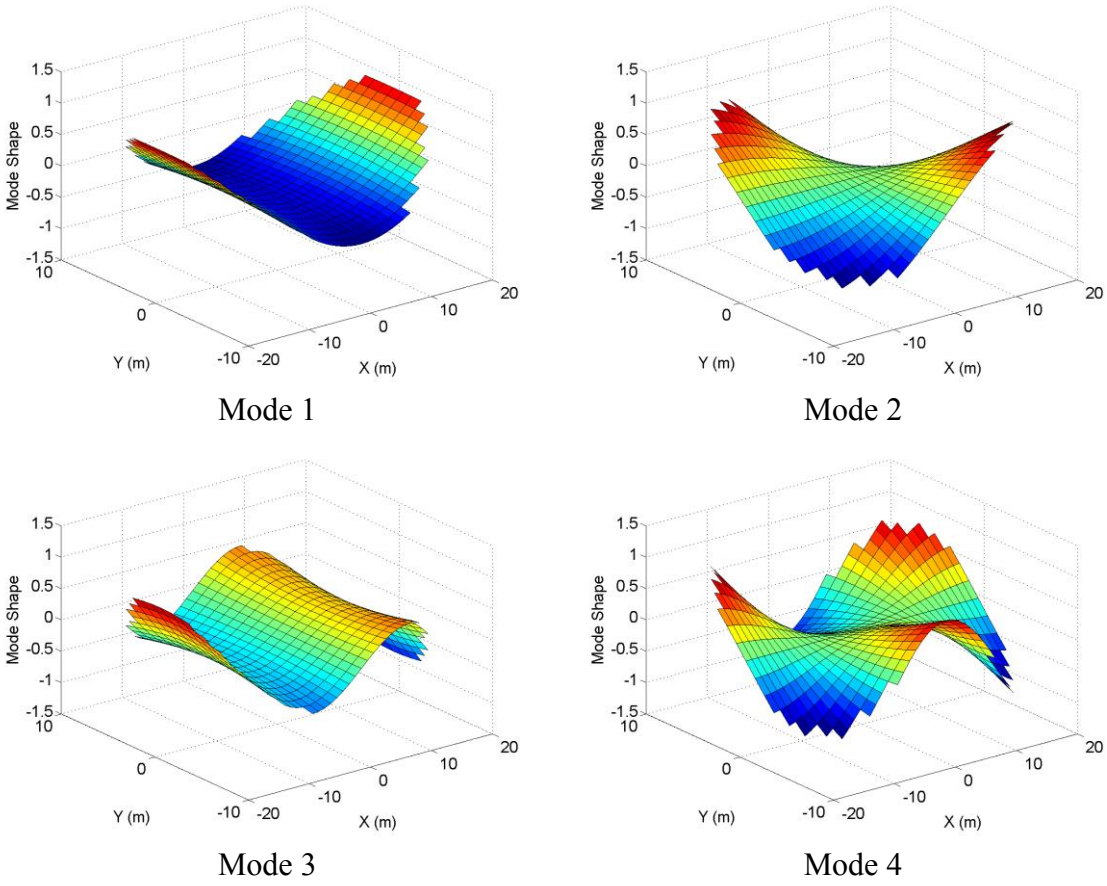

Mode 1 Mode 2

Mode 3 Mode 4

Fig. 4.60 Mode shapes of the elliptical ice sheet.

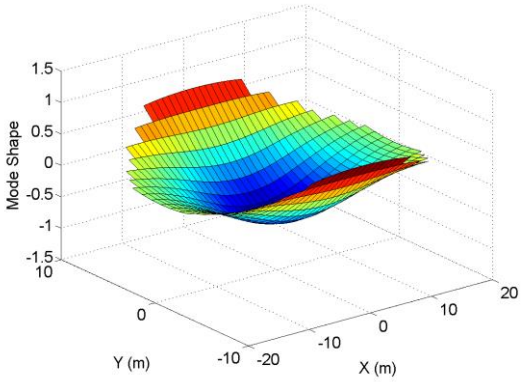

Mode 5

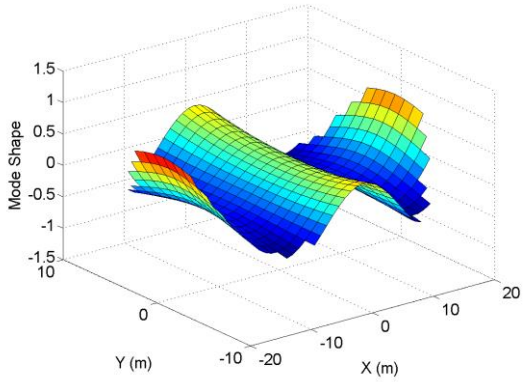

Mode 6

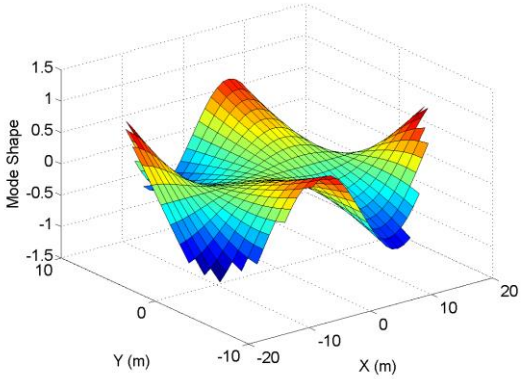

Mode 7

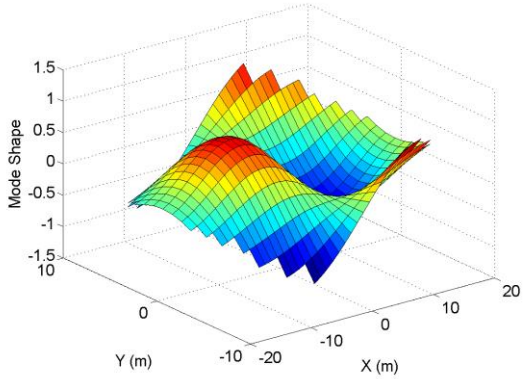

Mode 8

Fig. 4.60 Continued.

Damage index method was employed to study the possible damages. Selected cases are presented in Fig. 4.61. The damage detection results are summarized in Table 4.8. The elliptical shape added complexity to the problem, however, the damage index method was shown to be a robust algorithm, which successfully located and sized the damage in 5 of the 6 cases. The damage detection failed in the 4 GPa case which was acceptable considering the slight change in stiffness.

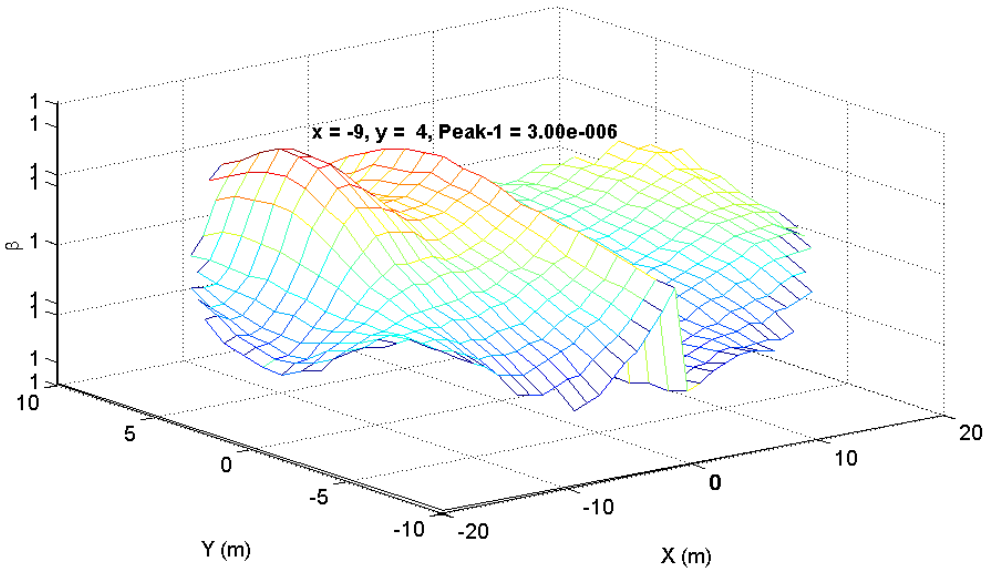

(a) Damaged area, E = 2.0 GPa

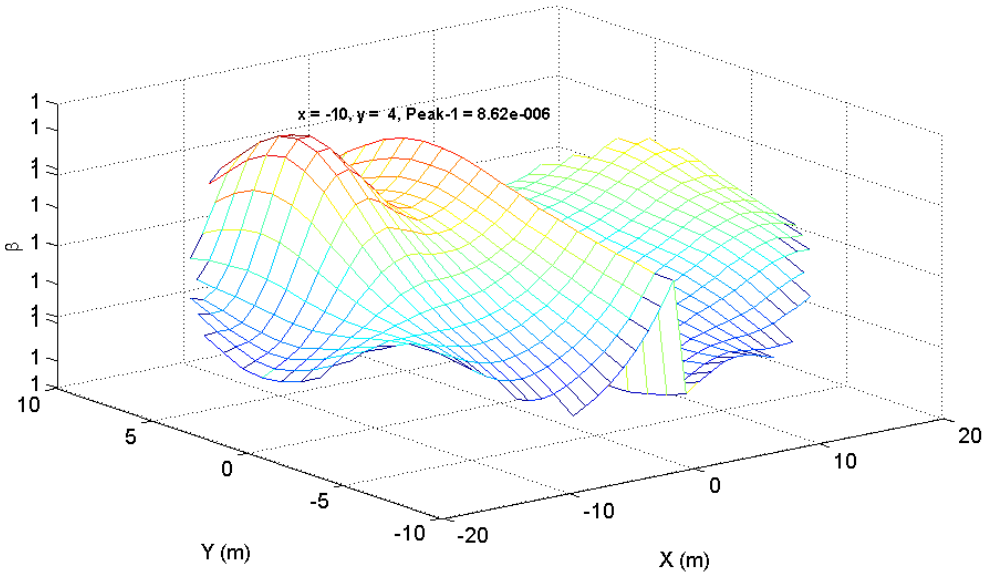

(b) Damaged area, E = 0.2 GPa

Fig. 4.61 Damage indices computed for the elliptical ice plate in selected cases.

Table 4.8 Identification of damaged area of the elliptical ice sheet.

Cases of damaged E GPa	$\beta - 1$ $*10^{-6}$	X coordinate m	Y coordinate m
0.2	10.9	-10	4
0.5	8.6	-10	4
1	6.0	-9	4
2	3.0	-9	4
4	0.08	1	9
6	-1.5	-9	4

The following section of the study focuses on strength analysis of a multi-year ice (MYI), which generally has a much lower level of salinity due to the continuous salt expelling process and a much stronger strength due to the long term consolidation in ages. In addition, the ridges embedded in a multi-year ice can be even stronger due to long term consolidation and excessive thicknesses. The physical properties of the multi-year ice used in the study are presented in Fig. 4.62 for non-ridge areas and in Fig. 4.63 for ridge areas.

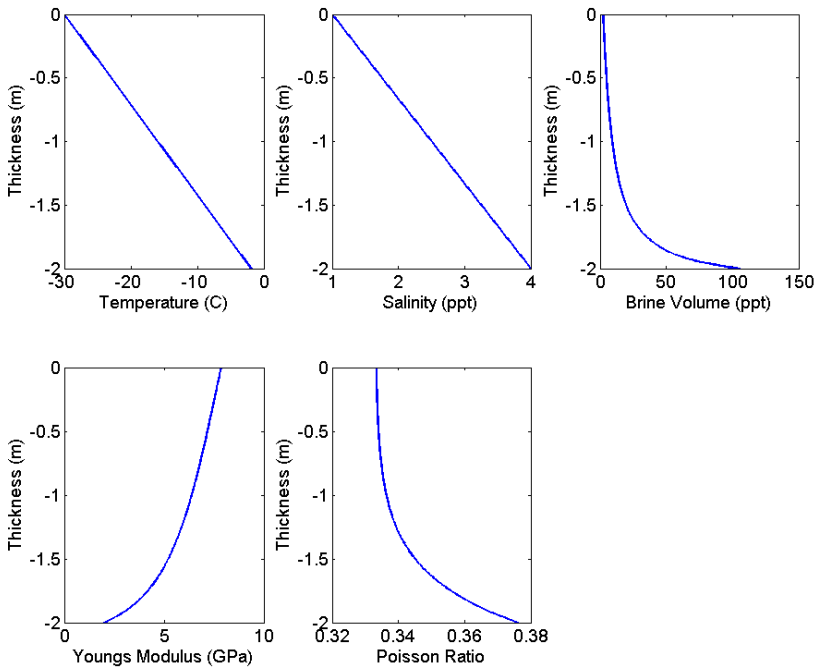

Fig. 4.62 Physical properties of non-ridge areas of a multi-year ice.

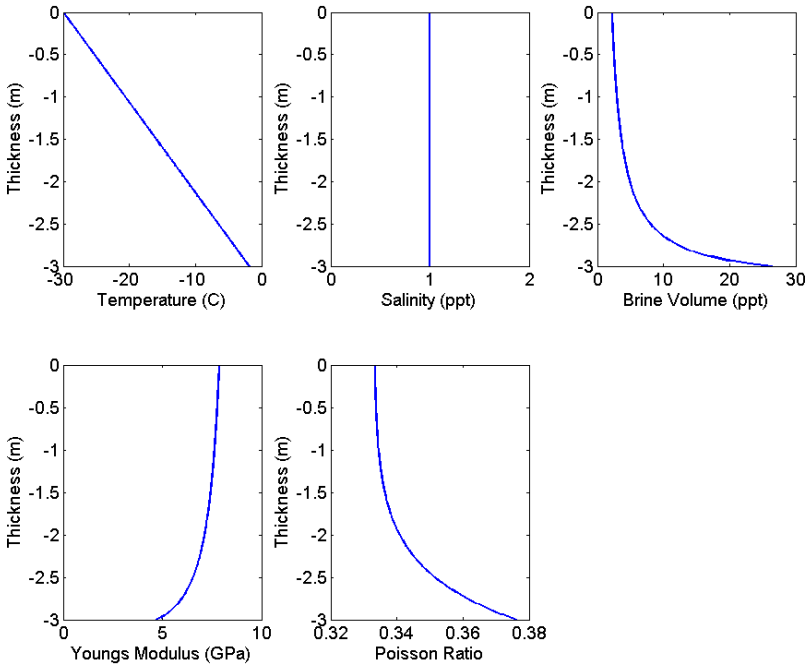

Fig. 4.63 Physical properties of ridge areas of a multi-year ice.

Comparison of the Young‟s modulus between the simplified first-year ice and multi-year ice used in the current study is presented in Fig. 4.64. Note that the non-ridge areas in the multi-year ice were stronger than the first-year ice, and the multi-year ice ridges were the strongest of the three types.

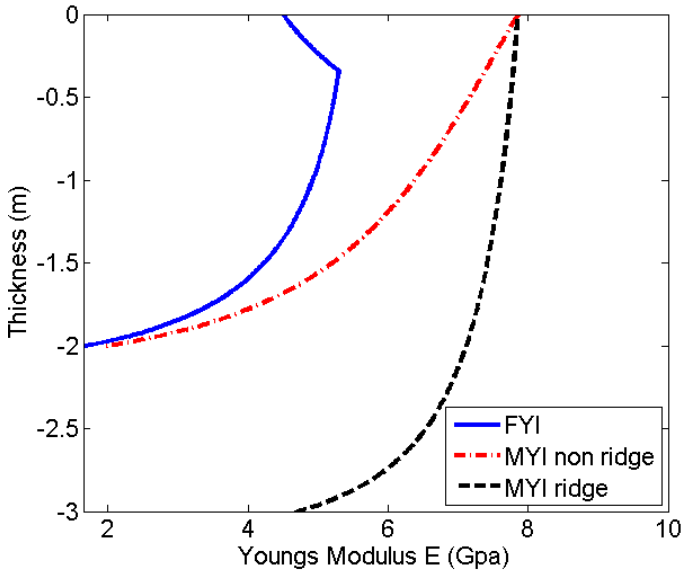

Fig. 4.64 Young"s modulus comparison of first year ice and multi-year ice.

A simplified case of multi-year ice containing one ridge is illustrated in Fig. 4.65. The ellipical ice plate had a scale of 20 m by 40 m, with the origin of the coordinate system lying in the center. An irregularly shaped ridge was embedded in the top right area of the ice plate, with its position at $6.4 \le x \le 8.7, -0.5 \le y \le 6.6$ m. The non-ridge flat areas had a thickness of 2 m while the ridge area had a thickness of 3 m.

Prior to damage analysis on the ice sheet, damage index method was applied using mode shapes with and without the ridge to explore the strengh condition, and the results of which using the first 8 modes are presented in Fig. 4.66. As indicated by previous results, Fig. 4.46, when a structure was strengthened instead of being damaged, the damage indices corresponded to downward peaks near the strengthened areas. In this case, the primary downward peak occurred near the top end away from the ridge while the secondary downward peak occurred near the ridge. It was believed certain modes introduced noise in the computation. In spite of this, the results of the strength analysis were encouraging.

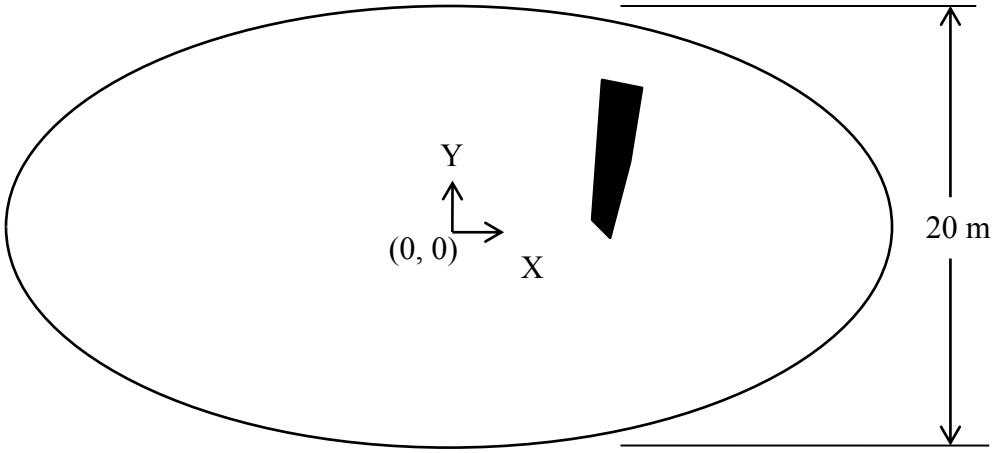

(a) Planar view of the ice sheet

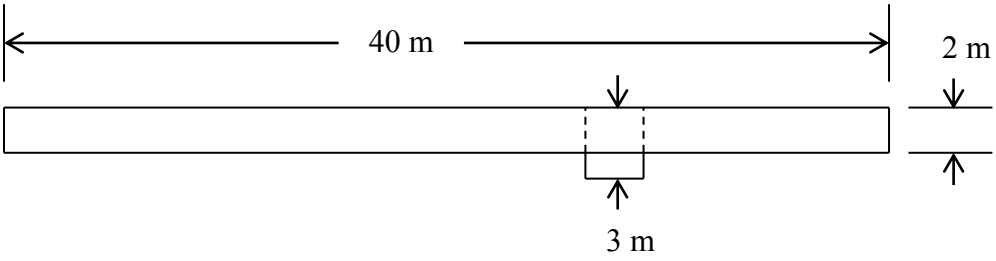

(b) Thickness profile of the ice sheet

Fig. 4.65 Sketch of the multi-year ice with an embedded ridge.

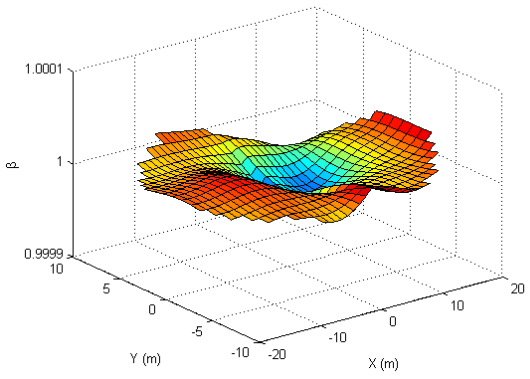

(a) Isometric view

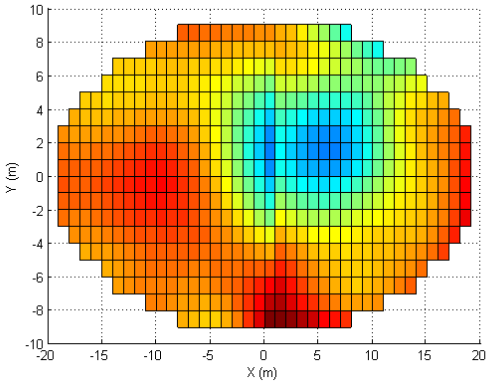

(b) X-Y view

Fig. 4.66 Damage indices of the elliptical ice sheet without/with ridges using 8 modes

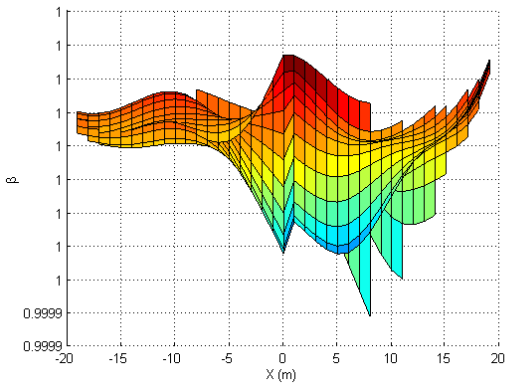

(c) X-Z view

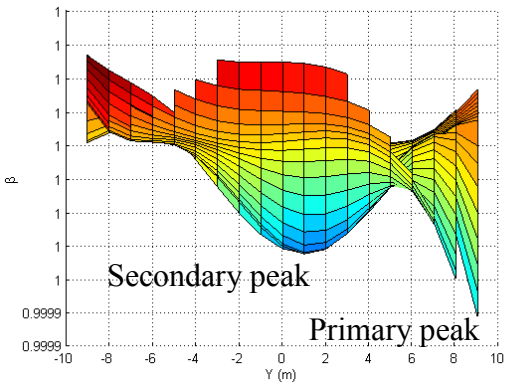

(d) Y-Z view

Fig. 4.66 Continued.

The performance of damage index method in detecting strengthened areas may vary according to the modes selected, as inferred by previous studies in detecting damage. The damage indices were computed with the first 7 modes and with selected four modes (mod 3 -7). Results presented in Fig. 4.67 and Fig. 4.68 indicate that the mode number and selection of various modes may affect the performance of damage index method in strength analyisis. The primary downward peak was located near the ridges. However, it is important to note that the ridge was a stripe but the damage indices computed located the center at $5 \le x \le 6, 0 \le y \le 2$ m, considering the actual location of the ridge, $6.4 \le x \le 8.7, -0.5 \le y \le 6.6$ m, the damage index method successfully located the strengthened area but in a rough manner, as shown in Fig. 4.69 where the damage indics in X-Y plane and the multi-year ice sketch were overlaid.

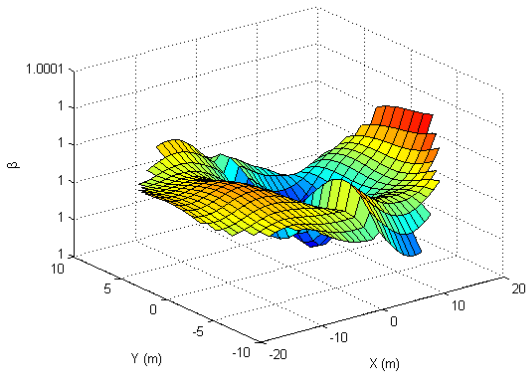

(a) Isometric view

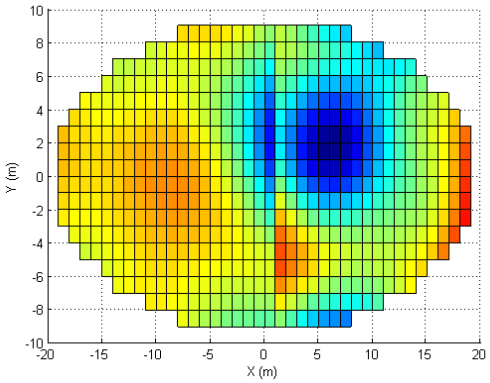

(b) X-Y view

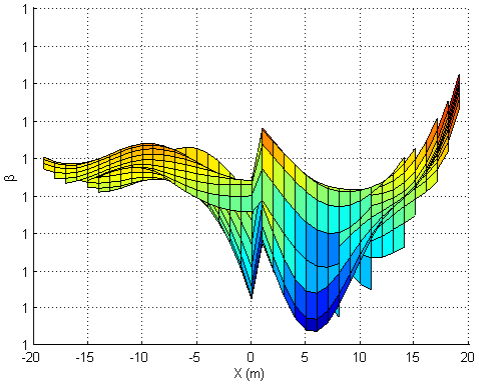

(c) X-Z view

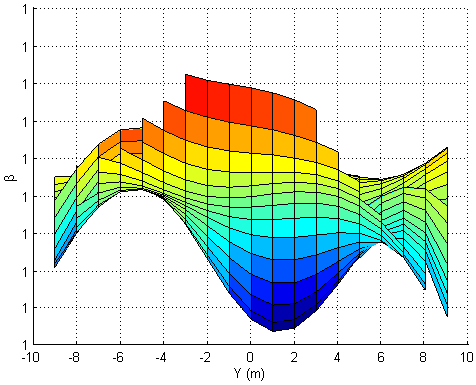

(d) Y-Z view

Fig. 4.67 Damage indices of the elliptical ice sheet without/with ridges using mode 1-7.

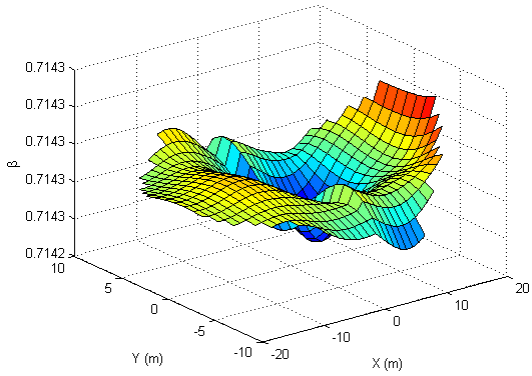

(a) Isometric view

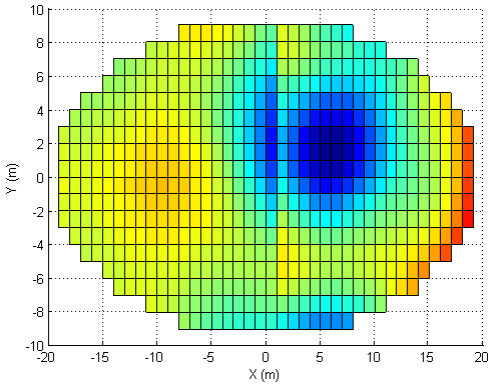

(b) X-Y view

Fig. 4.68 Damage indices of the elliptical ice sheet without/with ridges using mode 3-7.

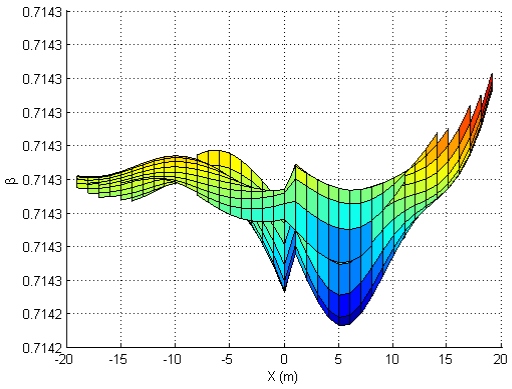

(c) X-Z view

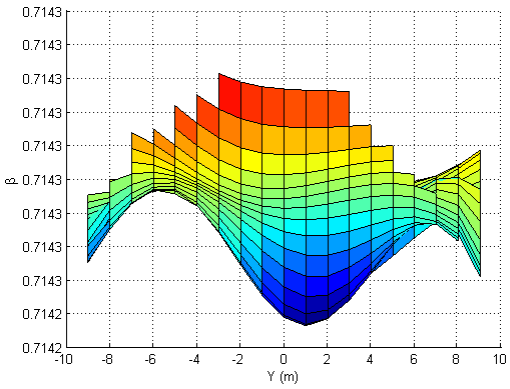

(d) Y-Z view

Fig. 4.68 Continued.

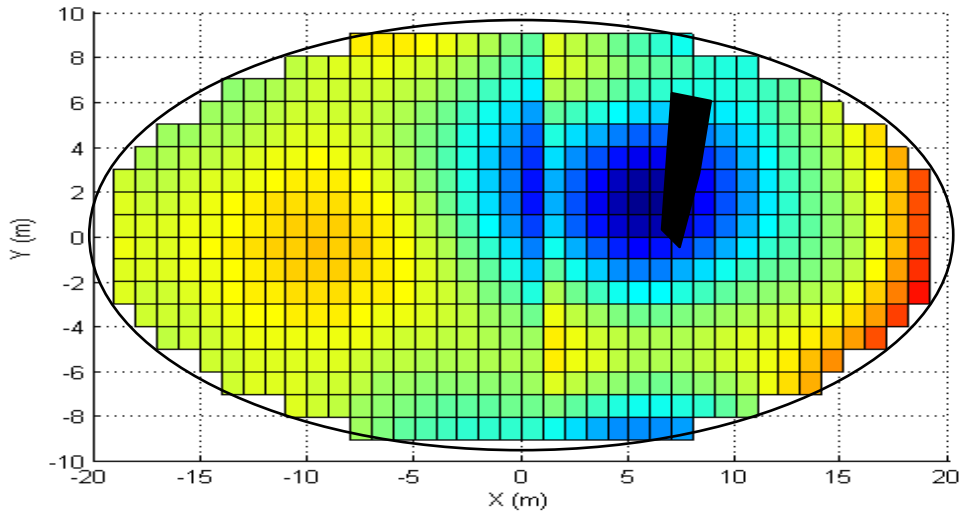

Fig. 4.69 Damage indices overlaid by the multi-year ice sketch.

One weak region in the form of various reduced stiffness was imposed on the multi-year ice. Specifically in this study, a uniform weak region with Young‟s modulus of 0.2 GPa and 2.0 GPa, at $-11.5 \le x \le -9.2, -1.0 \le y \le 1.2$ m were analyzed. The numerical model of the multi-year ice sheet is shown in Fig. 4.70.

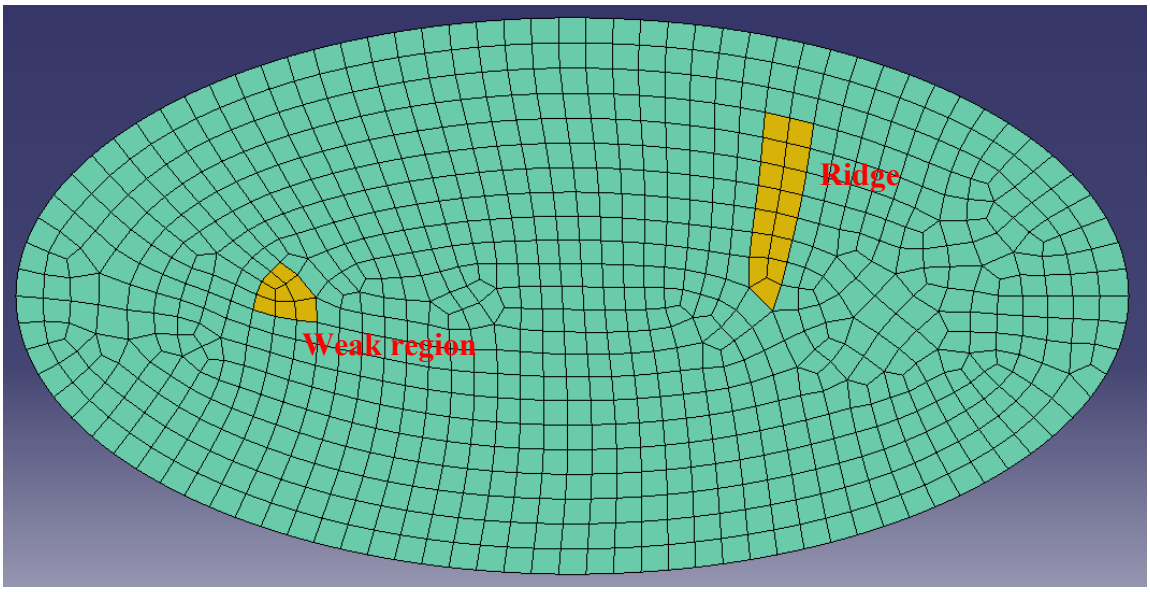

Fig. 4.70 The numerical model with 874 elements of the multi-year ice.

In order to use damage index method, the modal parameters of an intact ice sheet was needed in addition to the damaged ice sheet. In this case, the ridge information can be either known or unkown. When the ridge information was unkown, a flat ice sheet with no ridges was assumed as the intact ice in the analysis. Thus, the damage analysis was divided into computation with known ridge and with unknown ridge. The results are presented in Fig. 4.71 and 4.72 respectively. Clearly, in both cases, the damage was located at $-11 \le x \le -9, -1 \le y \le 1$ m despite of some numerical error since the actual location was at $-11.5 \le x \le -9.2, -1.0 \le y \le 1.2$ m. When the damaged ridgeous ice sheet was computed with intact flat ice sheet not considering ice ridge, the results in Fig. 4.72 indicate that the ice sheet had a damage on the left side and a strengthened region on the center right, which was favorable in a sense a full strength condition of the ice can be evaluated with one index.

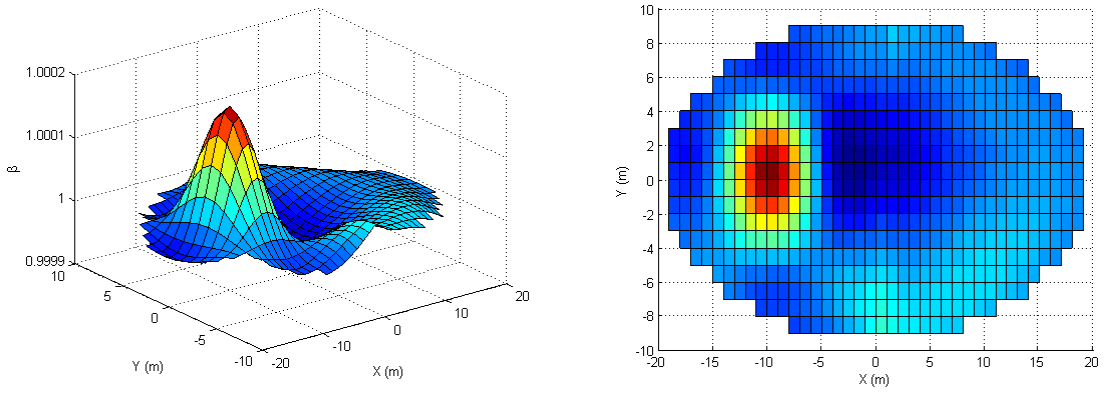

(a) Isometric view (b) X-Y view

Fig. 4.71 Damage indices of the ice sheet of 0.2 GPa weakness with known ice ridge information.

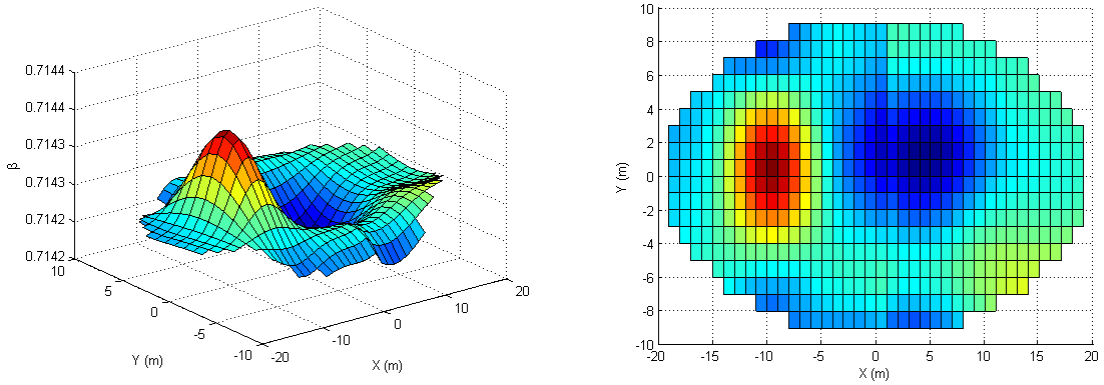

(a) Isometric view (b) X-Y view

Fig. 4.72 Damage indices of the ice sheet of 0.2 GPa weakness with unknown ice ridge information.

It is of interest to study the effect of damage severity in the strength analysis. A relatively less severe damage with Young‟s modulus of 2 GPa was imposed on the ice sheet and analyzed with the damage index method, with known or unknown ice ridge. The results are listed in Fig. 4.73 and 4.74. Compared to the analysis of 0.2 GPa case, Fig. 4.71 and 4.72, the damage index peak with known ice ridge in Fig. 4.73 slightly decreased though not in an obvious manner. However, the damage indices indicating

damage and the downward peak indicating strengthening significantly decreased, in spite of this, both strength conditions were still recognizable.

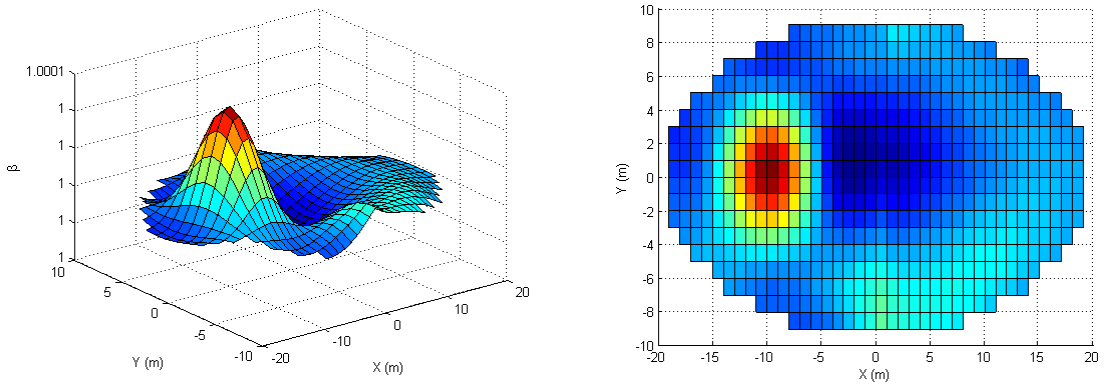

(a) Isometric view (b) X-Y view

Fig. 4.73 Damage indices of the ice sheet of 2.0 GPa weakness with known ice ridge information.

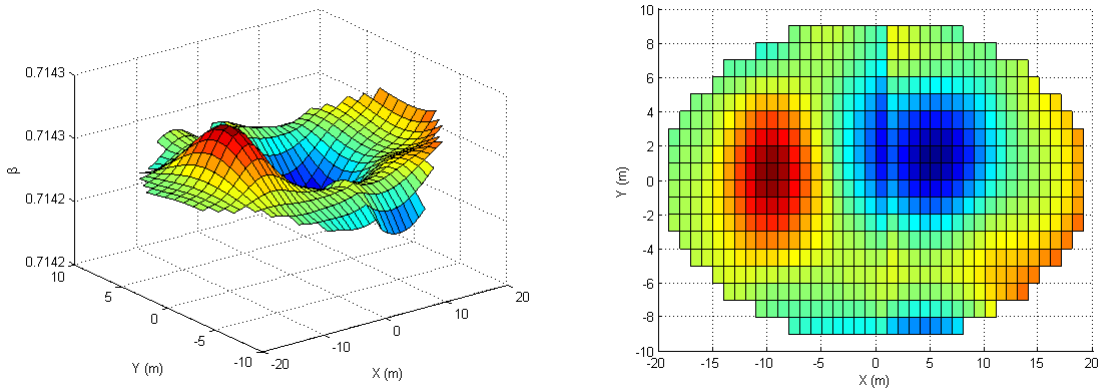

(a) Isometric view (b) X-Y view

Fig. 4.74 Damage indices of the ice sheet of 2.0 GPa weakness with unknown ice ridge information.

More than one weak region may exist for the same multi-year ice sheet. The following study focused on analyzing strength conditions of a mulit-year ice sheet with two weaknesses at $-11.5 \le x \le -9.2, -1.0 \le y \le 1.2$ m and $8.7 \le x \le 12.3, -2.2 \le y \le 1.6$ m. An example of a flat ice sheet without ridge was studied first as shown in Fig. 4.75, and the ice ridge was put back in the numerical model at a later stage. Note the two weak regions were intended to be unequally sized with a larger size on the right side.

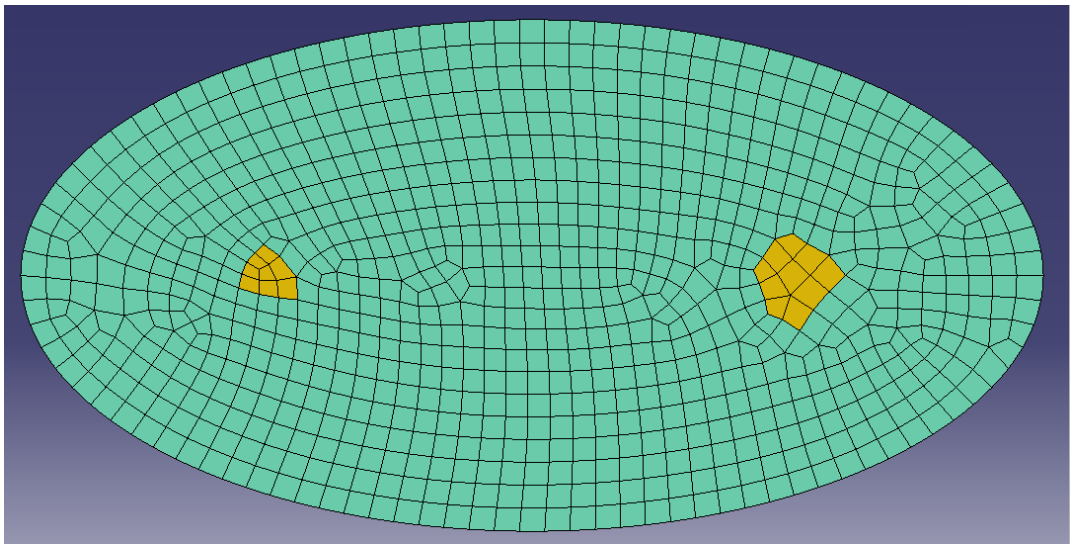

Fig. 4.75 A multi-year ice sheet with two weak regions.

Two different scenarios were examined here with various extents of damages. The first scenario placed a less severe damage on the left smaller area with Young‟s modulus of 2.0 GPa, and a more severe damage on the right larger area with Young‟s modulus of 0.2 GPa. The second scenario placed equal severe damages in both areas, 0.2 GPa of Young‟s modulus. The damage detection results are presented in Fig. 4.76 and 4.77. The damage index peak in the first scenario for the right damage was found to be $8 \le x \le 12, -1 \le y \le 2$ m and highlighted in red, which was a sucessful recognition. However, the method wasn‟t able to detect the less severe damage on the left.

When equal severity of damages were imposed on the ice sheet, the two weaknesses were both detected, located and sized as shown in Fig. 4.77. The damage on the left was located at $-11 \le x \le -9, -1 \le y \le 2$ m and The damage on the left was located at $8 \le x \le 12, -1 \le y \le 2$ m. Moreover, the larger damage on the right had a higher damage index peak than the smaller damage on the left, which sized the weaknesses correctly.

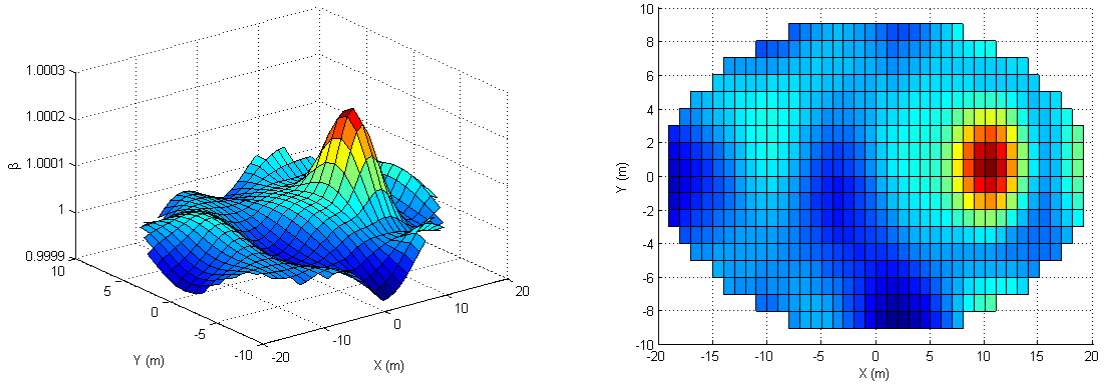

(a) Isometric view (b) X-Y view

Fig. 4.76 Damage indices of the ice sheet (2 weaknesses, 2.0 GPa in the left and 0.2 GPa in the right) with known ice ridge information.

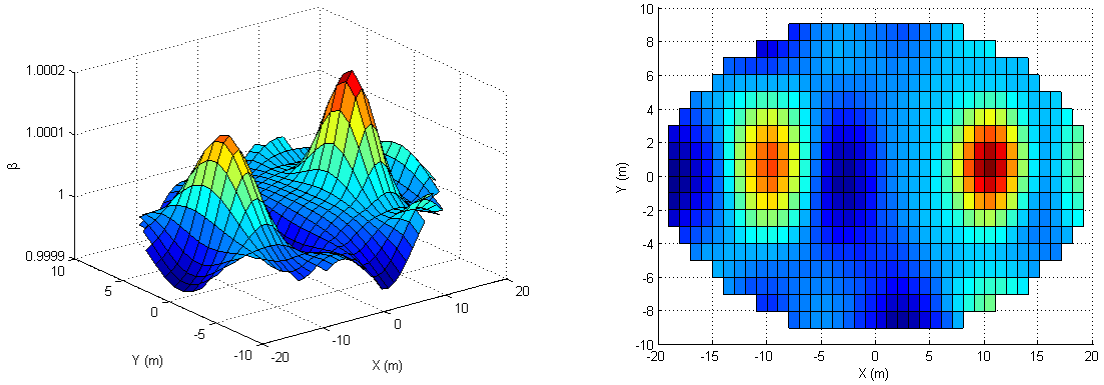

(a) Isometric view (b) X-Y view

Fig. 4.77 Damage indices of the ice sheet (2 weaknesses, 0.2 GPa in the left and 0.2 GPa in the right) with unknown ice ridge information.

At this point, the damage index method was applied to evaluate the strength conditions of the multi-year ice containing one ice ridge in the center right. The same two equal sized damages with Young‟s modulus of 0.2 GPa were assigned to the ice sheet. Again the damage indices were computed with both known and unknown ice ridges. When the ice ridge was known as illustrated in Fig. 4.78, the strength analysis results were very much similar to those in Fig. 4.77 for a non-ridge ice. The two damages were located and sized correctly. When the ice ridge was unkown, the strength analysis in Fig. 4.79 still can locate and size the two weaknesses, however, the ridge was only vaguely indicated.

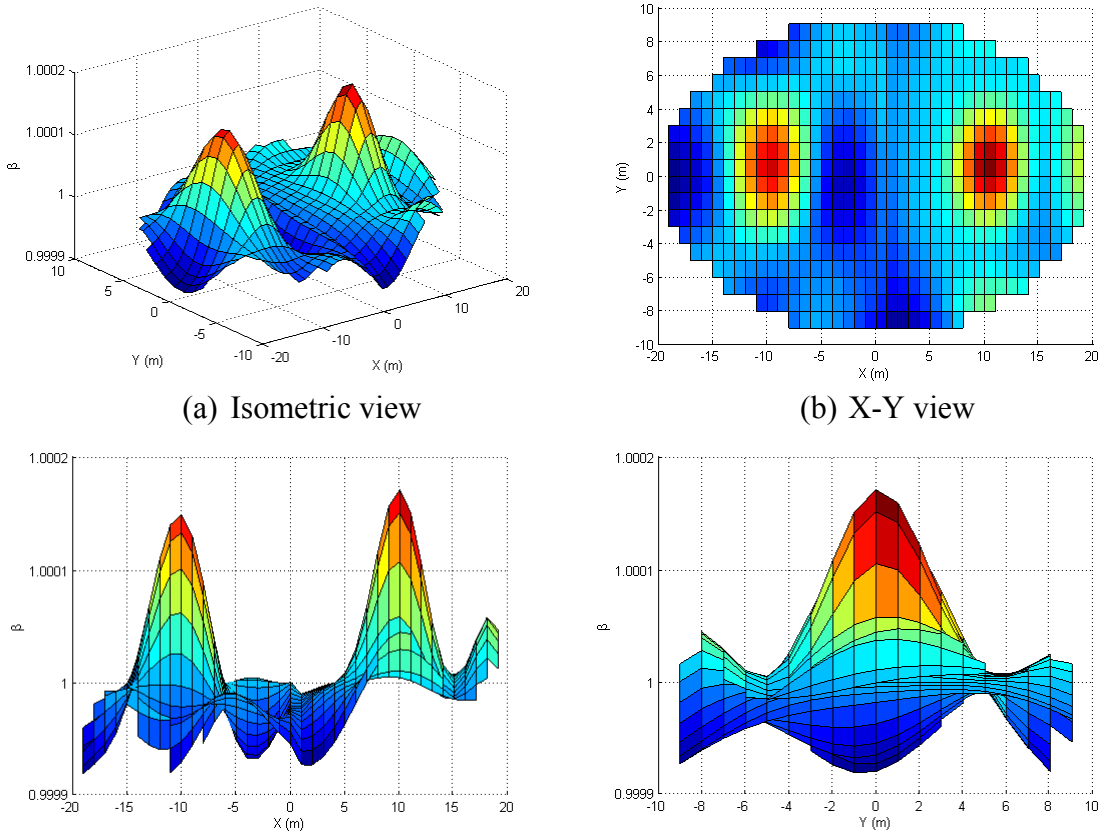

(a) Isometric view (b) X-Y view

(c) X-Z view (d) Y-Z view

Fig. 4.78 Damage indices of the ice sheet (2 weaknesses, 2.0 GPa in the left and 0.2 GPa in the right) with known ice ridge information.

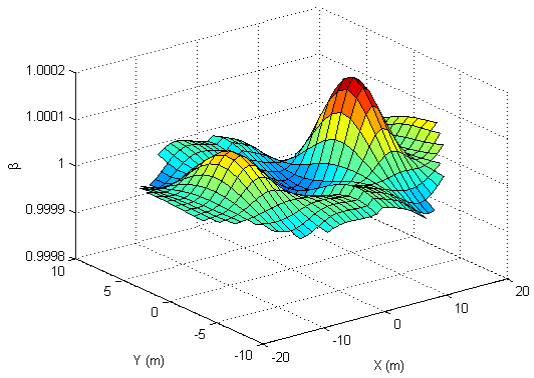

(a) Isometric view

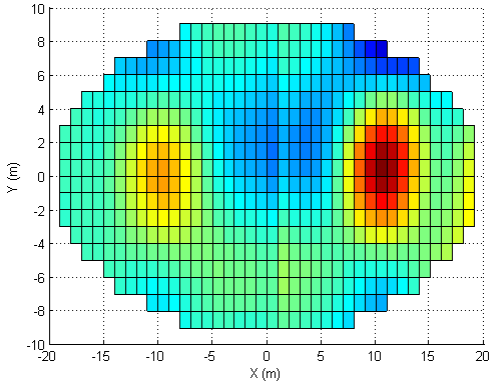

(b) X-Y view

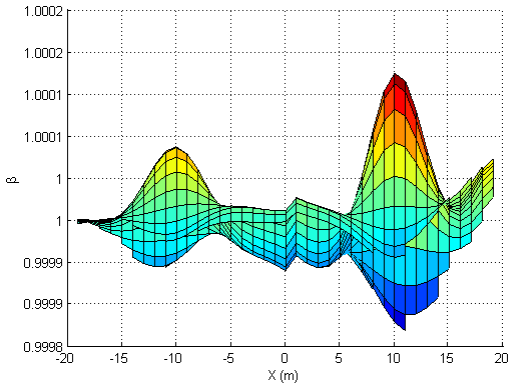

(e) X-Z view

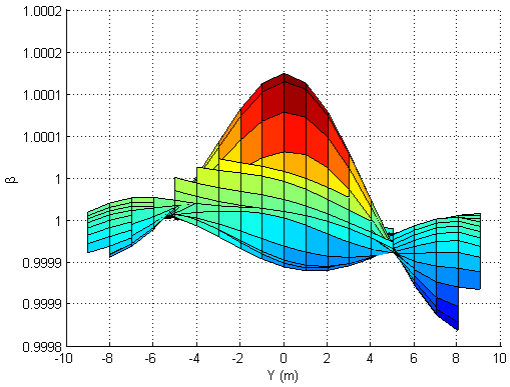

(f) Y-Z view

Fig. 4.79 Damage indices of ice sheets (2 weaknesses, 0.2 GPa in the left and 0.2 GPa in the right) with unknown ice ridge information.

5. SUMMARY

The search for new oil and gas resources has continually led the offshore industry to explore and recover these resources at worldwide sites that are often remote and pose very different design challenges. The designs of the needed offshore structures for these sites are expected to withstand harsh environmental conditions. Consequently, design engineers need to gather data prior to and after platform installation in order to validate or improve design criteria used in offshore engineering practice. The placement of sensors to recover global or localized response behavior is often limited by practical considerations, such as structural obstructions or limitations of the sensors selected. This leads to non-uniform spacing of the sensor information and naturally to questions about the ability to interpret the data, specifically what is the quality of the data that can be found regarding response behavior. Further this leads to questions regarding the optimal location for sensors to achieve the often multiple engineering objectives associated with the actual sensor measurements. This research study provides the necessary mathematical framework leading to a Matlab implementation that allows one to address practical examples in flow-induced experimental data as well as numerical simulation of ice floes.

The current research study focused on developing a comprehensive computational tool that could interrogate data collected from strategically deployed sensor arrays, review the dynamic responses of the structures of interest, evaluate the performances of response altering conditions, and identify regions of concern along the structure regarding possible failures. In addition, the computation tool was developed with the ability to evaluate the data recovered from various combinations of the sensors. The practical concern was to consider the number and location of sensors that must be developed in order to gather design information. This led to the investigation of sensor optimization using genetic algorithms in order to maximize the utility of available sensor arrays regarding specific engineering objectives. The modified time domain decomposition method and the damage index method were introduced to enable modal

parameter extraction and recognition, and the level III damage detection analysis. With this information, single or multi-objective optimization was pursued.

The first application of this new computational tool was to interpret various flow induced vibrations, which can be viewed as a 1-D problem regarding slender beam-like structures. The first issue addressed was to resolve the challenges in modal recognition and performance evaluation of attached devices, brought about by the multi-modal response behavior of marine risers and free-spanning pipelines. For example, natural frequencies of the structure may be too closely spaced to be differentiated resulting in a vague identification of vortex-induced vibration (VIV) excited modes using traditional lock-in criteria. Response evaluation of this computation tool was illustrated with two laboratory studies with different focuses and using both accelerometers and fiber optic sensors respectively. The test with acceleration input focused on the performance evaluation of two VIV suppression devices, an airfoil fairing and a less common ribbon faring, subjected to uniform current and a distinctive situation with combined loads of current and regular waves. The analysis results demonstrated the effectiveness of both fairings in suppressing VIV in uniform current. However, the ribbon fairing was effective in currents but not particularly effective in combined wave and current conditions. The airfoil fairings in the combined loads due to the dominance of waves were not effective and actually increased the amplitude of the motion. It was found that the airfoil fairings actually provided larger critical damping ratios than the ribbon fairings. The test with fiber optic sensors focused on extending analytical formulation for the time domain decomposition method to be compatible with strain input. This formulation was employed to study a unique experimental configuration of asymmetric buoyancy elements and helical strakes in comparison to the baseline bare cylinder case. The attachment of the devices resulted in distorted mode shapes and increased critical damping ratios.

The second important aspect in implementing the computation tool was sensor optimization via genetic algorithms which allowed one to address the number and location of the sensors. Initially, this was studied with a well-controlled numerical model

to fine tune the algorithm and then applied to the sufficiently instrumented fiber optic sensor test. The fine-tuned algorithm could successfully locate the optimal sensor array with limitations in placing sensors, and could work with a complicated multi-objective problem, namely, locating the optimal sensor array with the data collected through which to best recover two modes simultaneously using the modified time domain decomposition method.

The third aspect in implementing the computational tool was the application of the optimized sensor arrays, e.g. to perform damage analysis of subsea transmission lines using recovered mode shapes. Special efforts were made to tackle the challenges facing such structures in practice; specifically, the transmission lines may have non-uniform stiffness profiles due to localized strengthening and non-uniform mass profiles due to marine growth. The modified damage indices, included in the computational tool, located and sized the damages in most cases though excessive noises were present in the diagnosis.

The second application of the computational tool addressed the strength analysis of selected ice sheet formations, which was further simplified as a 2-D problem regarding plate-like structures. The vibration based strength analysis using strategized sensor arrays can be a valuable means to evaluate the ice threat toward offshore facilities in high Arctic waters. Besides having to deal with the exponentially increased computational volume from 1-D to 2-D, the analysis needed to address other challenges as well. One interesting challenge was to build an appropriate numerical model considering many of the unique physical features of sea ice. When extending the time domain decomposition technique for a plate-like structure, it was found with spline fitting and smoothing, a mode shape recovered from a coarse sensor array can potentially achieve similar levels of accuracy as from a fine sensor array. Moreover, when optimizing the sensor arrays, the effect of number of available sensors due to cost considerations, boundary conditions supporting the ice sheet, and regional restriction in placing sensors due to for example water ponds were investigated. The study confirmed that with increased numbers of sensors, the quality of modes recovered improved. The

same trend existed for placement restricted sensor arrays though the flaws of recovered mode shapes were still recognizable due to lack of the information in the restricted area. Multi-objective genetic algorithms were applied in search of the optimal sensor arrays for two modes with increased number of sensors. As a result of the search, a series of solutions on the Pareto front, dominating other solutions, converged yet with variation over generations of evolution. The damage detection analysis of ice sheet formations utilized multiple mode shapes to detect a series of damages with varied severity and the weighted damage index method performed better by excluding irrelevant noises. When water elasticity was considered in the analysis as it should be, the damage detection can still be done yet with less significant peaks. In addition, in light with the actual shape of floating pack ice, a more universal elliptical shaped ice sheet was considered for the analysis and results showed more noise in the resolved indices. As a final case, a multi-year ice with a strip shaped ice ridge was built for the analysis to detect one or two weaknesses. By constructing an intact ice sheet without prior information of the ice ridge, the damage index method actually can yield a more integrated result in a relative sense with both strengthened areas and weak areas identified and potentially sized.

Overall, the new computational tool, which integrated the modified time domain decomposition method, extreme response analysis, the damage index method, spectral analysis, sensor optimization, and the genetic algorithm, proved to be useful in dealing with sensor related problems involved in the offshore industry. The methodologies and application examples presented in this study suggest that with proper installation of the sensor arrays and analysis of the data collected, in depth knowledge of the dynamic responses and strength conditions of offshore structures can be achieved, which may lead to favorable technical and economic impact to the industry.

REFERENCES

Abaqus, 2011. *Abaqus, 6.11, Getting started with Abaqus: keywords edition*, Simulia, Providence, RI.

Abdul Razak, H., Choi, F.C., 2001. The effect of corrosion on the natural frequency and modal damping of reinforced concrete beams. Engineering Structures, 23(9), 1126-1133.

Aggarwal, R., D'Souza, R., 2011. Deepwater arctic-technical challenges and solutions. In: Proceedings of the annual OTC Arctic Technology Conference, OTC 22155, Houston, TX.

Alampalli, S., 2000. Effects of testing, analysis, damage, and environment on modal parameters. Mechanical Systems and Signal Processing, 14(1), 63-74.

Allen, D.W., 1993. Current tank tests of helical strakes on long slender tubes, vortex-induced vibration suppression of cylindrical structures data licensing. Data report 2. Shell Development Bellaire Research Center, Houston, TX.

Allen, D.W., Henning, D.L., Lee, L., 2004. Performance comparisons of helical strakes for VIV suppression of risers and tendons. In: Proceedings of the annual Offshore Technology Conference, OTC 16186, Houston, TX.

Allen, D.W., Henning, D.L., Lee, L., 2007. Drilling riser fairing tests at prototype Reynolds numbers. In: Proceedings of the 26th International Conference on Offshore Mechanics and Artic Engineering, OMAE 29219.

Allen, D.W., Henning, D.L., 2008. Fairings versus helical strakes for suppression of vortex-induced vibration: technical comparisons. In: Proceedings of the annual Offshore Technology Conference, OTC 19373, Houston, TX.

Allenmang, R.J., Brown D.L., 1982. A correlation coefficient for modal vector analysis. In: Proceedings of the 1st International Modal Analysis Conference, Orlando, FL.

Bai, Y., Bai, Q., 2005. *Subsea pipeline and risers*, 2nd ed., Elsevier Science.

Barroso, L.R., Rodriguez, R., 2004. Damage detection utilizing the damage index method to a benchmark structure. Engineering Mechanics, 130(2), 142-151.

Begg, R.D., Mackenzie, A.C., Dodds, C.J., Loland, O., 1976. Structural integrity monitoring using digital processing of vibration signals. In: Proceedings of the annual Offshore Technology Conference, OTC 2549, Houston, TX.

Bendat, J.S., Piersol, A.G., 1980. *Engineering applications of correlation and spectra analysis*, Wiley, NY.

Blevins, R. D, 1990. *Flow induced vibration*, 2nd ed., Van Nostrand Reinhold, NY.

Brown, M., Brown, M., Marr, D., English, M., Snell, R., 2005. Floating production mooring integrity JIP - key findings. In: Proceedings of the annual Offshore Technology Conference, OTC 17499, Houston, TX.

Brown, A.J., King, R., 2008. Tests with a flexible quasi-fairing to reduce riser drag, suppress VIV and limit drilling down-time. In: Proceedings of the annual Offshore Technology Conference, OTC 19161, Houston, TX.

Carrasco, C.J., Osegueda, R.A., Ferregut, C.M., Grygier, M., 1997. Damage localization in a space truss model using modal strain energy. In: Proceedings-SPIE the International Society for Optical Engineering, 1786-1792.

Catbas, F.N., Gul, M., Burkett, J.L., 2008. Conceptual damage-sensitive features for structural health monitoring: laboratory and field demonstrations. Mechanical Systems and Signal Processing, 22(7), 1650-1669.

Chance, J., Tomlinson, G.R., Worden, K., 1994. A simplified approach to the numerical and experimental modelling of the dynamics of a cracked beam. In: Proceedings-SPIE the International Society for Optical Engineering, 778-785.

Chitwood, J.S., 1998. Vortex-induced vibration of a slender horizontal cylinder in currents and waves, OTRC report No. 2/98-A9575.

Choi, S., Stubbs, N., 1997. Nondestructive damage detection algorithms for 2D plates. In: Proceedings of SPIE 3043, Smart Structures and Materials 1997: Smart Systems for Bridges, Structures, and Highways, San Diego, CA.

Chung, T.Y., 1987. Vortex-induced vibration of flexible cylinders in sheared flows, Ph.D. dissertation, MIT Department of Ocean Engineering, Cambridge, MA.

Coley, D.A., 1999. *An introduction to genetic algorithms for scientists and engineers*, World Scientific, Singapore.

Cornwell, P., Doebling, S.W., Farrar, C.R., 1999. Application of the strain energy damage detection method to plate-like structures. Journal of Sound and Vibration, 224(2), 359-374.

Cox, G.F.N., Weeks, W.F., 1988. Numerical simulations of the profile properties of undeformed first-year sea ice during the growth season. Journal of Geophysical Research: Oceans (1978–2012), 93(C10), 12449-12460.

Croasdale, K.R., Bruce, J.R., Liferov, P., 2009. Sea ice loads due to managed ice. In: Proceedings of the 20th International Conference on Port and Ocean Engineering under Arctic Conditions, Luleå, Sweden.

Culwell, A.S., 1997. Removal and disposal of deck and jacket structures. In: Proceedings of public workshop decommissioning and removal of oil and gas facilities offshore California: recent experiences and future deepwater challenges, Ventura, CA.

Dai, W., Bai, Y., 2011. Development of deepwater riser monitoring systems. In: Proceedings of the 3rd International Conference Measuring Technology and Mechatronics Automation, 1, 1050-1055.

Deb, K., Pratap, A., Agarwal, S., Meyarivan, T.A.M.T., 2002. A fast and elitist multiobjective genetic algorithm: NSGA-II. IEEE Transactions on Evolutionary Computation, 6(2), 182-197.

Det Norske Veritas (DNV), 1998. *Free spanning pipelines*, Guideline No. 14, DNV, Høvik, Norway.

Dickins, D., Wetzel, V., 1981. Multi-year pressure study. In: Proceedings of port and ocean engineering under arctic conditions, Quebec City, Queen Elizabeth Islands, Canada.

Doebling, S.W., Farrar, C.R., Prime, M.B., Shevitz, D.W., 1996. Damage identification and health monitoring of structural and mechanical systems from changes in their vibration characteristics: a literature review (No. LA--13070-MS). Los Alamos National Laboratory, Los Alamos, NM.

Doebling, S.W., Hemez, F.M., Peterson, L.D., Farhat, C., 1997. Improved damage location accuracy using strain energy-based mode selection criteria. The American Institute of Aeronautics and Astronautics, 35(4), 693-699.

Duggal, A., 2013. Invited lecture for the course Frontiers in Civil Engineering at Texas A&M University in Spring, 2013.

Dürr, S., Thomason, J., 2010. *Biofouling*, Wiley-Blackwell, Singapore.

Edmond, C., Liferov, P., Metge, M., 2011. Ice and iceberg management plans for Shtokman Field. In: Proceedings of the annual OTC Arctic Technology Conference, OTC 22103, Houston, TX.

Eik, K.J., 2011. Ice management in Arctic offshore operations and field developments, PhD thesis, Norwegian University of Science and Technology, 2010.

Every, M.J., King, R., 1979. Suppression flow induced vibrations – an experimental comparison of clamp-on devices. RHRA Report RR 1576.

Every, M.J., King, R., Weaver, D.S., 1982. Vortex-excited vibrations of cylinders and cables and their suppression, Ocean Engineering, 9(2), 135-157.

Fan, W., Qiao, P., 2011. Vibration-based damage identification methods: a review and comparative study. Structural Health Monitoring, 10(1), 83-111.

Fang, S.M., Niedzwecki, J.M., 2013. Comparison of airfoil and ribbon fairings for suppression of flow-induced vibrations, International Journal of Computational Methods and Experimental Measurements, 2(1).

Farrar, C.R., Jauregui, D.A., 1998. Comparative study of damage identification algorithms applied to a bridge: I. Experiment. Smart Materials and Structures, 7(5), 704.

Farrar, C.R., Worden, K., 2007. An introduction to structural health monitoring. Philosophical Transactions of the Royal Society A: Mathematical, Physical and Engineering Sciences, 365, 303-315.

Fardy, K.J., 1985. Gulf resources Canada well history report of Gulf et al. Akpak P-35 / 2P – 35, October 1985. In: http//gateway.nwtgeoscience.ca/(compilation of Canadian Beaufort Sea exploration well histories).

Fayyadh, Abdul Razak, 2001. Detection of damage location using mode shape deviation: Numerical study. International Journal of the Physical Sciences, 6(24), 5688-5698.

Fissel, D.B., Marko, J.R., Melling, H., 2008. Advances in marine ice profiling for oil and gas applications. In: Proceedings of Ice Tech Conference, 20-23.

Fox, C.H.J., 1992. The location of defects in structures: A comparison of the use of natural frequency and mode shape data. In: Proceedings of the 10th International Modal Analysis Conference, San Diego, CA, 522-528.

Frank, W.R., Tognarelli, M.A., Slocum, S.T., Campbell, R.B., Balasubramanian, S., 2004. Flow-induced vibration of a long, flexible, straked cylinder in uniform and linearly sheared currents. In: Proceedings of the annual Offshore Technology Conference, OTC 16340, Houston, TX.

Frankenstein, G., Garner, R., 1967. Equations for determining the brine volume of sea ice from -0.5 ^{o}C to-22.9 ^{o}C. Journal of Glaciology, 6, 943-944.

Fu, S., Ren, T., Li, R., Wang, X., 2011. Experimental investigation on VIV of the flexible model under full scale Re number. In: Proceedings of the 30th International Conference on Offshore Mechanics and Arctic Engineering, OMAE2011-49042, Rotterdam, The Netherlands.

Gao, H., Rose, J. L., 2006. Sensor placement optimization in structural health monitoring using genetic and evolutionary strategy. Smart Structures and Materials, 617410-1-617410-12.

Gere J.M., Timoshenko S.P., 1997. *Mechanics of materials*, 4th ed., PWS Publishing Company, Boston, MA.

Guo, H.Y., Zhang, L., Zhang, L.L., Zhou, J.X., 2004. Optimal placement of sensors for structural health monitoring using improved genetic algorithms.Smart Materials and Structures, 13(3), 528.

Hamilton, J., Holub, C., Blunt, J., Mitchell, D., Kokkinis, T., 2011. Ice management for support of Arctic floating operations. In: Proceedings of the annual OTC Arctic Technology Conference, OTC 22105, Houston, TX.

Heaf, N., 1979. The effect of marine growth on the performance of fixed offshore platforms in the North Sea. In: Proceedings of the annual Offshore Technology Conference, OTC 3386, Houston, TX.

Holden, O.M., Paulsen, G., Marthinsen, T., 2006. Ormen Lange pipelines seabed intervention design in deep water. In: Proceedings of International Offshore and Polar Engineering Conference, ISOPE, San Francisco, CA.

Horn, J., Nafpliotis, N., Goldberg, D.E., 1994. A niched Pareto genetic algorithm for multiobjective optimization. In: Proceedings of the 1st IEEE Conference on Evolutionary Computation, 82-87.

Howell, G., Duggal, A., Lever, G., 2001. The terra nova FPSO turret mooring system. In: Proceedings of the annual Offshore Technology Conference, OTC 13020, Houston, TX.

Hu, H., Wu, C., 2009. Development of scanning damage index for the damage detection of plate structures using modal strain energy method. Mechanical Systems and Signal Processing, 23(2), 274-287.

Huffingtonpost, 2013. Arctic sea ice decline accelerated by more melt ponds, study finds. http://www.huffingtonpost.com/2013/01/22/arctic-sea-icedecline_n_2526355.html

Humphries, M., Pirog, R., Whitney, G., 2010. U.S. Offshore oil and gas resources: prospects and processes. CRS report for Congress.

Ibrahim, S.R., Mikulcik, E.C., 1977. A method for the direct identification of vibration parameters from the free response. Shock and Vibration Bulletin, 47 (4), 183–198.

Inaudi, D., Glisic, B., 2006. Fiber optic sensing for innovative oil gas production and transport systems. In: Proceedings of the18th International Conference on Optical Fiber Sensors, Cancun, Mexico.

ISO 19906, 2010, Petroleum and natural gas industries – Arctic offshore structures, European Committee for Standardization, published in Switzerland.

Jaiswal, V., Vandiver, J.K., 3007. VIV response prediction for long risers with variable damping. In: Proceedings of the 26th International Conference on Offshore Mechanics and Arctic Engineering, OMAE2007-29353, San Diego, CA.

Jhingran, V., Zhang, H., Lie, H., Bratten, H., Vandiver, J.K., 2012. Spacing implications for fatigue damage due to vortex-induced vibrations on a steel lazy wave riser (SLWR). In: Proceedings of the annual Offshore Technology Conference, OTC 23672, Houston, TX.

Juang, J.N., Pappa, R.S., 1985. An eigensystem realization algorithm for modal parameter identification and model reduction. Journal of Guidance, Control, and Dynamics, 8(5), 620-627.

Kaasen, K.E., 2001. Optimizing sensor locations for identification of riser VIV modes. In: Proceedings of the 11th International Offshore and Polar Engineering Conference, ISOPE, Stavanger, Norway.

Kammer, D.C., 1991. Sensor placement for on-orbit modal identification and correlation of large space structures. Journal of Guidance, Control, and Dynamics, 14(2), 251-259.

Kirkegaard, P.H., Brincker, R., 1994. On the optimal location of sensors for parametric identification of linear structural systems. Mechanical Systems and Signal Processing, 8(6), 639-647.

Kim, B.H., Stubbs, N., Park, T., 2005. A new method to extract modal parameters using output-only responses. Journal of Sound and Vibration, 282, 215-230.

Kim, B.H., Park J.C., Park, M.S., 2008. Modal parameter extraction for Soehae cable-stayed bridge using TDD technique. In: Proceedings of the 4th International IABMAS Conference, Seoul, Korea.

Kim, B.H., Lee, J., Lee, D.H., 2010. Extracting modal parameters of high-speed railway bridge using the TDD technique. Mechanical Systems and Signal Processing, 24(3), 707-720.

Konak, A., Coit, D.W., Smith, A.E., 2006. Multi-objective optimization using genetic algorithms: A tutorial. Reliability Engineering System Safety, 91(9), 992-1007.

Kovacs, A., 1997. The bulk salinity of Arctic and Antarctic sea ice versus thickness. In: Proceedings of the 16th International Conference on Offshore Mechanics and Arctic Engineering, OMAE, Yokohama, Japan.

Kumar, R.A., Sohn, C.H., Gowda, B.H.L., 2008. Passive control of Vortex-Induced Vibrations: An Overview. Recent Patents on Mechanical Engineering, 1, 1-11.

Kwon, S.H., Cho, J.W., Park, J.S., Choi, H.S., 2002. The effects of drag reduction by ribbons attached to cylindrical pipes. Ocean Engineering, 29, 1945-1958.

Lake, R.A., Lewis, E.L., 1970. Salt rejection by sea ice during growth. Journal of Geophysical Research, 75(3), 583-597.

Li, L., Fu, S., Yang, J., Ren, T., 2011. Experimental investigation on VIV of risers with staggered buoyancy. In: Proceedings of the 30th International Conference on Offshore Mechanics and Arctic Engineering, OMAE2011-49046, Rotterdam, The Netherlands.

Li, X., Bose, N., Zhu, L., Spencer, D., 2005. Multi-modal VIV tests for a highly flexible model riser. International Symposium on Technology of Ultra Deep Ocean Engineering, Tokyo, Japan.

Lie, H., Larsen, C.M., Vandiver, J.K., 1997. Vortex Induced Vibrations of long marine risers; Model test in a rotating rig. In: Proceedings of the 16th International Conference on Offshore Mechanics and Arctic Engineering, OMAE, Yokohama, Japan.

Liu, W., Gao, W.C., Sun, Y., Xu, M.J., 2008. Optimal sensor placement for spatial lattice structure based on genetic algorithms. Journal of Sound and Vibration, 317(1), 175-189.

Marcellus, R.W., Morrison, T.B., Morrison, T. B., 1982. Ice design statistics for the Canadian Beaufort Sea. Canada Marine Engineering Limited.

McCann, D.M., Forde, M.C., 2001. Review of NDT methods in the assessment of concrete and masonry structures. NDT E International, 34(2), 71-84.

Moe, G., Teigen, T. Lie, H., 2004. Predictions and model tests of a SCR undergoing VIV in flow at oblique angles, In: Proceedings of the 23rd International Conference on Offshore Mechanics and Arctic Engineering, OMAE 2004-51563, Rotterdam, The Netherlands.

Morikawa, S.R.K., Camerinia, C.S., Pipaa, D.R., Santosa, J.M.C., Piresa, G.P., Bragab, A.M.B., Llergenab, R.W.A., Ribeirob, A.S., 2008. Monitoring of flexible oil lines using FBG sensors. In: Proceedings of the 19th International Conference on Optical Fibre Sensors, Perth, WA, Australia.

MXAK, 2013. BeauDril: Kulluk – conical drilling unit. http://www.mxak.org/community/kulluk/kullukmore.html

Nakamura, M., Koterayama, W., 1992. A study on cable fairing. In: Proceedings of the 2nd International Offshore Polar Engineering Conference, San Francisco, CA.

Natarajan, S., Howells, H., Deka, D., Walters, D., 2006. Optimization of sensor placement to capture riser VIV response. In: Proceedings of the 25th International Conference on Offshore Mechanics and Arctic Engineering, OMAE, Hamburg, Germany.

Natarajan, S., Podskarbi, M., Karayaka, M., Chevron, E.T.C., Howells, H., 2007. Deepwater spar steel catenary riser monitoring strategy. In: Proceedings of the 26th International Conference on Offshore Mechanics and Arctic Engineering, San Diego, CA.

Nicholson, D.W., Alnefaie, K.A., 2000. Modal moment index for damage detection in beam structures. Acta Mechanica, 144(3-4), 155-167.

Niedzwecki, J.M., Fang, S.M., 2013. Suppression of flow-induced vibrations using ribbon fairings, International Journal of Computational Methods and Experimental Measurements, 1(4).

Niedzwecki, J.M., Liagre, P.-Y.F., 2003. System identification of distributed-parameter marine riser models, Ocean Engineering, 30, 1387-1415.

Niedzwecki, J.M. and Moe, G., 2005. Investigation of a catenary riser undergoing VIV. In: Proceedings of the 3rd International Conference on Fluid Structure Interactions, La Coruna, Spain, 217-224.

Nielsen, G.F., Soreide, T.H., Kvarme, S.O., 2002. VIV response of long free spanning pipelines. In: Proceedings of the 21st International Conference on Offshore Mechanics and Arctic Engineering, OMAE 2002-28075, Oslo, Norway.

NOAA, 2013. The GRIP ice coring effort. http://www.ncdc.noaa.gov/paleo/icecore/greenland/summit/document/

Owen, J. C., Bearman, P.W., 2001. Passive control of VIV with drag reduction. Journal of Fluids and Structures, 15, 597-605.

Offshorediver, 2013. Photo gallery of divers in past projects. www.offshorediver.com/content/

Page, H.M., Dugan, J.E., Piltz, F., 2010. Fouling and antifouling in oil and other offshore industries. Biofouling, 252-266.

Palmer, A., Croasdale, K., 2012. *Arctic offshore engineering,* World Scientific Publishing Company, Hackensack, NJ.

Pandey, A.K., Biswas, M., Samman, M.M., 1991. Damage detection from changes in curvature mode shapes. Journal of Sound and Vibration, 145(2), 321-332.

Pandey, A.K., Biswas, M., 1994. Damage detection in structures using changes in flexibility. Journal of Sound and Vibration, 169(1), 3-17.

Prastianto R.W., Otsuka, K., Ikeda, Y., 2007. A small scale experiment for multi-modal VIV response of a long flexible horizontal cylinder. In: Proceedings of the 17th International Offshore and Polar Engineering Conference, ISOPE, Lisbon, Portugal.

Rao, M.A., Srinivas, J., Murthy, B.S.N., 2004. Damage detection in vibrating bodies using genetic algorithms. Computers & Structures, 82(11), 963-968.

Rao, S.S., 2007. *Vibration of continuous systems*, John Wiley Sons, Hoboken, NJ.

Rechenberg, I., 1965. Cybernetic solution path of an experimental problem. Ministry of Aviation, Royal Aircraft Establishment (U.K.).

Rytter, A., 1993. Vibration based inspection of civil engineering structures, PhD Dissertation, University of Aalborg, Aalborg, Denmark.

Sanderson, T.J., 1988. *Ice mechanics and risks to offshore structures*, Graham & Trotman, London, UK.

Sarpkaya, T., 2010. *Wave forces on offshore structures*, 1st ed., Cambridge University Press, NY.

Seyedpoor, S.M., 2012. A two stage method for structural damage detection using a modal strain energy based index and particle swarm optimization. International Journal of Non-Linear Mechanics, 47(1), 1-8.

Shi, Z.Y., Law, S.S., Zhang, L.M., 1998. Structural damage localization from modal strain energy change. Journal of Sound and Vibration, 218(5), 825-844.

Shi, Z.Y., Law, S.S., Zhang, L., 2000. Structural damage detection from modal strain energy change. Journal of Engineering Mechanics, 126(12), 1216-1223.

Shi, Z.Y., Law, S.S., Zhang, L.M., 2002. Improved damage quantification from elemental modal strain energy change. Journal of Engineering Mechanics, 128(5), 521-529.

Snel, J, 2008. Mooring systems in Arctic environments. Master‟s thesis, Delft University of Technology, Delft, Netherland.

Sohn, H., Farrar, C.R., Hemez, F.M., Shunk, D.D., Stinemates, D.W., Nadler, B.R., Czarnecki, J.J., 2004. A review of structural health monitoring literature: 1996–2001. Los Alamos National Laboratory, LA-13976-MS, Los Alamos, NM.

Squire, V.A., 1996. *Moving loads on ice plates*, Kluwer Academic Publishers, Dordrecht, The Netherlands.

Staszewski, W.J., Worden, K., 2001. Overview of optimal sensor location methods for damage detection. In: Proceedings of SPIE‟s 8th Annual International Symposium on Smart Structures and Materials, 179-187.

Stubbs, N., Fang, S.M., Li, R., 2012. Class lecture for the course System Identification at Texas A&M University in Spring, 2012.

Stubbs, N., Kim, J.T., Topole, K., 1992. An efficient and robust algorithm for damage localization in offshore platforms. In: Proceedings of ASCE‟s 10th Structures Congress, San Antonio, Texas, 543-546.

Stubbs, N., Kim, J.T., Farrar, C.R., 1995. Field verification of a nondestructive damage localization and severity estimation algorithm. In: Proceedings of 13th International Modal Analysis Conference, Jacksonville, FL, 210-218.

Stubbs, N., Park, S., 1996. Optimal sensor placement for mode shapes via Shannon's sampling theorem. Computer-Aided Civil and Infrastructure Engineering, 11(6), 411-419.

Stubbs, N., 2011. A literature review of recent methods for structural health monitoring systems to evaluate structural capacity and remaining service life of bridges, Final Report, Iowa State University Bridge Engineering Center.

Subsea Explore Services, 2013. Diving solutions. http://www.subsearov.com

Taggart, S., Tognarelli, M.A., 2008. Offshore drilling riser VIV suppression devices – What‟s available to operators? In: Proceedings of the 27th International Conference on Offshore Mechanics and Artic Engineering, OMAE2008-57047, Estoril, Portugal.

Timco, G.W., Weeks, W.F., 2010. A review of the engineering properties of sea ice. Cold Regions Science and Technology, 60(2), 107-129.

Trim, A.D., Braaten, H., Lie, H., Tognarelli, M.A., 2005. Experimental investigation of vortex-induced vibration of long marine risers, Journal of Fluids and Structures, 21, 335-361.

Unger, J.F., Teughels, A., De Roeck, G., 2006. System identification and damage detection of a prestressed concrete beam. Journal of Structural Engineering, 132(11), 1691-1698.

US Geological Survey, 2008. Circum-Arctic resource appraisal: Estimates of undiscovered oil and gas north of the Arctic Circle. US Department of the Interior.

UCL, 2013. Information about research: sediment deformation. http://www.es.ucl.ac.uk/ripl/research/sed_def_res.htm

Vandiver, J.K., 1975. Detection of structural failure on fixed platforms by measurement of dynamic response. In: Proceedings of the annual Offshore Technology Conference, OTC 2267, Houston, TX.

Vandiver, J.K., 1977. Detection of structural failure on fixed platforms by measurement of dynamic response. Journal of Petroleum Technology, 305–310.

Vandiver, J.K., 1993. Dimensionless parameters important to the prediction of vortex-induced vibration of long, flexible cylinders in ocean currents. Journal of Fluids and Structures, 7(5), 423-455.

Vandiver J.K., Peoples W.W., 2003. The effect of staggered buoyancy modules on flow-induced vibration of marine risers. In: Proceedings of the annual offshore technology conference, OTC 15284, Houston, TX.

Vandiver, J.K., Swithenbank, S., Jaiswal, V., 2006. The effectiveness of helical strakes in the suppression of high mode number VIV. In: Proceedings of the annual Offshore Technology Conference, OTC 18276, Houston, TX.

Voice of Russia, 2013. Latvian anglers picked from ice floe. http://voiceofrussia.com/2013_03_29/Latvian-anglers-picked-from-ice-floe-080/

Wang, J., Qiao, P., 2008. On irregularity-based damage detection method for cracked beams. International Journal of Solids and Structures, 45(2), 688-704.

Weeks, W.F., Assur, A., 1967. The mechanical properties of sea ice. Cold Regions Science and Engineering, Part II, Physical Science, Section C, Physics and Mechanics of Ice, Cold Regions Research & Engineering Laboratory, Hanover, NH.

Weeks, W.F., Gow, A.J., 1980. Crystal alignments in the fast ice of Arctic Alaska. Journal of Geophysical Research: Oceans (1978–2012), 85(C2), 1137-1146.

Weeks, W.F., Mellor, M., 1984. Mechanical properties of ice in Arctic seas. Arctic Technology and Policy, ed. I. Dyer and C. Cryssostomidis, Hemisphere, WA, 235-259.

Wilde, I.J.J.D., Huijsmans, R.H.M., 2004. Laboratory investigation of long riser VIV response. In: Proceedings of the 14th International Offshore and Polar Engineering Conference, ISOPE, Toulon, France.

Worden, K., Burrows, A.P., Tomlinson, G.R., 1995. A combined neural and genetic approach to sensor placement. In: Proceedings of 13th International Modal Analysis Conference, Jacksonville, FL, 1727-1736.

Worden, K., Burrows, A.P., 2001. Optimal sensor placement for fault detection. Engineering Structures, 23(8), 885-901.

Yam, L.H., Li, Y.Y., Wong, W.O., 2002. Sensitivity studies of parameters for damage detection of plate-like structures using static and dynamic approaches. Engineering Structures, 24(11), 1465-1475.

Yang, B., 2005. *Stress, strain, and structural dynamics: an interactive handbook of formulas, solutions, and MATLAB toolboxes*, Academic Press, Burlington, MA.

Yao, L., Sethares, W.A., Kammer, D.C., 1993. Sensor placement for on-orbit modal identification via a genetic algorithm. The American Institute of Aeronautics and Astronautics, 31(10), 1922-1928.

Yi, T.H., Li, H.N., 2012. Methodology developments in sensor placement for health monitoring of civil infrastructures. International Journal of Distributed Sensor Networks, 2012.

Zhao, J., DeWolf, J.T., 1999. Sensitivity study for vibrational parameters used in damage detection. Journal of Structural Engineering, 125(4), 410-416.

Zdravkovich. M.M., 1981. Review and classification of various aerodynamic and hydrodynamic means for suppressing vortex shedding. Journal of Wind Engineering and Industrial Aerodynamics, 7(2), 145-189.